Dynamic Characteristics and Wind-induced Response of a Tall Building

Alan James Moore

A thesis submitted in fulfillment
of the requirements for the degree of
Doctor of Philosophy

School of Civil Engineering
The University of Sydney

June 2016

Declaration

I hereby declare that this submission is my own work and that, to the best of my knowledge and belief, it contains no material previously published or written by another person nor material which to a substantial extent has been accepted for the award of any other degree or diploma of the University or other institute of higher learning, except where due acknowledgement has been made in the text.

Alan James Moore

30 June 2016

Abstract

The design of tall buildings requires an accurate understanding of the expected wind loads and the resulting responses. The techniques used to estimate the wind-induced response are subject to uncertainty, which can result in unsatisfactory building performance or an over-designed structure. Altering the structure to rectify unsatisfactory performance can be extremely difficult and prohibitively expensive, while an over-designed structure represents unnecessary cost to the owner. This implies that accurate estimates of wind loads and responses are crucial to tall building design.

Two aspects of tall building wind-induced response estimation are investigated: the estimation of natural frequencies and damping ratios; and the understanding of mechanisms causing wind-induced responses. This was primarily conducted via full-scale testing of a tall building. The building used for full-scale measurements is Latitude tower, an office tower located in the Sydney central business district, with a height of 187 m above ground and 28 m of underground levels. The building has a composite design including a reinforced concrete core, and reinforced concrete floor slabs supported by steel beams spanning between the core and perimeter columns. Outriggers linking the core and perimeter columns, as well as offset outriggers at the facade, are located at mid-height.

The full-scale testing was conducted in two parts: vibration testing during construction; and a two year monitoring programme commenced after construction completion. Vibration testing during construction was conducted to determine the natural frequencies and damping ratios as the structure changed. Forced vibration testing and ambient vibration testing techniques were used. The Frequency Domain Decomposition and Stochastic Subspace Identification techniques were used to estimate the natural frequencies and damping ratios from the ambient vibration test outputs. The natural frequencies and damping ratios from the forced and ambient vibration tests differed by less than 5% and 30% respectively.

Changes in the fundamental natural frequencies during construction were discussed in conjunction with the structural changes to further the understanding of how changes in the stiffness and mass of a tall building influence the natural frequencies. The measured natural frequencies during the early stages of construction were used to update a finite element model representing the structure at the time

of testing. The material properties and floor beams were the primary focus of the model updating. The knowledge gained from partial structure updating was applied to a model of the completed structure, and the natural frequency estimate errors improved from 17% to 7%. The fundamental mode damping ratios measured during construction changed by less than 15% between the first test, conducted when 38% of the tower height was reached, and the final test at construction completion.

The wind-induced monitoring programme included the measurement of wind velocities, accelerations, and displacements at the top of the building. The peak events for southerly and westerly wind directions were discussed. It was found that the acceleration response was dominated by the fundamental vibration mode. For southerly winds this corresponded to an along-wind response, but for westerly winds this corresponds to a cross-wind response. The probability distributions of upcrossings for along-wind and cross-wind responses where not significantly different to a Gaussian distribution for both southerly and westerly winds. The slope of the linear least squares fit was greater than two in all cases, which suggested intermittent characteristics were present in the responses. The standard deviation resonant acceleration responses from a high frequency base balance wind tunnel test were within 29% of the measured values.

Conference Papers

Moore, A.J. and Wood, G.S., 'Comparison of dynamic characteristics from full-scale measurements and finite element models of a tall building,' 12th Australasian Wind Engineering Society Workshop, Queenstown, New Zealand, February 2006.

Moore, A.J. and Wood, G.S., 'Measurement of dynamic characteristics of a tall building,' 11th Australasian Wind Engineering Society Workshop, Darwin, Australia, June 2004.

Acknowledgements

My thanks also to the Graduate School of Engineering at The University of Sydney, particularly George Carayannopoulos, Emily Major, and Lesley Vanderkwast. Their help and guidance through the administration of my candidature and submission of the final thesis was excellent, and much appreciated.

This research was supported via a scholarship jointly funded by the Wind Engineering Services at The University of Sydney, the Allen D. McConnell Scholarship, and The Civil Engineering Foundation at The University of Sydney. I am most grateful for the generosity and opportunities afforded to me, and in particular to the late Allen McConnell and Joan McConnell for their support of research in the field of fluid mechanics.

The final thank you is saved for my supervisor, Graeme Wood. He is the person who sparked my interest in wind engineering and experimental research during my undergraduate honours thesis. His support and guidance has been greatly appreciated for facilitating and enriching my research, and his character has always provided a wealth of positive influences.

Contents

List of Figures

List of Tables

Nomenclature

Notation

A	Cross sectional area [m²]
$\boldsymbol{A}_c$	Continuous time state matrix for state space model
$\boldsymbol{A}_d$	Discrete time state matrix for state space model
a_r	Reference amplitude for RD trigger condition
$\boldsymbol{B}_c$	Continuous time input matrix for state space model
$\boldsymbol{B}_d$	Discrete time input matrix for state space model
b	Plan breadth of building normal to the wind direction [m]
C_i	Constant of integration ($i = 1, 2, 3, \ldots, n$
$\boldsymbol{C}$	Damping matrix
$\boldsymbol{C}_c$	Continuous time output matrix for state space model
$\boldsymbol{C}_d$	Discrete time output matrix for state space model
$\boldsymbol{C}_{yy}$	Response covariance matrix
c_{cr}	Critical damping coefficient
c_i	Viscous damping coefficient of element i
$\boldsymbol{D}_c$	Continuous time direct transmission matrix for state space model
$\boldsymbol{D}_d$	Discrete time direct transmission for state space model
D_{xx}	Random decrement function
d	Plan depth of building in direction of vibration motion [m]
E	Elastic modulus [MPa]
E_c	Elastic modulus of concrete [MPa]
E_{cR}	Dynamic elastic modulus of concrete [MPa]
f	Frequency of vibration for the fundamental translational mode [Hz]
f_f	Fundamental natural frequency of a flexural beam model [Hz]
f_i	Frequency of vibration for the ith translational mode [Hz]
f_s	Fundamental natural frequency of a shear beam model [Hz]
f_t	Frequency of vibration for the fundamental torsional mode [Hz]
f_{ti}	Frequency of vibration for the ith torsional mode [Hz]

f_{xi}	Frequency of vibration for the ith x-axis translational mode [Hz]
f_{yi}	Frequency of vibration for the ith y-axis translational mode [Hz]
f'_c	Concrete characteristic compressive cylinder strength at 28 days [MPa]
G	Shear modulus [GPa]
$\boldsymbol{G}_{qq}$	Modal coordinates spectrum matrix
$\boldsymbol{G}_{yy}$	Response spectrum matrix
g	Peak factor
g_f	Peak factor based on a distribution of largest values
$g_{(\mathrm{P}>a)}$	Peak factor related to a specific probability level
h_b	Building height measured from base of structure [m]
h	Building height measured from ground level [m]
$\boldsymbol{I}$	Identity matrix
I	Area moment of inertia [m^4]
I_p	Polar area moment of inertia [m^4]
I_u	Turbulence intensity of longitudinal wind speed
J	Torsion constant [m^4]
j	Imaginary unit $j = \sqrt{-1}$
$\boldsymbol{K}$	Stiffness matrix
k_i	Stiffness of element i
L	Length of a beam [m]
$\boldsymbol{M}$	Mass matrix
m	Mass per unit length [kg/m]
m_i	Mass of element i [kg]
N_c	Number of cycles in a RD signature
N_s	Number of segments used to generate a RD signature
n_0	Mean value crossing rate for peak factor estimation
$\boldsymbol{P}$	Input influence matrix
$q_i(t)$	ith generalised coordinate at time t
$\boldsymbol{S}$	Singular value matrix
S_{xx}	Spectral density of x
T	Period of vibration for the fundamental translational mode [s]
T_i	Period of vibration for the ith translational mode [s]
T_t	Period of vibration for the fundamental torsional mode [s]
T_{ti}	Period of vibration for the ith torsional mode [s]
T_c	Random decrement trigger condition
t	Time [s]

t_{cR}	Loading rate of concrete [s]
U	Wind speed [m/s]
$\boldsymbol{U}$	Singular vector matrix
$\boldsymbol{w}(t)$	Process noise vector
x	Displacement [m]
$\boldsymbol{y}(t)$	Output vector
β	Angle of wind direction measured clockwise from North
Δa_r	Reference amplitude tolerance for RD trigger condition
δ	Logarithmic decrement
λ_i	Continuous time eigenvalue
$\boldsymbol{\Omega}$	Diagonal matrix of circular eigenfrequencies ω_i
ω_i	Circular eigenfrequency [rad/s]
ω_d	Damped natural frequency [rad/s]
ω_n	Natural frequency [rad/s]
κ	Shear coefficient
$\boldsymbol{\eta}(t)$	Normalised principal coordinate at time t
ν	Poisson's ratio
$\boldsymbol{\Lambda}$	Diagonal matrix containing the discrete time eigenvalues $\mu_i,\ \mu_i^*$
μ_i	Discrete time eigenvalue
$\boldsymbol{\nu}(t)$	Measurement noise vector
ρ	Mass density [kg/m^3]
$\boldsymbol{\Phi}$	Real eigenvector matrix
$\boldsymbol{\phi}_i$	Real eigenvector
$\boldsymbol{\Psi}$	Complex eigenvector matrix
$\boldsymbol{\psi}_i$	Complex eigenvector
τ	Time variable
θ	Angle of the wind direction to the building orthogonal axes
$\boldsymbol{\xi}_d, \boldsymbol{\xi}_v, \boldsymbol{\xi}_a$	Output location matrices for displacement, velocity, and acceleration
ζ_i	Damping ratio for the ith vibration mode [%]
σ_ζ	Standard deviation of damping ratio estimate [%]
$\bar{\cdot}$	Mean value
$\hat{\cdot}$	Peak value
$\sigma_\cdot$	Standard deviation
$\dot{\cdot}$	Velocity
$\ddot{\cdot}$	Acceleration
$(\cdot)^{-1}$	Matrix inverse

$(\cdot)^T$	Matrix transpose
$(\cdot)^*$	Complex conjugate
$(\cdot)^H$	Complex conjugate transpose
$\lceil \diagdown \rfloor$	Diagonal matrix
$\mathrm{E}[\cdot]$	Expected value
$\mathrm{Re}(\cdot)$	Real component
$\mathrm{Im}(\cdot)$	Imaginary component

General Symbol Format

Matrix symbols are represented by bold type capitol letters.

Vector symbols are represented by bold type lower case letters.

Abbreviations

ACU	Accelerometer Conditioning Unit
ADC	Analogue to Digital Converter
AVT	Ambient Vibration Test
CMIF	Complex Mode Indication Function
CQC	Complete Quadratic Combination
DGPS	Differential Global Positioning System
FDD	Frequency Domain Decomposition
FE	Finite Element
FEA	Finite Element Analysis
FEM	Finite Element Method
FVT	Forced Vibration Test
GPS	Global Positioning System
HFBB	High Frequency Base Balance
LL	Live Load
NMEA	National Marine Electronics Association
NTP	Network Time Protocol
RC	Reinforced Concrete
RD	Random Decrement
RTK-GPS	Real Time Kinematic Global Positioning System
SDL	Standard Dead Load
SSI	Stochastic Subspace Identification
SVD	Singular Value Decomposition
USCGS	United States Coast and Geodetic Survey

Units

g_n	Standard value of acceleration due to gravity; $1\,g_n = 9.81\,\mathrm{m\,s^{-2}}$
mg_n	milli-gravity

Glossary of Terms

amplitude beat an interference between two vibration modes with frequencies that are close together, and manifests as periodic variations in the amplitude of vibration.

Beaufort Scale An empirical measure for describing wind speed.

BNC connector Used for signal connections between devices that are transferred using coaxial cable.

degrees of freedom set of independent coordinates that specify the range of motion of a system.

generalized coordinates any set of indepedent spatial coordinates that completely describes a dynamic system.

Hermitian matrix A complex valued square matrix that is equal to its own complex conjugate transpose. It is the complex extension of real symmetric matrices.

narrowband system a system where the area under the response power spectral density function is concentrated near the natural frequency of the system. It is an indication of a system with low damping.

NMEA 0183 A specification for the communication between marine electronic devices. The specification is also known as NMEA, and was developed by the National Marine Electronics Association.

periodogram An estimate of the spectral density of a signal.

rank (linear algebra) The number of linearly independent rows or columns of a matrix.

spectral leakage Occurs when transforming finite length signals from the time domain to the frequency domain using discrete Fourier transforms, and results in energy from a particularly frequency band being incorrectly represented in adjacent frequency bands. The discrete Fourier transform assumes the input

signals are periodic, and the leakage is caused when a finite length periodic signal is abruptly truncated midway through a cycle.

shear modulus Ratio of shear stress to shear strain ($G = E/[2(1 + \nu)]$)

tribrac A surveying instrument attachment device consisting of two triangular plates connected at their corners by thumbscrews. By adjusting the thumbscrews, the top triangular plate can be levelled when the bottom plate is mounted atop a tripod.

zero-order hold method of converting a continuous signal to a discrete, stepwise signal by holding each sample value for one sample interval. The input is assumed to be piecewise constant over the sampling interval.

Chapter 1

Introduction

In order to achieve the design goals for a tall building, it is important to know the response of the structure to the expected loading conditions. Therefore, estimating the loads and subsequent responses is a crucial consideration for the design. Current methods for estimating tall building response to loading involve numerous steps that collectively form a combination of techniques, including theoretical, empirical, and scaled model tests. These techniques are based on fundamental mechanics and years of development, but uncertainty in the response estimates are still encountered. This is particularly true for tall building designs that are considered significantly different and complex relative to previous designs.

Notably absent from the list of techniques for estimating tall building response is prototype testing. This is because tall buildings are essentially unique products. Constructing a tall building represents a singular production run. This is in contrast to other industries, such as the automotive or aerospace industries, which have the ability to test multiple full-scale prototypes, and improve subsequent designs with test results before releasing a product for general use. Applying such a design approach to tall buildings is infeasible. Even if a prototype of a tall building could be constructed purely for testing and design improvement, applying a controlled lateral load equivalent to an ultimate earthquake or wind event would be inconceivable.

In addition to the uniqueness of tall buildings, any alterations to the structural arrangement after it has been established can be difficult and expensive to conduct. The level of difficulty and expense depends on how far the design and construction has progressed. In particular, any alterations to the completed form can be extremely difficult to undertake and very costly. It is sufficient to say that altering the structural arrangement to rectify a building response problem is to be avoided, and when absolutely necessary, is best executed as early as possible in the design and construction process. The ability to make effective structural changes is often hampered by the fact that in all but the most structurally sensitive buildings, the structural arrangement is essentially subservient to both architectural and financial

requirements. This can constrict the structural design to inferior solutions, and therefore further restrict the options for changing the structural arrangement.

The preceding paragraphs have introduced two crucial points for accurately predicting tall building response to loading. Firstly, there is virtually no means to test a full-scale prototype and use the results to improve the design. Secondly, alterations can be costly once the structural arrangement has been finalised. These two aspects imply that estimates of the loads and responses must be accurate prior to finalising the structural arrangement. The response parameters of interest for tall building global design are the base overturning moments, base shears, lateral deflections, and accelerations at the top of the building. Sources of lateral loading include earthquakes and wind, amongst others, and tall buildings can be sensitive to either source.

1.1   Design Criteria for Tall Buildings

According to current limit state design codes [75, 150], the design of civil engineering structures include the following four aspects: ultimate, serviceability, fatigue, and robustness. The ultimate aspects include strength and stability requirements for peak load events, such as earthquakes and large return period wind events. Serviceability aspects include the deflection and motion requirements for normal use under all expected design loads. Fatigue aspects relate to the cyclical nature of loading, and are rarely critical for tall building design. Robustness aspects refer to the ability of a structure to withstand an event without incurring damage that is disproportionate to the event, for example progressive collapse.

For the ultimate limit state, the design criteria requires a tall building to have sufficient strength to resist the peak probable load events likely to occur during the design life of the building. This requires an analysis of the forces and stresses within the structural elements for the critical load combinations. An additional check is also required to assess stability. The dead load of the structure, in conjunction with any base anchoring arrangements, must be sufficient to ensure the applied lateral loads will not cause the structure to topple. An understanding of lateral deflections from ultimate loads are required when checking stability. The case may arise that second-order load-deflection effects may cause structural instability.

For the serviceability limit state, the design criteria requires a tall building to perform adequately for normal use under all expected actions. The serviceability design criteria for tall buildings are numerous, however the most pertinent for overall structural design are deflection and motion related criteria. In the case of structural deflections, sufficient lateral stiffness must be provided to ensure the operation of building components, such as elevators and doors, are not hampered by excessive

deflections. Furthermore, excessive lateral deflections can cause the transfer of loads to non-load-bearing components, such as partition walls and facades. In the case of motion related criteria, a tall building subjected to fluctuating wind loads can result in oscillatory movements that have adverse effects on occupant comfort. Motions that cause undesirable cognitive or physical effects for occupants may result in an otherwise acceptable building becoming undesirable to prospective tenants. A tall building design may have sufficient capacity to satisfy the ultimate limit state, but could fail the occupant comfort criteria if accelerations experienced by occupants under normal operating conditions exceed a threshold value.

For tall buildings, wind loads often form the critical load combinations when determining structural actions and responses, for both ultimate and serviceability limit states. This is particularly the case for ultimate base reactions, inter-storey drift, and lateral deflections and accelerations at the top of the building. During the design process of a tall building, a routine wind tunnel model test may be conducted to determine the wind-induced responses of the structure. The wind tunnel test results can include base reactions, wind forces, deflections, and accelerations. Most design standards provide methods to calculate the wind-induced response of rectangular prismatic tall buildings [153]. However, there are significant differences between the standards, and wind tunnel model tests are considered more accurate, particularly for buildings with complex geometries or eccentricities between mass and stiffness centres.

Whether conducting wind tunnel tests or using desk calculation methods, information regarding the architectural, structural, and dynamic characteristics of the building are required to determine the wind-induced responses. The architectural characteristics include the external geometry. The structural characteristics include the distribution of mass and stiffness. The dynamic characteristics include the natural frequencies, mode shapes, and damping ratios of the structure. The architectural and structural characteristics generally require little effort to obtain or calculate. Depending on the structure, estimates of the dynamic characteristics can require considerably more effort to determine, and are prone to the greatest errors. Any errors in the architectural, structural, or dynamic characteristics will cause inaccurate estimations of the wind-induced response of the building, which may result in substandard performance, or excessive construction costs.

1.2   Response Sensitivity to Dynamic Characteristics

The wind-induced response of a tall building is sensitive to its dynamic characteristics: natural frequencies, mode shapes, and damping ratios. Each of these three
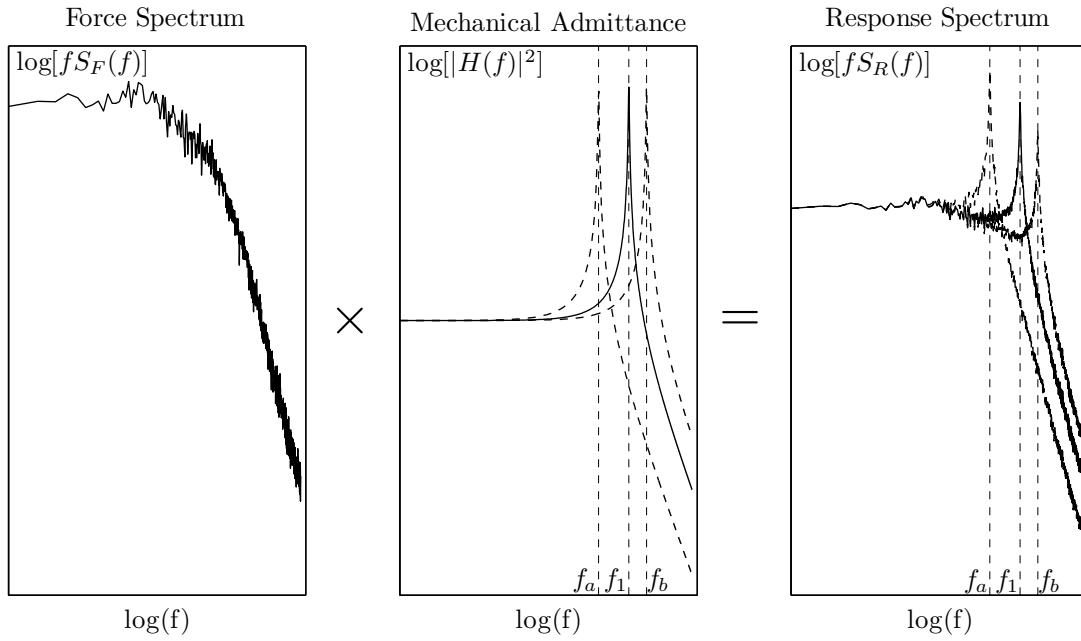
Figure 1.1: Sensitivity of response to natural frequency (f) for a single degree of freedom system.

dynamic characteristics influence the wind induced response in different ways. The important point is that incorrect predictions of these dynamic characteristics during design can lead to either performance issues in the completed structure or unnecessarily excessive construction costs. Therefore, the accurate prediction of these parameters can be crucial to optimising the structure.

The natural frequency determines the point on the force spectrum at which the building is operating. The spectral representation of fluctuating wind velocities generally peaks in the range 0.01–0.05 Hz, and reduces thereafter. Therefore, most of the energy in the wind is in the lower frequencies. Figure 1.1 displays a typical wind force spectrum for a tall structure, along with the mechanical admittance function of a single degree of freedom system, and the resulting response spectrum. The natural frequency of the fundamental mode of vibration for tall building structures are generally between 0.1–1 Hz. In this range, as the frequency increases, the force spectrum decreases. Three mechanical admittance functions are displayed, which correspond to the actual natural frequency (f_1), the natural frequency underestimated by 50% (f_a), and the natural frequency overestimated by 50% (f_b). Overestimating the natural frequency tends to decrease the wind induced response estimate, leading to the possibility of performance issues such as excessive accelerations and compromised occupant comfort criteria. An underestimation tends to increase the response estimate, which results in the structure being designed for a greater response than necessary.

Mode shape estimates are also used to predict the wind induced response of tall

structures. Since mode shapes describe the deformed shape of the structure, they are used to determine the magnitude of the loading and the various response parameters: displacement, accelerations, and base reactions. An incorrect mode shape estimate can lead to large errors in the response estimates, even if the natural frequency and damping ratios are accurately estimated. An example is the torsional component of a complex mode shape. Torsional responses are magnified by the distance from the centre of the rotation. When considering a torsional response as the vector sum of translations in the orthogonal directions (x and y axis), the magnitude of the translations increases with increasing distance from the centre of rotation. Therefore, a complex mode shape that incorrectly excludes or underestimates the torsional component will result in a significantly reduced motion response at the extremities of the building plan. Compromised occupant comfort criteria is the most likely performance issue in this circumstance. Similarly, overestimating the torsional component of the mode shape can lead to the building being over designed.

The final dynamic parameter, the damping ratio, has a significant impact on the wind induced response of tall buildings. The damping ratio is a measure of the energy dissipation characteristics inherent to a structure, and its estimation can be subject to significant uncertainty. Of the three dynamic characteristics, the wind induced response is arguably most sensitive to the damping ratio. Increasing the damping ratio via auxiliary damping devices is regularly implemented in tall building designs to mitigate the wind induced response [66, 162]. Figure 1.2 displays the influence of the damping ratio on the mechanical admittance function of a single degree of freedom system. An overestimation of the damping ratio can lead to an underestimated response of the building. This can lead to substandard performance of the final structure relating to strength, stability, or occupant comfort criteria. Underestimating the damping can lead to the structure being over designed, which represents unnecessary construction costs.

For most tall buildings, the relative errors for damping ratio estimates, and the subsequent influence on the response, can be significantly greater than for relative errors in natural frequency. This highlights the damping ratio as the most critical dynamic parameter in the calculation of wind-induced resonant response. However, this fails to consider other aspects, such as the need for accurate natural frequency figures and mode shape descriptions for designing and installing damping devices. Therefore, it is appropriate to broaden the scope of criteria when scrutinising the relative importance of dynamic parameters. A broader scope tends to conclude that all dynamic parameters are important when analysing the wind-induced resonant response of a tall building because all dynamic parameters are required in order to form a definitive description of the dynamic system for subsequent design.

Improving the accuracy of the dynamic characteristic estimates is beneficial at
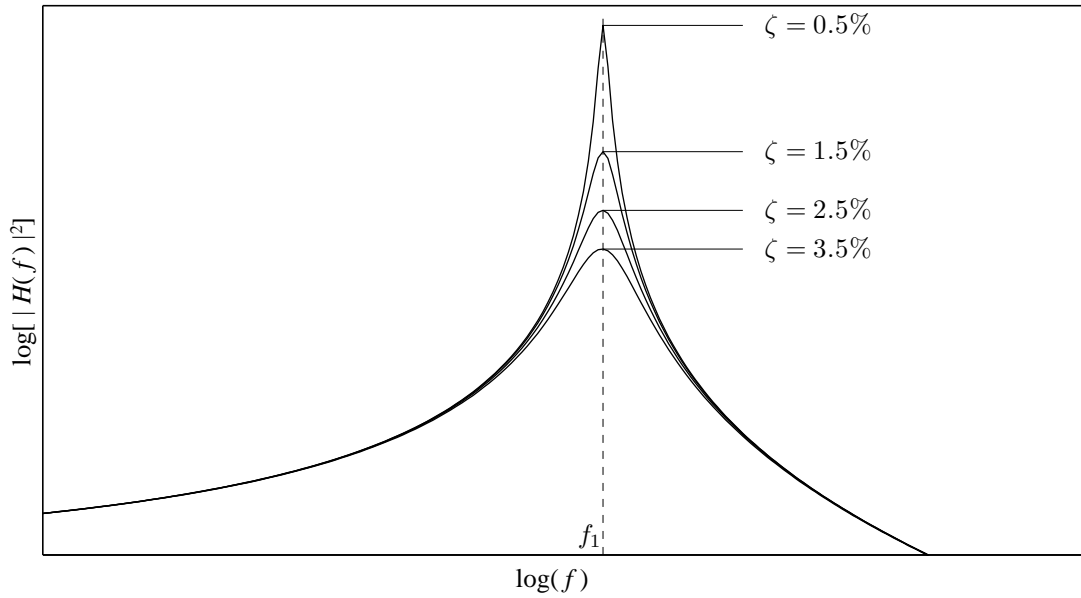
Figure 1.2: Sensitivity of the mechanical admittance function to the damping ratio (ζ).

any stage of the structure life cycle, even during the construction phase. The primary reason for conducting full-scale vibration testing is to evaluate the assumptions and theories used in design. Despite the fact that results from these tests provide valuable information that can be used to improve current as well as future designs, vibration testing of tall buildings is not a routine procedure. Consider the design of an auxiliary damping device to be installed in a tall building. In most cases, dampers are installed at the top of buildings, where deflections are greatest. Since the damper installation time is governed by the completion of the main structural elements, a more accurate estimation of the dynamic parameters of the structure prior to installation of the damper is achievable via vibration testing, and the results can be used to improve the design. Furthermore, early detection of damping levels in tall buildings is extremely beneficial to assessing the need for auxiliary damping devices [99].

Another example of the benefit of vibration testing is the confirmation of numerical models, such as finite element models. While empirical formulas can estimate the natural frequencies, they are unable to provide reliable mode shape estimates. This is particularly the case for tall buildings with complex mode shapes resulting from eccentricities between the centre of mass and centre of stiffness. For this reason, creating a finite element model is almost routine during the early stages of tall building design, as the mode shape estimates from these models are used in response estimates from wind tunnel tests. By comparing finite element models and full-scale measurements, it is possible to improve the understanding of the mechanisms that affect the dynamic behaviour of tall buildings.

1.3   Response Estimation and Verification

Numerous techniques are used to estimate the response of tall buildings to dynamic loading, including theoretical techniques, empirical formulas, numerical models, and scaled model tests. All of the techniques involve assumptions, and despite advances in these techniques, uncertainty in the response estimates is still encountered. A definitive confirmation of the response is only attained once the structure is completed and full-scale measurements are conducted. Even then, the response estimates may still lack confirmation if the measured responses are for loading conditions that fail to match the design loads.

As for the vibration testing of tall buildings, monitoring the wind-induced response of tall buildings is not routine. Compared with vibration testing, fewer tall buildings are monitored over a long period to determine the wind-induced response. More recently a number of monitoring programmes have been conducted on some of the taller buildings located in North America and Asia [18, 20, 91, 107, 110]. These studies represent a small portion of the current tall building stock available for monitoring, and only include a small fraction of the many combinations of structural systems and external geometries that are used in tall building design.

1.4   Objectives

The estimation of dynamic characteristics and the wind-induced response of tall buildings is the focus of this research. The aims of this research are, firstly to improve the accuracy of tall building dynamic characteristic estimates and to conduct a validation of the values used in the estimation of the wind-induced response. Secondly, to validate the wind-induced response estimates of tall buildings from wind tunnel testing using the full-scale monitoring of an as-built structure. It is important to note that the full-scale experiments in the thesis are rarely undertaken due to the difficulty of such experiments. The results of this thesis are adding to a body of knowledge for which there are very few full-scale measurements recorded and published. Furthermore, the research is closing the design loop, whereby the response estimates from models are validated using full-scale measurements. The full-scale experiments included vibration testing of the structure during construction, and the long term monitoring of the wind-induced response after completion of the structure.

The building used for full-scale measurements is Latitude tower, an office tower located in the Sydney central business district, with a height 187 m above ground level. The structure is of a composite design with a reinforced concrete core, and reinforced concrete floor slabs supported by steel beams spanning between the core and perimeter columns. The construction used a previous building that was partially

completed and abandoned. The new structure utilised much of the existing structure and foundations, but significant alterations were made to the core walls and floor slabs.

Full-scale experiments at Latitude tower commenced during the early stages of construction and progressed periodically through the construction cycle. The vibration tests during the construction cycle were conducted to record the change in natural frequency and structural damping as the building was constructed, and to investigate the possibility of improving natural frequency and damping ratio estimates using the construction cycle data. Post completion of the structure, the wind-induced response was monitored for approximately two years. The following points summarise the objectives of this research:

- to determine if natural frequency and damping ratio estimates, from full-scale vibration testing, of a structure during the construction phases can mitigate the uncertainty in estimated values for the completed structure,

- to model a tall building using the finite element method for determining the dynamic characteristics, and update the model using full-scale measurements of the dynamic characteristics during the construction phase to improve the understanding of the structural mechanisms that are significant to the determination of dynamic characteristics from a modelling perspective,

- to monitor the full-scale wind-induced response of a tall building, with a focus on measuring the accelerations at the top of the building, and

- to validate the predicted wind-induced response from scaled model wind tunnel tests with the full-scale results from the long term monitoring of the wind-induced response of the building.

1.5   Outline

- Chapter 2 includes a literature review of material relating to this research. The techniques used to estimate the natural frequencies and damping ratios of tall buildings are initially discussed, followed by a review of previous full-scale vibration testing of tall buildings. The final sections of this chapter review previous studies that have monitored the wind-induced response of tall buildings.

- Chapter 3 details the full-scale experiments conducted on Latitude tower. A description of the structure is followed by the instrumentation details and configurations. The experimental details for the vibration testing, conducted during the construction of Latitude tower, and the wind-induced response

monitoring of the tower, conducted post construction, are discussed at the end of the chapter.

- Chapter 4 describes the system identification techniques used to estimate the natural frequencies and damping ratios from forced vibration tests and ambient vibration tests of Latitude tower. Two system identification techniques are used with ambient vibration test data: a frequency domain technique and a time domain technique. A comparison between the estimates from these techniques is presented for response data recorded after the completion of construction of Latitude tower. The random decrement method is described for determining the amplitude dependence of the natural frequencies and damping ratios.

- Chapter 5 presents the results from the vibration testing conducted during the construction of Latitude tower. Estimates of the natural frequencies and damping ratios at particular stages of construction are discussed with reference to the structural changes that occurred. The final section of the chapter includes the finite element model updating using the vibration test results.

- Chapter 6 presents the results from the full-scale monitoring of the wind-induced response of Latitude tower. A description of the wind events recorded during the monitoring period are presented, and followed by a discussion of the wind-induced response, which includes the acceleration response, background response, and the peak factors. The final sections comprise the wind tunnel testing results for the estimation of the accelerations at the top of the building, as well as comparisons with the full-scale measurements.

- Chapter 7 presents a summary and conclusions of each segment of the research. This chapter ends with recommendations for future research.

Chapter 2

Literature Review

2.1 Introduction

This chapter presents a review of previous research for estimating the dynamic characteristics and wind-induced response of tall buildings. Theoretical, empirical, and numerical techniques for estimating the dynamic characteristics of tall building structures are described and compared. The techniques have varying complexity in their application. Choosing a more complex technique does not necessarily produce improved estimation accuracy, and the opposite can be true for less complex techniques. Empirical formulas are traditionally the least complex, as they rely on simple correlations between full-scale results and building properties, such as geometry and structural system. The method used often depends on the importance of the structure and the stage of the design process. The discussion is focused on the fundamental modes of vibration, which for most structures includes two translational modes, in orthogonal directions, and one torsional mode.

This review also includes earthquake engineering literature in sections that discuss the dynamic characteristics of tall buildings. There is a wealth of knowledge regarding the dynamic characteristics of buildings in the earthquake engineering literature. Earthquake engineering code formulas for natural frequency are not included in the review, because they are often intentionally adjusted to give a more conservative earthquake design. If used for calculating the wind-induce response, the natural frequency values that provide conservative earthquake design will result in an unconservative wind engineering design.

2.2 Natural Frequency Estimation

There are three techniques currently used to determine the natural frequencies of a tall building: empirical formulas, theoretical models, and numerical models. The technique selected by designers depends on a number of factors that include the

accuracy required, the number of modes to be estimated, the complexity of the structure, available information, and time constraints. In practice, all three techniques are usually applied during design. Empirical formulas are the least intensive techniques to use, because they generally involve the input of one or two building geometry measurements into a simple formula. This makes empirical formulas the initial choice for quick estimates at the beginning of tall building design.

Empirical formulas may be the only option at the start of design, because insufficient information regarding the structural arrangement could preclude a more rigorous analysis using theoretical or numerical methods. The type of building — reinforced concrete shear wall, reinforced concrete moment frame, steel moment frame — and external dimensions such as height and plan width are the input requirements for most empirical formulas, and at least these aspects are known when structural design commences. Theoretical models and numerical models have the ability to include more details of the structure in the estimation, and therefore generally require more effort to conduct. The application of theoretical or numerical models will often start with simple models, which include numerous simplifying assumptions, and progressively become more detailed if required by the particular structure being analysed.

The techniques are generally used in design according to the following order: empirical, theoretical, and then numerical. The level of time and detail required generally increases when ascending the order, as does the intended accuracy. In the following sections, the theoretical methods are discussed first, because this establishes the theory upon which empirical formulas are initially based.

2.2.1 Theoretical Models

The theoretical modelling of any structure attempts to incorporate simplifying assumptions that improve the computation efficiency, without significant detriment to the resulting natural frequency estimation. Aspects of modelling a tall building for natural frequency estimation include, but are not limited to, the distribution of mass and stiffness, the type of deflection actions, and the interaction between the soil and foundations. The assumptions adopted are directly linked to the complexity of a tall building structural system. Some simple structural systems may be accurately modelled as an idealised beam with simple boundary conditions, while more complex structures may require significantly more detail.

The theoretical modelling of tall building structures has two options for representing the dynamic system: a lumped parameter system, or a distributed parameter system. For lumped parameter systems, the structure is discretised into a set of points, and the motion of each point in the system is modelled with a tributary mass that is concentrated at the point. The set of lumped masses are typically con-

(a) System Representation (b) Free Body Diagram
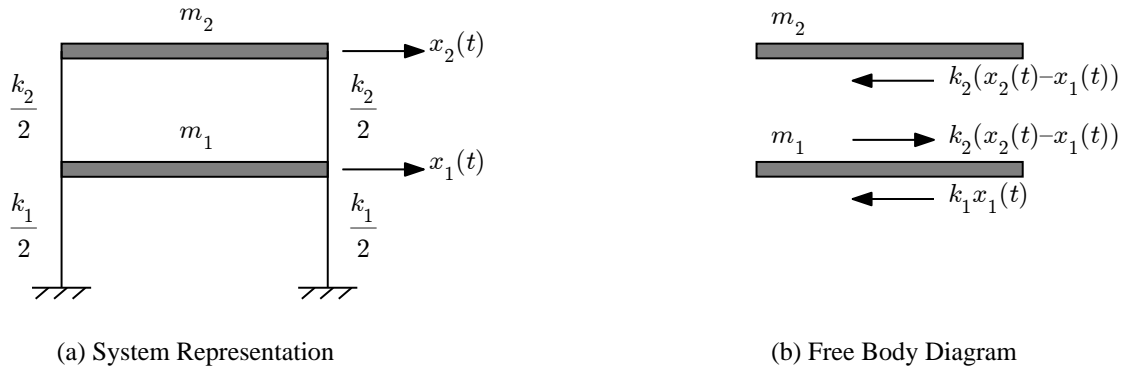
Figure 2.1: Lumped prarmeter model of a two-storey building experiencing translational vibration.

nected by elements that represent the stiffness and damping of the structure. Most often the models represent the stiffness by springs or equivalent beam elements. The damping is typically represented by dash-pots, or more often ignored due to its insignificance on the natural frequency for large civil engineering structures. Once the system model has been established, the natural frequencies of the system can be determined using modal analysis techniques [74]. The dynamic behaviour is described by second order differential equations, and the discretisation of the structure limits the results to a finite number of natural frequencies.

An example of a lumped parameter system model of a two storey building is presented in Figure 2.1. The example can be extended to include structures that include more than two storeys, and the mass and stiffness parameters can vary throughout the system. The lumped masses are readily calculated, and the stiffness parameters can be calculated based on the arrangement and specification of walls, columns, and other structural elements that resist lateral deformation. It is noted that the model presented assumes a rigid connection between the first storey and the foundations. If required, this assumption can be replaced with a more suitable alternative that models soil structure interactions.

Depending on the number of degrees-of-freedom contained within a model, lumped parameter systems can be computationally intensive to solve for the natural frequencies. Degrees-of-freedom are the set of independent displacements or rotations that define the deformed position of the system. For example, Figure 2.1 has two degrees-of-freedom, x_1 and x_2. A coarse discretisation of a system can aid in reducing the degrees-of-freedom, but the effect on estimation accuracy needs to be considered.

A coarse discretisation coupled with an approximation technique, such as Rayleigh's method [74], is a common approach when using lumped parameter models for quick theoretical estimates of the fundamental natural frequency [68]. The premise of Rayleigh's method is that the maximum kinetic energy and the maximum potential

energy must be equal in a conservative system. The estimates from this method are an upper bound for the fundamental natural frequency. Approximations of higher mode frequencies can be obtained by applying the Ritz method [171], which is an extension of the Rayleigh method.

For the distributed parameter case, the mass of the structure is considered to be a series of infinitely small elements that are distributed throughout the system. Vibration of the structure causes each of the infinite number of elements to continuously move relative to each other. A continuous function of the relative position along the system is used to spacially describe the time response of the system. As for the lumped parameter system representation, the assumptions used in formulating the model are critical to the accuracy of the results.

Of particular interest to expeditious estimates of natural frequency is the modelling of a tall building as an idealised beam. For tall buildings with relatively constant properties throughout height, the discrete set of elements (beams, columns, walls, etc.) that comprise the structure are replaced by a continuous medium of equivalent properties. By assuming the incompressibility of the continuous medium, the estimation of the natural frequencies is reduced to a single linear differential equation with constant coefficients.

A number of fundamental theories exist for the analysis of the transverse vibration of idealised beams [88]. The Euler-Bernoulli beam model, also known as the classical beam model, is one such theory that models the flexural action of uniform, slender beams that are composed of linear, homogeneous material. Note that the classical beam model only incorporates flexural deformations via the assumption that plane sections remain plane. Equation (2.1) presents the formula for estimating the natural frequency of a fixed base uniform cantilever using classical beam theory;

$$f_i = \frac{\lambda_i{}^2}{2\pi L^2}\sqrt{\frac{EI}{m}} \qquad i = 1, 2, 3, \ldots, n \tag{2.1}$$

i	λ_i	i	λ_i
1	1.875	4	10.996
2	4.694	5	14.137
3	7.855	$i > 5$	$(2i-1)\frac{\pi}{2}$

where L is the length of the beam, E is the modulus of elasticity, I is the area moment of inertia about the neutral axis, m is the mass per unit length, and the subscript i denotes the mode of vibration.

Another potentially important translational deformation action in tall buildings is shear deformation. Flexural deformations generally dominate when considering a slender structure, however shear deformations become important with reduced slenderness ratios and for analysing higher modes of vibration. Equation (2.2) presents

the formula for estimating the natural frequencies of a fixed base uniform cantilever assuming only shear deformations [7];

$$f_i = \frac{\lambda_i}{2\pi L}\sqrt{\frac{\kappa G}{\rho}} \qquad i = 1, 2, 3, \ldots, n \qquad (2.2)$$

$$\lambda_i = (2i - 1)\frac{\pi}{2}$$

where κ is the shear coefficient, G is the shear modulus, and ρ is the mass density. The natural frequency estimates from the shear beam model is proportional to $1/L$, as opposed to $1/L^2$ for the flexural beam model, and the natural frequencies increase linearly with the mode number.

For most tall buildings, the lateral stiffness is not constant with height, and tends to decrease from a maximum at the base to a minimum at the top. This is certainly the case for tall buildings with a core comprised of reinforced concrete shear walls. A small percentage of the walls will extend from the foundations to the roof, while others will be terminated, or have reduced dimensions, at various levels according to the design lateral load resistance requirements. Equations for idealised beams with tapers are applicable in these cases, which take the form of Equations (2.1) or (2.2), and have adjusted values of λ_i that account for a tapering effect [115, 182]. A taper in the dimension perpendicular to the vibration motion tends to increase the natural frequency for all modes of vibration. For a taper in the plane of vibration motion, the first mode natural frequency tends to increase, while the second and third modes tend to decrease. More complex theoretical models that account for arbitrary distributions of mass and stiffness have also been developed [105].

Rotatory inertia is also ignored in classical beam theory. Rotatory inertia is the inertia associated with the local rotation of a beam cross section during flexural deformation. Corrections to classical beam theory to account for rotatory inertia were established by Rayleigh [133]. A model proposed by Timoshenko [172] incorporates the flexural deformations, shear deformations, and rotatory inertia effects. The effect of rotatory inertia on natural frequency is generally less than shear deformation, and both tend to reduce the natural frequencies of beams compared with flexural theory predictions.

Closed form solutions of models that incorporate flexural and shear deformations are generally not attainable, which leads to the application of numerical methods for solving such models to determine the natural frequencies. Alternatively, the flexural and shear deformations can be combined using Dunkerley's formula [45] to calculate a lower bound estimate of the fundamental natural frequency [78]. Dunkerley's formula is not limited to combining the flexural and shear deformations. The generic form of Dunkerley's formula, Equation (2.3), allows the input of multiple

deformation actions.

$$\frac{1}{f^2} = \frac{1}{f_f{}^2} + \frac{1}{f_s{}^2} + \dots \tag{2.3}$$

Where f_f and f_s are the fundamental frequencies from a flexural beam model and shear beam model, respectively.

The application of Dunkerley's formula implies the system is modelled as isolated components. This approach has been applied to shear wall buildings [60], coupled shear wall buildings [135], and wall-frame buildings [57, 64, 147] by decomposing the deflections into the component actions. The fundamental natural frequency from each action is then combined using Dunkerley's formula, with results found to be within 3% of estimates from Rayleigh's method [60]. Furthermore, the soil structure interaction can be incorporated into the model by modelling the deflection actions from the rotatory and translational motion of foundations on elastically yielding soils.

Rotatory, or rocking motion, of structures becomes more pronounced as the stiffness of the building increases relative to the stiffness of the ground. Rocking motion can manifest as part of the translational mode of a building, or as a rocking mode for a very stiff building resting on soft ground. Salvadori and Heer [138] combined linearly varying shear and flexural rigidities with rocking and translational motion using Dunkerley's formula. The resulting formula for the fundamental natural frequency was able to match the upper and lower bounds of a large full-scale measurements database, when using inputs that bounded expected structural and soil parameters.

Another action that can influence the natural frequency estimation is the axial compression and deformation of walls and columns. In some cases this action is excluded since it is deemed insignificant relative to the desired accuracy of the estimation. When axial compression has been included in the estimation method, a decrease in the natural frequency was observed [36, 134]. The decrease was most significant for the fundamental natural frequency, and reduced with each increase in mode of vibration considered. This result can be explained by the increasing dominance of shear deformations with increasing mode order. Furthermore, the effect of axial deformation becomes important when building height and slenderness ratios increase [158], or in other words, when flexural deformations are dominant.

The preceeding discussion has focused on the estimation of translational modes of vibration. Attention is now turned to estimating the natural frequency of torsional modes of vibration. Both the lumped parameter and distributed parameter systems of modelling are applicable for estimating the torsional natural frequencies. For the case of an idealised uniform beam, exact closed form solutions are only obtainable for circular cross sections. Non-circular cross sections tend to warp during torsional deformations, however this effect is not significant for simple closed sections. The

equation for estimating the torsional natural frequency of a uniform beam is given by,

$$f_i = \frac{\lambda_i}{2\pi L} \sqrt{\frac{JG}{\rho I_p}} \qquad i = 1, 2, 3, \ldots, n \tag{2.4}$$

$$\lambda_i = (2i - 1)\frac{\pi}{2}$$

where J is the torsion constant, G is the shear modulus, ρ is the mass density, and I_p is the polar area moment of inertia of the cross section about the axis of torsion. Similar to the shear beam model, the natural frequency estimates from the torsion beam model is proportional to $1/L$, and the natural frequencies increase linearly with the mode number.

The theoretical techniques discussed in this section are not extensive, but form the core of available methods that are relatively quick to apply for tall building natural frequency estimation. More complex techniques are available, and may be useful for certain structure types. Those included in the discussion also present the foundation for understanding the formation of empirical estimates, which are discussed in the following section.

2.2.2 Empirical Formulas

The natural frequency empirical formulas discussed in the following paragraphs are those that relate to buildings that use shear-walls as the primary lateral load resisting structure, either by historical application of the formulas to such structures, or by the establishment of the formula for exclusive application to such structures. Formulas recommended by design codes for earthquake design purposes are not discussed, regardless of applicability to shear-wall tall buildings, due to the common practise of intentionally adjusting the formulas to ensure a conservative earthquake design [29, 34, 60]. It is important to note that a conservative estimation of the natural frequency for tall building earthquake design will cause an unconservative natural frequency estimation being used for wind-induced response design.

A number of previous studies have attempted to derive empirical formulas for estimating natural frequencies of tall buildings. Two methods are used to develop the formulas: Measured values of natural frequency are plotted as a function of one or multiple building properties and a regression analysis is conducted; or, a semi-empirical approach that checks the validity of a theoretical model with full-scale measurements. Both methods require full-scale measurements from multiple buildings in order to create a database of natural frequencies. Parameters describing the building, such as dimensions, construction material, structural system, foundation material, and intended use, are included in the database for correlating with natural frequencies.

A substantial database of full-scale natural frequencies for buildings was compiled by the United States Coast and Geodetic Survey (USCGS), which commenced the dynamic testing of buildings and other structures in the early 1930's in California [24] for earthquake engineering purposes. This database includes buildings up to 125 m (409 feet) high, with most below 61 m (200 feet) high. The soil conditions, foundation type, construction materials, structure type, building dimensions, and number of storeys are included in the database, and the buildings are categorised according to common plan forms: rectangular building, hollow rectangular building, "set-back" building, L-shaped, U-shaped, E-shaped, T-shaped, H-shaped, irregular shaped, and flat-iron. The vibration data includes the fundamental translational and torsional periods and the maximum building displacement. An indication of the wind velocity during testing is included using the Beaufort Scale. By mid 1949, 430 buildings, amongst other structure types, had been tested.

Using the USCGS database, Anderson et al. [3] investigated the correlation of period versus h^2/d, where h is the building height measured in feet and d is the plan building depth in the direction considered, in feet. Figure 2.2 displays a plot of the results. Considerable scatter is observed in the results, which could be partially explained by the lack of categorisation of results based on structural types and building materials. The best fit curve for the data is,

$$T = 0.06\frac{h}{\sqrt{d}} \tag{2.5}$$

The error between Equation (2.5) and the points plotted in Figure 2.2 are between +100% and -50%. The choice of correlating natural period with $h/\sqrt{d}$ indicates the use of a fixed base uniform cantilever shear beam model, which is demonstrated in Equation (2.2) for the fundamental translational mode. Substituting $\rho = m/A$ into Equation (2.2), where A is the cross sectional area and is equal to the breadth b times the depth d of a uniform beam, and rearranging;

$$T_1 \quad = \quad 4\sqrt{\frac{m}{\kappa Gb}}\frac{h}{\sqrt{d}} \tag{2.6}$$

The regression coefficient in Equation (2.5) is essentially an empirical estimate for the terms on the right hand side of Equation (2.6), excluding $h/\sqrt{d}$. Empirical formulas are essentially aggregating numerous variables relating to the vibration mechanism into a single parameter.

Another early and significant database of full-scale dynamic observations of buildings was compiled by researchers in Japan [65, 85, 89, 124, 159]. Like the USCGS database, the impetus for collecting the observations was for earthquake engineering purposes. Approximately 60 buildings of mostly reinforced concrete,
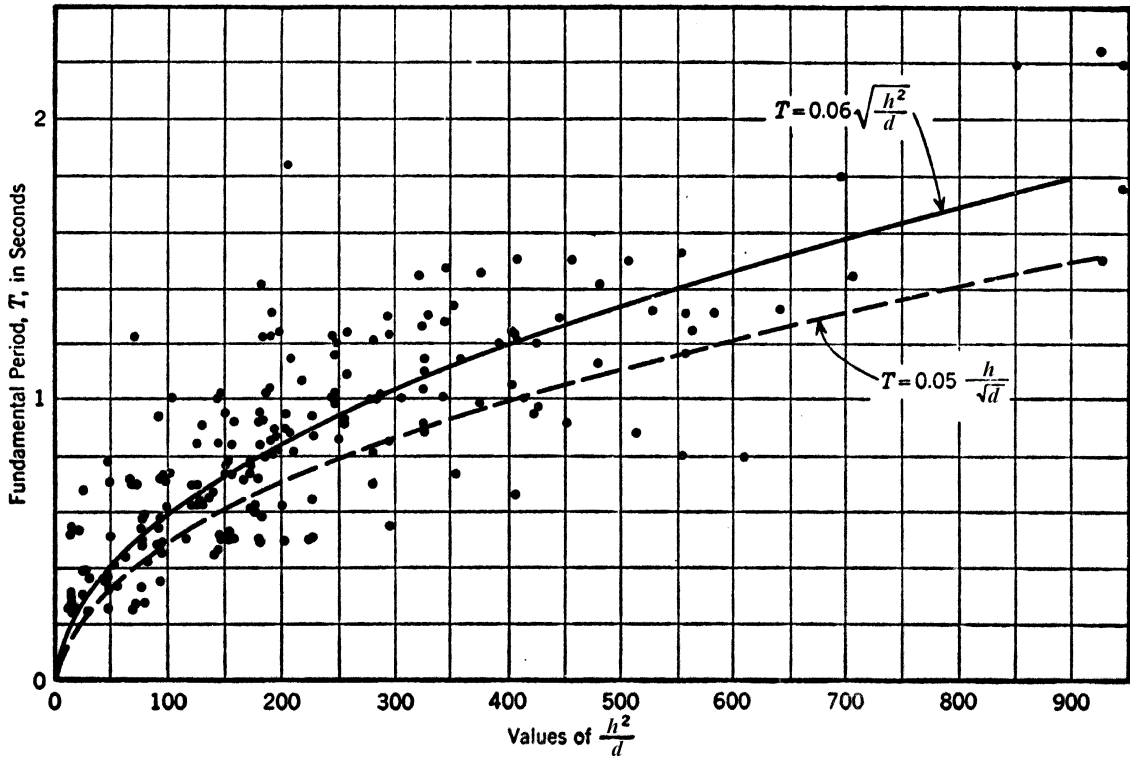
Figure 2.2: Fundamental Periods of Buildings versus h^2/d (Source: Anderson et al. 1951 [3] with notation adjustments)

with mixed structural form, are included in the Japan building database. The design code requirements under which most of the Japan buildings had been designed imposed a height limit of 31 m (100 feet), as well as larger seismic design coefficients compared with other countries. This results in the Japan building database having much shorter and stiffer buildings compared with those of the USCGS database. Combining this with the softer soil conditions reported for a majority of the buildings, resulted in rocking motion observations as the predominant form of lateral drift in some buildings [89, 124]. Essentially, the buildings act as rigid body structures on elastic foundations.

Using data sourced from the Japan building database and from the USCGS survey, Kanai and Yoshizawa [86] reported that natural frequency was not sensitive to the plan dimension in the direction of motion considered. The best fit formula for the analysed data was;

$$T = 0.04 \frac{h}{\sqrt[4]{d}} \tag{2.7}$$

The two data sets used where individually analysed, and no classification of the data was indicated. Since the degree of the power applied to d was relatively low, this parameter was ignored and a new formula was recommended based on the mean values of the ordinate T/h, which was approximately 0.02 for both the Japan building data in Figure 2.3 and the USCGS database in Figure 2.4. The
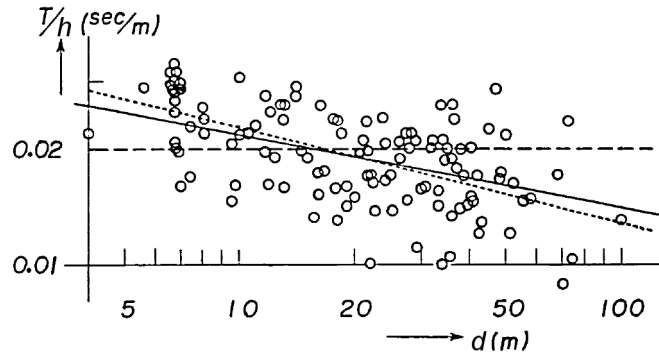
Figure 2.3: Relation between the fundamental period, the height, and the depth of buildings in Japan (Source: Kanai and Yoshizawa 1961 [86] with notation adjustments)
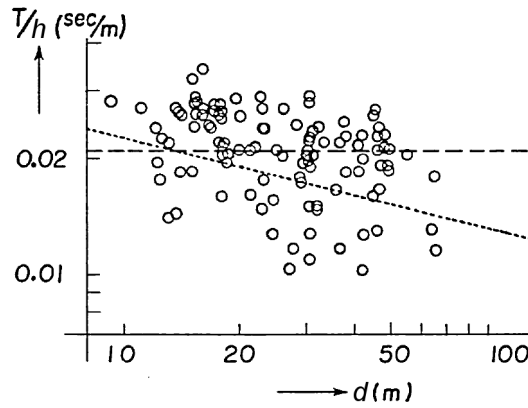
Figure 2.4: Relation between the fundamental period, the height, and the depth of buildings in the USCGS database (Source: Kanai and Yoshizawa 1961 [86] with notation adjustments)

recommended empirical formula for practical use was;

$$T = 0.02h \qquad (2.8)$$

$$T = 0.08N \qquad (2.9)$$

where N is the number of storeys. The empirical estimate in Equation (2.8) is used in the Architectural Institute of Japan guidelines.

The strong relationship between height and natural frequency was understood by the first attempts to establish simple empirical formulas for natural frequency estimation. The problem that hindered estimation improvements appeared to be the inability to capture the stiffness, in either a single constant or using a building plan dimension. Housner and Brady [68] used theoretical expressions for uniform rectangular buildings as a starting point for studying the influence of particular parameters on the natural frequencies of shear-wall buildings. Using the USCGS

data, Housner and Brady [68] found the equation $T = CN/\sqrt{d}$ to be less accurate than $T = CN$, and also less accurate than $T = CN\sqrt{b}$. The best fit formula included the depth and breadth of the structure. However, the best fit formula produced practically identical results to $T = CN$, even when some of the variability in the USCGS data was reduced by choosing a subset of buildings that had relatively uniform characteristics. But, none of the formulas gave consistently accurate results, with significant scatter still present, which lead to the conclusion that the properties of the analysed buildings are so variable that a simple equation cannot provide a good fit. Furthermore, it was stated that a good estimate can only be obtained if the actual wall stiffness is taken into account, and appears explicitly in the equation. This idea was previously expressed by Takeuchi [159] and more recently by Goel and Chopra [60], the latter using a more sophisticated analysis that attained relatively modest improvements from the addition of a dedicated stiffness parameter.

Increasing the number of input parameters required in natural frequency estimates can potentially dilute the effectiveness of such formulas at fulfilling their intended purpose, which is to provide a quick estimate for initial design purposes. Estimating wall stiffness may be particularly difficult if the structural arrangement has not been determined, which is often the case at the start of the design process.

The USCGS data and Japan building data has also been used in more recent studies regarding natural period estimation of buildings. The most notable was conducted by Ellis [47]. This study compiled details for 163 rectangular plan buildings from three sources: the USCGS database, Japan building tests reported by Naito et al. [123], and from new data collected presumably by the author. As discovered earlier by Kanai and Yoshizawa [86], the results of the regression analysis showed that natural frequency was sensitive to building height, but not sensitive to the plan dimensions. The best correlation was achieved by a formula of the form $T = Ch^{1.2}d^{-0.2}$, with a correlation coefficient $r = 0.8918$. However, a formula of the form $T = Ch$ achieved a correlation coefficient $r = 0.8828$, and was therefore recommended as the best simple estimate for the analysed data. Including the coefficient, the formula recommended was;

$$T = h/46 \tag{2.10}$$

A plot of the data used by Ellis and the recommended empirical formula is displayed in Figure 2.5. As observed in previous research, there is considerable scatter in the results, particularly for buildings with height less than 100 m. And there is paucity in the data for building heights greater than 100 m. Applying the statistical analysis to other modes of vibration, Ellis recommended $T = h/58$ ($r = 0.838$) for the fundamental orthogonal translational mode, and using a subset of 63 buildings the fundamental torsional mode was best estimated by $T_t = h/72$ ($r = 0.657$). Equation (2.10) is used in multiple design standards including the
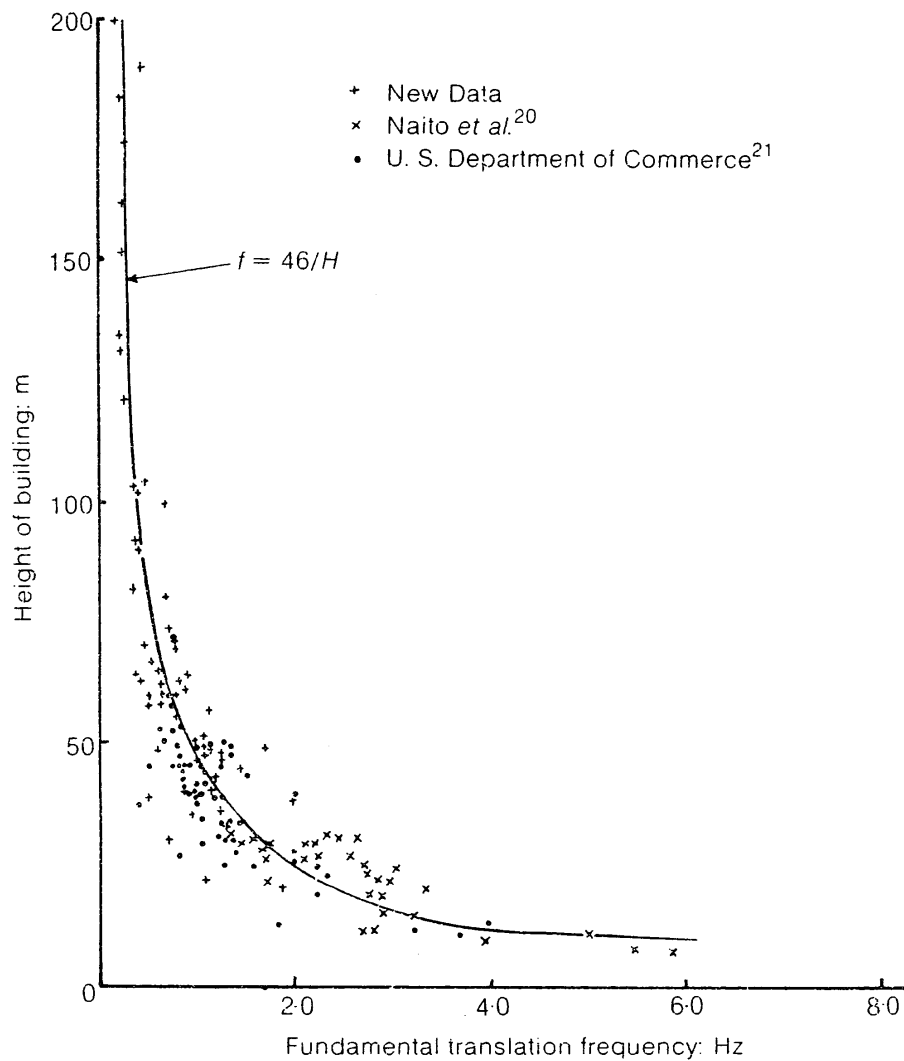
Figure 2.5: Building height versus fundamental translational natural frequency for 163 rectangular plan buildings (Source: Ellis 1980 [47])

Australian wind actions code [151] and the Eurocode wind actions code [51], the latter code recommending its application only to buildings with height greater than 50 m.

Lagomarsino [100] used a database of 185 buildings with mixed material and construction type up to a height of 330 m. Most buildings were less than 100 m, and some standardizing of the database was conducted by removing buildings deemed to be highly irregular. A similar analysis to that of Ellis [47] was conducted, namely the regression analysis using the shear beam model $T = Ch$. For all buildings in the database, the coefficient for the first translation mode was $C = 1/50$. The fundamental translational natural period in the orthogonal direction was also included in the estimate, as the regression coefficient was virtually unchanged by its presence or omission in the analysis. This point is in contrast to the empirical formulas recommended by Ellis [47], which indicated an appreciable difference between the first

mode natural periods in orthogonal directions. Lagomarsino also analysed individual subsets of the database by categorising the buildings according to construction materials. The analysis of the categorised data produced the following formulas;

$$T = h/45 \quad \text{steel buildings} \quad (2.11)$$

$$T = h/55 \quad \text{RC buildings} \quad (2.12)$$

$$T = h/57 \quad \text{mixed buildings} \quad (2.13)$$

The categorisation of the buildings by construction material did not improve the scatter of the data. A potentially more useful categorisation based on structural type was conducted, but no qualitative results were presented. It was also found that the addition of other parameters — plan dimensions, foundation type, soil type, partition walls, slenderness — in the regression model did little to improve the estimation reliability. The correlation between the fundamental torsional period of vibration and building height resulted in considerable scatter in the data, which was particularly evident for building heights greater than 150 m. The regression analysis of the entire dataset produced an estimate of $T_t = h/78$ for the fundamental torsional period, while a categorisation of the data into two bracing types, frame bracing and other bracing (reinforced concrete core, truss bracing, et al.), produced the following formulas;

$$T_t = h/60 \quad \text{frame bracing} \quad (2.14)$$

$$T_t = h/108 \quad \text{other bracing} \quad (2.15)$$

The reliability of the torsional period estimates were less than for the translation case, and the categorisation of buildings by construction material type had little influence on improving the reliability.

The empirical estimates reviewed thus far have been based on test results for generally older style structures. The design techniques, materials, and construction methods have all progressed since the first building vibration measurements were recorded. In addition the accuracy of vibration measurement equipment and analysis techniques has also improved over time. A more modern database was compiled for buildings in Japan, with information sourced from publications issued after 1970. Data for 137 steel-framed buildings, 25 reinforced concrete (RC) buildings, and 43 steel-frame reinforced concrete (SRC) buildings are included in the database. Most of the steel-framed buildings are 50–150 m and used for offices or hotels. RC/SRC buildings are mostly between 50–100 m and are used as apartments, and maximum height was approximately 282 m. Almost all data was obtained during low amplitude vibrations generated by numerous excitation techniques, but mostly from mechanical shaker, human-induced, and microtremors.

(a) Steel-framed Buildings (b) RC/SRC Buildings
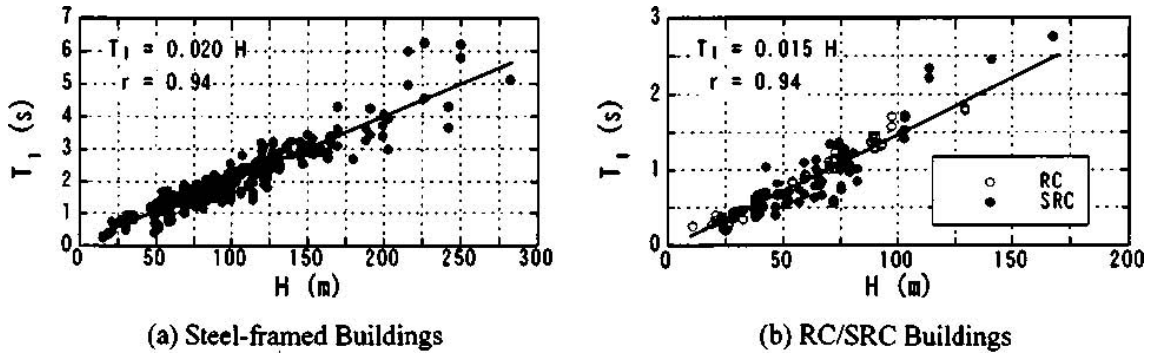
Figure 2.6: Fundamental translational period versus building height(Source: Satake et al. 2003 [139])

Regression analyses [139, 140, 160] of the modern Japan building data included the categorisation of data into construction type. The results are displayed in Figure 2.6, and the recommended formulas for the fundamental translational period were;

$$T_1 = 0.020h \qquad \text{Steel-frame buildings} \qquad (2.16)$$

$$T_1 = 0.015h \qquad \text{RC/SRC buildings} \qquad (2.17)$$

Both datasets returned a regression coefficient $r = 0.94$ for the chosen shear beam model relationship between period and height, and both orthogonal translational modes are included in the analysis. Despite being a modern database, it is interesting to note the results are similar to those obtained by Kanai and Yoshizawa [86] 40 years earlier. The RC/SRC estimate returns a shorter period for any given height compared with steel buildings, which can be explained by these buildings being used as apartments, which often have higher instances of internal walls — either structural or non-structural — which generally makes for a stiffer structure at low vibrtaion amplitudes. The fundamental torsional period was related to the fundamental translational period by the following relationship;

$$T_t = 0.75T_1 \qquad \text{Steel-frame buildings} \qquad (2.18)$$

$$T_t = 0.77T_1 \qquad \text{RC/SRC buildings} \qquad (2.19)$$

The results are displayed in Figure 2.7, and both datasets returned regression coefficients greater than or equal to $r = 0.94$ for the torsional period analysis.

Attention is now focused on the prediction of higher mode natural frequencies. The fundamental translational and torsional natural frequencies generally constitute the majority of tall building responses to dynamic loading [82], however the higher modes can also have significant influence on the response. Furthermore, the ratio of higher modes of vibration to the first mode can provide an indication of the
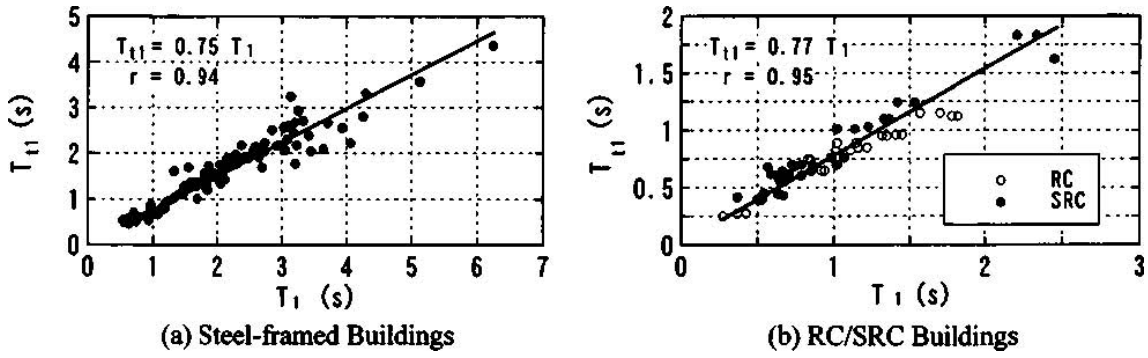
Figure 2.7: Fundamental torsional period versus fundamental translational period (Source: Satake et al. 2003 [139])

deformation action a structure is experiencing. The ratios are compared with ratios obtained from idealised beam models, such as Equations (2.1) for flexural models and Equation (2.2) for shear models.

The estimation of higher mode natural frequencies from empirical data has focused on the ratio between the natural frequencies of the higher modes and the fundamental mode. For the first three translational modes of vibration, research has shown [100, 139, 157] these ratios to be approximately $f_2/f_1 = 3.2$ and $f_3/f_1 = 5.6$, which closely match the ratios for the shear beam model given in Equation (2.2). The classification of the data according to construction type — steel, and reinforced concrete — resulted in higher ratios for the reinforced concrete buildings by up to 6% [139, 157].

Consolidating the literature regarding empirical formulas for estimating natural frequencies of tall buildings, the following two conclusions can be stated. Firstly, the empirical formulas imply, or the researchers have assumed, that a shear beam model ($f \propto 1/L$) rather than a flexure beam model ($f \propto 1/L^2$) is more appropriate for the analysed buildings. Secondly, previous empirical formulas that include more input parameters than height have not significantly improved estimates for the current stock of full-scale data.

For the intended purpose of empirical formulas — the quick estimation for initial analysis — it is unnecessary to increase the calculation complexity above that of the current formulas. Having multiple formulas, each being applicable to a particular type of building, maintains the simplicity of the formula while improving accuracy. This is implemented in most design codes by offering different formulas for each construction type. A lack of full-scale data restricts the ability to offer statistically significant empirical formulas to a relatively narrow range of tall building structure types.

Natural frequency empirical formulas are somewhat insular to the region in which the underlying data was collected, and also possibly influenced by the governing

design code criteria at the time the structure was constructed. This is a reflection of the differing design codes throughout the world, and the effect they have on the dynamic performance of buildings. The natural frequency data sourced from earthquake prone regions, such as Japan, may be ill-suited for application to other areas, via an empirical formula, due to these geographical and temporal influences.

The empirical formula proposed by Ellis [47] uses data sourced from three regions — America, Japan, UK — that was collected over approximately five decades, commencing in the 1920's. The broad geographical and temporal range of the data used is a potential reason for design codes [51, 151] to recommend $f = 46/h$ for estimating the fundamental natural frequency, with reasonable accuracy for initial design purposes, of buildings that could be described as normal.

The description of buildings as normal stems from irregular buildings often being removed from the datasets prior to analysis, which improves regression results for empirical estimates [47, 100, 139]. This highlights the need for a better understanding of the mechanics of modern tall buildings that are considered irregular compared with previous tall buildings. Nevertheless, large variations are encountered even for buildings that are expected to conform to what is defined as normal. This leads to $\pm 50\%$ confidence intervals being recommended when applying empirical formulas [79].

Empirical formulas also do not consider the nature of the mode or coupling between modes. Theoretical and empirical techniques do not do well when complex modes of vibration are present — coupled modes caused by mass and stiffness eccentricities. More complicated models could be devised, but then the benefits of speed of application would be reduced. In such cases, finite element models are essential to the natural frequency estimation process.

It is important to note that empirical formulas can provide more accurate results in some cases where incorrect assumptions are used in theoretical or numerical models. More detail does not necessarily produce improved estimates. This highlights the important role of empirical formulas as a checking option for more complicated, and therefore potentially more error prone, theoretical and numerical models. It also highlights the need for more understanding of structural elements that influence the natural frequency of tall buildings, which will lead to improved modelling assumptions.

2.2.3 Numerical Models

Many numerical techniques exist for estimating the natural frequency of tall buildings. The most widely used of those techniques is finite element analysis. This technique simulates the structure by discretising the structure into a group of small, finite elements over which stresses and displacements vary. The equations of motion

of the discretised system describe the forces and displacements at the node points that define each finite element. The finite element method models a large complex structure via the combination of smaller, simpler structures.

The principle advantages of finite element analysis are generality and scalability. With regard to generality, the method can be used to determine the natural frequency and mode shapes of any linear elastic structure. The application of finite element analysis differs only by the input details from structure to structure. The scalability advantage arises because the method is amenable to the use of matrix and linear algebra techniques, which facilitates the use of digital computers for solving the equations. The number of finite elements contained in a model is only restricted by the computing resources available.

Once the finite element model of the structure is established, the solution is attained via a modal analysis. This approach is identical to the previous discussion regarding lumped parameter systems. The solution provides the undamped natural frequencies in the form of eigenvalues, and the mode shape coordinates in the form of eigenvectors.

2.2.4 Sources of Uncertainty

The uncertainties in natural frequency estimation are related to assumptions made during the modelling of the structure. Tall buildings are complex structures, with relatively large numbers of structural elements and varying material properties. Therefore, modelling a tall building requires simplifying assumptions, mostly to reduce the time required to create the model. These assumptions may not match the behaviour of the actual structure in numerous aspects, including: participation of non-structural elements, soil-structure interaction, type of deformation action, material properties (degree of concrete cracking), connection stiffnesses.

Another source of uncertainty is attributed to variations in the mass and stiffness of structural elements between the model and the prototype. Tall building construction is subject to variability between documented designs and the final, as built, structure. While physical dimensions are generally within aceptable tolerances, the same cannot be said for material proporties and construction quality.

Property estimates for materials such as steel are reported with sufficient accuracy from industrially controlled processes. In contrast, concrete properties are subjected to many factors outside a controlled manufacturing environment, resulting in large differences between design specified concrete properties and the actual used for construction. Concrete suppliers also have the incentive to deliver concrete with properties that exceed the specification. Supplying concrete that does not meet specification attracts the risk of expensive removal or remedial works, as well as litigation. The practice of supplying over specified concrete is known, however the

degree of over specification is not known during the design stage.

The construction quality is difficult to measure and quantitatively relate to the natural frequency. At best it can be viewed as a deviation from the design, but can be difficult to detect post construction without accurate records of the construction process. For example, two tall buildings constructed from factory pre-cast concrete panels, with identical designs and situated at the same site, had fundamental natural frequencies that differed by over 21% [50]. Assuming the use of pre-cast panels removed much of the material variability between the two structures, this highlights the variability in construction quality, and the impact on the natural frequency.

The sources of uncertainty are expanded when non-linear behaviour is included, which is necessary when determining natural frequencies for high vibration amplitudes. Increased vibration amplitudes may reduce stiffness due to decreased participation of non-structural elements, cracking of members, joint slippage, or formation of plastic hinges. Increased vibration amplitude tends to reduce the stiffness of a structure, and therefore reduce the natural frequency.

An extensive amount of research has been conducted on reducing the uncertainties when estimating tall building natural frequencies. The goal is improved understanding of structures in order to formulate, or validate, more accurate assumptions for modelling tall building structures. The methodologies have included: full-scale dynamic studies, correlating models with full-scale results, and compiling databases of full-scale results.

Full-scale dynamic studies

The first method involves the full-scale dynamic study of one or multiple tall buildings, with focus on particular aspects of the structure, such as soil-structure interaction and the effect of structural or non-structural elements. This approach provides valuable insight into the factors that affect the natural frequency of vibration of structures. Unfortunately, the unique nature of tall buildings often limits the transfer of knowledge between structures due to lack of similarity.

The lack of similarity between structures is overcome by conducting multiple tests on a single structure that is undergoing controlled changes, such as during construction or refurbishment. Using this approach allows the effect of structural elements on natural frequency to be observed, and is most effective when structural changes are made individually, such that the effects can be observed in isolation. Refurbishments are particularly useful for observing the influence of non-structural elements, as they often entail stripping a building to its primary structural elements before adding back non-structural elements, such as internal partition walls and facade. In this scenario, the effect of the non-structural elements on the dynamic characteristics can be determined by multiple vibration tests; one test before and

another after the addition or removal of the non-structural elements.

Unfortunately, construction sequences tend to schedule multiple tasks in parallel, which hinders observations focused on a single structural element. This is certainly the case for tall building construction. Shorter buildings have previously provided the construction schedules required to observe discrete changes. For shorter steel frame buildings, an increase in natural frequency has been observed after the addition of non-structural elements [8, 23, 49, 145]. In addition, non-structural elements were found to be effective only during low amplitude vibrations, and increased the non-linear nature of the response; natural frequency decreased considerably with increasing vibration amplitude [55].

The type and design of the non-structural elements has a considerable influence on the extent of the effect on the natural frequency. The presence of internal partition walls does not guarantee a stiffness increase. Observations from a 30 storey reinforced concrete building [178] and a six storey steel frame building [117] reported little influence of partition walls on the natural frequency.

Correlating models with full-scale results

The correlation of mathematical models with experimental results allows the sensitivity of the modelling assumptions to be assessed. This is often achieved via the calibration of finite element models with full-scale measurements [19, 94, 108, 126, 186]. The effectiveness of this method depends on the range of data collected and the complexity of the tested structure.

The range of data that can be collected from full-scale testing can be broadly categorised into two groups: global data and local data [54]. Global data includes the dynamic characteristics of the structure, such as natural frequencies and mode shapes. The local data category incorporates the smaller scale aspects of the structure, such as the measurement of beam stresses and strains. These two categories, and the full-scale data they include, influence the methodology used when updating finite element models using full-scale data.

The assumptions used when creating a finite element model of a tall building are typically due to simplifications to reduce modelling time, as well as due to estimates of how particular structural elements will perform under various load levels. For example, under serviceability loads a non-structural element may be considered to participate in the structural system, and then not participate under ultimate loading conditions. These estimates can be influenced by design conservatism that seeks to ensure a higher factor of safety regarding the strength and stability of a structure.

Previous research has shown that numerical models of reinforced concrete tall buildings that only include the bare frame and wall elements are likely to underestimate the natural frequency [84, 94, 109, 156]. In some cases, the difference was

greater than 50%, which would be considered excessive for design. Excluding floor plates is a common practice in tall building finite element modelling, and is conducted to improve the numerical efficiency of the model. In the place of the floor plate elements, a rigid diaphragm assumption is applied to the nodes located on the plane for the floor plate. The rigid diaphragm essentially connects each node via an infinitely stiff link, and forces all nodes to move as one plane without affecting any out of plane actions.

The modelling of shear walls and coupled shear walls is another aspect of finite element modelling that attracts simplifying assumptions. The accurate modelling of major and minor wall penetrations, as well as thin internal walls, has been shown to have a strong influence on torsional modes of vibration [19]. Non-structural elements and their influence on structural stiffness has received considerable research attention [55, 104, 156]. Conclusions regarding the stiffening effect of non-structural elements are mixed. Ultimately, the structural capacity of non-structural elements and their connection to the primary structure must be analysed on a case by case basis to determine if they will have any influence on the lateral stiffness.

The strength and variability of construction materials is another aspect of finite element modelling that can cause discrepancies with full-scale measurements. The use of concrete that exceeds the design specification has been discussed previously. Furthermore, concrete strength increases with time, and the level of cracking in the concrete from previous loading events will also influence the effective strength.

Compiling databases of full-scale results

The final method of reducing uncertainties in natural frequency estimation is via collecting natural frequencies and structural properties for a large set of buildings. This reduces uncertainty by permitting a comparison between a large number of existing buildings with the structure to be designed.

The classification and summarising of the data reduces, in theory, the variations within each category. The lack of data may limit the sample sizes required to achieve meaningful comparisons. An extension of this approach is the development of empirical formulas discussed previously. This method becomes less effective when building designs deviate from the buildings contained in the database.

2.3   Damping Ratio Estimation

Damping refers to the energy dissipation inherent to a mechanical system that tends to reduce vibration amplitudes. In most cases the mechanical energy is converted to heat. Despite the history of research on the subject, the understanding of damping forces in vibrating structures has not reached a well developed state. The funda-

mental mechanisms causing damping forces in mechanical systems and materials are yet to be confidently proven, and remain the major barrier to the understanding of damping forces. In contrast, the inertial forces and stiffness forces that contribute to the natural frequency are well understood for most vibrating structures. By using the dimensions, material properties, and elastic properties of structural and non-structural components of a system, such as a tall building, it is possible to accurately determine the mass and stiffness contributions to the system with little difficulty. This is not the case for damping.

2.3.1 Sources of Damping

Damping in tall buildings originates from a number of sources that are both internal and external to the structure. These sources are as follows [41, 168];

- Material damping: This form of damping is intrinsic to the materials present in the structure. The sources of material damping are associated with plastic flow, magneto-mechanical effects, or dislocation movement within the crystalline structure of the material. When subjected to cyclical loading, these mechanisms result in a stress-strain hysteresis loop. Significant non-linearity of the damping characteristics for structural materials has been observed, particularly at high stress levels [101]. A measure of this form of damping is typically represented by the *specific damping capacity*, which is a ratio of the energy dissipation per cycle to the strain energy at maximum strain.

- Frictional damping: The sources of friction damping are associated with boundary shear effects that arise from abutting surfaces. In tall buildings this includes connections or shared boundaries between structural components as well as non-structural components. The energy dissipation mechanism at the interface may be due to dry sliding (Coulomb friction), lubricated sliding (viscous forces), or cyclical strain in a separating adhesive (damping in a visco-elastic layer) [62]. One model of this type of damping is a stick-slip model [41, 187], which assumes certain elements in the structure deform elastically to a defined force threshold, and then slip.

- Foundation damping: This source of damping arises due to radiation of energy from the structure to the underlying ground. It is typically a function of the characteristics of the ground, such as density, Poisson's ratio, shear and elastic modulus, and the depth to which the structure is embedded in the ground. Therefore, a detailed knowledge of the local ground constituents and their properties is important when determining the influence of foundation damping.

- Aerodynamic damping: This source of damping is external to the structural system and is caused by the interaction between a vibrating structure and the fluid medium in which it is immersed. For low to moderate reduced wind velocities the aerodynamic damping is positive, but negative aerodynamic damping can be created at certain wind speeds.

- Auxiliary damping: This source of damping represents a designed addition of energy dissipation to a structure in order to reduce the vibration response. Additional damping systems, either passive or active in design, are effective in reducing the wind-induced response of tall buildings [97, 120, 188], and are implemented in numerous buildings for this purpose [66, 162].

The first two damping sources discussed — material and frictional damping — constitute the structural damping. The quantitative definition of the local energy dissipation mechanisms that contribute to the structural damping is very difficult to obtain. Consequently, the structural damping is typically described by a single parameter that incorporates all the local energy dissipation mechanisms.

A range of models for structural damping have been developed, and the most commonly used is the viscous damping model, where the damping force is expressed as the product of a constant and the velocity of oscillations. When solving the equations of motion for a damped system, using the viscous damping model leads to a convenient form of the equations that facilitate the solution process. The viscous model assumes that the energy loss per cycle at a fixed amplitude is dependent on the response frequency. Section 4.2 discusses viscous damping models in the context of solving the equations of motion for a multi-degree of freedom dynamic system.

An alternative model to the viscous damping model is the hysteretic damping model, which is valid in the case of harmonic excitation. It is defined as a damping force that is proportional to the displacement amplitude, and is in phase with the velocity of the system. In contrast to the viscous damping model, the hysteretic damping model is independent of the natural frequency.

For the elastic range of response, research has shown [77] that combining all sources of damping into one equivalent viscous damping model is a sufficiently accurate assumption. Once the response moves out of the elastic range and becomes non-linear, the viscous damping assumption is no longer valid. For analysis purposes during the design of a structure, the damping ratios can be obtained from full-scale dynamic testing of similar structures. This type of testing has been performed on many buildings, and a large database of values has been compiled from numerous independent research sources.

2.3.2   Full-scale Measurements

The history of full-scale measurements of tall building damping ratios closely follows the history of natural frequency estimations discussed in Section 2.2.2. Since this research focuses on damping ratios for modern tall buildings, the discussion will be focused on recent studies. A combination of engineering judgement and historical full-scale results is used to estimate the damping ratios in practice. Matching the structure to previous structures with similar properties — structural system, materials, soil, foundation, etc — is the approach adopted by some design codes. Almost all of the previous research reports damping ratios for low amplitude excitations below serviceability levels.

A survey of 12 tall buildings was conducted in Australia [99], and all of the buildings used RC construction except one that was comprised an RC core with steel frame. The heights ranged from 31 to 68 storeys. The autocorrelation function from ambient excitation was used to determine the damping ratios for the fundamental translational modes. The damping ratios were between 0.5–2.1 % for the RC buildings, and 1.0–1.9 % for the RC steel building. The mean value of all measurements was 1.1 %. The Australian building database was expanded with the addition of eight RC tall buildings [98], and the damping ratio estimates for the fundamental modes were reported to be in the range 0.40–1.65 %. A database of damping ratios for RC buildings in Japan [139, 157] with heights greater than 150 m reported similar damping ratios of approximately 1.0–1.5 %.

Four RC buildings in Hong Kong were studied for one year return period wind events [21] using the random decrement technique, as well as controlled forced vibration tests [22]. For the ambient vibration tests of amplitudes up to approximately $1.0\,\text{mg}_\text{n}$, the mean values for the translational modes was between 0.96–1.4 %, while the torsional mode damping ratios were between 1.03–1.32 %. The controlled forced vibration testing of these buildings established the translational damping ratios between 0.5–1.0 %, and the torsional damping ratios between 1.0–1.3 %.

2.4   Full-scale Dynamic Testing

Dynamic tests on full-scale structures are of two main types: forced vibration tests (FVT), and ambient vibration tests (AVT). The FVT approach is further categorised into two types: free vibration tests, and steady-state forced vibration tests. For free vibration tests, an initial controlled excitation source is introduced to the structural system, and then removed, which causes the structure to perform damped free vibrations. The response of the structure to the initial excitation is then recorded for analysis, but the input excitation force is not necessarily measured. The structure can be set in motion by either a sudden release from an initial displacement, by

imparting an initial velocity on the structure, or by imparting a force. Methods that have been successfully used to impart an initial excitation on tall buildings for free vibration tests are listed below;

- Mechanical shakers have been extensively used in previous vibration studies [9, 70, 111]. They are normally used for steady-state forced vibration tests, but are equally suited to imparting an initial force for a free vibration test. The input force from the mechanical shaker is repeated over a number of oscillations to increase the vibration amplitude to the required level. The maximum amplitude of vibration achievable depends on the input force capability and the energy dissipation inherent to the structure. To achieve an accurate free vibration response for damping estimation, the force input from the mechanical shaker needs to be suddenly halted when the required vibration amplitude is attained. This requirement makes linear mechanical shakers [22] more suitable than rotary mechanical shakers [69] for tall building dynamic testing. Furthermore, rotary mechanical shakers become ineffectual at low vibration frequencies associated with tall buildings, because the accurate control of the shaker and the input forces generated both diminish with decreasing vibration frequency.

- Initial displacements of the structure can be achieved via an attached cable that is subsequently loaded to cause a desired level of displacement in the test structure [24]. In order to achieve an accurate free vibration result, a suitable release method is required to ensure the instantaneous and total relaxation of the tensile forces in the load cable. This method is more suitable for smaller buildings, as for taller buildings the length of cable and the angle of the applied force may be prohibitive.

- Synchronised movement of one or more humans at the natural frequency of the test structure has been shown to achieve vibration amplitudes suitable for free oscillation tests [59, 72, 166]. Best results are achieved if all involved in generating the excitation force are pushing in unison against a common structural wall. This method is essentially the same as using a mechanical shaker, except that measurement of the input force would require much more effort. Like a mechanical shaker, a number of input pushes can be made in succession to increase the vibration amplitude. The main benefits of this method are simplicity, cost effectiveness, and the ability to instantaneously halt the excitation force.

- A construction crane attached to a building can be used as an excitation source by lowering a mass and suddenly breaking the fall [42, 59]. Multiple fall and

braking cycles can be made in succession to increase the vibration amplitudes, and the boom can be positioned at different locations relative to the building axes to target particular vibration modes.

If damping ratios are required from free vibration tests, it is important that ambient excitations are minimised during testing so that the applied initial excitation is the only significant action on the test structure. Examples of ambient excitations for tall buildings include wind loading, earthquake tremors, construction crane activity, and elevator car movements. Minimising these sources of unmeasured force inputs will ensure errors for damping values are within acceptable limits.

The second type of FVT, the steady-state forced vibration test, requires sinusoidal forces of varying frequency and amplitude to be applied to the test structure. Both the input force and output response are recorded, and combined to generate resonance curves or frequency response functions [74]. The dynamic characteristics of the test structure can then be extracted from the resonance curves. A mechanical shaker is used to apply the sinusoidal forces, and like the free vibration tests, the minimisation of the unmeasured ambient excitation forces is important to avoid excessive errors in results. This method has been successfully used for the dynamic testing of numerous tall buildings [9, 71, 112, 154].

Dynamic tests using the AVT approach have also been extensively used in previous studies [17, 33, 173]. Like the free vibration test method, the input excitation force is not measured. However, the output from ambient vibration tests are not free vibration responses from a single excitation. Rather, the output response is generated by multiple excitation forces acting on the test structure, which vary with time and have various degrees of spacial correlation.

Ambient loading has the advantage of exciting multiple natural modes of vibration that can be recorded during a single test, and viewed individually using digital techniques while post processing the vibration signals. In comparison to FVT, the forced loading of large civil engineering structures has a number of disadvantages. Development and logistical disadvantages are usually the most apparent when considering forced loading. Development of mechanical shakers used to conduct forced loading is often time consuming and costly in comparison to ambient loading, which requires no development of loading equipment.

Conducting forced loading is often accompanied by logistical problems associated with the transportation and installation of the loading equipment. Depending on the size of the structure to be tested, the loading equipment can be extremely large and heavy, and therefore difficult to transport, in addition to causing potential disruptions to the regular operation of the structure while conducting the tests. Another disadvantage of forced loading arises from requiring almost complete control of the various input loads on the structure. This results in forced loading tests being

conducted when ambient loads are minimised — calm wind conditions for example. Control of ambient loads is practically impossible, which means forced loading tests are at best scheduled when ambient loads are expected to be minimised.

Previous research [121, 154, 175] has concluded that dynamic testing of buildings using ambient excitation can provide reliable estimates of natural frequencies and mode shapes. However, until more recently the estimation of structural damping ratios from ambient excitation tests was particularly unreliable. In contrast, under ideal forced excitation tests, structural damping ratios can be reliably determined.

The primary reason for this is under ideal conditions the input force can be accurately determined when conducting a FVT. The known input force is used along with the response output to determine the dynamic properties. Furthermore, FVT can also force a particular mode to be excited with-out other modes ocurring simultaneously. For AVT there is also the issue of separating structural damping and aerodynamic damping components from AVT test results.

More recent techniques [14, 17, 127, 136] for post processing ambient excitation test results have improved the structural damping ratio estimates, however most techniques are more computationally intensive when compared with the processing requirements of forced excitation test data.

Vibration amplitudes generated by ambient excitation forces are usually orders of magnitude less than those generated by forced excitation. Unless a broad spectrum of vibration amplitudes are experienced during the testing phase, the results will only be valid for a small subset of potential loading conditions. This is a weakness of ambient vibration testing, particularly when considering the influence of response amplitude on natural frequency and structural damping ratios. It has been observed that as vibration amplitude increases, the natural frequencies decrease and the structural damping ratios increase [80, 87, 165]. This effect is reflected in many building design codes, which specify larger values for structural damping ratios for ultimate load cases compared with the values for serviceability load cases [151].

2.4.1 Dynamic Testing during Construction

The previous sections highlight the large amount of data and knowledge obtained on the full-scale dynamic characteristics of completed structures. Much of this has been due to research focused on earthquake engineering of civil structures. Very few previous research efforts have investigated vibration testing of partially completed structures during construction, either as a means of understanding the structural mechanisms that influence the dynamic characteristics, or for enhancing the prediction of dynamic characteristics. Compared with testing completed structures, testing during construction presents more obstacles to achieving optimum outcomes.

It is difficult to control the construction of a building to maximise the information

from vibration tests during construction. The schedule of the builder, who is under pressure to meet cost and time budgets, governs how the structure is built. In most cases, vibration testing during construction can only aim to conduct tests at the most opportunistic stages of construction, in order to observe the effects of structural changes on the dynamic characteristics.

Tall building construction is a particularly good example, because the construction schedule tends to progress based on levels, as opposed to structural elements. It would be advantageous to conduct vibration tests when certain parts of the structure are completed, for example at the completion of the shear walls, columns, floor slabs, facade, and internal non-structural walls. However, tall building construction tends to overlap all of these parts. For example, the installation of the facade is generally commenced once the structure has been completed far enough ahead, but not entirely completed, to avoid clashes between construction processes. In this arrangement, the facade and structure are built simultaneously, with the facade trailing until the structure reaches completion.

Complete control over the construction of the structure would be ideal for understanding the structural mechanisms and the influence of both structural and non-structural elements, but this is not practical or economical for tall buildings. Despite not having complete control — to add or remove structural and non-structural elements at any time — during construction, determining the dynamic characteristics at partially completed states can provide insight into the structural mechanisms that influence the dynamic characteristics.

Due to the construction schedule mentioned above, it is unlikely that one study will ever provide comprehensive understanding of tall building dynamics. Each study of a building during construction offers a unique opportunity to further the understanding, particularly if the construction schedule differs from previous studies.

Dynamic tests of partially completed buildings, or buildings undergoing alterations, are not a recent occurence. The earlier studies conducted in the 1930's were mostly confined to steel frame buildings of under fifteen storeys [23], which were the dominant form of construction at that time. For this type of building, the main focus appeared to be determining the influence of curtain walls, partition walls, and concrete encasement of the steel frame [8, 24, 145]. Furthermore, the results focused attention on the natural periods of oscillation, and little information was provided on the damping ratios. More recent studies have since included damping ratio estimates [118].

The most comprehensive study for steel frame structures is perhaps the Cardington steel frame building [49]. This steel frame structure comprised eight storeys and was designed to represent an office building. The entire structure was constructed within a laboratory, which allowed for practically complete control of the

input excitation. Furthermore, the construction was undertaken in discrete stages to accurately determine the influence of each stage on the dynamic characteristics. This controlled laboratory experiment is at the extreme end of full-scale testing, and generally not a viable option for larger structures.

Taller buildings have also been tested during construction and alterations, and of particular interest to this research are those [16, 42, 141, 178] that use a reinforced concrete core as the primary lateral load resisting structure. These few studies represent the current breadth of research that use full-scale testing of tall buildings during construction to improve the estimation of dynamic characteristics.

2.4.2 Natural Frequency during Construction

A majority of the research on the estimation of natural frequencies during construction has focused on the influence of non-structural components, such as internal partitions and facades. Shorter buildings have been more successful test cases because the reduced number of levels, compared with taller buildings, means the primary lateral system is more likely to be completed prior to the construction of the facade and non-structural partitions. Therefore, the changes can be observed in discrete stages.

For taller buildings during construction, the ability to observe the influence of the facade and internal partitions is limited to the final stages of construction. This is due to the main structure being completed while the remaining fit-out and facade are conducted at lower levels, thus creating a stage at the end of construction where only the facade and fit-out are changing. The observation of this stage in previous studies of reinforced concrete core buildings has found the facade and partitions did not significantly influence the dynamic characteristics [16, 42, 178]. This is a similar result to that obtained for a steel frame tower of 24 storeys, which found the cladding had little influence on the first modes, but tended to increase the natural frequencies of the higher modes of vibration [118]. Regardless of the initial aim of the previous studies, all the results have reported a decrease in natural frequency with increasing height.

A relatively complete study of natural frequencies for a tall building during construction was conducted on a reinforced concrete tower in Vancouver [141]. The tower included 30 storeys, with 85 m height above ground and 9.4 m of basement below ground. Using ambient vibration measurements, the natural frequencies of the fundamental vibration modes — two sway and one torsion — and the second and third set of higher modes was estimated. The results found the spacing between the fundamental and higher order modes decreased as the building height increased. For the sway modes, the ratios between the higher modes and the fundamental mode was considerably higher, by as much as two times, than the ratios for an idealised shear

beam model in Equation (2.2). The ratios for the torsional modes were generally within 10% of the idealised shear beam model.

2.4.3   Damping Ratios during Construction

As for the investigation of natural frequencies during construction, previous research has also focused on determining the influence of non-structural components on the damping ratios. A common obstacle shared amongst the previous research is the difficulty in obtaining a consistent set of accurate estimates for the damping ratios during construction [42, 141]. This is understandable since the estimation of damping ratios is very sensitive to the loading conditions. And this fact is not avoided if a mechanical shaker is used to excite the structure, as ambient vibrations can still influence the results.

Regardless of the incomplete results sets for damping ratios, potentially useful results have been reported. For a 24 storey steel frame tower, the facade was found to increase the damping ratios, with the effect being more pronounced for the torsional modes [118]. Forced vibration tests of a 94 m high apartment building with reinforced concrete core found the damping ratios to be more dependent on the stage of fit-out in the lower levels, as opposed to the fit-out in the higher levels [42].

2.5   Wind-induced Response

The wind-induced response of tall buildings consists of three components: a static component due to the mean wind force; a quasi-static component due to low frequency wind force fluctuations; and a resonant component due to wind force fluctuations that have frequencies equal or similar to the natural frequencies of the building. The quasi-static component is dynamic in nature — it involves movement of the structure over time — however the frequency of the force fluctuations do not coincide with the natural frequencies of the structure, which means resonance does not occur. The static and quasi-static components are collectively referred to as the background component.

The monitoring of a structure requires the recording of both the resonant response and the background response. For the wind resistant design of tall buildings, the required indicators include member stresses, structural deformations, and displacements. The static and quasi-static components will influence these indicators and cannot be ignored. Therefore, the measurement of static and quasi-static components are important for tall building design and performance assessment.

In theory, the measurement of either displacement, velocity, or acceleration will yield a complete result set for describing the responses, because the measured parameter can be differentiated or integrated to produce the unmeasured parameters.

The accuracy of the integration results depends on the quality and properties of the input data. Considering the basic equations for velocity and displacement derived from the integration of acceleration;

$$\dot{x} = \int \ddot{x}\,dt + C_1 \tag{2.20}$$

$$x = \int \dot{x}\,dt + C_1 t + C_2 \tag{2.21}$$

each integration step in Equations (2.20) and (2.21) introduces an unknown constant (C_1 and C_2) that can be resolved if the velocity and displacement are known at a particular time. Since accelerometers are prone to drift and other errors over time, it is not feasible to know with certainty the instantaneous velocity and displacement. To make this approach feasible would require continuous compensation of the acceleration output for drift and other errors. Without such knowledge, Equations (2.20) and (2.21) are not applicable for determining the quasi-static response of a structure subjected to random loading. For this reason, both accelerations and displacements are simultaneously measured by separate sensors to produce a complete results set describing the wind-induced response of a structure.

2.5.1 Full-scale Monitoring

Prior to the 1970's, the most significant full-scale study of the wind-induced response of tall buildings was the study conducted on the Empire State Building (380 m) in New York during the 1930's [132]. A re-analysis of the results by Davenport [37] established the increase in tip displacements according to wind speed. Furthermore, the difference in stiffness between the orthogonal axes of the building were established and attributed to the geometry and structural system of the building.

Wind loads on tall buildings received more focus in the 1960's and 1970's as an increase in tall building construction occurred during this period. The study conducted on the Commerce Court Tower (239 m) in Toronto [35] is one of the most extensive and well documented of the period. The acceleration response measurements established the significance of torsional motion combined with sway motion for one of the building orthogonal axes. This highlighted the influence of eccentricities between the centre of mass and centre stiffness on the mode shapes and subsequent response. The torsional motion was found to increase accelerations by a factor of 1.4 at points furthest from the centre of rotation.

More recently, the focus on monitoring the wind-induced response of tall buildings has continued due to the increase in heights for some of the current tall building designs. A number of studies have been conducted in the Asia-Pacific region, which have focused on the response of tall buildings to typhoon winds [20, 107, 110]

2.5.2   Displacement Measurement Techniques

The earliest recorded wind-induced displacement measurements of large flexible structures were undertaken using optical techniques [46]. This method works by sighting a target, perpendicular to the line of sight, through a telescope or similar instrument. It is simple and easily implemented, but lacks the ability to attain accurate measurements with high frequency. Automation is another key aspect missing from such an approach to long term displacement measurement, an aspect that is now easily accounted for by utilising relatively cheap and high resolution personal movie cameras. The need to maintain an unobstructed view to the target can be difficult to achieve, especially since many modern tall building designs incorporate multiple set-backs, as well as the influence of weather conditions and pedestrian or vehicle traffic. Target illumination must be considered for low light operation.

In the 1930's, displacement monitoring techniques investigated the abilities of plumb-bob methods [132]. Measurements are observed from the movements of a small mass suspended by thin wire from the upper levels of a structure. Placement of the wire and mass is restricted to internal shafts, such as service shafts, to avoid wind disturbance. The biggest disadvantages of this method is space limitations, temperature effects on the wire, and the need to dampen the swinging mass to remove inertial components of displacement. The use of a plumb-bob coupled with a tracking laser allows automated monitoring of the displacements [112].

Most limitations of optical and plumb-bob techniques are overcome using a laser. More specifically, laser interferometery is capable of recording highly accurate displacements, although the accuracy degrades with increasing travel distance of the laser. Particles suspended in the air, including dust and water vapour, disperse the laser beam and reduce the concentration of light resulting in reduced accuracy. Despite these limitations, laser techniques have proved suitable for tall building displacement monitoring [96]. Adding a photo-sensitive sensor [58] and computer to digitize and record the laser beam, this system becomes automatic in operation. However, to avoid the effects of water vapour and precipitation, internal installation of laser displacement systems is desirable, which introduces space limitations inherent within tall building shafts.

Displacement measurements can be determined from tilt angles of the structure [58]. The tilt angle is measured using a sensitive acceleromter. The main disadvantage is the drift inherent to accelerometers, which will cause errors in tilt angle estimates.

More recently, displacement measurement systems based upon the Global Positioning System (GPS) have been used to monitor large flexible structures [15, 61, 114, 161]. Using GPS, the unknown position of objects are determined from the known position of other objects via the concept of triangulation. GPS is designed to allow

precise estimation of position, velocity and time in all weather conditions. The all weather operation of the GPS design is an advantage over other displacement measurement techniques. The disadvantage of using GPS displacement measurements stem from the sources of error in the estimates, which include: atmospheric effects, multipath effects, inadequate satellite position, satellite ephemeris errors, and timing errors. The atmospheric effects and multipath effects are likely to contribute most to the total error when monitoring tall buildings.

A GPS receiver measures the incoming phase of satellite signals. As the satellite signals travel from the source to the receiver, they pass through and are affected by the atmosphere. The atmosphere consists of the ionosphere and the troposphere, and changes in these zones cause a degradation in the accuracy of observations. Satellite signals passing through the ionosphere can be slowed due to an effect similar to the refraction of light as it passes through mediums of differing density. Such atmospheric delays can introduce error in the range calculation as the velocity of the signal is affected. Furthermore, the delay induced by the atmosphere is not constant and depends on a number of factors; satellite elevation, density if the ionosphere and the presence of water vapour.

Atmospheric errors can be mitigated by using two receivers: one configured as a reference receiver, and another as a roving receiver. The reference receiver is fixed at a point, and therefore static. When the two receivers observe the same set of satellites simultaneously, the reference receiver can be used to correct the errors from atmospheric effects in the roving receiver. The baseline between the two sensors should be minimised to ensure that identical atmospheric conditions are recorded at both receivers.

The multipath error source relates to the reception of GPS signals that have travelled indirectly from the satellite to a receiver. Multipath signals travel further than a direct line of sight signal, which causes overestimation of the distance travelled by the signal and significant errors in the recorded positions. GPS signals can be reflected by any surface or object, including buildings and natural surroundings.

2.5.3   Response and Peak Factors

Wind forces on structures tend to have random amplitudes that are distributed over a wide frequency range. The response of wind sensitive structures tend to be dominated by resonant responses to energy in the wind spectrum that coincide with the narrow bands about the fundamental natural frequencies of the structure 2.8. For most structures, a majority of the wind energy is at lower frequencies than their natural frequencies. Furthermore, the energy decreases with increasing frequency. Therefore, only the fundamental modes need to be considered. Tall buildings with eccentricities between centre of mass and centre of stiffness are an exception, as
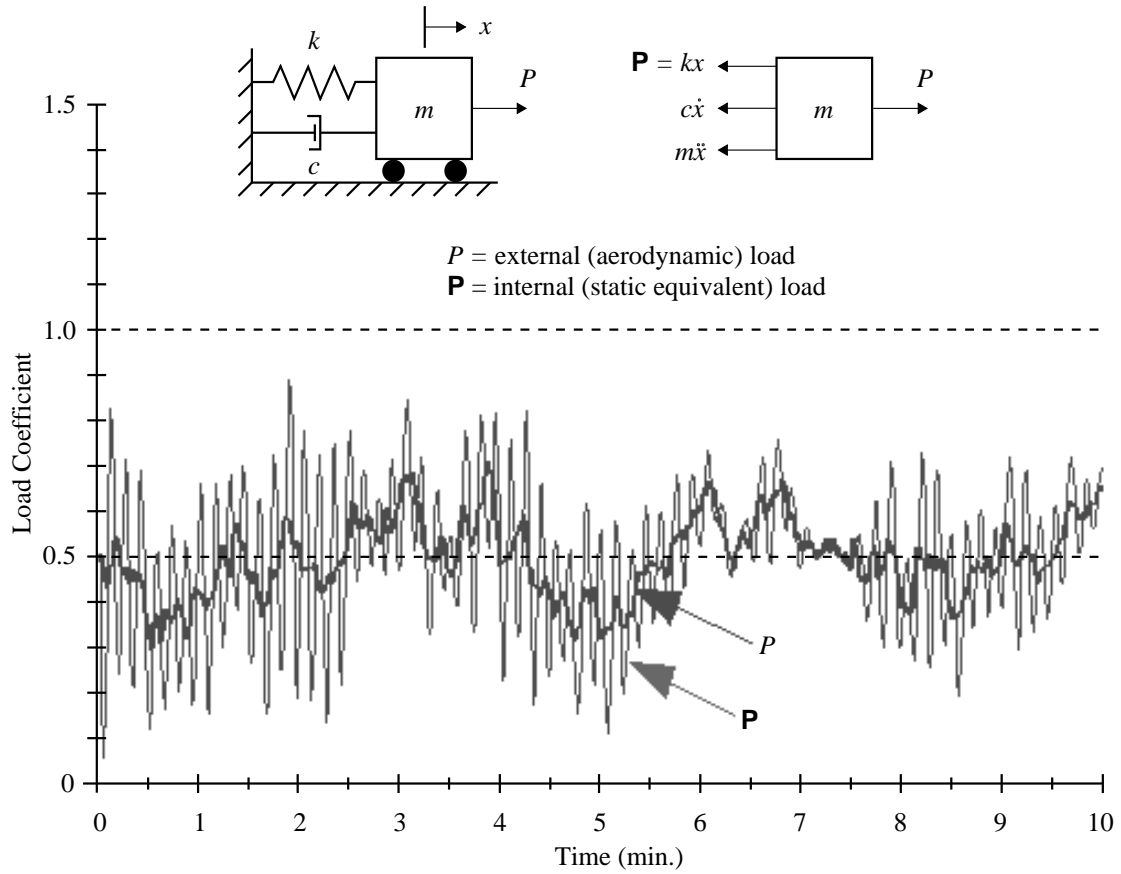
Figure 2.8: Single degree of freedom narrow band response to external (aerodynamic) load

higher modes with torsional responses become important to consider.

The wind-induced response of structures is divided into along-wind and cross-wind components. This classification is made due to the different forcing mechanisms that cause responses in these directions relative to the incident wind. The combination of these components results in an elliptic response envelope.

Since the total response of a structure is composed of mean and dynamic components, it is convenient to describe structural actions in terms of a mean value plus the average maximum likely to occur. Probability distributions of the random variables can be used to determine the peak value, and it has been shown that the average peak response can be expressed via the number of standard deviations by which the peak exceeds the mean [40]. The average peak response is then described as;

$$\hat{x} = \bar{x} + g\sigma_x \qquad (2.22)$$

where $\hat{x}$, $\bar{x}$, and σ_x are the peak, mean, and standard deviation of x respectively, and g is the reduced variate called the peak factor. The peak response is dependent on the time period, and is often, but not exclusively, related to a duration of one

hour [38].

The wind-induced response of structures is randomly distributed, and the estimation of the maximum value is an import consideration when designing structures. For most cases the response distribution can be considered as Gaussian, because the Central Limit Theorem states the probability distribution of a continuous variable that is the sum of a large number of independent variables is approximately normal. For a normally distributed process, the peak factor can be based on the mean of the distribution of largest values [39], which gives the equation;

$$g_f = \sqrt{2\ln(n_0 T)} + \frac{0.577}{\sqrt{2\ln(n_0 T)}} \tag{2.23}$$

where n_0 is the mean value crossing rate and T is the time period. Equation (2.23) allows prediction of peak factors based on the mean crossing rate, which is typically equal to the natural frequency of the structure, and the length of time T over which the process is recorded. Depending on the time period considered, the peak factor of an approximately Gaussian process is typically between 3.3 to 4.6.

In some cases, the process differs significantly from a Gaussian distribution. The investigation of these non-Gaussian processes can provide insight into the nature of the excitation mechanisms. The peak value and peak factor can be related to a specific probability level [116]. For a lightly damped structure oscillating at its fundamental natural frequency, it is possible to express the probability of exceedance in terms of a frequency. Specifically, the peak value can be defined as the value crossed with positive slope, following a zero crossing, once only on average during a period T. For a narrow band, stationary, ergodic, normal process, this definition of the peak value takes the form of a Weibull distribution and defines the probability of upcrossing exceedance as;

$$P(x > a) = e^{(a/c)^k} \tag{2.24}$$

For a Gaussian process, $k = 2$, $c = \sqrt{2}\sigma_x$, and the peak factor is 3.7 for P > 0.001. The Gaussian process provides a boundary between extreme behaviours. For increasing values of k, the upcrossing variables become increasingly dependent such that a sine wave results when $k = \infty$ and the peak factor is constant at a value of $\sqrt{2}$. For $k > 2$, intermittent characteristics become more significant and the peak factor is typically greater than 4 for P > 0.001. The peak factors using this method are subscripted with the probability level to avoid confusion with the peak factor based on a distribution of largest values.

2.6 Summary

The previous research and current methods for the estimation of natural frequency and damping of tall buildings have been presented in this chapter. The uncertainty in the estimates provided by the current methods have been discussed with reference to theoretical, empirical, and numerical estimation methods. The theoretical and numerical methods have deficiencies in their ability to model structures with complex interactions between primary structural elements and non-structural elements. The empirical methods have the disadvantage of relying on a finite database of full-scale results from existing structures to establish common trends. The quality of empirical estimates are only as good as the quality of the database and how applicable they are to modern structures.

Errors in the natural frequency or damping estimates can have a significant impact on the design of a tall building as it can lead to incorrect estimates of the wind-induced response. In turn the structure may be over or under-designed for the actual wind loads. In the case of an over-designed structure the unnecessary use of resources is the downside. For the under-designed case the structure will not perform to acceptable criteria, such as occupant comfort criteria, resulting in discomfort for tenants and possibly financial costs for the building owner due to owning a poorly performing building.

From the material discussed in this chapter there is a need to improve the natural frequency and damping ratio estimates for tall buildings. Particularly in the early phases of design and construction to enable improved designs and to identify if errors have been made. The full-scale testing of tall buildings provides a number of benefits in this respect. It adds to the database of tested structures to improve empirical methods. It allows the improvement of modeling techniques in numerical methods through insight to appropriate assumptions about the structure and material properties. And as outlined in the thesis objectives, it may help to reduce uncertainty in the natural frequency and damping estimates when testing is conducted during the early stages of construction.

The estimation of wind-induced response involves a chain of steps. The estimation of natural frequency and damping are steps in the chain, and they are used in the estimation of wind loads via wind code calculations and wind tunnel testing. Errors in these later steps have similar outcomes: over or under-designed structures. And similarly they can benefit from full-scale testing. The following chapter outlines the full-scale experiments and the tested structure that is used to address the research needs discussed in this chapter.

Chapter 3

Description of Full-Scale Experiments

3.1 Introduction

The benefits of full-scale testing of tall buildings has been discussed in Chapters 1 and 2. In this research the results of full-scale testing will be used to reduce the uncertainty in natural frequency and damping estimates and to validate wind tunnel testing results. This chapter describes the structure used for full-scale experiments, Latitude tower (Figure 3.1), and the instrumentation and experimental methods used to measure it's response to various excitations. The description of Latitude tower includes the geometry, structural system, construction methods, location, and surrounds of the building. The description of the structural system and construction methods are included to support the results of the vibration testing conducted during construction of Latitude tower, which are presented in Chapter 5.

The data recorded during experiments included acceleration, displacement, wind speed, and wind direction. The instrumentation consisted of accelerometers to measure the dynamic response, GPS receivers to measure the displacements, and an anemometer to record the wind speed and direction. Supporting instrumentation, such as signal conditioners and data acquisition systems, are also described in addition to the calibration, setup, and installation of the components.

The phases of the full-scale experiments are; firstly, periodic vibration testing to record accelerations during the construction phase, and secondly, a continuous monitoring phase to record accelerations, displacements, and wind velocity. In total the periodic vibration testing lasted for one and a half years, and was followed by a two year period of continuous monitoring.

Figure 3.1: Architectural impression of Latitude tower viewed from the south-west (Source: Crone Nation Architects)

3.2   Description of the Test Structure

Latitude tower is a 46 storey office tower, with a maximum height of approximately 187 m above street level and 28 m of underground levels. An elevation of the eastern facade of the building is displayed in Figure 3.2. Level 1 is the bottom of the basement levels, level 10 is ground level, and level 55 is the roof. The development of the Latitude tower site also included a six storey building located to the rear of Latitude tower. The two buildings are structurally connected below street level via the basement floor slabs, but no structural connections exist above street level.

3.2.1   External Geometry

The following descriptions of the external geometries refer to the widths and depths of the plan views displayed in Figures 3.3 to 3.7. The width refers to distances measured in the east-west direction (x-axis), and the depth refers to distances measured in the north-south direction (y-axis). The width is quoted first when both distances are written together; for example, 9 m × 2 m, the width is 9 m and the depth is 2 m.

The external geometry of Latitude tower remains uniform for most levels, with floor plan changes occurring in the first ten levels above street level and the last four levels at the top. At level 10 and 11 (Figure 3.3), the total width is 59 m and the total depth is 36 m. The north-east, south-east, and south-west corners of these levels have rectangular cut-outs with dimensions of 9 m × 2 m, 4 m × 15 m, and 15 m × 9 m respectively. Between levels 12 and 16 (Figure 3.4), the width increases to 71 m and the depth increases to 38 m. The rectangular cut-outs in the north-east, south-east, and south-west corners are still present from the preceding levels, and have dimensions of 20 m × 3 m, 13 m × 13 m, and 10 m × 10 m respectively. Levels 17 to 19 have similar external geometries as levels 10 and 11.

The typical external geometry (Figure 3.5) starts at level 20 and finishes at level 51. For these typical levels the total width and depth are 54 m × 44 m. At level 20, the southern facade extends outwards by approximately 6 m and accounts for the increased depth of the typical levels. The typical levels have two rectangular cut-outs; one in the north-east corner with dimensions of 11 m × 6 m, and another in the south-west corner with dimensions of 6 m × 16 m.

At level 52 (Figure 3.6) the southern facade moves 6 m back towards the centre of the building, which decreases the total depth to 38 m. The total width is unchanged from the typical levels at 54 m. The depth of the north-east rectangular cut-out increases, with dimensions of 11 m × 14 m, and the south-west rectangular cut-out is 6 m × 10 m. The external dimensions of level 54 (Figure 3.7) decrease further to 53 m × 33 m, and the north-east and south-west rectangular cut-outs have dimensions of 11 m × 23 m and 5 m × 13 m respectively. Level 55 has similar dimensions as level
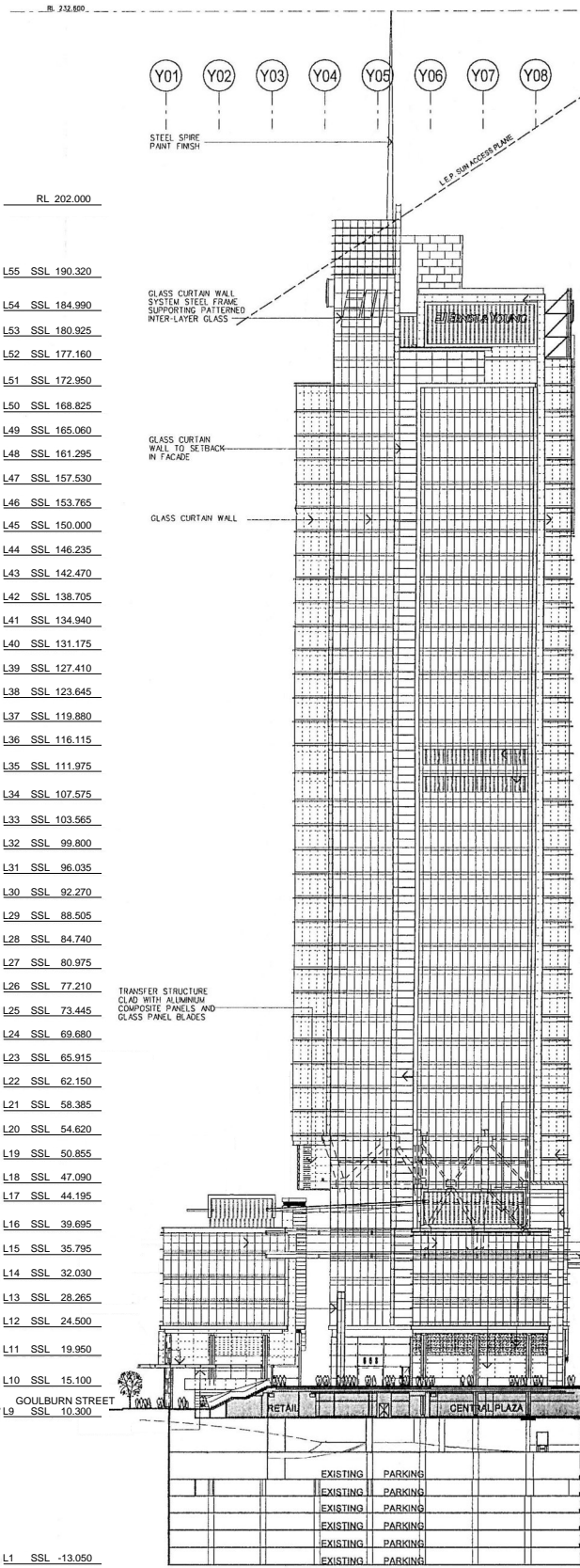
Figure 3.2: Eastern elevation of Latitude tower (Source: Crone Nation Architects)
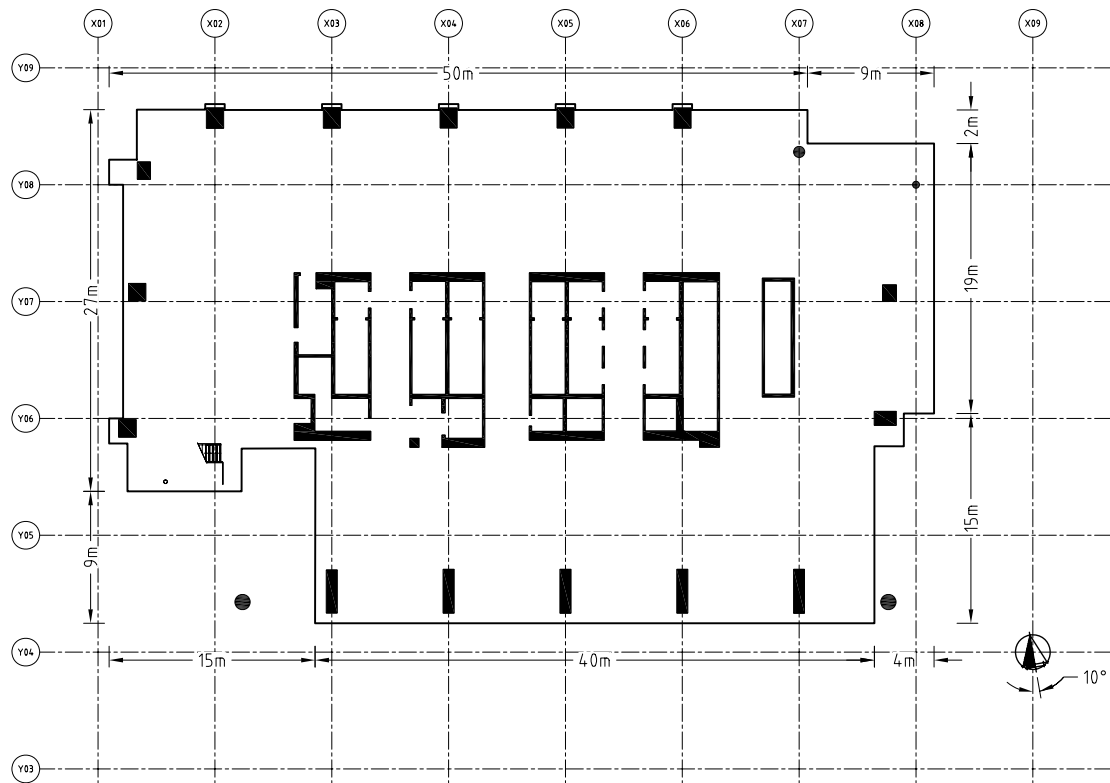
Figure 3.3: General Arrangement for Levels 10 to 11 (Source: Hyder Consulting)

54.

3.2.2 Structural System

The lateral stability design of Latitude tower uses an outrigger-braced structural system. The system consists of a centrally located core, comprising reinforced concrete shear walls, in conjunction with outrigger trusses connecting the core to the perimeter columns at mid-height. The outrigger design increases the effective structural depth of the building, which augments the lateral stiffness of the core and reduces horizontal deflections and moments in the core [146]. Outrigger arrangements are suitable for buildings with a significant flexural component of deformation, as opposed to shear dominated deformations.

Core and Service Shafts

The centrally located rectangular core is the primary lateral load bearing element and is constructed of reinforced concrete shear walls. Figures 3.8 to 3.14 display core wall plans at levels where changes occur in the wall configuration from the previous level. Walls W1 and W5 form the ends of the lift shafts and are 700 mm thick at level 1, and reduce to 650 mm at level 9, 500 mm at level 20, 400 mm at level 28,
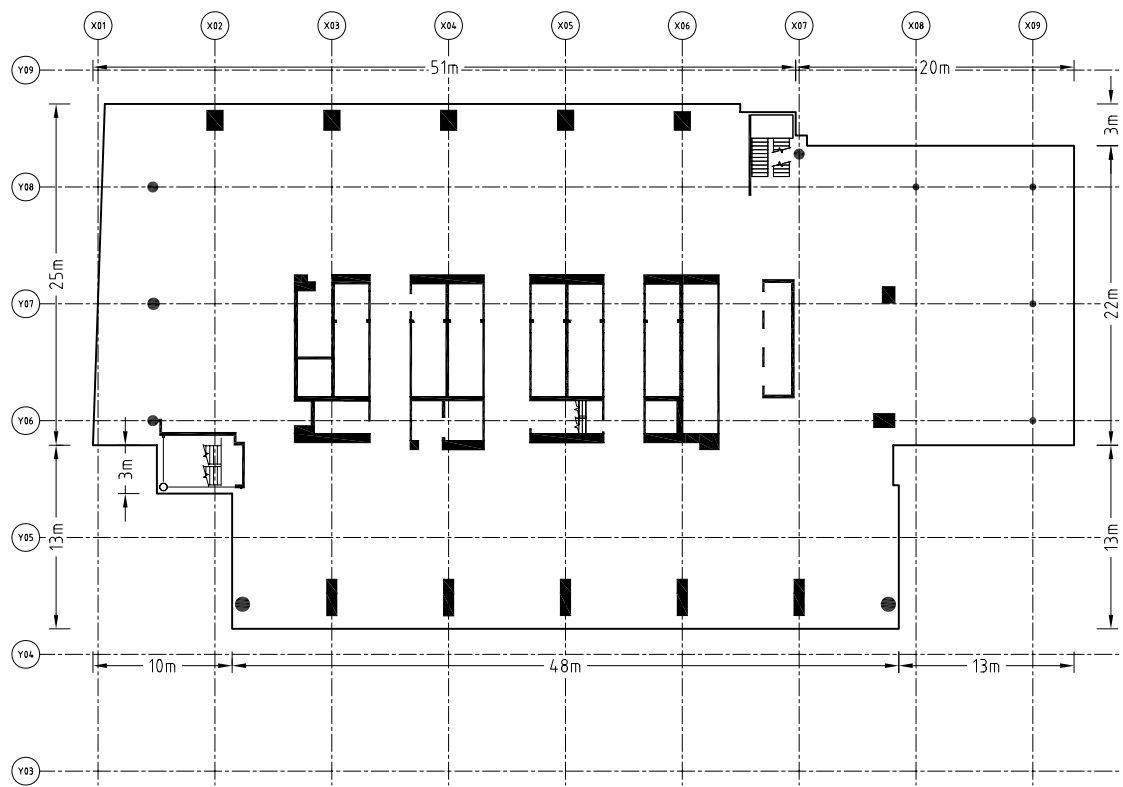
Figure 3.4: General Arrangement for Levels 12 to 16 (Source: Hyder Consulting)
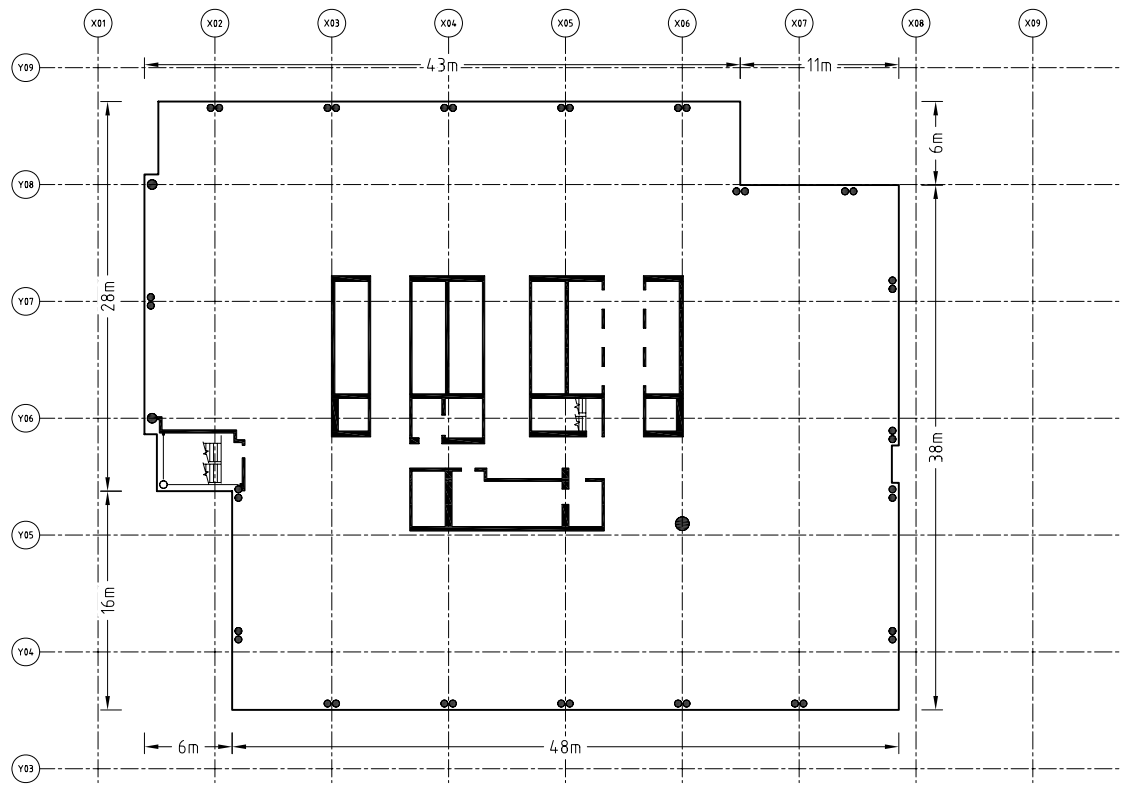
Figure 3.5: General Arrangement for Levels 20 to 51 (Source: Hyder Consulting)
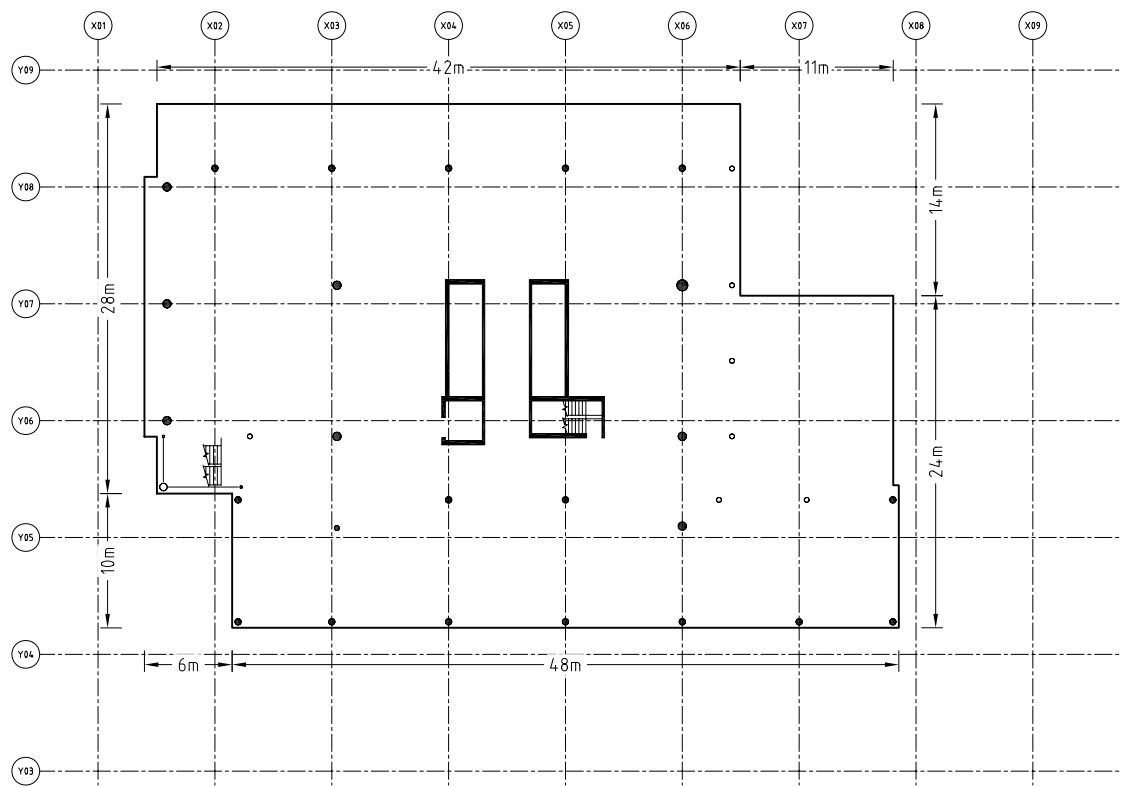
Figure 3.6: General Arrangement for Levels 52 to 53 (Source: Hyder Consulting)
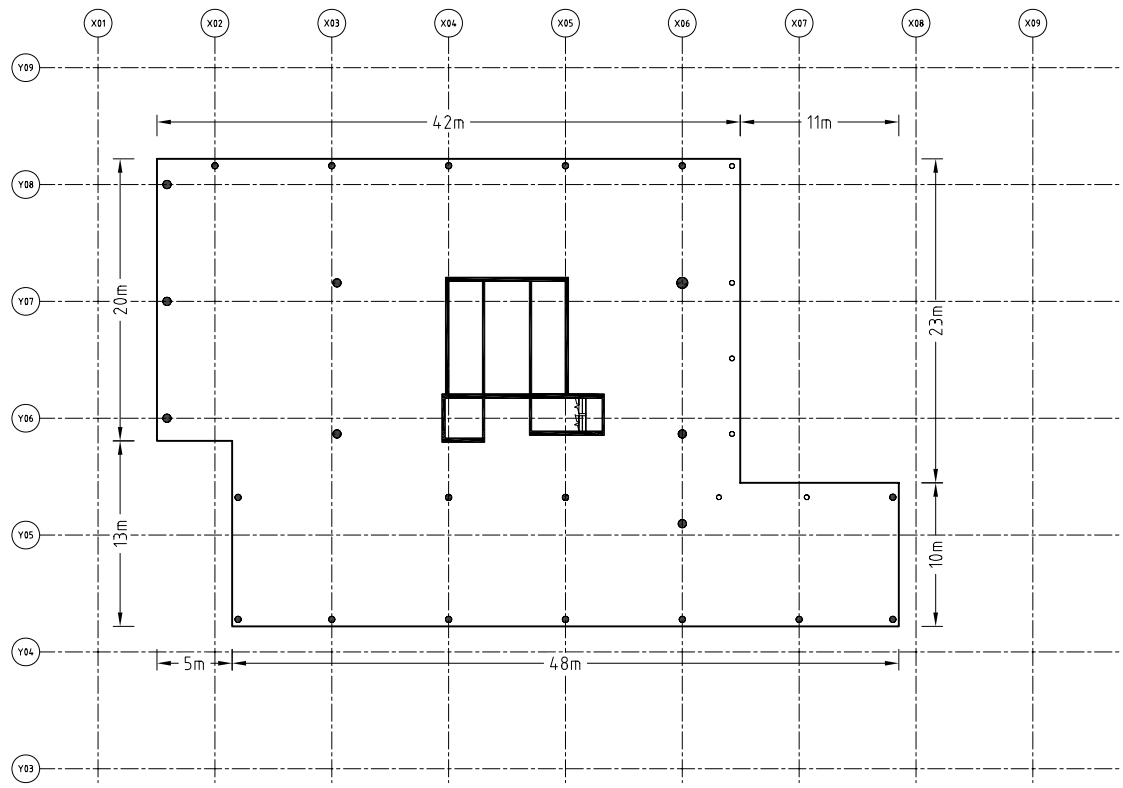
Figure 3.7: General Arrangement for Levels 54 to 55 (Source: Hyder Consulting)

and finally 300 mm at level 37. Walls W7, W10, W13, and W16 form the centre of each lift shaft and have a constant thickness of 250 mm. Walls W8, W9, W11, W12, W14, W15, and W17 form the outer walls of the lift shafts and have a typical thickness of 170 mm for level 25 and above. For levels 1 to 24, these walls have a typical thickness of 175 mm. Wall W17 has a thickness of 300 mm for levels 1 to 8, and reduces to 170 mm for level 9 and above.

The total width of the core remains relatively constant between levels 1 to 19. The distance between W16 and W17 is increased at level 9 to accommodate a lift shaft, which increases the overall width of the core from 30 125 mm in Figure 3.8 to 30 610 mm in Figure 3.9. Above level 19, the total width of the core decreases at discrete points as core walls terminate. The total width of the core reduces by approximately 60% between its base and top. The total depth of the core is 12 660 mm at level 1, and decreases as the thickness of walls W1 and W5 are reduced.

Latitude tower also includes two other reinforced concrete shafts in addition to the centrally located core. The first is a low-rise lift and services shaft located adjacent to W17 in Figure 3.9, between grids X06 and X07. The walls comprising this additional shaft, W20 and W21, extend between levels 9 to 16 and are supported by columns that transfer the vertical loads directly to the foundations.

The second reinforced concrete shaft is a high-rise services shaft adjacent to W5 in Figure 3.10, between grids Y05 and Y06. This shaft extends between levels 20 to 52, and is supported by trusses that transfer the vertical loads to both wall W5 and the columns situated on the perimeter of the lower levels, between grids Y04 and Y05 of Figure 3.4. The size and location of the high-rise services shaft, relative to the central core, creates a significant eccentricity between the centre of mass and the centre of stiffness.

The concrete strength f_c' used for the core and shafts was typically 50 MPa. The walls between levels 34 and 36 were constructed with 80 MPa concrete. The increased concrete strength was required because these levels link the core lift shafts together and also accommodate the outrigger trusses.

Outriggers

Outrigger trusses require large depths to be effective, and their configurations inevitably clash with architectural aims. Plant rooms that occupy multiple consecutive levels are the most structurally effective and architecturally convenient location for such structures [146]. Latitude tower includes two outrigger trusses located in the plant rooms between levels 34 and 36. The depth of each truss spans between the level 34 and level 36 floor slabs. Figure 3.15 displays the location of the outrigger trusses at grids X03 and X06.

The outrigger trusses at the level 34 plant room directly connect only two
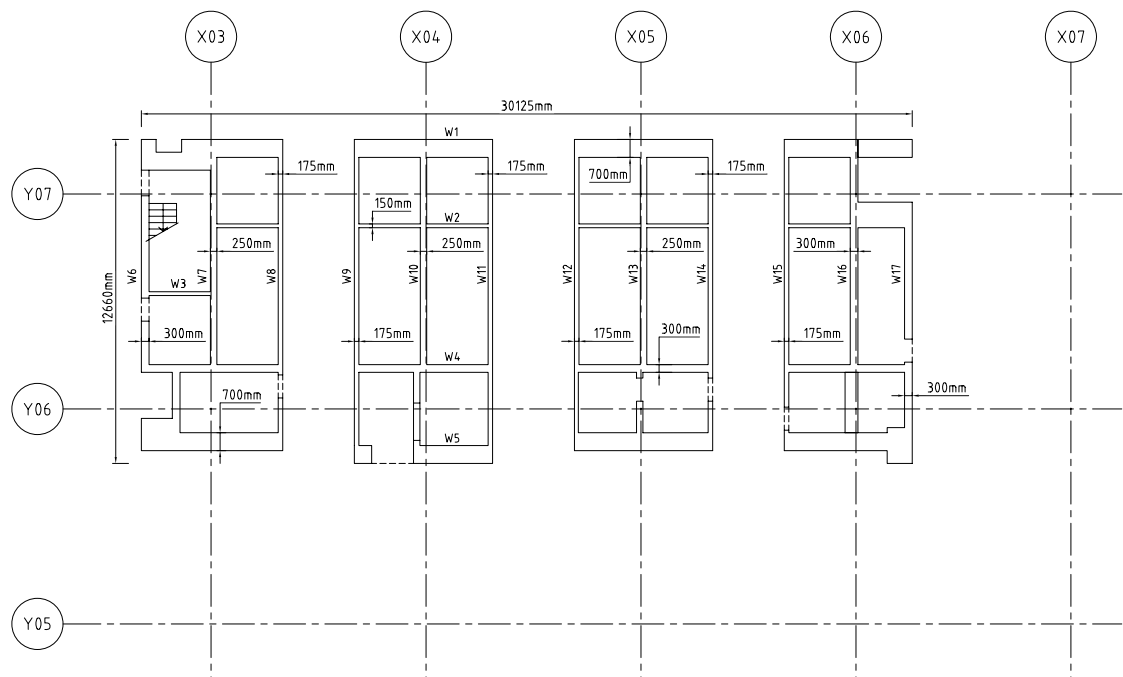
Figure 3.8: Level 1 Core Plan (Source: Hyder Consulting)
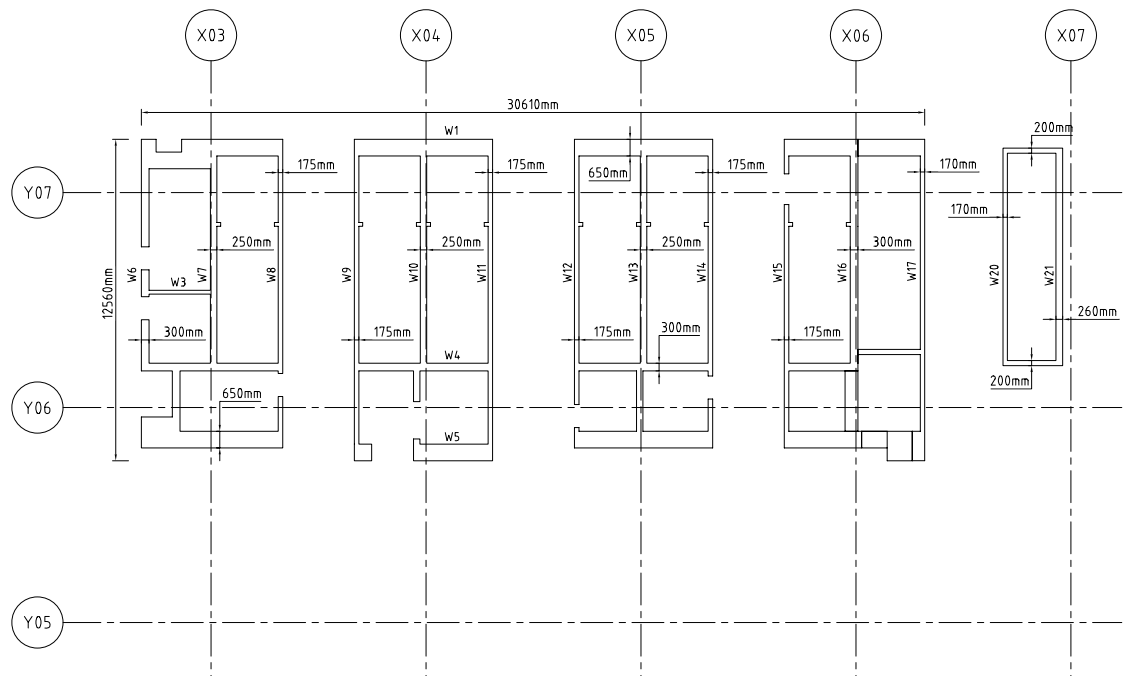
Figure 3.9: Level 9 Core Plan (Source: Hyder Consulting)
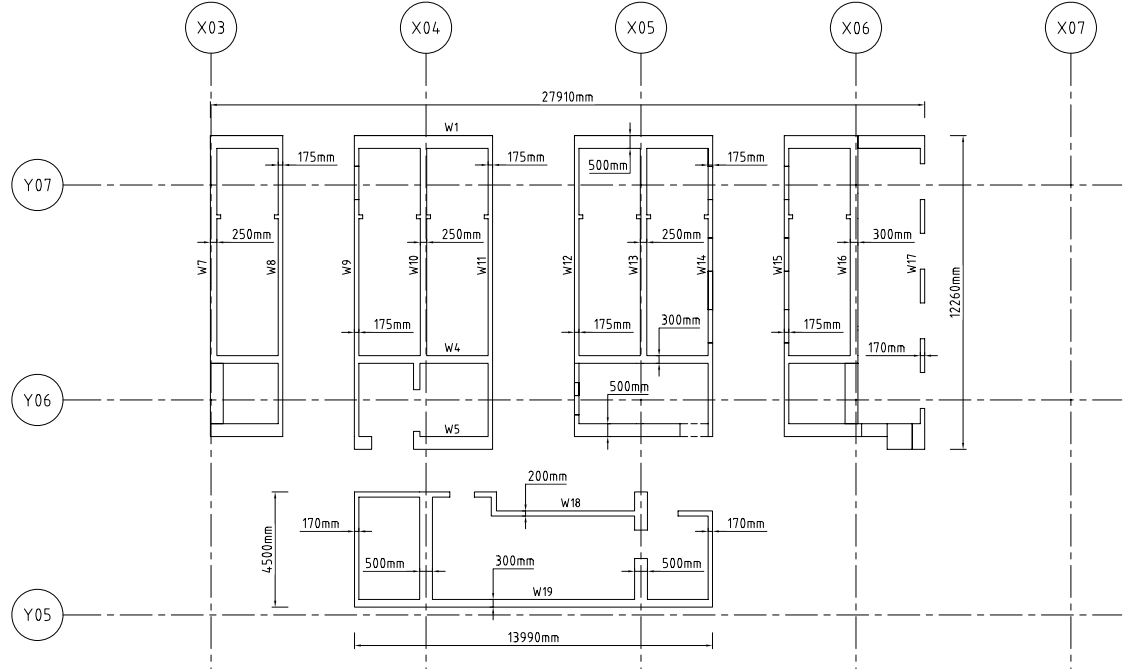
Figure 3.10: Level 20 Core Plan (Source: Hyder Consulting)
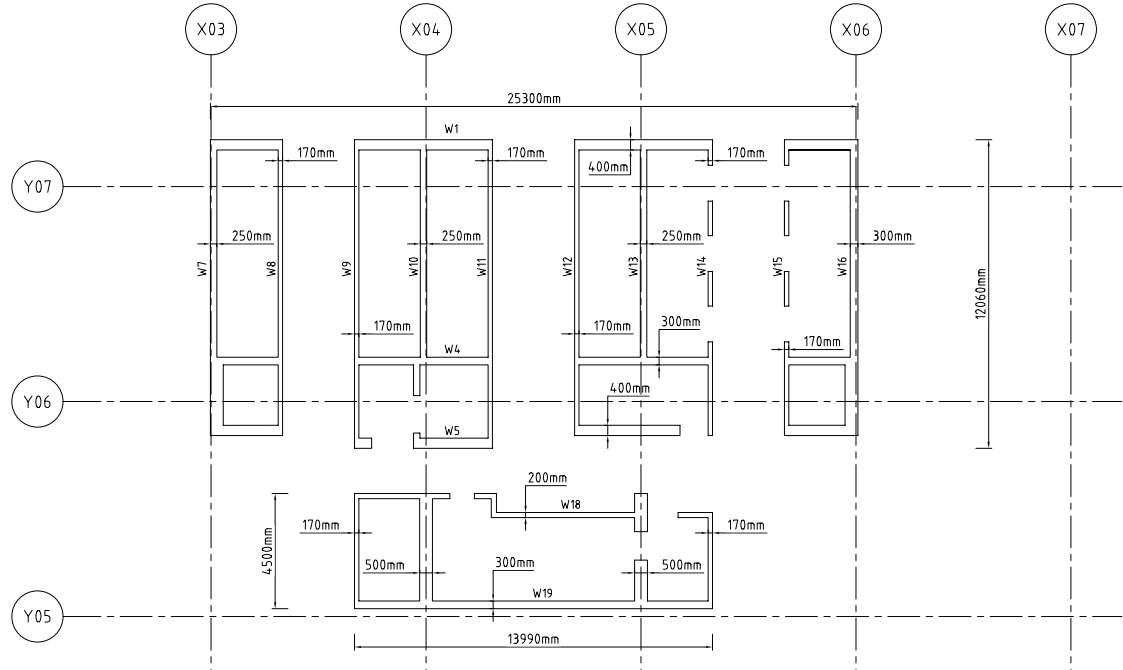
Figure 3.11: Level 28 Core Plan (Source: Hyder Consulting)
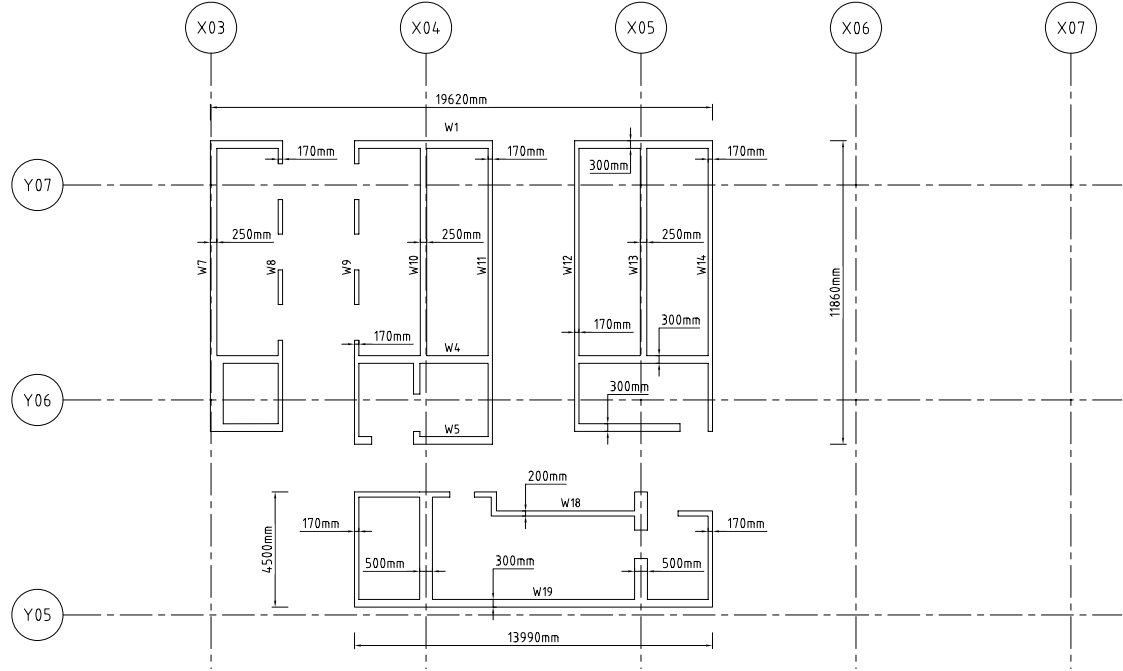
Figure 3.12: Level 37 Core Plan (Source: Hyder Consulting)
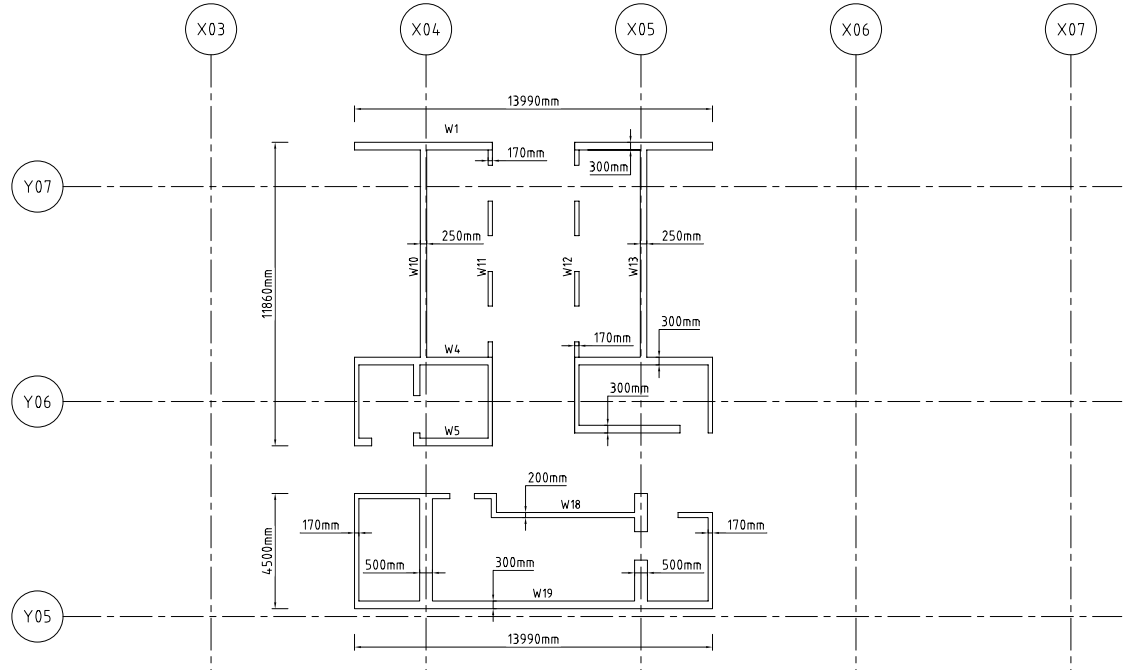
Figure 3.13: Level 48 Core Plan (Source: Hyder Consulting)
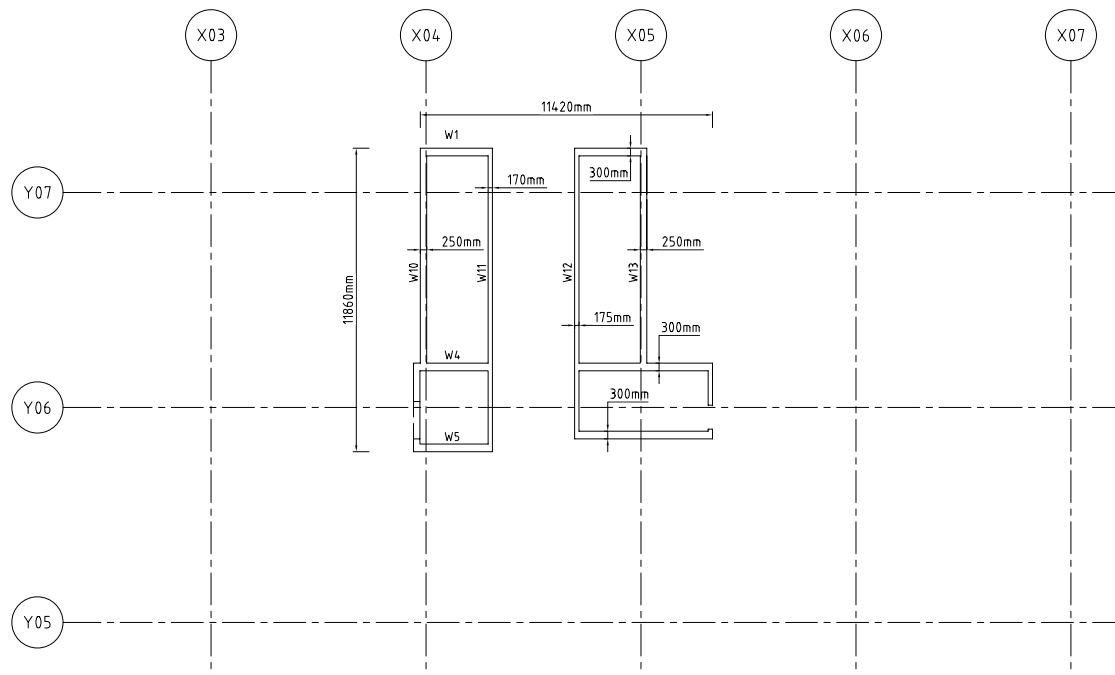
Figure 3.14: Level 53 Core Plan (Source: Hyder Consulting)

columns to the core. A two storey high belt truss [167] surrounds the level 34–35 plant room at the facade, which joins all the perimeter columns together. This design theoretically forces all perimeter columns that are collinear with the line through the outrigger columns to participate in the moment resisting characteristics of the outrigger-bracing system. The belt truss also acts as an offset outrigger [122], in conjunction with the level 34 and level 36 floor slabs, that is effective for deflections in either the north-south or east-west directions. Figure 3.15 displays the location of the belt truss along the northern facade, between grids Y08 and Y09.

Floor Plates

A composite steel-concrete floor system is typically used for level 16 and above. Steel beams and reinforced concrete floor slabs span from the core to the perimeter columns, which are constructed of concrete filled steel circular hollow sections. The steel beams are connected at the core and perimeter columns by bolted connections, which are not designed to support significant moment reactions. Shear studs welded along the top flange of the supporting beams protrude into the floor slab to ensure a composite action between the beam and floor slab is attained. In this configuration, the concrete floor slab serves as a compression flange.

For levels 15 and below, the floor plates are constructed of reinforced concrete. The floor slabs are supported by reinforced concrete beams that span from the core to the perimeter columns, or an edge beam.
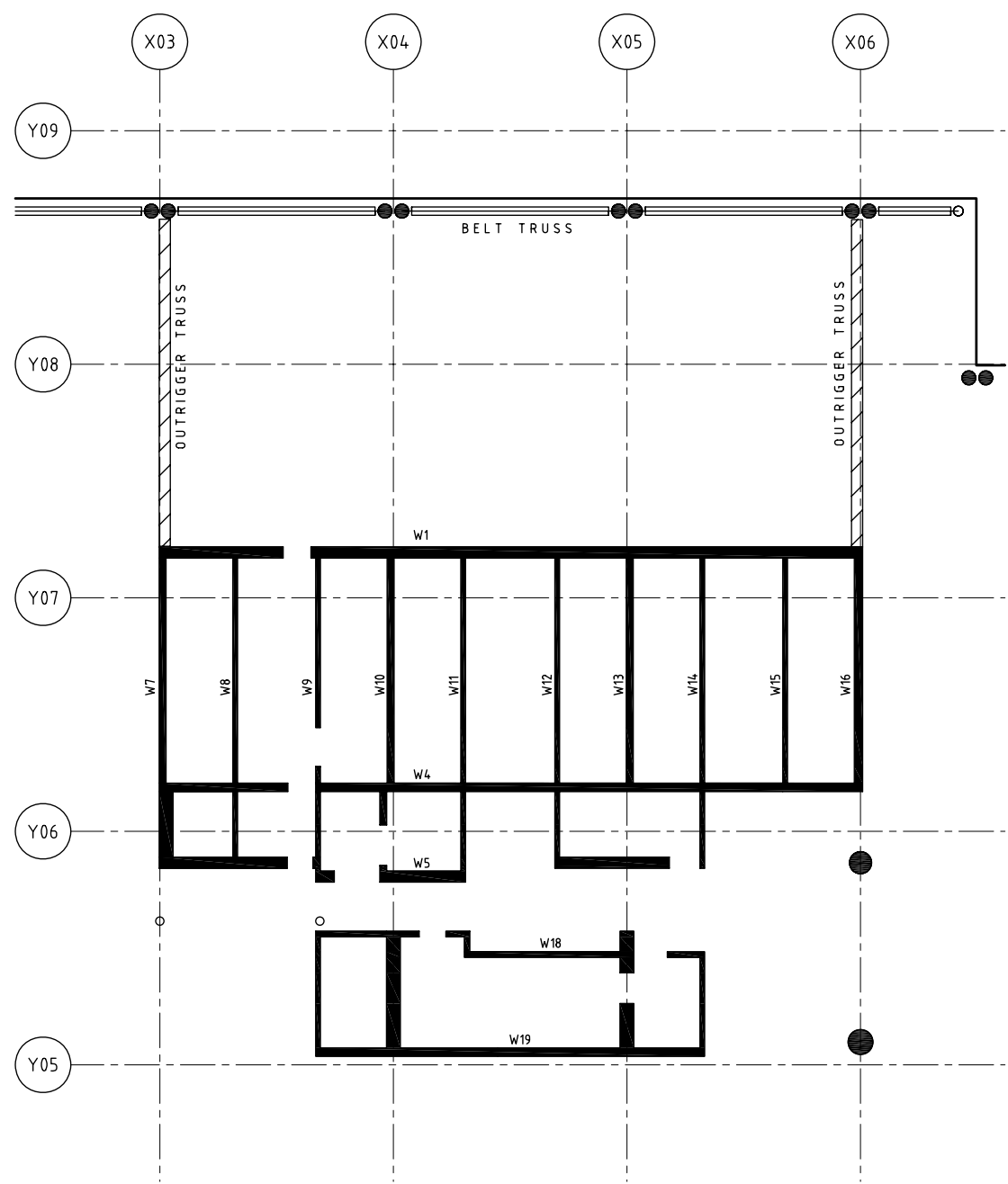
Figure 3.15: Level 34 outrigger truss locations (Source: Hyder Consulting)

At all levels the floor slabs are typically 120 mm thick, and increase to 150 mm for slab sections within the core and service shaft areas. The floor slabs forming the boundaries of plant rooms, such as level 34 and level 36, are 200 mm thick.

Block-work and Infill Walls

The intended use of the structure as an office tower results in mostly uninterrupted floor spaces. The columns are typically located at the facade, and block-work infill is scarce. In contrast, residential towers are characterised by extensive internal partitions. Depending on the design and construction of internal partitions, they can influence the structural behaviour by acting as braced shear walls capable of supporting moment reactions [146]. For the test structure, block-work infill is confined to areas in the main core of the building, mainly for service shafts and stair wells, and is unlikely to have any significant influence on the structural system.

Foundations

The interface between the base of the structure and the ground uses reinforced concrete pad footing foundations. For the reinforced concrete core, a 1300 mm thick reinforced concrete pad footing extends 920 mm to 1450 mm beyond the perimeter of the core walls. Pad footings for the columns are similar in design to the core pad footing. The underlying ground material is high class sandstone with a bearing pressure capacity of 9 MPa to 12 MPa. Very little change to the existing foundations was conducted apart from minor upgrades to some footings. The new structure was designed to suit the existing foundations. For example, the new levels used a composite steel and reinforced concrete floor plate design to reduce the mass of the structure.

Cladding

The cladding consists of prefabricated sections constructed of glass and aluminium. Steel brackets embedded in the floor slabs provide bolt eyelets as attachment points for the cladding sections. The connections between the facade elements and the brackets, as well as the connections between adjacent facade elements, consist of movement joints that prevent the transfer of inter-storey shear forces to the cladding elements. From a serviceability perspective, this ensures the glass in the facade elements does not act as a compression strut in resisting inter-storey displacements.

3.2.3 Construction Methods

Construction of the tower utilised an existing reinforced concrete tall building, which was partially completed approximately ten years prior to the commencement of

Latitude tower in late 2002. The existing core was completed to level 24, and the floor plates to level 15. However, the existing floor plates were not at levels that suited the new designs and were scheduled for demolition.

To reduce construction times, a new construction deck was installed at level 15 and supported by the existing level 14 reinforced concrete columns. This new construction deck allowed the construction of levels 15 and above to proceed, while the floor plates at levels 11 to 14 were demolished and re-constructed according to revised designs. Temporary bracing of the columns was installed at the demolished levels, and removed once the floors had been re-constructed.

A jump-form was used to construct the core walls, and during the construction phase the core was often four to five storeys ahead of the floor plates. The construction of the floor plates followed an upward spiral scheme. For a typical floor plate, construction of one quadrant would commence with the installation of steel columns and beams followed by steel decking atop the beams to act as unre-coverable formwork. At this stage the erection of steel columns and beams in an adjacent quadrant would commence, while steel reinforcement was placed in the first quadrant in preparation for poring the concrete slab.

The facade trailed the floor plates by six to eight levels during the construction of typical levels. Sections of the facade that spanned multiple levels were also not installed until the end of construction. This was to allow for construction equipment, such as cranes and hoists.

3.2.4 Location and Surrounds

Latitude tower is located at the southern end of the Sydney central business district. It is part of the World Square development, which includes three tall buildings contained within a city block measuring approximately $144\,\text{m} \times 155\,\text{m}$. Figure 3.16 displays the location of Latitude tower relative to the surrounding coastal waters. The other locations plotted on the figure correspond to meteorological stations operated by the Australian Bureau of Meteorology. Wind velocity data from these stations were used to verify the measurements from the anemometer installed at Latitude tower during the monitoring period. A satellite image covering a $5\,\text{km}$ radius around Latitude tower is displayed in Figure 3.17. To the north is the Sydney CBD and Sydney Harbour, and from the east around to the north west is mostly low-rise industrial and residential buildings and park lands. The relationship between the cardinal wind directions (β) and the building orthogonal axes (θ) are displayed in Figure 3.18.

The terrain surrounding Latitude tower varies. Winds approaching from the north initially travel over land that mostly comprises suburban buildings. At a distance of approximately $1.8\,\text{km}$ north of Latitude tower, a mixture of high density
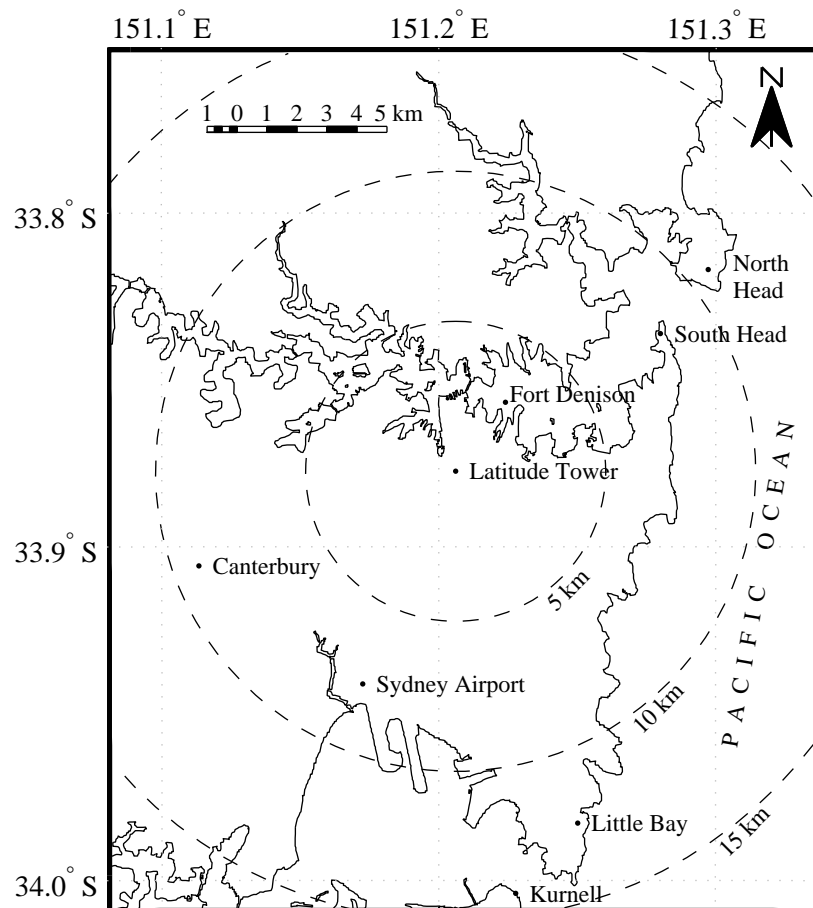
Figure 3.16: Latitude tower location map.
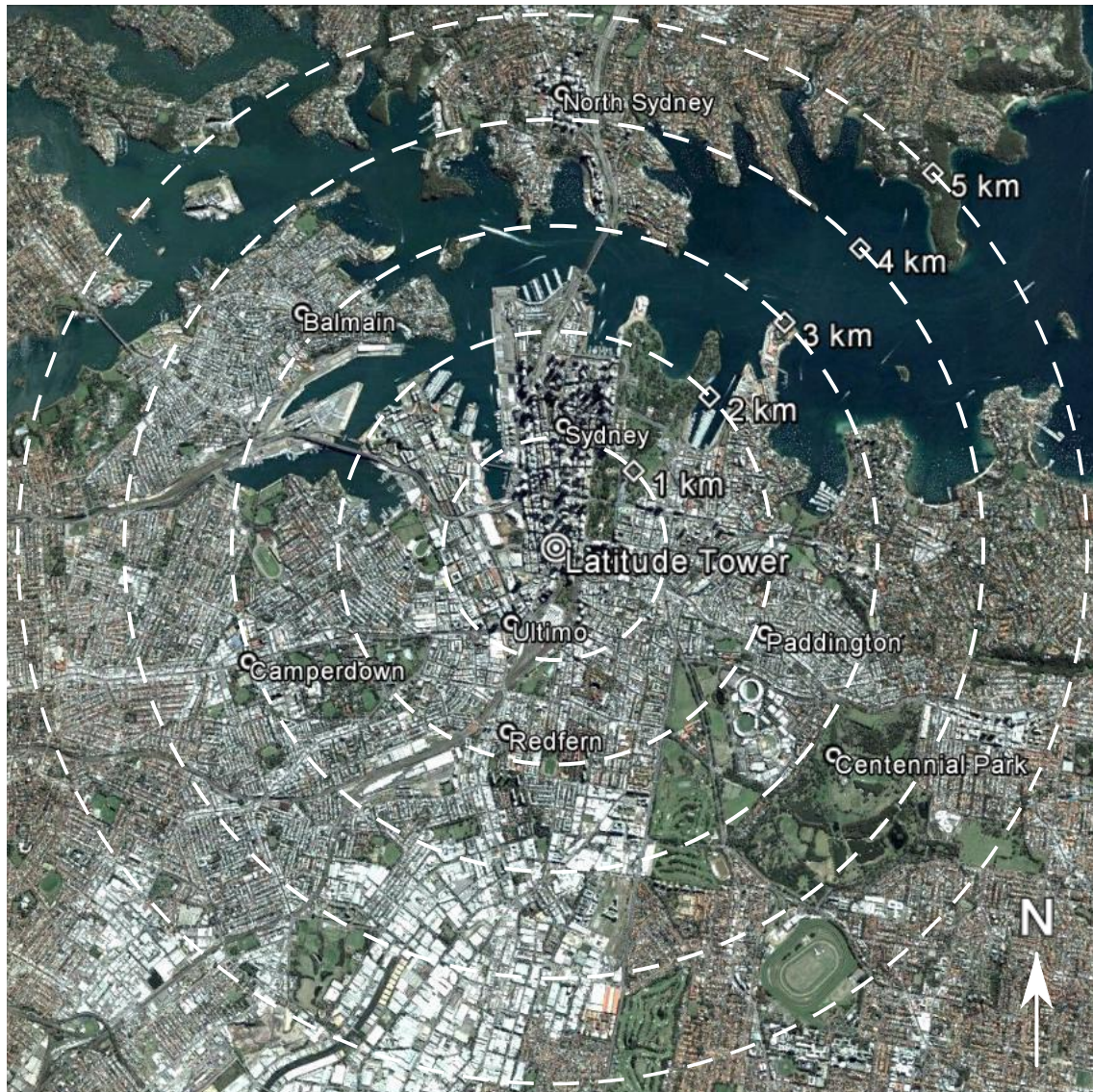
Figure 3.17: Latitude tower location satellite image.
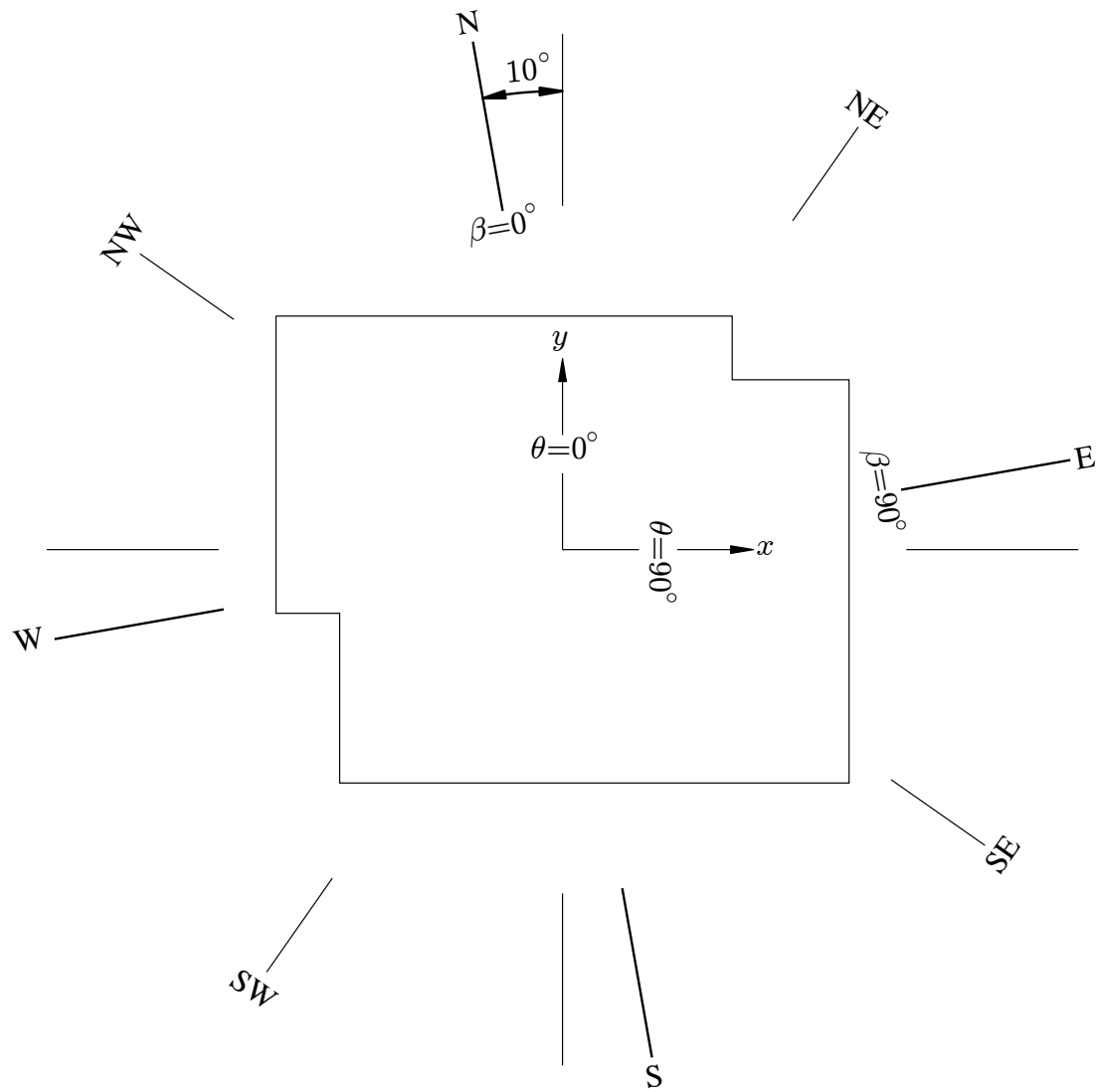
Figure 3.18: Relationship between the cardinal wind directions and the building orthogonal axes.

Figure 3.19: View from Latitude tower to the North.

metropolitan buildings and tall buildings becomes the predominant terrain. For wind directions approaching from the north-east to south-east, winds initially travel over the Pacific Ocean, before reaching land at approximately 7.5 km from Latitude tower. For these wind directions, the dominant terrain type is low-rise suburban buildings. Winds from the south also initially travel over the Pacific Ocean, and reach land approximately 18 km from Latitude tower. The dominant terrain type for southerly winds is also low-rise suburban buildings. For winds originating from the south-west to the north-west, winds blow over long fetches comprised mostly of low rise, suburban dwellings. Figures 3.19, 3.20, 3.21, and 3.22 display views from the top of Latitude tower to the north, east, south, and west respectively.

As can be seen at the right side of Figure 3.19, a neighbouring building is located in the immediate vicinity north of Latitude tower. This neighbouring building, known as World Tower, stands approximately 230 m above street level. Figure 3.23 is a plan view of World Square, the city block containing Latitude tower, and shows the size and location of World Tower relative to Latitude tower.

Figure 3.20: View from Latitude tower to the East.

Figure 3.21: View from Latitude tower to the South.

Figure 3.22: View from Latitude tower to the West.

3.3 Instrumentation Specification and Calibration

3.3.1 Accelerometer Specification

Selecting the appropriate acceleration transducer first requires the specification of the anticipated vibrations to be measured. The expected frequency range of interest for the periodic vibration tests was determined from previous vibration studies of tall building structures ([47], [139]). These studies included natural frequency values for the fundamental translational mode, the orthogonal fundamental translational mode, and the fundamental torsional mode for tall buildings with heights ranging from below 20 m to a maximum height of approximately 275 m. The natural frequency values that encompassed all heights and modes of vibrations from these studies ranged from approximately 0.16 Hz to 4.3 Hz. From this historical data, the frequency range of interest for the vibration testing of a 187 m tall building during construction is expected to be between 0.1 Hz to 5.0 Hz.

Over the frequency range of interest, acceleration responses under $0.1\,\mathrm{mg_n}$ were anticipated to be recorded and used for analysis. The predicted maximum acceleration varies with the height of the structure, with maximum values expected when the structure reaches the final design height of 187 m. The sources of significant ambient excitation during construction include wind loading and crane induced loading, and both sources require consideration to estimate peak responses. For the ambient wind
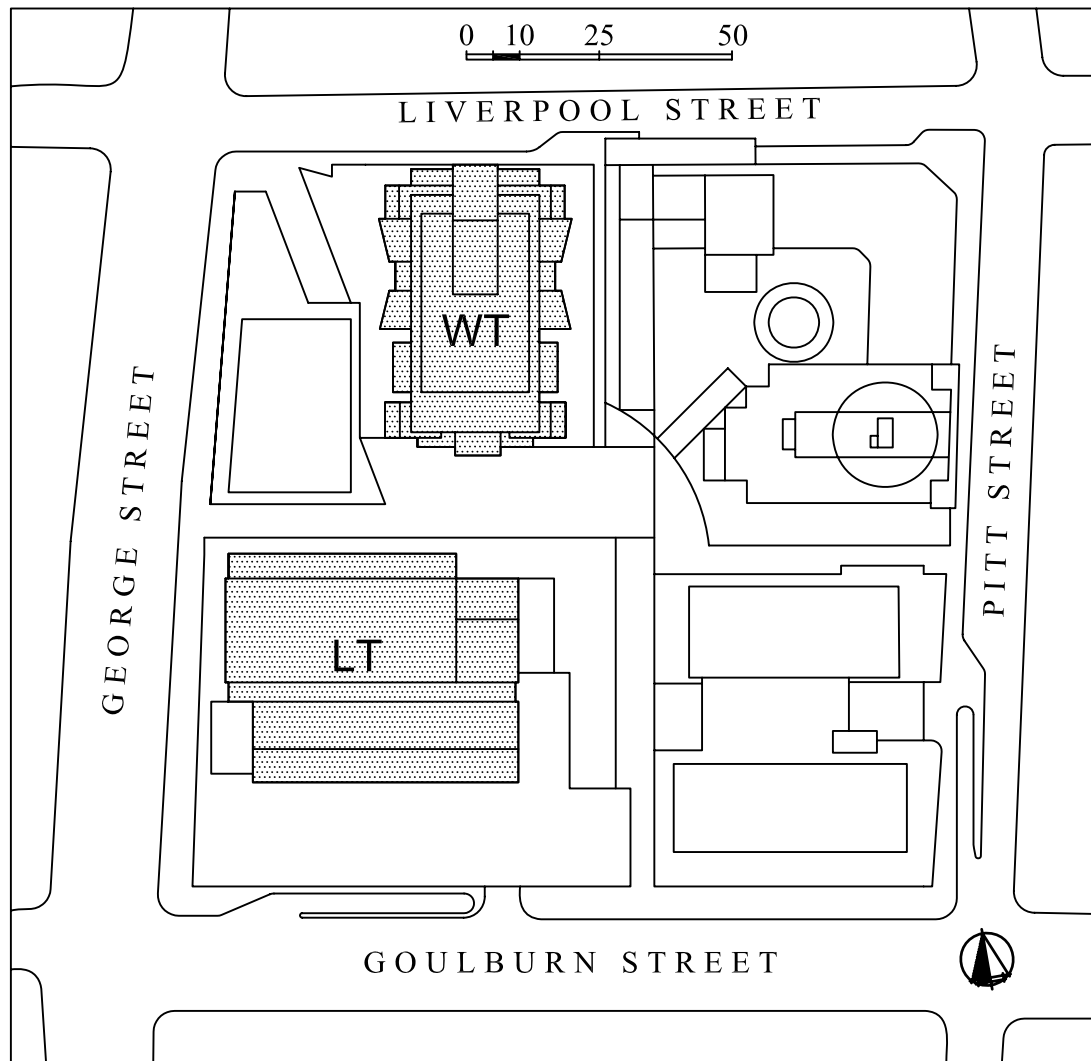
Figure 3.23: Plan view of World Square displaying the size and location of World Tower (WT) relative to Latitude tower (LT).

Input range	$\pm 30\,\mathrm{g_n}$
Bias	$< 15\,\mathrm{mg_n}$
One year repeatability	$< 2500\,\mu\mathrm{g_n}$
Temperature sensitivity	$< 100\,\mu\mathrm{g_n}/°\mathrm{C}$
Scale Factor	$1.33\,\mathrm{mA/g_n}\ \pm 10\,\%$
One year repeatability	$< 2500\,\mathrm{ppm}$
Temperature sensitivity	$< 200\,\mathrm{ppm}/°\mathrm{C}$
Resolution	$< 10\,\mu\mathrm{g_n}$
Intrinsic Noise	$< 3000\,\mu\mathrm{g_n}\mathrm{rms}$ (0–10 kHz)
Bandwidth	$> 300\,\mathrm{Hz}$

Table 3.1: Honeywell Q-Flex® QA650 Accelerometer Specification

excitation, results from a high frequency base balance wind tunnel test, presented in Section 6.4, indicated the peak acceleration from a 1 year return period event for a westerly wind would reach approximately $4.0\,\mathrm{mg_n}$. The crane induced excitation depends on the loads carried and the operation of the crane — rate of acceleration and deceleration of lifting and slewing actions of the crane. These factors are highly variable under regular crane operations, and estimating the crane induced accelerations is therefore difficult. During construction it would be anticipated that regular crane operations would be unlikely to create sufficient impulse loads to induce accelerations above those predicted from ultimate wind loading. A controlled sequence of repeated crane induced impulse loads could theoretically induce higher accelerations, however this method was not to be used or expected to occur during normal construction activities.

The Honeywell Q-Flex® QA650 Accelerometer [67] was chosen for the full-scale acceleration measurements. The design of the QA650 uses an etched-quartz-flexural seismic system with integrated electronics that develops an output current proportional to the acceleration input. A user supplied output load resistor, appropriately scaled for the acceleration range of the application, is required to convert the output current to a voltage, which is discussed in the following section regarding signal conditioning.

From the specifications listed in Table 3.1, the frequency response and resolution of the accelerometers satisfies the low frequency and low acceleration requirements. The use of quartz as the piezoelectric material results in reduced sensitivity compared with other materials, but has superior stability over time and temperature fluctuations [30]. The stability is an important factor for the long term monitoring of structures.

The QA650 Accelerometer is a uniaxial transducer. The full-scale experiments require the measurement of accelerations in orthogonal directions at a single point. To facilitate the alignment of the accelerometers into orthogonal pairs, each ac-

celerometer was securely fitted into a precision machined cube of brass. Screw holes located around the edges of the cubes allowed pairs of accelerometers to be fastened together in orthogonal directions.

3.3.2   Accelerometer Signal Conditioning

Each accelerometer was connected to an Accelerometer Conditioning Unit (ACU), model number ASC650V2 [4]. The ASC650V2 ACU is a proprietary design of Wind Engineering Services, The University of Sydney. Both the design and construction was conducted at The University of Sydney. The ASC650V2 ACU is specifically designed for the Honeywell QA650 Accelerometer, and includes a power supply for the accelerometer, input offset control, amplifier, high pass filter and low pass filter.

The ACU initially converts the accelerometer output current to a voltage using a load resistor with a fixed value of $1\,\text{k}\Omega$. Therefore, the output from each ACU is $S_c = R \times S_a$, where S_c is the ACU scale factor in V/g_n, R is the load resistance in ohms, and S_a is the accelerometer scale factor in mA/g_n. From the Honeywell supplied accelerometer specification [67], the sensor and conditioning unit combination has an output of approximately $1.33\,\text{V}/\text{g}_n$ at a gain of one.

Both the high and low pass filters are fourth-order Butterworth types with a characteristic roll-off of $24\,\text{dB}/\text{octave}$. At the cut-off frequency the signal is attenuated by $3\,\text{dB}$. The low pass filter attenuates frequencies above the cut-off frequency, and the high pass filter attenuates frequencies below the cut-off frequency. Simultaneous use of the high and low pass filters is possible to create a band pass filter.

3.3.3   Anemometer Specification

Selecting an anemometer for the meteorological observations was governed by two factors; measurement performance and durability. In the field, anemometers are exposed to the elements for extended periods. The presence of water, dirt, and the sun can be detrimental to performance over time. A level of durability is required that permits sustained operation without the need for regular maintenance. This becomes increasingly important as the accessibility to the installation point of the anemometer becomes more difficult. Reduced accessibility is almost inevitable, because anemometers are often installed atop tall masts or long booms. Ideally, the anemometer is positioned to measure the free stream wind velocity, hence the need for masts and booms to locate the anemometer away from the influence zone of surrounding structures or topographic features. The influence zone refers to the region surrounding an object where the free stream flow is disturbed by the presence of the object. The influence zone diminishes with increasing distance from the object.

One of the primary operating requirements for the anemometer was maintenance

Wind Speed

Range:	0–60 m/s
Accuracy:	±0.3 m/s
Starting threshold:	1 m/s
Distance constant:	2.7 m (63% recovery)
Output:	AC voltage (3 pulses per revolution)

Wind Direction

Range:	0–355° electrical (5° open)
Accuracy:	±3°
Starting threshold:	1.1 m/s
Delay distance:	1.3 m (50% recovery)
Damping ratio:	0.25%
Damped natural wavelength:	7.4 m
Undamped natural wavelength:	7.2 m
Output:	Analogue DC voltage

Table 3.2: R.M. Young 05103 Wind Monitor Specification

free operation. This requirement became more important due to difficulties associated with accessing the anemometer installation point. As a result, the anemometer selection criteria focused on simple, robust designs with corrosion-resistant construction.

The selected anemometer, the R.M. Young 05103 Wind Monitor, incorporated a helicoidal propeller and direction vane, and utilised construction materials suited to harsh working environments. The wind speed range and accuracy for this anemometer is 0–60 m/s and 0.3 m/s respectively, and the wind direction accuracy is 3°. The anemometer was coupled with an R.M. Young 06201 Wind Tracker, which facilitated the integration of the anemometer with the data acquisition equipment by providing a voltage output of the wind speed and direction via standard BNC connectors. The Wind Tracker voltage output for wind speed is 0–5 V for 0–50 m/s, and for wind direction is 0–5 V for 0–355°. The accuracy of the Wind Tracker was ±0.6%. The anemometer was connected to the Wind Tracker using shielded, twisted pair cable to minimise noise contamination of the signals. Lightning protection equipment for isolating the anemometer from the instrumentation was not installed. The full specification for the anemometer is provided in Table 3.2.

3.3.4 GPS Receiver Specification

Two Leica MC500 GPS receivers were used to record displacements. These receivers are capable of capturing GPS satellite signals on two L-band frequencies: L1 and L2. Each frequency band incorporates twelve channels, and establishes position coordinates based on carrier phase, C/A code, and P-code information within the

signals. The dual frequency and carrier phase detection capabilities are important aspects of the specification, as they allow a theoretical sub-centimetre accuracy for position measurement. The scan rate is user selectable up to 10 Hz, and a number of operating modes are supported, including static, real time kinematic (RTK), and post processing. The acquired data can be recorded to internal memory, or automatically transferred to external data storage for long term data acquisition.

Each GPS receiver were connected to a Leica AT504 dual frequency antenna. The antenna is machined from a solid block of aluminium and incorporates features to improve the overall accuracy of GPS measurements by mitigating multipath signals. Firstly, the base of the antenna is designed to prevent low elevation signals from reaching the antenna sensor. Secondly, the antenna incorporates four concentric choke rings surrounding the antenna sensor, which trap indirect signals approaching from above the antenna sensor.

3.3.5 Data Acquisition Equipment

Two types of data acquisition hardware were used during the full-scale measurements. For the vibration testing, an IOTech Daq/216B PC-Card analogue to digital converter (ADC) installed in a laptop computer was used to digitize and record the accelerometer signals. The Daq/216B has a 16 bit resolution with a maximum input range of ± 10 V, and a maximum sampling frequency of 125 kHz.

For the monitoring programme, an IOTech DaqBoard/2000$^{\text{TM}}$ ADC installed in a desktop computer was used to digitize and record the accelerometer and anemometer signals. The DaqBoard/2000 has a 16 bit resolution with a maximum input range of ± 10 V, and a maximum sampling frequency of 200 kHz. The IOTech DaqView$^{\text{TM}}$ software was used to configure and control the ADC equipment.

The smallest change that can be resolved by an ADC, referred to as the least significant bit, is attained by dividing the input range by the number of output levels. Both types of ADC used have the same input range and number of output levels. In this case the input range was 20 V and the number of output levels was 2^{16}, resulting in a least significant bit of 0.3 mV/bit. Dividing the least significant bit by the accelerometer sensitivity gives an accuracy of $0.2\,\mu g_{\text{n}}$/bit, which is less than the accelerometer resolution of $10\,\mu g_{\text{n}}$ and more than adequate for the data acquisition requirements.

The latency of the data acquisition system was an important consideration when selecting the equipment. Both the Daq/216B and DaqBoard/2000 allowed simultaneous sampling of all analogue input signals, with latencies less than $8\,\mu$s and $5\,\mu$s respectively. Furthermore, the digitizing of all accelerometer and anemometer measurements were conducted on a single ADC.

3.3.6 Accelerometer Calibration

Static accelerometer calibration was conducted by measuring output voltages for a specified component of gravity induced by tilting the accelerometer along its axis. The tilting subjects the accelerometer to an acceleration of gravity multiplied by the sine of the tilt angle. Accurate measurement of the tilt angle was achieved using a Sine bar and gauge blocks. A Sine bar consists of a flat bar supported between two identical cylinders, which are aligned parallel and have a known separation distance L and a known relation to the reference surface of the bar. In this arrangement, the bar becomes the hypotenuse of a triangle for angle measurement. The working axis of the accelerometer was aligned with the longitudinal axis of the Sine bar. After levelling the accelerometer and setting the output offset to zero, gauge blocks of various height H_{gb} were placed under one cylinder to incline the bar at an angle α such that $H_{gb} = L \tan \alpha$. The component of gravity applied along the accelerometer axis is then $\sin \alpha$. The accelerometer gain was calculated from the ratio of the accelerometer output voltage and the acceleration induced by gravity. The output voltages were measured at several angles to check linearity over the range of accelerations anticipated during full-scale testing. A zero reading was also recorded at each change in gauge block height. Figure 3.24 shows the results of the static calibration for a single accelerometer, and includes a least squares linear regression fit of the data points. The other accelerometers displayed similar calibration results. The static calibration was conducted at regular intervals to ensure any time related physical changes in the accelerometers were accounted for. The maximum difference between calibration results recorded between the start and end of full-scale testing was 0.8%.

Dynamic accelerometer calibration was determined via a frequency-sweep experiment, which recorded the accelerometer outputs for constant amplitude sinusoidal motion at varying frequencies. The sinusoidal motion was generated by a crank shaft attached to a long pendulum that was restricted to movement along a single axis. Motion of the crank shaft was controlled by a steel disc driven by an electric motor. The distance between the centre of the disc and the point of connection between the disc and the crank shaft sets the peak displacement amplitude $\hat{x}_p$. The number of revolutions of the disc in a specified time interval was recorded for calculating the natural frequency f_n. The acceleration of the system is then $\ddot{x}_p = -x_p \omega^2 \cos(\omega t)$, where $\omega = 2\pi f$. A variable speed gear box was located between the electric motor and the disc. The gear box allowed adjustment of the rotational speed of the disc, and subsequently the frequency of the sinusoidal motion. To allow the observation of the phase between the accelerometer outputs, all accelerometers were simultaneously calibrated. Prior to commencing the frequency-sweep testing, each accelerometer axis was aligned to the direction of motion of the
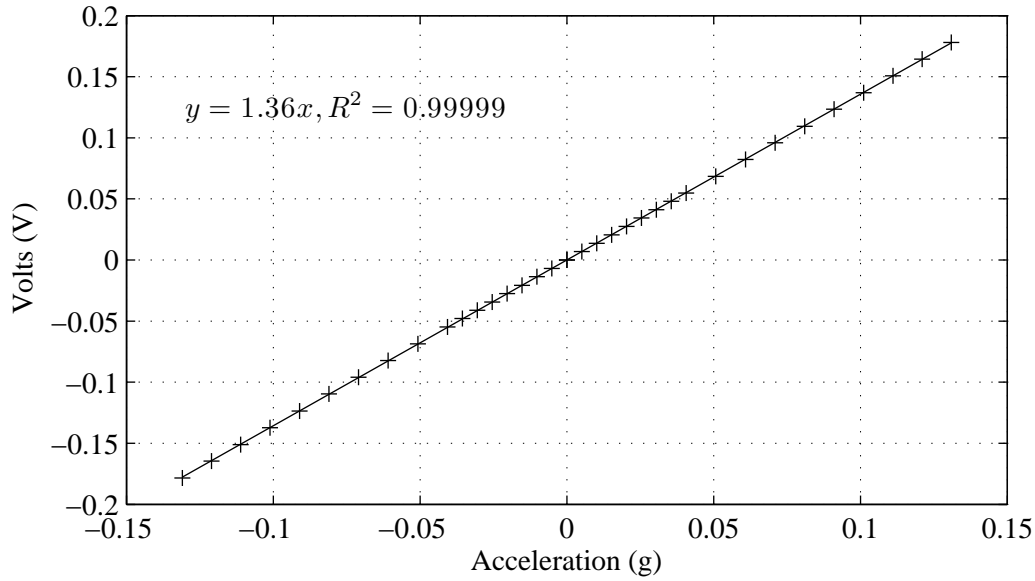
Figure 3.24: Accelerometer Static Calibration Results

pendulum and levelled. The output offset for each accelerometer was then zeroed using the ACU. The frequency response of one accelerometer is displayed in Figure 3.25, and all accelerometers had similar frequency response graphs. The magnitude of the accelerometer response is approximately linear over the range of frequencies important for full-scale monitoring of tall buildings. Most important is the lack of any mechanical amplification due to resonance. The maximum absolute deviation from 0 dB amounts to a $\pm 2\%$ change in the static accelerometer coefficient. Most of this deviation is likely due to mechanical tolerances inherent to the calibration apparatus, which will cause motion that is not purely sinusoidal. In addition to checking the accelerometer output from the dynamic calibration, the cross-power spectral densities were calculated to determine the phase of the accelerometer outputs. The phase deviations for each accelerometer were less than 1%, and therefore the accelerometers displayed no significant phase differences during the dynamic calibration.

For both the static and dynamic calibrations, the cables, signal conditioning equipment, and data acquisition hardware used during full-scale experiments were also used for the calibrations. This ensured any influence on the accelerometer outputs from these components were included in the calibration coefficients. In addition, the data collected during the calibration allowed the estimation of the noise floor for the entire acceleration measurement system. A sample of the static accelerometer data was used to generate histograms of the noise fluctuations about the mean values. The histograms closely matched a Gaussian distribution, with a standard deviation of approximately $0.077\,\mathrm{mg_n}$. This level of noise was also confirmed once
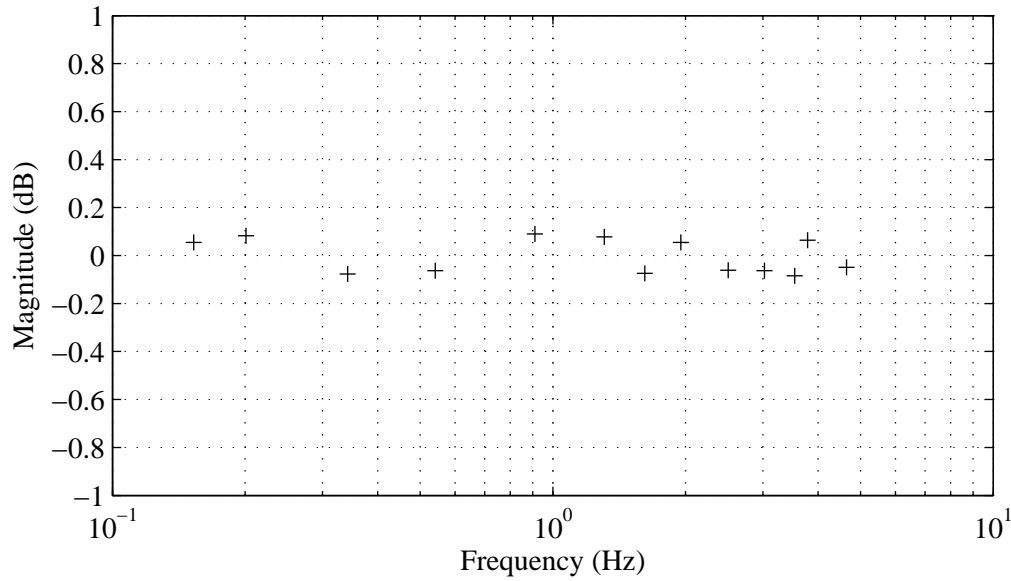
Figure 3.25: Accelerometer Dynamic Calibration Results

the equipment was installed at Latitude tower, using a similar analysis of data collected during calm wind conditions. This confirmation is important to ensure local noise influences at the point of installation are not adversely affecting the recorded data. The measured noise floor implies that recording a measurement as low as one standard deviation (68.2%) results in a 31.8% chance of what was measured is noise. Measurements as low as two and three standard deviations results in a 4.6% and 0.4% chance of what was measured is noise, respectively.

3.3.7 Anemometer Calibration

The anemometer was calibrated in a wind tunnel to confirm the wind speed specifications. The anemometer, along with the Wind Tracker and cabling used during the monitoring programme, were setup in The University of Sydney, School of Civil Engineering Thunderstorm Wind Tunnel. A Pitot static tube measured the wind speed while the anemometer was subjected to increasing wind speeds from approximately 5 m/s to 16 m/s.

Once installed, the anemometer was continuously exposed to harsh weather conditions that could damage internal and external components. Potential sensor damage includes increased bearing friction from dust ingress and corrosion. Regular checks of the anemometer output data was conducted to detect any changes in sensor characteristics.

3.4   Vibration Tests

At various stages in the construction cycle of the structure, the acceleration response to ambient loading was recorded. Considering the strengths and weaknesses of both ambient and forced vibration testing discussed in Section 2.4, the vibration testing programme used a combination of each method. Ambient vibration data was collected at every opportunity, and when possible the data sets were augmented by the collection of forced vibration data. During the early stages of construction, the size of the tower was such that forced excitation was possible using a small group of people — four in total — pushing in unison against a common wall. As construction progressed, the tower's increasing mass became a restriction to forced excitation using synchronised human movement with a small group, and site access limitations restricted an increase in group size. The next preferred excitation method was a form of forced loading using one of the two cranes attached to the structure during construction, but site specific limitations excluded this method. Consequently, forced vibration data was only collected during the early stages of construction.

At the completion of the main structure, forced vibration tests were conducted using a mechanical shaker loaned from the CLP Power Wind/Wave Tunnel Facility at The Hong Kong University of Science and Technology. The force imparted by the mechanical shaker on the structure can be determined, with a varying degree of accuracy, and therefore a more traditional modal analysis of the structure is permissible. This assumes the mechanical shaker is the only input source. As mentioned previously, the ambient input forces are assumed to be minimised and therefore have negligible influence on the vibration outputs. Further details regarding the forced vibration testing of the structure conducted after completion of construction is presented in Section 3.4.4.

3.4.1   Accelerometer Installation

The dynamic characteristics of the first two modes of vibration for each of the orthogonal translations and the torsional modes were the minimum required outputs from the vibration testing. The first three modes of vibration for a tall building, with minimal eccentricity between mass and stiffness centres, typically include translation in the major and minor axes and one torsional mode. Measuring the accelerations at any level of the structure could yield such information. However, all acceleration measurements were conducted at the highest accessible level of the building to capture the largest acceleration amplitudes possible, consequently maximising the quality of the recorded signals.

The extraction of natural frequencies alone from ambient vibration data of a rigid body requires a single measurement of any kinematic property, provided the
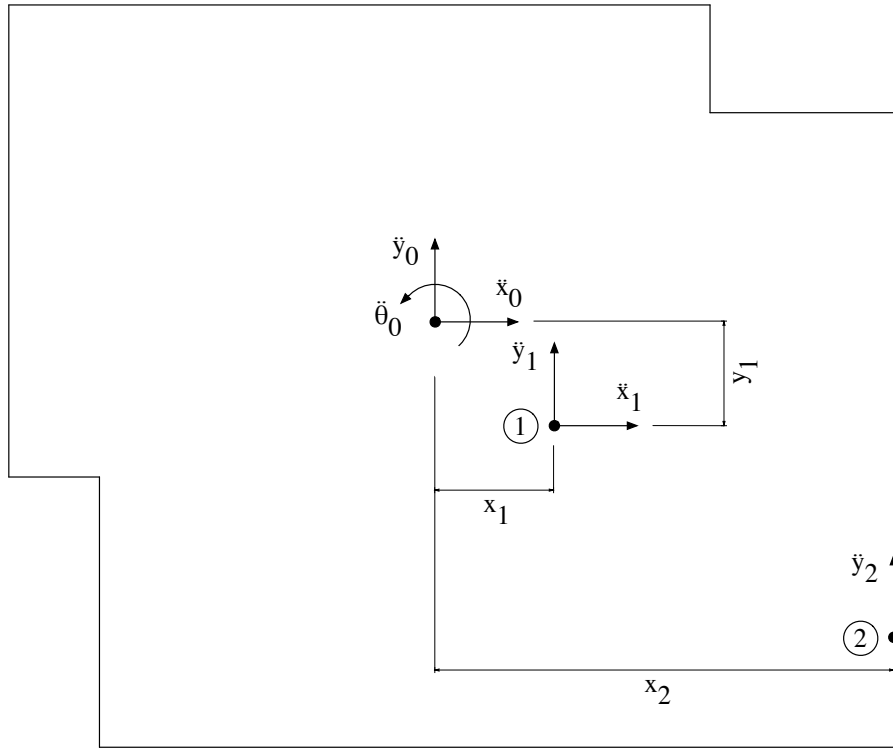
Figure 3.26: Vibration test accelerometer locations and axes.

measuring sensor is not located at a vibration node. To resolve the translations and rotations of a rigid body undergoing two dimensional plane motion a minimum of three appropriately placed sensors are required. Each level of the test structure can be considered to experience two dimensional plane motion.

For the vibration tests, one pair of orthogonally aligned accelerometers was positioned near the centre of the floor plan and aligned to the x and y axes of the building. A third accelerometer was positioned at the extremity of the floor plan and aligned to the y-axis. In practice, locating the accelerometers was dictated by the construction activity at the time of testing, and placement variations occurred between consecutive tests. Figure 3.26 displays the nominal accelerometer placements at points 1 and 2 with reference to the nominated origin and the defined axis directions.

Due to the ongoing construction and constant changing of the structure, the accelerometer pair could not be permanently attached. Instead, the accelerometer pair was securely connected to a steel disc, with a diameter of 120 mm and 25 mm thickness. The combined mass of the steel disc and accelerometers was approximately 2.9 kg. Three levelling screws evenly distributed around the circumference of the disc allowed horizontal alignment of the accelerometers, with the aid of a bullseye bubble level. This mounting configuration facilitated installation and removal, whilst preserving the useful frequency range of the accelerometers, particularly at

the lower frequencies.

3.4.2   Accelerometer Setup

At the accelerometer signal conditioning stage, a gain of 900 was applied to the accelerometer signals to maximise the $\pm 10\,\text{V}$ input range of the ADC and therefore minimise quantization errors [5]. Also prior to digitization, the accelerometer signals were filtered using an analogue low-pass fourth order Butterworth filter with a 20 Hz cut-off frequency, which is significantly greater than the frequency range of interest and avoided any filter roll-off effects. The resulting signal was sampled at 80 Hz. According to sampling theory, a significantly reduced sampling rate would be required to capture the acceleration signals. The larger sampling rates were used to enable the application of time domain data analysis techniques.

3.4.3   Test Schedule

The construction progress governed the vibration test schedule of the structure. A consecutive test was only performed once significant structural changes had occurred, for example the addition of a core level. Regular communication with design engineers and site foremen ensured significant structural changes were documented. A total of seventeen vibration tests were conducted between 27th May 2003 and 22nd December 2004.

Figure 3.27 displays the progress of the structure at the time of conducting the vibration tests. The dates of all eighteen vibration tests are listed on the left hand side of the figure. The lines link the vibration test date to the progress of the core, floor plates, and facade. These three elements of the structure were considered to have the most influence on the mass and stiffness of the structure. Note that the floor plates between levels 11 to 15 were demolished and re-built according to revised alignments. This was conducted while the upper levels were being built, which is reflected in the dates listed for the demolition and re-building of these lower levels.

The construction progress at the vibration test dates is also listed in Table 3.3. The table includes the reduced levels (RL) of the core, steel, and floor plates. Note that the steel components lead the floor plates by approximately two levels. The base of the tower is located at RL $-13.050\,\text{m}$.

Three cranes were used during the construction of the tower: located at the core, the eastern facade in the south-east corner, and the western facade in the north-west corner. The core crane was supported by the core walls, while the cranes located at the facades were supported at ground level. The core crane was removed between the vibration test dates 2004-03-01 and 2004-06-07. The western facade crane was removed between the test dates 2004-06-07 and 2004-08-06. The eastern facade

Date	Core Level	Core RL (m)	Steel Level	Steel RL (m)	Floor Level	Floor RL (m)
2003-05-27	24	65.915	20	54.620	18	47.090
2003-06-17	26	77.210	22	62.150	20	54.620
2003-07-08	27	80.975	23	65.915	22	62.150
2003-08-01	32	99.800	24	89.680	23	65.915
2003-08-07	33	103.585	25	73.445	24	89.680
2003-08-27	35	111.975	29	88.505	27	80.975
2003-09-12	36	116.115	32	99.800	30	92.270
2003-09-30	37	119.880	34	107.575	31	96.035
2003-10-10	37	119.880	34	107.575	32	99.800
2003-10-27	40	131.175	35	111.975	34	107.575
2003-11-17	44	146.235	38	123.645	37	119.880
2003-12-17	46	153.765	41	134.940	38	123.645
2004-02-12	53	180.925	47	157.530	45	150.000
2004-03-01	54	184.990	50	168.825	48	161.295
2004-06-07	55	190.320	55	190.320	55	190.320
2004-08-06	55	190.320	55	190.320	55	190.320
2004-12-22	55	190.320	55	190.320	55	190.320

Table 3.3: Schedule of vibration tests at Latitude tower showing reduced levels (RL) of the core, steelwork, and floors — base of tower at RL -13.050 m.

crane was removed prior to the final vibration test on 2004-12-22.

3.4.4   Mode Shape Testing

To conduct the mode shape testing, an array of twelve accelerometers distributed throughout the completed structure were used to record accelerations induced by a mechanical shaker. Most levels at the time of testing were secured for the new tenants, which limited access to the floors that permitted general access for the facilities management staff — namely the basement, ground level lobby areas, and plant rooms located on levels 16, 34 and 52. The plant room levels correspond to approximately quarter, half, and full height of the structure, and provide three suitably spaced locations at which to place accelerometers for determining the fundamental modes of vibration. Accelerations were also recorded at level 10, which corresponds to ground level.

Three accelerometers were positioned at each of the four test levels. Two orthogonally mounted accelerometers were placed near the centre of the core, and aligned to the x and y axes of the building. A third accelerometer was positioned at the western facade and measured the y-axis acceleration component to resolve the
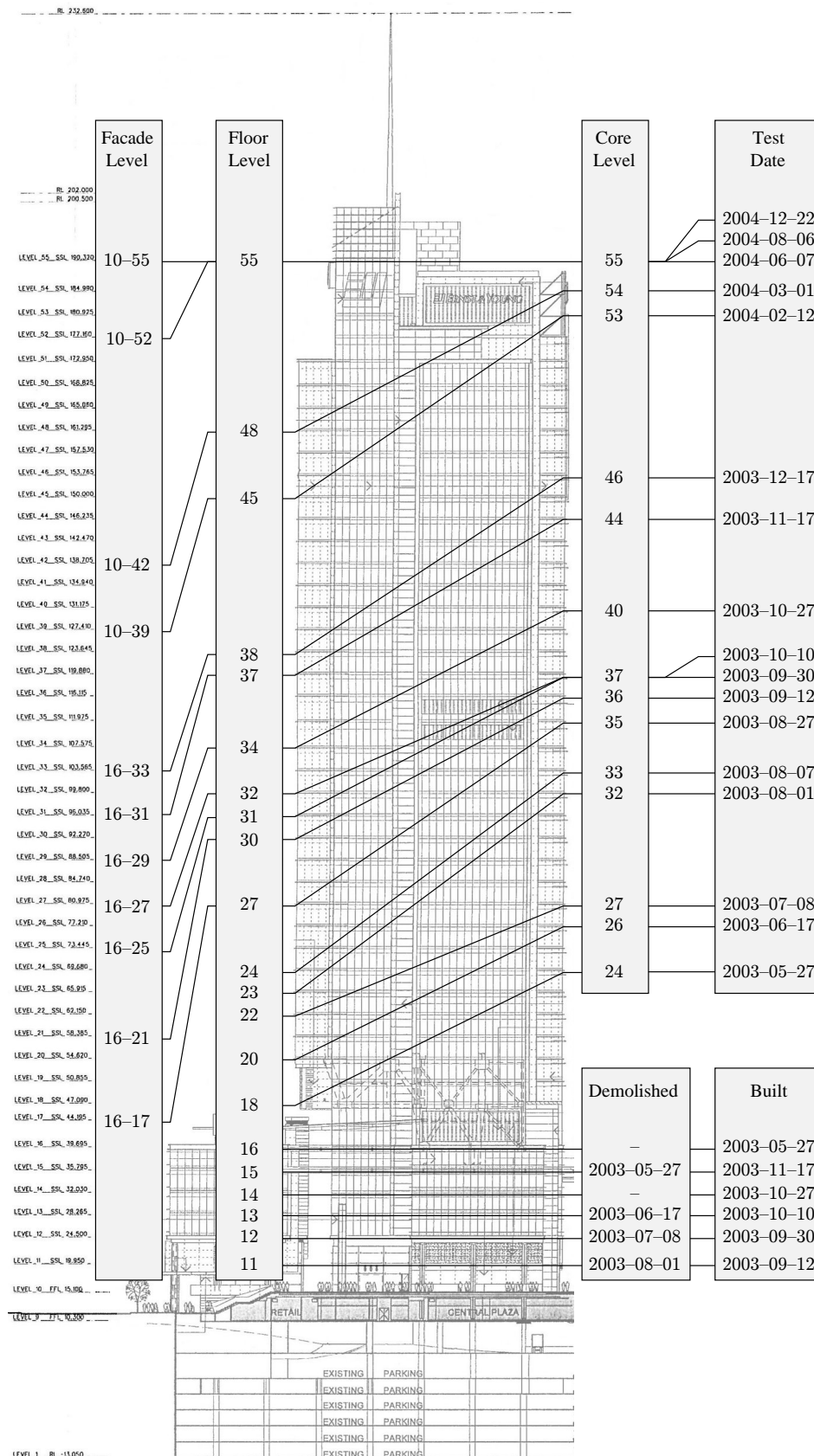
Figure 3.27: Schedule of vibration tests at Latitude tower showing completed core, floor plate, and facade levels at time of testing.

torsional components of the acceleration response. The specification, signal conditioning, data acquisition, and calibration of the accelerometers was identical to the description in Section 3.3.

All twelve accelerometers were connected via four computers and an ethernet network. This allowed simultaneous measurement of accelerations at all four levels. Each test level operated as a separate unit, with a single computer recording the output from the three accelerometers positioned on the respective test level. An ethernet network joined the four computers and enabled simultaneous triggering of the data acquisition systems, which ensured synchronisation of the four separately sampled data sets.

A mechanical shaker with a payload of approximately 1000 kg was used to excite the building. The electronically controlled shaker generated the excitation force by moving a mass along a linear axis in a sinusoidal manner. A ball-screw mechanism smoothly moved the mass at a specified rate and allowed instantaneous stopping of the mass for accurate damping detection. To minimise other sources of loading on the structure, particularly wind loading, the testing was conducted during calm wind conditions.

3.5 Monitoring Programme

A full-scale monitoring programme commenced shortly after construction of the structure was completed. Small scale construction activities were still in progress, for example the internal fit-out within plant rooms and office areas, however the structural system and cladding were completed before commencing the monitoring programme. Hence, unlike the vibration testing, results from the monitoring programme are not significantly influenced by changes in structural parameters, such as mass, stiffness, and damping, that occur from construction activity.

Starting in April 2005, the monitoring programme continuously recorded the wind-induced response of the structure for approximately two years. The recorded data included accelerations, displacements, and wind velocity. The instrumentation system, summarised in Figure 3.28, includes four accelerometers to monitor the translational and torsional responses. Tip displacements of the structure and the approaching wind velocity were monitored by a GPS receiver and anemometer respectively. The data acquisition system was configured to automatically record data according to a wind speed threshold criteria, which avoided the recording of data during periods of insignificant structural response. The following sections provide more detail regarding the monitoring system components and configuration.
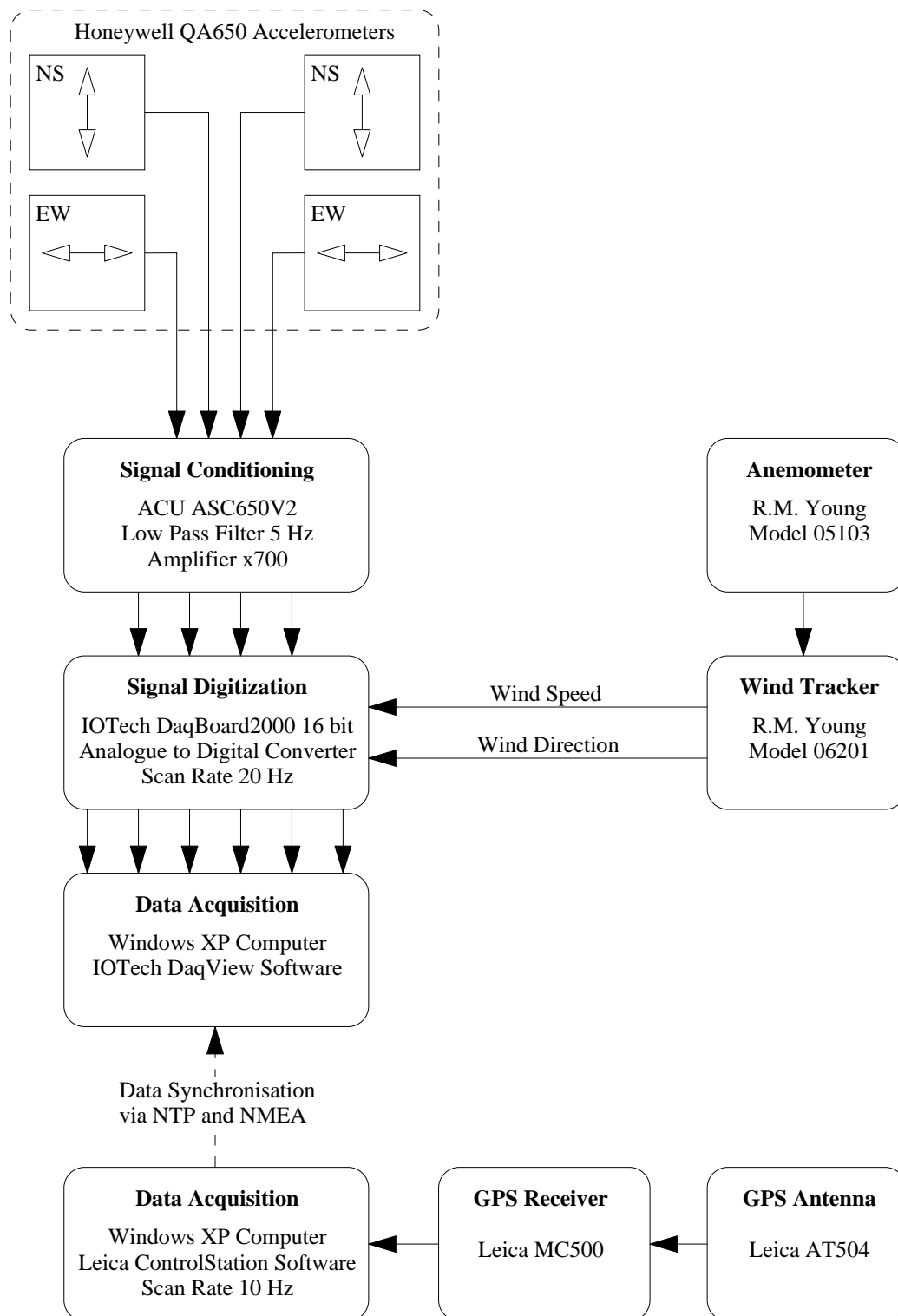
Figure 3.28: Schematic of the monitoring system equipment and setup.

3.5.1 Accelerometer Setup

Two pairs of orthogonally mounted accelerometers were installed in the plant room located at the top of the structure. The specification and calibration of the acceleromters are discussed in Section 3.3. Each pair of accelerometers were installed at opposite sides of the structure, one pair at the eastern facade and another at the western facade, and aligned to the x and y axes of the building. This spatial arrangement enabled the recording of both translational and rotational responses. The points labelled 1 and 2 in Figure 3.29 display the locations of the accelerometers in relation to the floor plan. Due to the longevity of the monitoring programme, a robust accelerometer mounting system was required. Each accelerometer pair was securely bolted to the bottom flange of the level 54 spandrel beams. A tribrach permanently fitted between the flange attachment and the accelerometer pair was used for levelling, with the aid of a bulls-eye bubble level. The alignment of each accelerometer pair was confirmed using a laser to site the orientations.

The accelerometer configuration used for the monitoring programme includes one redundant sensor. In theory only three appropriately positioned accelerometers are required to measure two dimensional plane motion of a rigid body. Including an extra accelerometer offers a contingency in the event a sensor fails. Given the potential time length required to measure responses from peak wind events, this contingency, and indeed any other contingencies, is a valuable attribute. The accelerometer arrangement could have been improved by increasing the perpendicular distance between the accelerometers aligned to the x-axis. However, this could not be achieved due to restricted access areas within the plant room. Considering the possible accelerometer installation points within the level 52 plant room, those displayed in Figure 3.29 represented the optimum allowable configuration.

Results of the vibration tests presented in Table 4.1 indicated the frequency values of the first three modes of vibration for the completed structure were below 0.5 Hz, and the first six modes were below 2 Hz. For most tall buildings the first three modes of vibration encompass approximately 90% of the response energy [47]. This is due to the nature of the spectrum of wind forces, which generally contain most energy in the frequency bands below 1 Hz. Therefore, for the monitoring programme the accelerometer signals were low pass filtered at a 5 Hz cut-off frequency, which is significantly greater than the frequency range of interest and avoided any filter roll-off effects. To improve the sensitivity, the acceleration signals were amplified by a gain of 700 in order to utilise the ± 10 V range of the ADC. The accelerometers were connected to the signal conditioners using shielded, twisted pair cable to minimise noise contamination of the signals. Existing cable trays and ducting was used to route the accelerometer cables through the level 52 plant room to the signal conditioners and data logging equipment. The cable lengths, and therefore signal noise,
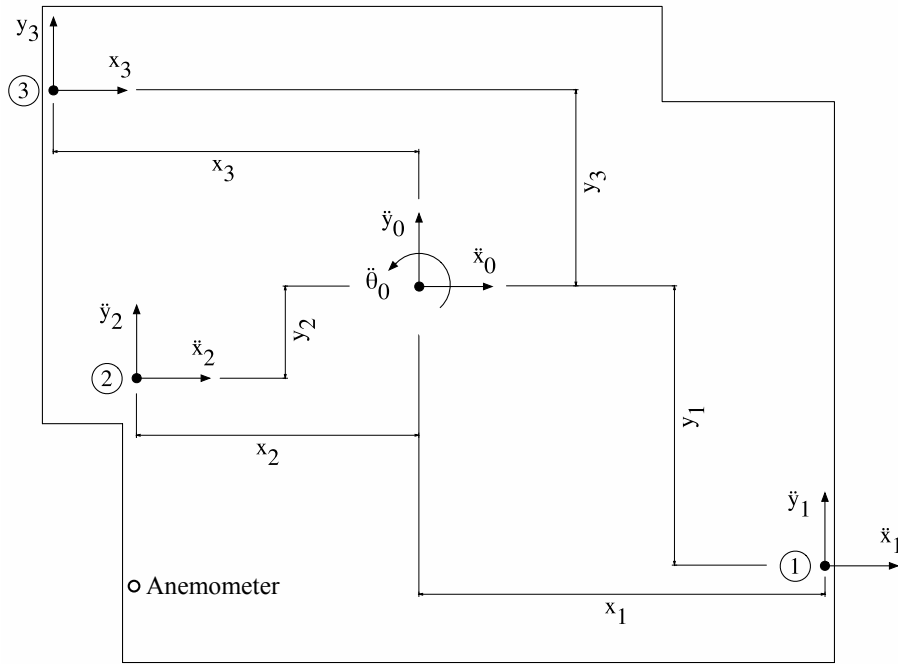
Figure 3.29: Monitoring programme sensor locations and axes.

was minimised by locating the data acquisition equipment approximately midway between the two accelerometer installation points.

3.5.2 Anemometer Setup

Measurement of the local wind velocity was via a propeller-vane anemometer located above the south-west corner of the roof. The anemometer location is displayed in Figure 3.29, and the specification and calibration are discussed in Section 3.3. The installation required a mast to elevate the anemometer above the roof cladding and cooling towers, thus reducing undesirable influences on the free stream wind velocity. Locating the anemometer in the south-west corner was suitable for measuring wind velocities originating from 90° to 330°, although outside this range reliable data was unattainable due to severe turbulence from wind-structure interaction. Installation restrictions imposed by the building owners precluded extending the anemometer mast height, or installing a second anemometer at the eastern extremity of the roof area.

Installation of the anemometer utilised a three metre cylindrical mast attached to the cladding support structure via two steel brackets. The mast protruded approximately 1.5 m above the roof cladding structure, and the final height of the anemometer above the level 55 roof was approximately 12 m, which corresponds to a height of approximately 190 m above street level. Figure 3.30 displays the location of the mast and anemometer in the south-west corner of the Latitude tower roof. Despite elevating the mast above the cladding support structure, the anemometer

Figure 3.30: Anemometer installation location in the south-west corner of the Latitude tower roof.

location remained within the structures influence zone rather than in the free stream flow; this was confirmed and accounted for by wind tunnel tests, which are described in Section 6.2. The horizontal alignment of the anemometer was according to the building orthogonal axes.

3.5.3 GPS Receiver Setup

The two GPS receivers were configured in a reference and rover arrangement to allow Differential GPS (DGPS), paired with differential phase positioning, to minimise atmospheric errors [102]. The reference antenna was located at the Electrical Engineering Department at The University of New South Wales (UNSW), which is located approximately 4.9 km south-east of Latitude tower. The reference antenna

Figure 3.31: Rover GPS antenna installation location in the North-West corner of the Latitude tower roof.

installation was atop a small building and assumed to be relatively static under serviceability wind events. The measurements recorded by the reference receiver were used to correct the rover measurements for atmospheric errors.

The rover antenna was located in the north-west corner of the Latitude tower roof. The installation location of the rover antenna, point 3 in Figure 3.29, was chosen to minimise multipath errors, and to maximise the number of viewable satellites. However, due to the proximity of neighbouring structures and the presence of structural and architectural steelwork near the antenna, it was not possible to completely mitigate the multipath errors from the recorded measurements. The reference antenna was mounted atop a steel pedestal, which was firmly secured to the base of the roof-top balustrade using three guy-wires with turn buckles. Figure 3.31 displays the rover GPS antenna installation in the north-west corner of the Latitude roof.

Both the reference and rover GPS receivers continuously streamed observation data at 10 Hz to dedicated computers using Leica GPS control software. Analysis of the GPS observations used a post-processing work flow, as opposed to real-time, where the displacements are calculated after acquiring the data.

3.5.4 Data Acquisition and Control System

The monitoring programme included three types of sensors that required integration into a single, synchronised system. To facilitate this integration, two separate systems were used to record the data from the sensors. The acceleration and wind velocity measurements comprised one acquisition system, while the GPS displacement measurements formed another separate acquisition system, Figure 3.28. To reduce the time and effort required to develop and implement the monitoring programme control system and data acquisition, it was decided to use proprietary software developed by the manufacturers chosen to supply the system components — specifically IOTech Inc. and Leica Geosystems AG, supplying the ADC and GPS receivers, respectively.

The accelerometer and anemometer output signals were digitized using an IOTech DaqBoard/2000™ 16 bit ADC and recorded to the internal hard drive of a desktop computer. The supplied IOTech DaqView™ software was configured to record data according to a wind speed threshold of $5\,\mathrm{m\,s^{-1}}$ or greater, which avoided the unnecessary acquisition of data during periods of insignificant building response. Each trigger event was recorded for 15 minutes, with two minutes pre-trigger scan included. The accelerometer signals had a bandwidth of $5\,\mathrm{Hz}$, and according to sampling theory [5] would require a sampling rate of at least twice the signal bandwidth for accurate reconstruction. Both the anemometer and acceleration data were recorded at $20\,\mathrm{Hz}$.

Unlike the accelerometer and anemometer data acquisition, all GPS data was continuously recorded regardless of the wind conditions or building response. Displacement data collected during calm wind conditions can be used to improve the estimation of the mean or centre point of the displacements as well as allowing a more detailed analysis of the influence of multipath and temperature effects on the displacement results. Multipath effects relate to the reception of GPS signals that have travelled indirectly from the GPS satellite to a GPS antenna, which causes significant errors in recorded positions. The temperature effects relate to the differential heating of a structure during the day, which also influences displacement results.

A notebook computer with Leica GPS Spider software was used to store the acquired data and control the GPS receiver. The Leica MC500 GPS receivers allowed a maximum sampling rate of $10\,\mathrm{Hz}$, and the next user selectable scan rate was $1\,\mathrm{Hz}$. The third mode frequency of vibration for the test structure was approximately $0.44\,\mathrm{Hz}$, which according to sampling theorem requires a sampling rate greater than $0.88\,\mathrm{Hz}$ — at least twice the highest frequency in the signal. [125] indicate that 2.5 samples per cycle is more appropriate, resulting in a sampling frequency above $1\,\mathrm{Hz}$. The GPS receivers main function was to record the background

and quasi-static response of the structure and in this capacity a 1 Hz sampling rate is sufficient. However, recording at higher sampling rates allows useful comparisons and checks between the displacement and acceleration data, in addition to combining the separate data sources to improve estimates of the wind-induced response of the structure. For these reasons, the GPS receiver data were sampled at 10 Hz.

Dividing the monitoring system components into two separate systems required a synchronisation mechanism for the acquisition of data. Acceleration and wind velocity measurements were recorded via one analogue to digital converter and were therefore synchronised, however the GPS receiver data was recorded separately. To synchronise the GPS data a second handheld GPS receiver was used to synchronise the clock of the computer used to log the acceleration and wind velocity data. Using Network Time Protocol (NTP) software [137] installed on the data logging computer, the software was configured to poll the serial port for incoming NMEA messages [43] from the handheld GPS receiver, and extract the appropriate segment related to time and update the internal clock. The handheld GPS receiver sent NMEA messages every second, and the computer updated the internal clock every ten seconds. This ensured the computer clock was regularly synchronised to GPS time, and therefore synchronised with the GPS receiver data. Each record containing acceleration and wind velocity data was time-stamped with the trigger time to provide a means to match with the GPS receiver data.

The continuous nature of the monitoring programme is arguably the most crucial aspect. The programme schedule only allowed two years for monitoring the structure, and ensuring the recording of all significant wind events was paramount. Should equipment or control systems fail during a significant wind event, the chances of a repeated event would be unlikely, given the relatively short monitoring period. A number of strategies were implemented to ensure the monitoring system operated continuously and mostly without constant human interaction. Firstly, an uninterrupted power supply was installed and used to power all equipment associated with the monitoring system. Secondly, all equipment was configured to reboot and restart logging in the event of a power failure. And finally, regular site visits were conducted to check equipment and manually download recorded data.

3.6   Summary

This chapter has described the full-scale experiments conducted on a 46 storey office tower located in the Sydney CBD. The experiments included two phases. Firstly, a periodic vibration testing period during the construction of the building to record horizontal accelerations of the building. These measurements are used to determine the natural frequencies, damping ratios, and mode shapes of the building. The

techniques used to estimate these values are discussed in the following chapter. The second phase involved a two year monitoring period to measure the building's tip accelerations, tip displacements, and the approaching wind velocity.

The excitations measured were from a number of sources, including ambient vibrations during and after construction, synchronised human movement during construction, and excitation from a mechanical shaker at the end of construction. In the test cases where human movement and the mechanical shaker was used, the testing times were selected to minimise, as best as possible, the ambient vibrations from wind and construction activities.

The full-scale testing phases highlighted the difficulties in gaining access to a test structure and attaining ideal conditions in which to conduct testing. This was particularly evident during the construction phase, where the pace of construction takes precedent over all other activities.

Chapter 4

Vibration Models and System Identification

4.1 Introduction

This chapter presents the theory of models of vibrating structures, and the system identification techniques used to analyse the data obtained from full-scale vibration measurements described in Section 3.4. The main purpose for describing the models and techniques is to introduce the theory and nomenclature, to highlight the assumptions of the chosen models and techniques, and to provide detailed examples that support the results discussed in Chapter 5.

Finite element models of undamped vibrating structures are initially introduced. Such models and the techniques used to solve them form the foundation of modal analysis of discrete models to determine the dynamic characteristics. The damped finite element model is subsequently introduced, with the proportional damping and general viscous damping cases being discussed. These models form the basis upon which the system identification techniques are developed.

Three system identification techniques are described: a frequency domain technique, and two time domain techniques. The frequency domain system identification technique is an extension of the peak picking technique [6, 53] and is known as Frequency Domain Decomposition (FDD) [14]. The first time domain system identification technique is based on a stochastic state space model of a vibrating structure and is known as Stochastic Subspace Identification (SSI) [127]. The second time domain technique described is known as the Random Decrement (RD) technique, and is based on the concept of ensemble averaging segments of a response time history based on a defined trigger condition. All three system identification techniques utilise operational modal analysis, which uses unmeasured ambient excitations during operational conditions as the input source.

The reasons for using multiple system identification techniques in the data analy-

sis is to enable comparisons between the results, because each technique has deficiencies, as well as allowing more rigorous investigations into the estimation of damping values. FDD and SSI are used due to their theoretical ability to estimate damping ratios using limited data, compared with the Random Decrement (RD) which generally requires large amounts of data to determine reliable damping estimates. Furthermore, the RD technique was used with the monitoring data to determine the amplitude dependence of natural frequency and damping ratio.

4.2 Finite Element Vibration Models

Consider the simplified model of a high-rise structure displayed in Figure 4.1 (a). The masses m_i are an approximation for the mass of each floor in a high-rise structure, and the walls and columns that typically span between levels are represented by vertical stick elements. For horizontal motion in the x direction, the walls and columns connecting the masses have an intrinsic stiffness k_i and act as springs that resist motion away from static equilibrium. The spring stiffness is dependent upon the elastic modulus, the second moment of area, and length of the individual wall and column elements. Energy dissipation is modelled via linear viscous damping elements that generate a force proportional to the velocity, and the constant of proportionality is the damping coefficient c_i. In Figure 4.1 (a), the horizontal elements are assumed to be axially rigid, and the rotations and vertical deflections at the top of the elements spanning between the masses are assumed to be zero. In essence, this simplified model represents an undamped multi-degree of freedom system with n masses connected by n springs.

The equations of motion for the system in Figure 4.1(a) can be formed by applying Newton's second law to each mass individually. To simplify the introduction of this concept, only two degrees-of-freedom will be considered, and therefore $n = 2$. Using the free body diagram displayed in Figure 4.1(b) and summing the dynamic forces on each mass in the horizontal direction, the equations for dynamic equilibrium are;

$$-c_1\dot{x}_1(t) - k_1x_1(t) + c_2(\dot{x}_2(t) - \dot{x}_1(t)) + k_2(x_2(t) - x_1(t)) + f_1(t) = m_1\ddot{x}_1(t)$$
$$-c_2(\dot{x}_2(t) - \dot{x}_1(t)) - k_2(x_2(t) - x_1(t)) + f_2(t) = m_2\ddot{x}_2(t)$$

These equations can be rearranged to;

$$m_1\ddot{x}_1(t) + (c_1 + c_2)\dot{x}_1(t) - c_2\dot{x}_2(t) + (k_1 + k_2)x_1(t) - k_2x_2(t) = f_1(t) \quad (4.1)$$
$$m_2\ddot{x}_2(t) - c_2\dot{x}_1(t) + c_2\dot{x}_2(t) - k_2x_1(t) + k_2x_2(t) = f_2(t) \quad (4.2)$$

Equations (4.1) and (4.2) represent two second-order linear differential equations

(a) System Representation   (b) Free Body Diagram
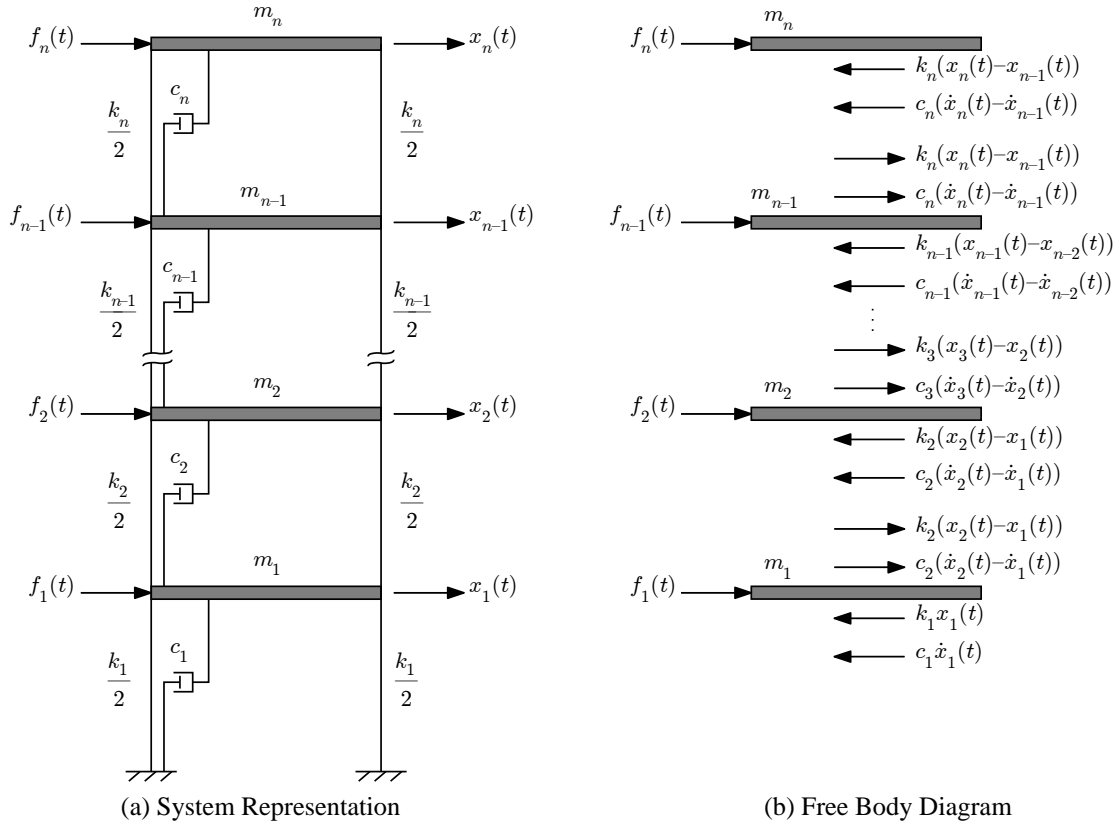
Figure 4.1: Damped horizontal vibration model of a multi-storey building with lumped masses and n degrees of freedom.

that are dependent, because both equations contain the terms $x_1(t)$ and $x_2(t)$. In other words, the motion $x_1(t)$ of m_1 is influenced by the motion $x_2(t)$ of m_2 and vice versa. In this case Equations (4.1) and (4.2) are coupled via the stiffness attributes k_1 and k_2, as well as the damping attributes c_1 and c_2.

Equations (4.1) and (4.2) can be expressed in matrix notation as;

$$\begin{bmatrix} m_1 & 0 \\ 0 & m_2 \end{bmatrix} \begin{bmatrix} \ddot{x}_1(t) \\ \ddot{x}_2(t) \end{bmatrix} + \begin{bmatrix} c_1 + c_2 & -c_2 \\ -c_2 & c_2 \end{bmatrix} \begin{bmatrix} \dot{x}_1(t) \\ \dot{x}_2(t) \end{bmatrix} + \begin{bmatrix} k_1 + k_2 & -k_2 \\ -k_2 & k_2 \end{bmatrix} \begin{bmatrix} x_1(t) \\ x_2(t) \end{bmatrix} = \begin{bmatrix} f_1(t) \\ f_2(t) \end{bmatrix}$$
(4.3)

or further condensed to;

$$\boldsymbol{M}\ddot{\boldsymbol{x}}(t) + \boldsymbol{C}\dot{\boldsymbol{x}}(t) + \boldsymbol{K}\boldsymbol{x}(t) = \boldsymbol{f}(t) \tag{4.4}$$

where $\boldsymbol{M}$ is the mass matrix, $\boldsymbol{C}$ is the damping matrix, $\boldsymbol{K}$ is the stiffness matrix, $\boldsymbol{x}(t)$ is the displacement vector, $\dot{\boldsymbol{x}}(t)$ is the velocity vector, $\ddot{\boldsymbol{x}}(t)$ is the acceleration vector, and $\boldsymbol{f}(t)$ is the force vector.

The displacement coordinates $x_1, x_2, \ldots, x_n$ are not the only set of coordinates that can be employed to describe the system in Figure 4.1. Any dynamic system can

be completely described using more than one set of independent spatial coordinates, each of which is referred to as a set of generalized coordinates. The selection of the generalized coordinates is arbitrary and often governed by convenience. Generally, the displacement from the static equilibrium positions of masses and the rotations about the mass centres are often used for coordinates. Let $q_i(t) \in \mathbb{R}^n$ denote the set of generalized coordinates selected to describe the system. For the case in Figure 4.1, the generalized coordinates can be taken as $q_1 = x_1$, $q_2 = x_2$, ... , $q_n = x_n$. Another example is the motion of a rigid floor plate within a tall building, which can be completely described by two orthogonal translations in the horizontal plane and a single rotation about a vertical axis. In this case the generalised coordinates are $q_1 = x_1$, $q_2 = y_1$, and $q_3 = \theta_1$.

The values of each element in the mass matrix, damping matrix, stiffness matrix, and force vector are dependent upon the generalized coordinates used to describe the system. Despite this fact, the inherent dynamic properties of the system are independent of the generalized coordinates. Applying the generalized coordinate notation introduced earlier to Equation (4.3), the generalized equations of motion for a two degree of freedom system are;

$$\begin{bmatrix} m_{11} & m_{12} \\ m_{21} & m_{22} \end{bmatrix} \begin{bmatrix} \ddot{q}_1(t) \\ \ddot{q}_2(t) \end{bmatrix} + \begin{bmatrix} c_{11} & c_{12} \\ c_{21} & c_{22} \end{bmatrix} \begin{bmatrix} \dot{q}_1(t) \\ \dot{q}_2(t) \end{bmatrix} + \begin{bmatrix} k_{11} & k_{12} \\ k_{21} & k_{22} \end{bmatrix} \begin{bmatrix} q_1(t) \\ q_2(t) \end{bmatrix} = \begin{bmatrix} p_1(t) \\ p_2(t) \end{bmatrix} \quad (4.5)$$

which can be condensed to;

$$\boldsymbol{M}\ddot{\boldsymbol{q}}(t) + \boldsymbol{C}\dot{\boldsymbol{q}}(t) + \boldsymbol{K}\boldsymbol{q}(t) = \boldsymbol{p}(t) = \boldsymbol{P}\boldsymbol{u}(t) \quad (4.6)$$

The mass matrix, damping matrix, stiffness matrix, and force vector, denoted by $\boldsymbol{p}(t)$, are now associated with the generalized coordinates. The force vector is factorised into a matrix $\boldsymbol{P} \in \mathbb{R}^{n \times r}$ that specifies the spatial position of the inputs, and a vector $\boldsymbol{u}(t) \in \mathbb{R}^{r \times 1}$ that describes the inputs in time. The matrix $\boldsymbol{P}$ is the input influence matrix and accounts for the situation in which not all degrees of freedom have an associated input. This is often the case for finite element models, which generally have significantly more degrees of freedom than the number of measured points in a full-scale vibration test.

In addition to the presence of the generalized coordinates, Equation (4.5) further generalizes the description of the system by representing each element within the mass matrix, damping matrix, and stiffness matrix with a generic element identifier instead of the actual value attained from summing the dynamic forces in Figure 4.1 (b). The two subscripts refer to the position within the matrix, for example m_{11} is the first row and first column of the mass matrix, and k_{21} is the second row and first column of the stiffness matrix. This extends the applicability of Equation (4.6)

to describe the motion of a system with n degrees of freedom, which would imply $\boldsymbol{M} \in \mathbb{R}^{n \times n}$, $\boldsymbol{C} \in \mathbb{R}^{n \times n}$, $\boldsymbol{K} \in \mathbb{R}^{n \times n}$, $\boldsymbol{p}(t) \in \mathbb{R}^{n \times 1}$, and $\boldsymbol{q}(t) \in \mathbb{R}^{n \times 1}$. Therefore, Equation (4.6) is also the general form of the equations of motion describing an n degree of freedom system.

For distributed parameter systems like large civil engineering structures, Equation (4.6) represents a finite element (FE) model of the system, with n degrees of freedom. The mass and stiffness matrices are generated from the geometry and material properties of the system. The inclusion of viscous damping allows the observed decaying vibrations of actual structures to be modelled. The general viscous damping assumption does not accurately model the actual damping mechanisms. Damping within a structure originates from numerous mechanisms, and the general viscous damping approach combines all the damping mechanisms into one mathematically convenient structural damping parameter. The complex nature of damping mechanisms within a structure precludes the formation of the damping matrix in the manner used for the mass and stiffness matrices.

4.2.1   Undamped Free Vibration

The solution of Equation (4.6) is presented for the case where damping is removed from the system. By assuming free vibration of the system, the force vector $\boldsymbol{p}(t)$ equals zero, resulting in the homogeneous form of the undamped vibration model,

$$\boldsymbol{M}\ddot{\boldsymbol{q}}(t) + \boldsymbol{K}\boldsymbol{q}(t) = 0 \tag{4.7}$$

The properties of Equation (4.8) make it a suitable candidate for particular solutions to the homogeneous differential equations;

$$\boldsymbol{q}_i(t) = \boldsymbol{\phi}_i e^{j\omega_i t} \tag{4.8}$$

where $\boldsymbol{\phi}_i$ is a vector of constants, ω_i is a constant, and $j = \sqrt{-1}$. Note that the scalar $e^{j\omega_i t}$ represents harmonic motion, since via Euler's formula $e^{j\omega t} = \cos \omega t + j \sin \omega t$. Substituting Equation (4.8), and its second derivative, into Equation (4.7) and re-arranging yields

$$(-\omega_i{}^2 \boldsymbol{M} + \boldsymbol{K})\boldsymbol{\phi}_i e^{j\omega_i t} = 0 \tag{4.9}$$

Since $e^{j\omega_i t} \neq 0$ for all values of t, $\boldsymbol{\phi}_i$ and ω_i must satisfy the equation

$$(-\omega_i{}^2 \boldsymbol{M} + \boldsymbol{K})\boldsymbol{\phi}_i = 0 \tag{4.10}$$

or alternatively

$$\boldsymbol{K}\boldsymbol{\phi}_i = \lambda_i \boldsymbol{M}\boldsymbol{\phi}_i \tag{4.11}$$

where $\lambda_i = \omega_i{}^2$. Equation (4.11) represents a generalised eigenvalue problem [74], where $\lambda_i \in \mathbb{R}^n$ are the eigenvalues and $\phi_i \in \mathbb{R}^n$ $(i = 1, \ldots, n)$ are the eigenvectors. All n generalised eigenvalue problems can be condensed into a single matrix expression;

$$\boldsymbol{K\Phi} = \boldsymbol{M\Phi\Omega}^2 \tag{4.12}$$

where $\boldsymbol{\Phi} \in \mathbb{R}^{n \times n}$ contains the eigenvectors in columns and $\boldsymbol{\Omega} = \left[\searrow \omega_i \searrow \right] \in \mathbb{R}^{n \times n}$ contains the square root of the eigenvalues, or more commonly termed the system natural frequencies, with units of radians per second. The eigenvectors are also known as the modal vectors and physically represent the natural modes of the system. In the context of structural vibration, the modal vectors are also termed the mode shapes, because they visually represent the deformed shape of the vibrating structure. The group of eigenvectors is also referred to as the modal matrix. The modal matrix acts as a transformation from the generalised coordinates to another set of coordinates, known as the principal coordinates, which uncouples the equations of motion by simultaneously creating diagonal $\boldsymbol{M}$ and $\boldsymbol{K}$ matrices, leading to a system of independent equations of motion. Therefore, the following orthogonality conditions can be proven;

$$\boldsymbol{\Phi}^T \boldsymbol{M} \boldsymbol{\Phi} = \left[\searrow m_i \searrow \right] \, , \; \boldsymbol{\Phi}^T \boldsymbol{K} \boldsymbol{\Phi} = \left[\searrow k_i \searrow \right] \tag{4.13}$$

The modal vectors are unique via the ratios between any two elements, but the values of each element are arbitrary. This property of the modal vectors occurs because Equation (4.7) is homogeneous, meaning any constant times the modal matrix is a solution of the equation. Therefore, the shape of the modal vectors are unique, but the amplitudes are not. For convenience, a normalisation process can be applied to the elements of the modal vectors to establish a unique amplitude, and the resulting vectors are termed normal modes. A mass normalisation scheme is a common choice, where Equation (4.13) becomes;

$$\boldsymbol{\Phi}^T \boldsymbol{M} \boldsymbol{\Phi} = \boldsymbol{I} \, , \; \boldsymbol{\Phi}^T \boldsymbol{K} \boldsymbol{\Phi} = \boldsymbol{\Omega}^2 \tag{4.14}$$

where $\boldsymbol{I}$ is the identity matrix with dimensions $n \times n$. Another useful normalisation scheme consists of dividing each element of the modal vector by the maximum value, which is a convenient option when plotting the modal vectors.

Substituting Equation (4.13) into Equation (4.12) yields the following fundamental relationship;

$$\omega_i{}^2 = \frac{k_i}{m_i} \tag{4.15}$$

The preceding method of solving the equations of motion is known as modal analysis. All mechanical systems have some form of energy dissipation in the form of damping

forces.

With the inclusion of damping into the system described by Equation (4.6), the modal analysis method used to solve the undamped free response case is not capable of uncoupling the equations of motion unless the damping matrix is assumed to be proportional to the mass and stiffness matrices. Proportional damping implies that the modal vectors $\boldsymbol{\phi}_i$ also diagonalise the damping matrix, in addition to the mass and stiffness matrices. This results in decoupled equations that can be solved by the modal analysis method. If the assumption of proportional damping is invalid for the modelled system, an alternative solution option is to transform the equations of motion to equivalent first order equations and apply a state space method. In addition, the experimental determination of damping often requires general viscous damping models. The proportional damping case and the general viscous damping case are discussed in the following sections.

4.2.2 Damped Response with Proportional Damping

By introducing the coordinate transform $\boldsymbol{q}(t) = \boldsymbol{\Phi}\boldsymbol{\eta}(t)$ and multiplying by $\boldsymbol{\Phi}^T$, the system model in Equation (4.6) becomes,

$$\boldsymbol{\Phi}^T \boldsymbol{M} \boldsymbol{\Phi} \ddot{\boldsymbol{\eta}}(t) + \boldsymbol{\Phi}^T \boldsymbol{C} \boldsymbol{\Phi} \dot{\boldsymbol{\eta}}(t) + \boldsymbol{\Phi}^T \boldsymbol{K} \boldsymbol{\Phi} \boldsymbol{\eta}(t) = \boldsymbol{\Phi}^T \boldsymbol{p}(t) \tag{4.16}$$

where the vector $\boldsymbol{\eta}(t) \in \mathbb{R}^{n \times n}$ is the normal coordinates of the system, which are the normalised principal coordinates as described in Section 4.2.1. With the assumption of proportional damping, the eigenvectors are also diagonalising the damping matrix;

$$\boldsymbol{\Phi}^T \boldsymbol{C} \boldsymbol{\Phi} = \left[\diagdown c_i \diagdown \right] = \left[\diagdown 2\zeta_i \omega_i m_i \diagdown \right] = \Gamma \left[\diagdown m_i \diagdown \right] \tag{4.17}$$

The second equality of Equation (4.17) follows from the definition of the modal damping ratios; $\zeta_i = c_i/c_{cr} = c_i/2m_i\omega_i$, where c_{cr} is the critical damping coefficient. The third equality defines $\Gamma = \left[\diagdown 2\zeta_i \omega_i \diagdown \right]$. Substituting Equations (4.13) and (4.17) into (4.16), the equations of motion are decoupled;

$$\boldsymbol{I} \ddot{\boldsymbol{\eta}}(t) + \boldsymbol{\Gamma} \dot{\boldsymbol{\eta}}(t) + \boldsymbol{\Omega}^2 \boldsymbol{\eta}(t) = \left[\diagdown m_i^{-1} \diagdown \right] \boldsymbol{\Phi}^T \boldsymbol{p}(t) \tag{4.18}$$

As for the undamped case, the solution for the homogeneous proportional damping case has the form $\boldsymbol{q}_i(t) = \boldsymbol{\phi}_i e^{j\omega_i t}$. The resulting eigenvectors are the same as for the undamped case, and from Equation (4.18), the eigenvalues are determined from the following characteristic equation,

$$\lambda_i{}^2 + 2\zeta_i \omega_i \lambda_i + \omega_i{}^2 = 0 \tag{4.19}$$

which can be solved via the quadratic equation to yield the following complex conjugate pairs as solutions,

$$\lambda_i, \lambda_i^* = -\zeta_i\omega_i \pm \omega_i\sqrt{1 - \zeta_i^2}j \tag{4.20}$$

where the superscript '$*$' denotes complex conjugate. Including damping descriptions in finite element models can be achieved by specifying individual modal damping ratios ζ_i for each mode of vibration within the range of interest. These modal damping ratios can be sourced from experimental data from full-scale structures, which is the approach taken by design codes that list damping ratios for varying structure types.

One form of proportional damping involves the formation of the damping matrix via a linear combination of the mass and stiffness matrices;

$$\boldsymbol{C} = \alpha_0\boldsymbol{M} + \alpha_1\boldsymbol{K} \tag{4.21}$$

where α_0 and α_1 are constants. This type of proportional damping is known as Rayleigh damping [133], and it assumes the damping distribution over the structure matches the distribution of the mass and stiffness. Equating the orthogonality criteria in Equation (4.17) with the Rayleigh damping criteria in Equation (4.21), the damping ratios in the proportional damping case are given by;

$$2\zeta_i\omega_i = \alpha_0 + \alpha_1\omega_i^2 \tag{4.22}$$

which simplifies to

$$\zeta_i = \frac{1}{2}\left(\frac{\alpha_0}{\omega_i} + \alpha_1\omega_i\right) \tag{4.23}$$

The constants α_0 and α_1 can be determined by using damping ratio values at two frequencies and solving two simultaneous equations based on the relationship in Equation (4.23), which yields;

$$\alpha_0 = \frac{2\omega_1\omega_2(\zeta_2\omega_1 - \zeta_1\omega_2)}{\omega_1^2 - \omega_2^2} \qquad \alpha_1 = \frac{2(\zeta_2\omega_1 - \zeta_1\omega_2)}{\omega_1^2 - \omega_2^2} \tag{4.24}$$

The frequencies are chosen such that they cover the upper and lower bounds of frequencies of interest in the design.

Rayleigh damping tends to underestimate the damping between the frequency range of interest, and overestimate the damping outside the range [28]. Therefore, to minimise errors when using the Rayleigh damping method, the chosen frequencies should be as close as possible to the upper and lower limits of the frequency range of interest. Alternatively, more rigorous methods of determining the proportional damping matrix that mitigate the limitation of the Rayleigh damping method are

available, such as Caughey damping [25] and Penzien-Wilson damping [185].

   Despite having no physical justification for its application, proportional damping is a reasonable approximation for cases with low levels of damping, such as those typically encountered on large civil engineering structures. Considering the difficulties associated with estimating the true structural damping mechanisms, the proportional damping assumption is considered sufficient for finite element models.

4.2.3   Damped Response with General Viscous Damping

The solution of Equation (4.6) is presented for the case where general viscous damping is included in the system. By assuming free vibration of the system, the force vector $\boldsymbol{p}(t)$ is set equal to zero, resulting in the homogeneous form of the damped vibration model,

$$\boldsymbol{M}\ddot{\boldsymbol{q}}(t) + \boldsymbol{C}\dot{\boldsymbol{q}}(t) + \boldsymbol{K}\boldsymbol{q}(t) = \boldsymbol{0} \tag{4.25}$$

By introducing $\boldsymbol{x}_1(t) = \boldsymbol{q}(t)$ and $\boldsymbol{x}_2(t) = \dot{\boldsymbol{q}}(t)$, Equation (4.25) can be written in terms of these new variables as follows:

$$\dot{\boldsymbol{x}}_1(t) = \boldsymbol{x}_2(t) \tag{4.26}$$
$$\dot{\boldsymbol{x}}_2(t) = -\boldsymbol{M}^{-1}\boldsymbol{C}\boldsymbol{x}_2(t) - \boldsymbol{M}^{-1}\boldsymbol{K}\boldsymbol{x}_1(t) \tag{4.27}$$

The second-order differential equation (4.25) can now be expressed as a pair of first-order differential equations for the two variables $\boldsymbol{x}_1(t)$ and $\boldsymbol{x}_2(t)$. Equations (4.26) and (4.27) can be written in matrix form by defining a state vector $\boldsymbol{x}(t) \in \mathbb{R}^{2n \times 1}$;

$$\boldsymbol{x}(t) = \begin{bmatrix} \boldsymbol{x}_1(t) \\ \boldsymbol{x}_2(t) \end{bmatrix} = \begin{bmatrix} \boldsymbol{q}(t) \\ \dot{\boldsymbol{q}}(t) \end{bmatrix} \tag{4.28}$$

Now the equations for the state variables can be written as a matrix differential equation:

$$\begin{bmatrix} \dot{\boldsymbol{x}}_1(t) \\ \dot{\boldsymbol{x}}_2(t) \end{bmatrix} = \begin{bmatrix} 0 & \boldsymbol{I} \\ -\boldsymbol{M}^{-1}\boldsymbol{K} & -\boldsymbol{M}^{-1}\boldsymbol{C} \end{bmatrix} \begin{bmatrix} \boldsymbol{x}_1(t) \\ \boldsymbol{x}_2(t) \end{bmatrix} \tag{4.29}$$

This equation can be abbreviated to the following form:

$$\dot{\boldsymbol{x}}(t) = \boldsymbol{A}_c\boldsymbol{x}(t) \tag{4.30}$$

The matrix $\boldsymbol{A}_c \in \mathbb{R}^{2n \times 2n}$ is known as the state matrix and contains the matrices $\boldsymbol{M}$, $\boldsymbol{C}$, and $\boldsymbol{K}$ as submatrices, and therefore provides a complete description of the system. The subscript c denotes this matrix as a continuous-time version, as opposed to the discrete-time version of the matrix which is introduced in Section 4.4.3.

As for the undamped case and the proportional damping case, it is assumed a solution for Equation (4.30) has the form,

$$\boldsymbol{x}_i(t) = \boldsymbol{\psi}_i e^{j\omega_i t} \tag{4.31}$$

Substituting Equation (4.31), and its first derivative, into Equation (4.30) yields,

$$j\omega_i \boldsymbol{\psi}_i e^{j\omega_i t} = \boldsymbol{A}_c \boldsymbol{\psi}_i e^{j\omega_i t} \tag{4.32}$$

Since $e^{j\omega_i t} \neq 0$ for all values of t, $\boldsymbol{\psi}_i$ and ω_i must satisfy the equation,

$$\lambda_i \boldsymbol{\psi}_i = \boldsymbol{A}_c \boldsymbol{\psi}_i \tag{4.33}$$

where $\lambda_i = j\omega_i$. Equation (4.33) represents a generalised eigenvalue problem of dimension $2n \times 2n$ [74], where $\lambda_i \in \mathbb{C}^{2n}$ are the eigenvalues and $\boldsymbol{\psi}_i \in \mathbb{C}^{2n}$ ($i = 1, \ldots, 2n$) are the eigenvectors. Note that unlike the undamped case and proportional damping case, the eigenvectors for the general viscous damping case are complex values — hence the reason for denoting the complex eigenvectors with alternative notation ($\boldsymbol{\psi}_i$). This results in complex valued physical mode shapes, which appear in complex conjugate pairs referred to as complex modes. The interpretation of the complex modes, as opposed to real modes, is that each degree of freedom reports the magnitude and phase of the motion experienced, relative to the other degrees of freedom. The real and imaginary parts of a complex mode correspond to the magnitude and phase of the motion respectively.

Similar to the proportional damping case, the complex eigenvalues are determined as complex conjugate pairs in the form;

$$\lambda_i, \lambda_i^* = -\zeta_i \omega_i \pm \omega_i \sqrt{1 - \zeta_i^2} j \tag{4.34}$$

Solving the eigenvalue problem of Equation (4.33) for the state matrix $\boldsymbol{A}_c$ produces a set of complex numbers of the form $\lambda_i = \alpha_i + j\beta_i$, where $\alpha_i = \text{Re}(\lambda_i)$ and $\beta_i = \text{Im}(\lambda_i)$. The natural frequency and damping ratios can be obtained by comparing these expressions with Equation (4.34);

$$\omega_i = \sqrt{\alpha_i{}^2 + \beta_i{}^2} = \sqrt{\text{Re}(\lambda_i)^2 + \text{Im}(\lambda_i)^2} = |\lambda_i| \tag{4.35}$$

$$\zeta_i = \frac{-\alpha_i}{\sqrt{\alpha_i{}^2 + \beta_i{}^2}} = \frac{-\text{Re}(\lambda_i)}{\sqrt{\text{Re}(\lambda_i)^2 + \text{Im}(\lambda_i)^2}} = \frac{-\text{Re}(\lambda_i)}{|\lambda_i|} \tag{4.36}$$

4.3 Frequency Domain System Identification

The system identification technique discussed in subsequent sections uses a non-parametric frequency domain method to estimate modal parameters. The peak picking method is initially discussed to introduce simple frequency domain system identification, and to provide the foundation upon which the applied technique is based.

4.3.1 Peak Picking

The peak picking technique is arguably one of the simplest and least computationally intensive methods for operational modal analysis of civil engineering structures. As described by Bendat and Piersol [6], for a lightly damped structure, the output response spectrum at any point will reach a maximum value at frequencies where either the input excitation spectrum displays a significant peak, or where the frequency response function of the structure peaks. Therefore, peaks identified in the output response spectra can be considered to originate from input excitation peaks or vibration modes of the structure.

Distinguishing structural vibration modes from input excitation peaks is achieved via interrogation of the phase angles of cross spectra between measurement points. For structural modes, the phase angles between measurement points will be either $0°$, in phase, or $180°$ out of phase. Also, if the input source is random excitation, it is inconceivable that any peaks will be due to excitation sources. The coherence function between two output channels can also be used to highlight structural modes, because at resonance frequencies the high signal-to-noise ratio means the coherence function tends to one.

The peak picking technique identifies operational deflection shapes, as opposed to mode shapes, via the magnitudes of the output spectra. Operational deflection shapes define the excitation of the structure when the input excitation is a pure harmonic, and will be a superposition of multiple modes if the modes of vibration are closely spaced. The phase angles from cross spectra are used to determine the nature of the operational deflection shapes — translational, torsional, or coupled motion as well as higher order modes of vibration. The damping value can be determined using the half-power bandwidth method [142, 148], however despite recent advances in this method [189], the presence of closely spaced vibration modes causes large errors in half-power bandwidth damping estimates.

4.3.2 Frequency Domain Decomposition

The FDD technique [11, 14] is a non-parametric frequency domain system identification technique that uses operational modal analysis concepts to determine modal

parameters. The main concept of the technique was previously applied to the analysis of structures using ambient vibrations as the input excitation [131]. The method was then applied to frequency response functions (FRF) to more accurately determine the number of modes in measured data, and became known as the Complex Mode Indication Function (CMIF) [2]. The CMIF is capable of identifying modal parameters from FRFs [143].

The FDD method can be illustrated by first considering that a physical response can be expressed in modal coordinates [12];

$$\boldsymbol{y}(t) = \boldsymbol{\phi}_1 q_1(t) + \cdots + \boldsymbol{\phi}_i q_i(t) = \boldsymbol{\Phi}\boldsymbol{q}(t) \tag{4.37}$$

The covariance matrix of the responses is given by the following;

$$\boldsymbol{C}_{yy}(\tau) = \mathrm{E}\left[\boldsymbol{y}(t+\tau)\boldsymbol{y}(t)^T\right] \tag{4.38}$$

Substituting Equation (4.37) into (4.38);

$$\boldsymbol{C}_{yy}(\tau) = \mathrm{E}\left[\boldsymbol{\Phi}\boldsymbol{q}(t+\tau)\boldsymbol{q}(t)^H\boldsymbol{\Phi}^H\right] \tag{4.39}$$

$$= \boldsymbol{\Phi}\boldsymbol{C}_{qq}(\tau)\boldsymbol{\Phi}^H \tag{4.40}$$

and applying the Fourier transform gives the following relationship;

$$\boldsymbol{G}_{yy}(\omega) = \boldsymbol{\Phi}\boldsymbol{G}_{qq}(\omega)\boldsymbol{\Phi}^H \tag{4.41}$$

where $\boldsymbol{G}_{yy}(\omega)$ is the response spectrum matrix and $\boldsymbol{G}_{qq}(\omega)$ is the modal coordinates spectrum matrix. Now consider the singular value decomposition (SVD) [103] of the response spectrum matrix, which is assumed to be a Hermitian matrix ($\boldsymbol{G}_{yy} = \boldsymbol{G}_{yy}^H$), at each frequency and for each response measurement;

$$\boldsymbol{G}_{yy}(\omega) = \boldsymbol{U}(\omega)\boldsymbol{S}\boldsymbol{U}(\omega)^H \tag{4.42}$$

where $\boldsymbol{U}(\omega)$ is an orthonormal matrix ($\boldsymbol{U}\boldsymbol{U}^H = I$) containing the singular vectors of $\boldsymbol{G}_{yy}(\omega)$, and $\boldsymbol{S}$ is a diagonal matrix containing the corresponding singular values.

The form of Equation (4.42) is identical to Equation (4.41), which indicates the following: firstly, the singular vectors from the SVD of the response spectrum matrix can be associated with the mode shapes; secondly, the singular values represent the spectra of single degree of freedom systems that have the same modal parameters as the vibration modes that contribute to the response of the multi degree of freedom system being analysed. In other words, the response spectrum matrix of a multi degree of freedom system is decomposed into equivalent single degree of freedom systems via the SVD of the response spectrum matrix. Therefore, the singular val-

ues represent the response of each vibration mode expressed as the spectrum of each modal coordinate. The links between Equations (4.41) and (4.42) assume that the response spectrum matrix $\boldsymbol{G}_{qq}(\omega)$ is a diagonal matrix, meaning the modal coordinates are uncorrelated, and the mode shapes (the columns in $\boldsymbol{\Phi}$) are orthogonal.

4.3.3 Modal Parameter Extraction

The initial step in FDD is to estimate the response spectrum matrix. This matrix is composed of the cross-spectral densities between the measured channels. The cross-spectral densities between all channels can be used to form the response spectrum matrix, which essentially means that each measurement channel is a reference channel. For cases with a large number of simultaneously measured channels, this can result in excessive noise contamination in the singular value plot, which reduces the accuracy of modal parameter estimates. This occurs because many channels will contain similar information regarding the vibration modes of the system, but the random errors originating from noise will differ between channels.

Reducing the noise can be achieved by reducing the number of channels used in the estimation process. Those channels selected for the estimation process must collectively contain all the information necessary to describe the vibration modes of interest. A suitable set of channels can be selected by observing the correlation coefficients between the channels [56]. The channel that has the highest correlation with all other channels is initially selected as a reference. compared with the other channels, this channel will generally contain the most information regarding the system. Depending on the tested system, multiple reference channels may be required.

Selecting non-reference channels is also achieved via inspection of the correlation coefficients between the channels, accept the correlations between reference and non-reference channels are minimised to ensure each channel brings a maximum amount of new information to the estimation process. This step requires minimum threshold correlation values to avoid selecting channels that contain only noise. The total number of channels selected will determine the ability to separate closely spaced modes. For two closely spaced modes, a total of three channels is required — two channels to separate the modes and a third channel to account for measurement noise.

The method used to create the cross-spectral densities is also important to the estimation process. A common method is the Cooley-Tukey algorithm for computing the discrete Fourier transform [32] to determine the periodogram of the input signal. When applying the algorithm, the most important considerations are the minimisation of spectral leakage and noise when transforming the measurement data from the time domain to the frequency domain. Spectral leakage occurs when trans-

forming finite length signals from the time domain to the frequency domain, and results in energy from a particular frequency band being incorrectly represented in adjacent frequency bands. The reason for the leaking of energy from one frequency band to those adjacent is that the transformation process — the discrete Fourier transform — assumes the finite length signal is periodic within the sample record length. Maintaining periodicity across all frequencies in a complex signal is difficult to achieve, resulting in some or all signals being abruptly truncated midway through a cycle.

The effect of spectral leakage in frequency domain system identification manifests as a broadening of the spectral peaks. This has implications for the identification of peaks, particularly for closely spaced modes, and for the estimation of damping. In the case of damping estimates, the broadening of spectral peaks due to leakage will result in overestimation of damping. Spectral leakage can be mitigated by applying a window function to the input signal, which forces the signal to be zero outside the sampling period and therefore reduces the effect of abrupt truncations of periodicity. Furthermore, the error caused by leakage is proportional to the square of the frequency resolution [5], which means increasing the frequency resolution will reduce spectral leakage errors.

Minimising noise variance in the spectral densities can be achieved via splitting the input signal into multiple data segments of equal length, then applying the discrete Fourier transform to each segment, and finally the periodograms for each segment are averaged. The Welch averaged modified periodogram method [184] of spectral estimation implements the averaging of segment spectral densities, with the addition of segment overlapping, and also includes a window function discussed previously. It is important to note that attempting to simultaneously minimise spectral leakage and noise presents a compromise. Increasing the number of data samples in each segment, which simultaneously decreases the number of averages, will reduce the effect of leakage and provide improved spectral resolution. However, the decrease in the number of averages will increase the noise and hence the stochastic uncertainty of damping estimates. This aspect needs to be considered when determining the amount of data to be collected to avoid compromising either segment size or number of averages when using the Welch method to estimate the cross-spectral densities.

The next step in FDD is the decomposition of the estimated response spectrum matrix by applying the SVD as described in Equation (4.42). The singular values are returned from the SVD in ascending order. For each value of frequency ω, the first singular value is an ordinate of the spectrum associated with the dominant vibration mode at that frequency. For a particular frequency, the number of non-zero singular values indicates the rank of the spectrum matrix, and therefore the

number of modes contributing to the system response at that particular frequency. If a single vibration mode is dominating at a particular resonance frequency, the spectrum matrix will have a rank of one, and the first singular vector is an estimate of the mode shape at that particular frequency. In the case of multiple modes dominating at a resonance frequency, the singular vectors corresponding to non-zero singular values are estimates of the mode shape, if the mode shapes are orthogonal.

By applying the SVD to the response spectrum matrix, this matrix is decomposed into single degree of freedom systems, which enables the application of single degree of freedom modal parameter estimation techniques. The task now is to both identify and define the extent of the spectral peaks belonging to modes of vibration. Vibration modes are represented by peaks in the plot of singular values versus frequency, but not all peaks necessarily indicate vibration modes. Peaks in the singular value plot can be due to noise as well as the cross singular value effect. The cross singular value effect occurs when two modes have equal contribution at a particular frequency, which causes the higher singular value curve to dip, while the lower singular value curve peaks. The peak in this case is not due to a vibration mode.

Identifying and defining the extent of the peak can be achieved by comparing the singular vector for the corresponding peak in the singular value plot with those in the immediate vicinity. If the spectral peak represents a vibration mode, then the singular vectors for points adjacent to the peak will be similar to the singular vector for the corresponding peak singular value. Peaks that do not represent structural modes will not display similarity between the singular vector for the peak and the adjacent singular vectors. The degree of similarity between the singular vectors can be determined using the modal assurance criteria (MAC) [1], which measures the degree of consistency between two modal vectors, and is given by;

$$\text{MAC} = \frac{|\phi_a{}^H \phi_b|^2}{(\phi_a{}^H \phi_a)(\phi_b{}^H \phi_b)} \tag{4.43}$$

The MAC ranges in value from zero, representing no consistency, to one, representing consistent correspondence. Therefore, if the two modal vectors considered have a linear relationship, the MAC value will approach unity.

When the spectral peaks for single degree of freedom modes of vibration are defined, a number of techniques can be applied to extract the modal parameters: either frequency domain or time domain based. A frequency domain example is the process of fitting a parametric model to the spectral peak [52]. Alternatively, the spectrum segment that corresponds to the single degree of freedom mode of vibration can be transferred to the time domain using an inverse discrete Fourier transform [13, 56]. Before applying the inverse Fourier transform, the singular values that do not form part of the spectral peak are set to zero.

After transitioning to the time domain, a plot of the resulting signal versus time will represent the auto correlation function of the single degree of freedom system. The natural frequency estimate is attained from a zero crossing analysis, and damping ratio estimates are attained by applying the logarithmic decrement [74]. The logarithmic decrement is described in Figure 4.2 and the following equation;

$$\zeta = \frac{\delta}{\sqrt{(2\pi n)^2 + \delta^2}}; \qquad \delta = \ln\left(\frac{y_1}{y_2}\right) \tag{4.44}$$

where δ is known as the logarithmic decrement. The technique can be applied to multiple peaks in the decay trace via a linear least squares fit of the natural logarithm of the peaks. When applying the linear least squares fit, it is appropriate to assume that the measurement noise is uncorrelated between observed values of the dependent variable. Therefore, the error in the damping estimation can be determined via the standard error of the regression line slope;

$$s_m = \sqrt{\frac{\frac{1}{n-2}\sum_{i=1}^{n}(y_i - \hat{y}_i)^2}{\sum_{i=1}^{n}(x_i - \bar{x})^2}} \tag{4.45}$$

where n is the number of observations, y_i is the dependent variable, $\hat{y}_1$ is the estimate of the dependent variable, x_i is the observed value of the independent variable, and $\bar{x}$ is the mean value of x_i.

Alternatively, the damping can be estimated by fitting the exponential function $y = Ae^{bt}$ to the peaks of the auto correlation function. Since the expression for the auto correlation function of a viscously damped single degree of freedom system is given by $y = Ae^{-\zeta\omega_n t}\sin(\omega_d t + \theta)$, the damping value can be extracted from the parameters of the fitted function via the relationship $b = -\zeta\omega_n$, noting that $\omega_n = 2\pi f_n$ is the natural frequency.

Example: Frequency Domain Decomposition

Using computer code developed in Matlab and the Signal Processing Toolbox R2007b [170], the FDD technique is applied to data obtained from measurements recorded approximately two years after construction completion of Latitude tower. At this time the wind induced monitoring system described in Section 3.5 was operational. The axes definition, and the location and orientation of the sensors, are presented in Figure 3.29. The acceleration response time series collected for this test is displayed in Figure 4.3. The mean wind speed for the time series is $10.2\,\text{m/s}$ and the mean wind direction is $250°$.

A plot of the singular values is presented in Figure 4.4. A segment size of 4096 was used to estimate the cross-spectral densities, which has been shown to be sufficient resolution to avoid impacting the damping ratio estimates [164]. In
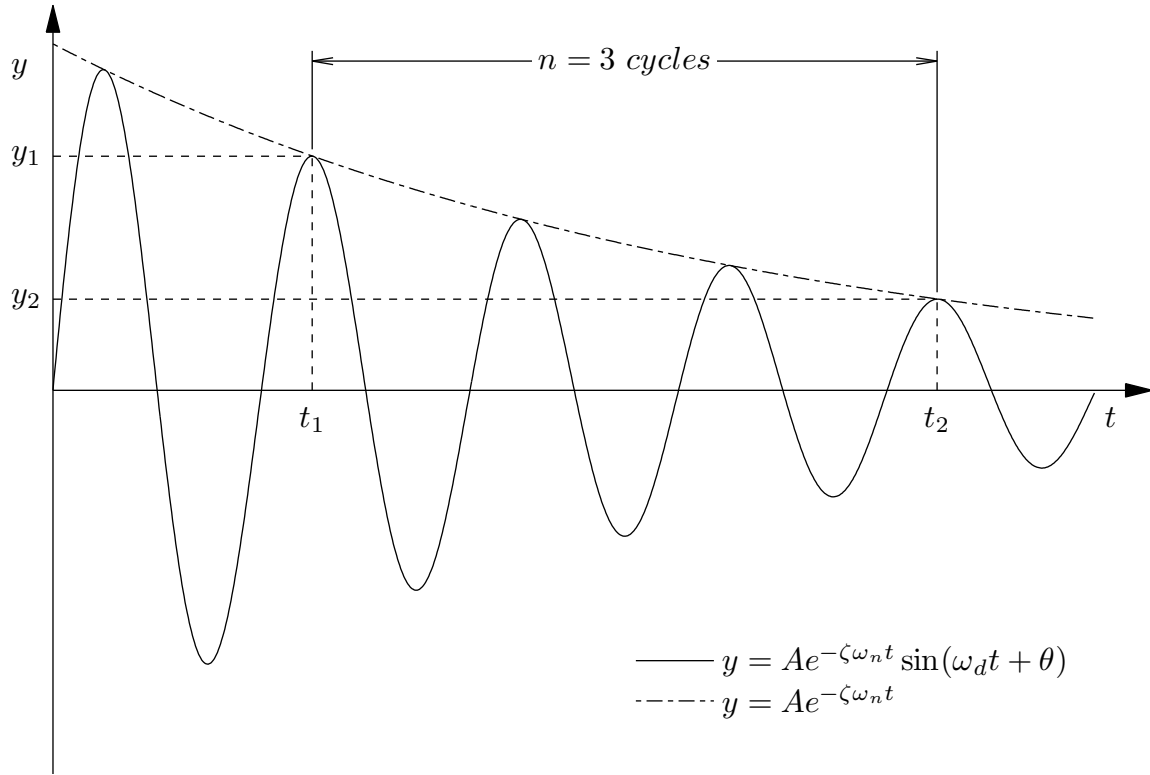
Figure 4.2: Logarithmic decrement of a viscously damped single degree of freedom system with $0 < \zeta < 1$

addition, a Hanning window function was applied to the segments to reduce leakage effects.

The first three peaks on the first singular value line in the frequency range 0.2–0.6 Hz correspond to the fundamental modes of vibration. In increasing order of natural frequency, these modes correspond to fundamental y-axis translation, x-axis translation, and torsion. The second modes of vibration are observed between the frequencies 0.8–1.2 Hz, and correspond to x-axis translation, y-axis translation, and torsion. Estimates for the natural frequency and damping ratio for these modes are displayed in Table 4.1, and the mode shapes are displayed in Figure 4.7.

The first and second x-axis mode shapes are a combination of translation and torsion. The torsional component is due to an eccentricity between mass and stiffness, caused by the floor plates extending away from the central core at the southern facade between levels 20 and above, which is evident in the comparison of the general floor arrangements in Figures 3.4 and 3.5. The second y-axis mode displays a significant torsional component. Above level 37 the eastern portion of the core terminates, which can be seen by comparing the core plans in Figures 3.11 and 3.12. This creates an eccentricity between mass and stiffness at this level and above, which is the cause of the torsional aspect in the mode shape at level 54.

Another peak is also observed in the singular value plot in Figure 4.4, and is

located on the second singular value line between the first and second peaks on the first singular value line. This peak is due to the cross singular value effect, since another smaller peak is observed to the left of the second mode peak. Analysis of the singular vector for this peak showed weak correlation with the adjacent frequency lines, and the mode shape was a superposition of the mode shapes for the first and second modes of vibration. Therefore, the presence of this peak in the singular value plot at the frequency 0.286 Hz is likely due to modal interference between the first and second modes of vibration.

The portion of the first singular value line displayed as a thick black line is the identified single degree of freedom spectral peak for the fundamental y-axis translation mode. This peak was identified by comparing the singular vector at the peak with those at adjacent frequency lines using the MAC method. A threshold of 0.8 was used for the MAC value acceptance criteria.

Spectral ordinates that do not form part of the identified peak are set to zero prior to converting the spectrum to the time domain using an inverse Fourier transform. The resulting auto-correlation function is displayed in Figure 4.5, which is normalised using the maximum value of the ordinate. An estimate of the decay envelope for a portion of the curve is also displayed.

A clearer picture of the auto-correlation envelope is presented in Figure 4.6, which plots the natural logarithm of the peaks from the normalised auto-correlation function. Both the positive and negative peaks are plotted. For a viscously damped linear system, this plot will be a straight line. Nominal correlation limits for modal parameter extraction are included, and they correspond to upper and lower bounds of 0.95 and 0.30 respectively. Broadband noise or non-linearities in the viscous damping can influence the initial and final time lags of the auto-correlation function, hence the reason for the maximum and minimum correlation threshold. It is important to estimate the model parameters, and particularly the damping ratio, from the linear portion of the plot. The minimum correlation threshold serves two purposes: firstly to reduce the impact of noise, which becomes more pronounced at higher time lags, and to avoid estimation uncertainty associated with large time lags. For this example, the plot is non-linear over the first 40 s, which extends below the nominal threshold limit and should not be used in the estimation process. Therefore, the logarithmic decrement technique was applied over the correlation values of approximately 0.7 to 0.3.

The acceleration values reported in Table 4.1 are the expected peak accelerations. These values were determined via an upcrossing analysis of the time series data with a probability of exceedance of 0.01. The upcrossing analysis theory is presented in Section 2.5.3.
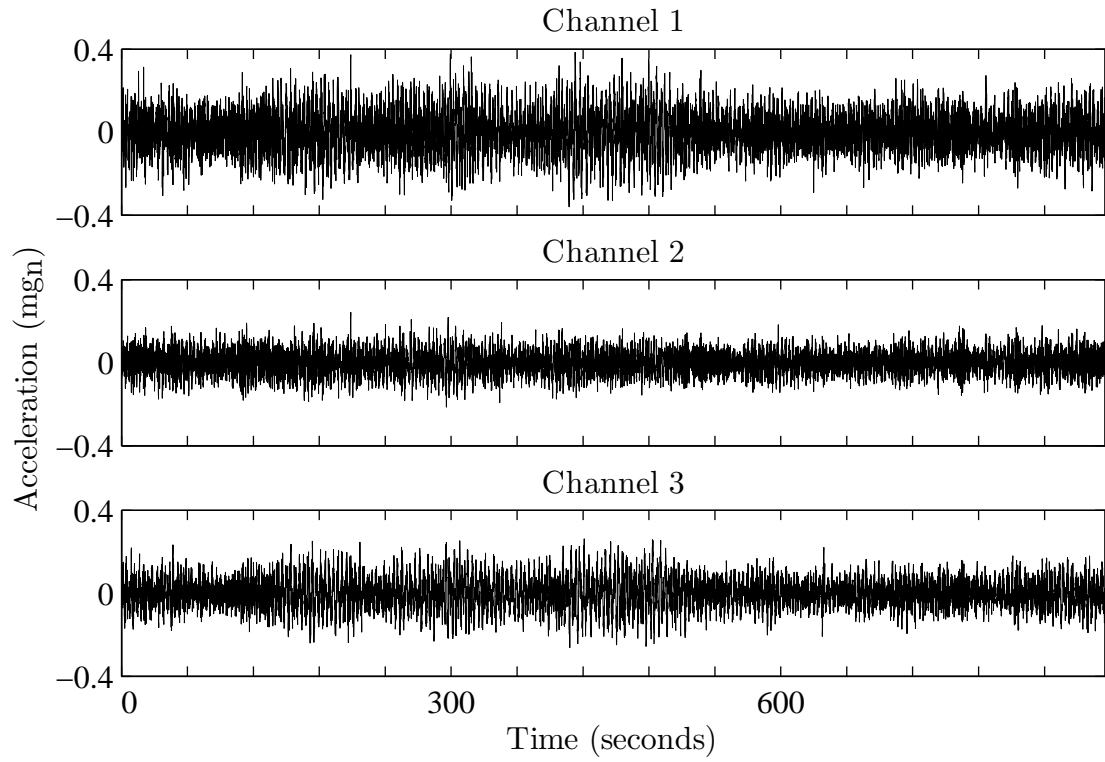
Figure 4.3: Acceleration response signals from Latitude tower. Referring to Figure 3.29, Channel 1 = $\ddot{y}_1$, Channel 2 = $\ddot{x}_1$, and Channel 3 = $\ddot{y}_2$
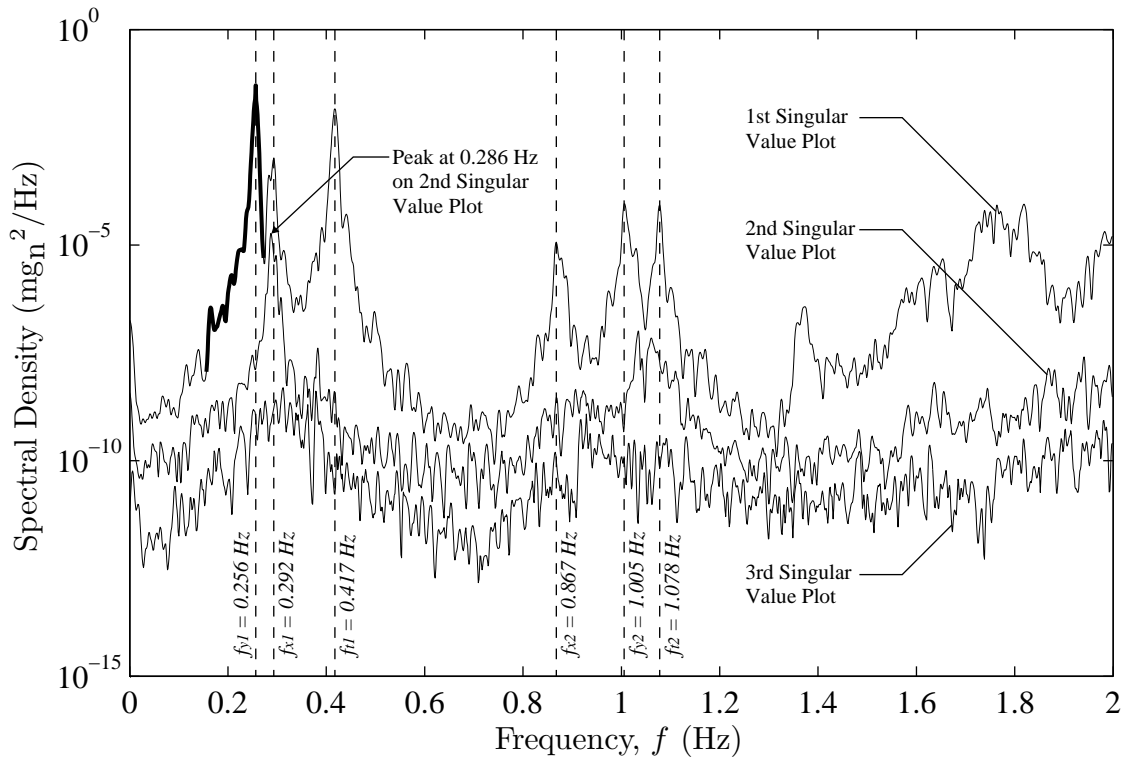
Figure 4.4: Singular value plot for acceleration responses displayed in Figure 4.3.
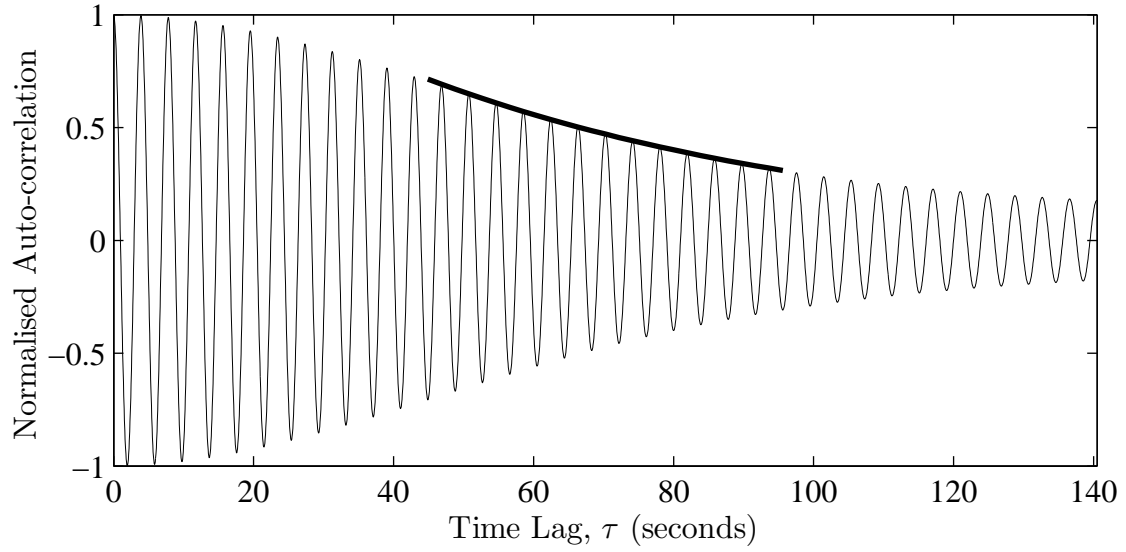
Figure 4.5: Normalised auto-correlation function with logarithmic decrement estimation.
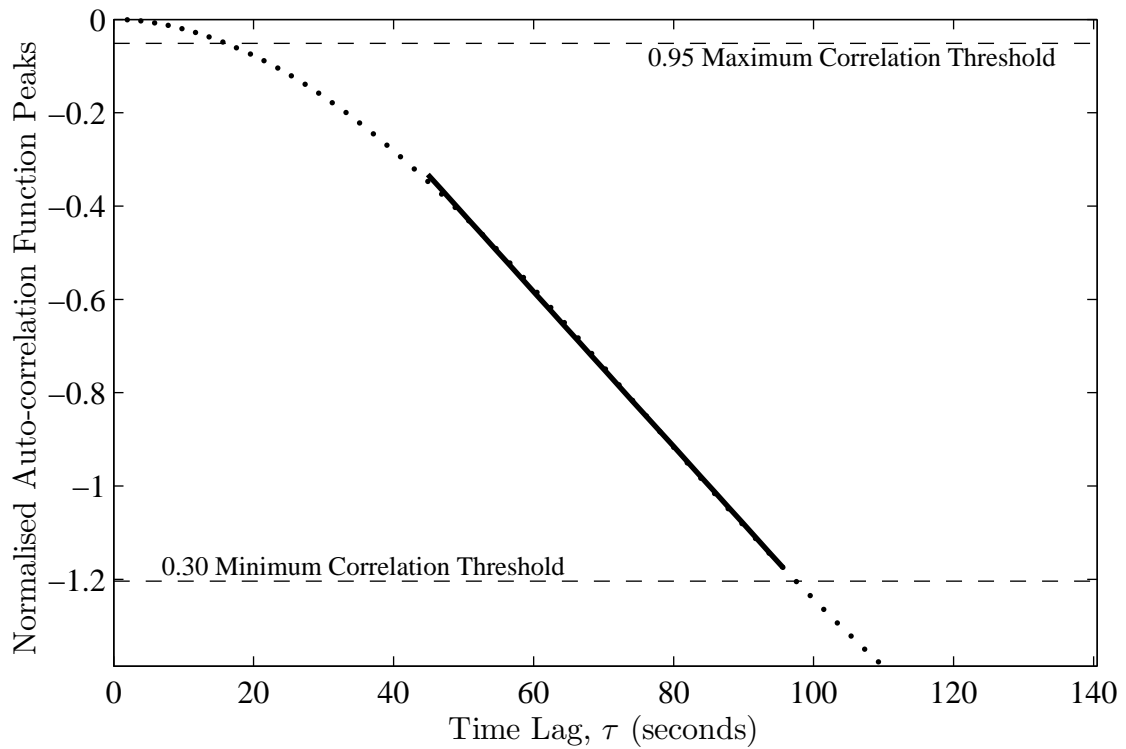
Figure 4.6: Natural logarithm of the peaks of the normalised auto-correlation function with logarithmic decrement estimate. Modal parameter estimates: $f_{y1} = 0.256$Hz, $\zeta = 1.03\%$.

X1: $f_{x1} = 0.292$ Hz

X2: $f_{x2} = 0.867$ Hz

Y1: $f_{y1} = 0.256$ Hz

Y2: $f_{y2} = 1.005$ Hz

T1: $f_{t1} = 0.417$ Hz

T2: $f_{t2} = 1.078$ Hz
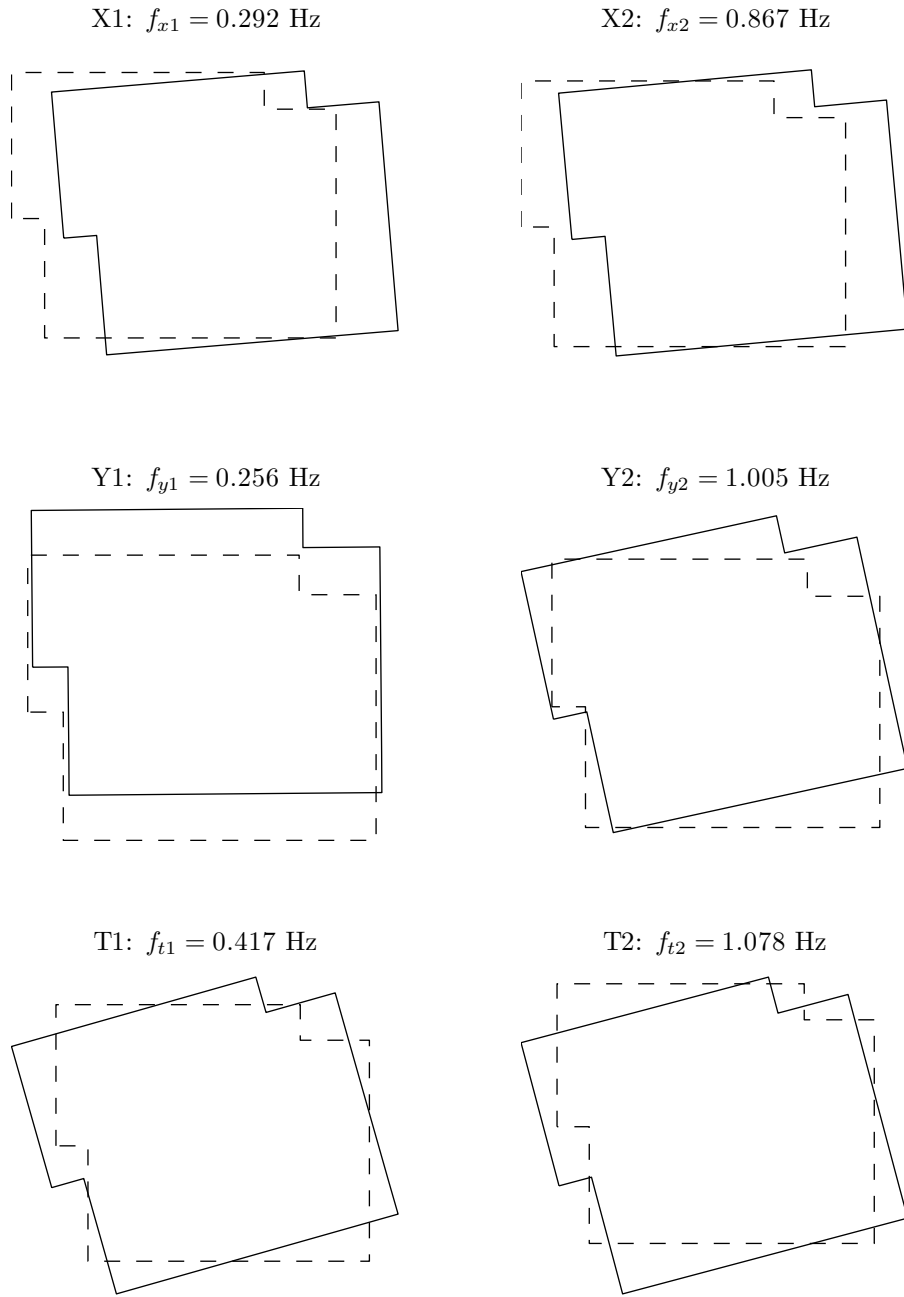
Figure 4.7: Plan view mode shapes at level 54 for the first six modes of vibration.

	f (Hz)	ζ (%)	σ_ζ (%)	$\ddot{q}_{max}$ (mg$_n$)
Translation X1	0.292	0.86	8.1	0.07
Translation Y1	0.256	1.03	6.5	0.13
Torsion T1	0.417	0.80	5.7	0.15
Translation X2	0.867	0.83	3.6	–
Translation Y2	1.005	0.43	4.7	–
Torsion T2	1.078	0.39	2.6	–

Table 4.1: Results for FDD frequency domain system identification.

4.4 Time Domain System Identification

The frequency domain system identification technique discussed in the previous section formulates the analysis of dynamic structural systems by viewing physical variables as outputs or responses to specified inputs. Another analysis approach is to formulate the dynamics of the structural system in terms of variables that describe the current state of the system. This approach is known as state space system modelling.

In essence, the state space approach converts an nth-order differential equation into a set of n first-order differential equations. Unlike nth-order differential equations, the set of first order differential equations can be conveniently expressed in matrix form, which allows the application of efficient numerical techniques to determine the response of the system. Forming the system equations in matrix notation also brings scalability to the state space approach by offering a means to analyse the stability of higher order systems. The basis of state space modelling is now presented, much of which is derived from introductory material [26, 52].

4.4.1 Continuous State Space Vibration Models

By introducing $\boldsymbol{x}_1(t) = \boldsymbol{q}(t)$ and $\boldsymbol{x}_2(t) = \dot{\boldsymbol{q}}(t)$, where $\boldsymbol{x}_1(t)$ and $\boldsymbol{x}_2(t)$ correspond to the displacement and velocity response vectors respectively, Equation (4.6) can be written in terms of these new variables as follows:

$$\dot{\boldsymbol{x}}_1(t) = \boldsymbol{x}_2(t) \tag{4.46}$$

$$\dot{\boldsymbol{x}}_2(t) = -\boldsymbol{M}^{-1}\boldsymbol{C}\boldsymbol{x}_2(t) - \boldsymbol{M}^{-1}\boldsymbol{K}\boldsymbol{x}_1(t) + \boldsymbol{M}^{-1}\boldsymbol{P}\boldsymbol{u}(t) \tag{4.47}$$

The original second-order differential equation (4.6) is now expressed as a pair of first-order differential equations for the two state variables $\boldsymbol{x}_1(t)$ and $\boldsymbol{x}_2(t)$. The term state variables is used because they completely describe the behaviour or state of the system. Equations (4.46) and (4.47) can be written in matrix form by defining a

state vector $\boldsymbol{x}(t) \in \mathbb{R}^{2n \times 1}$, which has two components representing the displacement and velocity response vectors:

$$\boldsymbol{x}(t) = \begin{bmatrix} \boldsymbol{x}_1(t) \\ \boldsymbol{x}_2(t) \end{bmatrix} = \begin{bmatrix} \boldsymbol{q}(t) \\ \dot{\boldsymbol{q}}(t) \end{bmatrix} \tag{4.48}$$

Now the equations for the state variables can be written as a matrix differential equation:

$$\begin{bmatrix} \dot{\boldsymbol{x}}_1(t) \\ \dot{\boldsymbol{x}}_2(t) \end{bmatrix} = \begin{bmatrix} \boldsymbol{0} & \boldsymbol{I} \\ -\boldsymbol{M}^{-1}\boldsymbol{K} & -\boldsymbol{M}^{-1}\boldsymbol{C} \end{bmatrix} \begin{bmatrix} \boldsymbol{x}_1(t) \\ \boldsymbol{x}_2(t) \end{bmatrix} + \begin{bmatrix} \boldsymbol{0} \\ \boldsymbol{M}^{-1}\boldsymbol{P} \end{bmatrix} \boldsymbol{u}(t) \tag{4.49}$$

This equation can be abbreviated to the following form:

$$\dot{\boldsymbol{x}}(t) = \boldsymbol{A}_c \boldsymbol{x}(t) + \boldsymbol{B}_c \boldsymbol{u}(t) \tag{4.50}$$

The matrix $\boldsymbol{A}_c \in \mathbb{R}^{2n \times 2n}$ is known as the state matrix, and contains all the information regarding the system and therefore provides a complete description of the system. The matrix $\boldsymbol{B}_c \in \mathbb{R}^{2n \times r}$ is the input matrix, and the vector $\boldsymbol{x}(t)$ is the state vector, as described in Equation (4.28). The subscript c in $\boldsymbol{A}_c$ and $\boldsymbol{B}_c$ denotes these matrices as continuous-time versions.

The response of the state space system is observed via an output vector $\boldsymbol{y}(t) \in \mathbb{R}^{l \times 1}$, which is also known as the observation vector. In practical applications, only a subset l of the total n degrees of freedom are measured during a vibration experiment. The measurement type and the particular process measured governs the output vector constituents, and for structural systems the measured responses are typically, but not restricted to, displacements, velocities, or accelerations. For the general case, the response $\boldsymbol{y}(t)$ can be considered as a linear combination of the measured displacements, velocities, and accelerations;

$$\begin{aligned} \boldsymbol{y}(t) &= \boldsymbol{\xi}_d \boldsymbol{q}(t) + \boldsymbol{\xi}_v \dot{\boldsymbol{q}}(t) + \boldsymbol{\xi}_a \ddot{\boldsymbol{q}}(t) \\ &= \boldsymbol{\xi}_d \boldsymbol{x}_1(t) + \boldsymbol{\xi}_v \boldsymbol{x}_2(t) + \begin{bmatrix} \boldsymbol{0} & \boldsymbol{I} \end{bmatrix} \boldsymbol{\xi}_a (\boldsymbol{A}_c \boldsymbol{x}(t) + \boldsymbol{B}_c \boldsymbol{u}(t)) \\ &= \left[\begin{bmatrix} \boldsymbol{I} & \boldsymbol{0} \end{bmatrix} \boldsymbol{\xi}_d + \begin{bmatrix} \boldsymbol{0} & \boldsymbol{I} \end{bmatrix} (\boldsymbol{\xi}_v + \boldsymbol{\xi}_a \boldsymbol{A}_c) \right] \boldsymbol{x}(t) + \begin{bmatrix} \boldsymbol{0} & \boldsymbol{I} \end{bmatrix} \boldsymbol{\xi}_a \boldsymbol{B}_c \boldsymbol{u}(t) \\ &= \boldsymbol{C}_c \boldsymbol{x}(t) + \boldsymbol{D}_c \boldsymbol{u}(t) \end{aligned} \tag{4.51}$$

where $\boldsymbol{\xi}_d, \boldsymbol{\xi}_v, \boldsymbol{\xi}_a \in \mathbb{R}^{l \times 2n}$ are the output location matrices for displacement, velocity, and acceleration respectively. $\boldsymbol{C}_c \in \mathbb{R}^{l \times 2n}$ is the output matrix and $\boldsymbol{D}_c \in \mathbb{R}^{l \times r}$ is the direct transmission matrix. The second line of the above derivation is achieved via the substitution of Equation (4.50). The combination of the state space equa-

tion (4.50) and the observation equation (4.51) completely describes the input and output behaviour of the continuous-time structural system, and is known as the continuous time-invariant deterministic state space system. Continuous time means the expression can be evaluated at each time instant, and deterministic implies the exact measurement of input $\boldsymbol{u}(t)$ and output $\boldsymbol{y}(t)$ is possible.

$$\dot{\boldsymbol{x}}(t) = \boldsymbol{A}_c \boldsymbol{x}(t) + \boldsymbol{B}_c \boldsymbol{u}(t) \tag{4.52}$$

$$\boldsymbol{y}(t) = \boldsymbol{C}_c \boldsymbol{x}(t) + \boldsymbol{D}_c \boldsymbol{u}(t) \tag{4.53}$$

4.4.2 Stochastic State Space Vibration Models

The state space system equations (4.52) and (4.53) imply the output can be precisely calculated once the input is known. This is unrealistic in almost all cases as inevitably there are uncontrollable signals that also affect the system. Such signals are often referred to as a disturbance or noise. For state space systems, it is common practice to split the noise into contributions from measurement noise $\boldsymbol{\nu}(t) \in \mathbb{R}^{l \times 1}$ and process noise $\boldsymbol{w}(t) \in \mathbb{R}^{2n \times 1}$ acting on the states. Measurement noise is introduced during the output signal measurement, and includes sensor inaccuracies such as drift and noise. Process noise arises from uncontrollable inputs, where the system is subjected to signals that have the characteristics of inputs, but are not controllable by the user. In the case of structural systems, process noise can affect the structural parameters that describe the system, for example a change in structural stiffness due to uncontrollable temperature changes. Including the disturbance terms in the state space equations (4.52) and (4.53) produces;

$$\dot{\boldsymbol{x}}(t) = \boldsymbol{A}_c \boldsymbol{x}(t) + \boldsymbol{B}_c \boldsymbol{u}(t) + \boldsymbol{w}(t) \tag{4.54}$$

$$\boldsymbol{y}(t) = \boldsymbol{C}_c \boldsymbol{x}(t) + \boldsymbol{D}_c \boldsymbol{u}(t) + \boldsymbol{\nu}(t) \tag{4.55}$$

The disturbance terms $\boldsymbol{w}(t)$ and $\boldsymbol{\nu}(t)$ are unmeasurable and assumed to be zero-mean sequences of independent random variables (white noise) [113] that are uncorrelated with the input $\boldsymbol{u}(t)$, which implies;

$$E \begin{bmatrix} \boldsymbol{w}(t) \\ \boldsymbol{\nu}(t) \end{bmatrix} = \boldsymbol{0}, \ E \left[\begin{bmatrix} \boldsymbol{w}(t) \\ \boldsymbol{\nu}(t) \end{bmatrix} \begin{bmatrix} \boldsymbol{w}^T(t) & \boldsymbol{\nu}^T(t) \end{bmatrix} \right] = \begin{bmatrix} \boldsymbol{Q} & \boldsymbol{S} \\ \boldsymbol{S}^T & \boldsymbol{R} \end{bmatrix} \delta(t) \tag{4.56}$$

where E denotes the expected value and $\delta(t)$ is Dirac's delta function. $\boldsymbol{Q} \in \mathbb{R}^{2n \times 2n}$, $\boldsymbol{R} \in \mathbb{R}^{l \times l}$, and $\boldsymbol{S} \in \mathbb{R}^{2n \times l}$ are covariance matrices of the disturbance terms $\boldsymbol{w}(t)$ and $\boldsymbol{\nu}(t)$. By treating the noise terms as stochastic processes and including them in the state space equation (4.52) and observation equation (4.53), the resulting pair of equations (4.54) and (4.55) are known as the continuous-time stochastic state space

system equations.

4.4.3 Discrete Stochastic State Space Vibration Models

It is often easier to define a parameterized state space model in continuous-time because physical laws — in this case, Newtown's laws of motion — are most often described in terms of differential equations. In this case, the matrices $\boldsymbol{A}_c$, $\boldsymbol{B}_c$, $\boldsymbol{C}_c$, and $\boldsymbol{D}_c$ contain elements with physical significance, for example, material properties. In practice, the input and output vectors of dynamical systems are discrete time sampled series of the original continuous-time analogue signals — often termed a sampled data system. A discrete-time formulation of the state space system equations is required to comply with the input and output vector formats. The continuous-time formulation also implies that all degrees of freedom are measured, which is not the case in practice. Furthermore, the transformation of continuous differential equations into discrete difference equations provides a suitable basis for more efficient numerical computation to resolve the system responses. For these reasons, the continuous-time stochastic state space system will be converted to a more suitable form: the discrete-time stochastic state space system.

The discrete-time version of the stochastic state space system can be obtained by applying a zero-order hold [129] approximation for the input $\boldsymbol{u}(t)$;

$$\dot{\boldsymbol{x}}(kT + T) = \boldsymbol{A}_d\boldsymbol{x}(kT) + \boldsymbol{B}_d\boldsymbol{u}(kT) + \boldsymbol{w}(kT) \tag{4.57}$$

$$\boldsymbol{y}(kT) = \boldsymbol{C}_d\boldsymbol{x}(kT) + \boldsymbol{D}_d\boldsymbol{u}(kT) + \boldsymbol{\nu}(kT) \tag{4.58}$$

where $k = \left\{1, 2, 3, \ldots, n\right\}$, T is the sampling interval, $\boldsymbol{u}(kT)$ is the input at time instant kT, and $\boldsymbol{y}(kT)$ is the output at time instant kT. The subscript d is added to matrices $\boldsymbol{A}_d$, $\boldsymbol{B}_d$, $\boldsymbol{C}_d$, and $\boldsymbol{D}_d$ to signify them as discrete-time versions of the continuous-time state space matrices $\boldsymbol{A}_c$, $\boldsymbol{B}_c$, $\boldsymbol{C}_c$, and $\boldsymbol{D}_c$. The relationship between the discrete-time and continuous-time matrices is as follows:

$$\boldsymbol{A}_d = e^{\boldsymbol{A}_c T} \tag{4.59}$$

$$\boldsymbol{B}_d = \int_0^T e^{\boldsymbol{A}_c \tau} \boldsymbol{B}_c d\tau = \boldsymbol{A}_c^{-1}(\boldsymbol{A}_d - \boldsymbol{I})\boldsymbol{B}_c \tag{4.60}$$

The observation matrix $\boldsymbol{C}_c$ and the direct term $\boldsymbol{D}_c$ are unchanged by the sampling, therefore $\boldsymbol{C}_c = \boldsymbol{C}_d$ and $\boldsymbol{D}_c = \boldsymbol{D}_d$. As for the continuous-time case, the noise terms $\boldsymbol{w}(t)$ and $\boldsymbol{\nu}(t)$ are assumed to be sequences of independent random variables with

the following properties;

$$E\begin{bmatrix} \boldsymbol{w}(kT) \\ \boldsymbol{\nu}(t) \end{bmatrix} = \boldsymbol{0},\ E\left[\begin{bmatrix} \boldsymbol{w}(kT) \\ \boldsymbol{\nu}(kT) \end{bmatrix}\begin{bmatrix} \boldsymbol{w}^T(kT) & \boldsymbol{\nu}^T(kT) \end{bmatrix}\right] = \begin{bmatrix} \boldsymbol{Q}_d & \boldsymbol{S} \\ \boldsymbol{S}^T & \boldsymbol{R}_d \end{bmatrix}\delta(t-j)\ \ (4.61)$$

where $\delta(t-j)$ is Kronecker's delta function and,

$$\boldsymbol{Q}_d = \int_0^T e^{\boldsymbol{A}\tau}\boldsymbol{Q}e^{\boldsymbol{A}^T\tau}d\tau \tag{4.62}$$

$$\boldsymbol{R}_d = \boldsymbol{R} \tag{4.63}$$

The equations (4.57) and (4.58) include an input vector $\boldsymbol{u}(kT)$ and output vector $\boldsymbol{y}(kT)$. For large civil engineering structures that are excited by ambient loading, the input vector is difficult to record and is therefore often excluded during experimental testing. Since only the output vector is known, the input vector is omitted from the state space equations (4.57) and (4.58), and the unmeasured input is assumed to be white noise and implicitly modelled by the noise terms $\boldsymbol{w}(kT)$ and $\boldsymbol{\nu}(kT)$. The resulting state space system is as follows;

$$\dot{\boldsymbol{x}}(kT+T) = \boldsymbol{A}_d\boldsymbol{x}(kT) + \boldsymbol{w}(kT) \tag{4.64}$$

$$\boldsymbol{y}(kT) = \boldsymbol{C}_d\boldsymbol{x}(kT) + \boldsymbol{\nu}(kT) \tag{4.65}$$

The white noise assumption of the noise terms is an important requirement for the described system identification method. If the input $\boldsymbol{u}(kT)$ contains dominant frequency components in addition to white noise, then the white noise assumption becomes invalid. Consequently, these dominant frequency components will be included in the eigenfrequencies of the system and will appear as poles of the state matrix $\boldsymbol{A}_d$. This can cause the system identification results to become unclear or inaccurate due to the mixing of poles that represent the stochastic response of the system with spurious poles that represent the dominant frequencies originating from the input. Only those poles representing the stochastic response are of interest.

4.4.4 Identification of Stochastic State Space Models

The stochastic state space model described by Equations (4.64) and (4.65) can be solved using the Stochastic Subspace Identification (SSI) technique [127], which involves directly fitting a parametric model to the output time series data from the measurement transducers. Numerous algorithms that implement SSI are available, and one of the more recent algorithms is the Numerical Algorithm for Subspace State Space System Identification (abbreviated by the algorithum author to N4SID) [176]. The data-driven identification scheme used in the algorithm can provide

reliable state space models for complex, multivariable, dynamic systems using only the measured outputs.

Subspace system identification algorithms generally consist of two steps. The first step estimates the state vector $\boldsymbol{x}(kT)$ by using two linear algebra tools: QR decomposition and singular value decomposition (SVD) [113]. Once the states are known, the identification of the unknown matrices, $\boldsymbol{A}_d$ and $\boldsymbol{C}_d$, is achieved via a linear least-squares solution [95].

The modal parameters of the system are then determined via the standard eigenvalue problem;

$$\boldsymbol{A}_d = \boldsymbol{\Psi}\boldsymbol{\Lambda}\boldsymbol{\Psi}^{-1} \tag{4.66}$$

where $\boldsymbol{\Psi} \in \mathbb{C}^{2n \times 2n}$ are the discrete time eigenvectors arranged in columns and $\boldsymbol{\Lambda} = \left[\diagdown \mu_i^{-1} \diagdown \right] \in \mathbb{C}^{2n \times 2n}$ is a diagonal matrix containing the discrete time complex eigenvalues. For under-damped systems, the structural modes are represented by complex conjugate pairs of eigenvalues $(\mu_i, \mu_{i+1}{}^*)$ and corresponding eigenvectors. The complex conjugate pair of discrete time eigenvalues can be expressed as eigenfrequencies f_i and damping ratios ζ_i by first converting to continuous time eigenvalues $\lambda_i = \ln(\mu_i)/\Delta T$, and then using the expressions established in Equations (4.35) and (4.36), resulting in the following relationships [95];

$$f_i = \frac{|\lambda_i|}{2\pi} \quad , \qquad \zeta_i = \frac{-\mathrm{Re}(\lambda_i)}{|\lambda_i|} \tag{4.67}$$

The estimated state vector $\boldsymbol{x}(kT)$ does not generally correspond to a physical meaning. Therefore the eigenvectors $\boldsymbol{\Psi}$ of the state vector are converted to physical values by multiplying by the output matrix $\boldsymbol{C}_d$, and the mode shapes are given by;

$$\boldsymbol{\Phi} = \boldsymbol{C}_d\boldsymbol{\Psi} \tag{4.68}$$

Implementing the SSI technique requires determining the number of parameters in the model, which is an essential but challenging process. The number of parameters in the model is also referred to as the model order. This model order establishes the state space dimension — the dimensions of the state matrix $\boldsymbol{A}_d$. If the order chosen is too small, then the dynamics and noise characteristics of the system cannot be accurately modelled. Alternatively, selecting a model order that is too high can lead to significant uncertainties of the model parameters.

Obtaining an estimate of the order can be achieved by doubling the number of peaks in a frequency plot of a non-parametric spectrum-driven estimate, such as the peak picking technique or from the complex mode indication function. The number of peaks counted is doubled because each corresponds to a pair of complex conjugate eigenvalues, and therefore the model order is twice the number of resonance frequen-

cies observed in the spectral plot. In practice, the main focus is the extraction of modal parameters as opposed to finding the order that produces the best model. For this reason, the most suitable approach is to view model results generated from multiple orders that range from a theoretical minimum, such as doubling the number of resonance peaks, to an over-specified order.

Due to the presence of measurement noise and other non-white-noise sources typical to ambient vibration measurements, non-structural modes will be included in the results set for each model order. Numerous methods are available to discern structural from non-structural modes [128]. The stability plot [10] is one such method that compares modal properties for each identified mode at a certain model order with those obtained for the previous model order. If the modal property differences are within pre-set limits, the identified mode is deemed stable. The stability limits are set for the change in frequency Δf, change in damping ratios $\Delta \zeta$, and for the change in mode shape, which can be measured via the modal assurance criteria (MAC) described in Equation (4.43). The stability limits are defined as;

$$\frac{f_i(p) - f_i(p+1)}{f_i(p)} < \Delta f \tag{4.69}$$

$$\frac{\zeta_i(p) - \zeta_i(p+1)}{\zeta_i(p)} < \Delta \zeta \tag{4.70}$$

$$(1 - \mathrm{MAC}(p, p+1)) < \Delta \mathrm{MAC} \tag{4.71}$$

where p denotes the model order at which modal properties are identified. Using these comparisons and considering the nature of the noise processes, the identified non-structural modes will not show stability between consecutive model orders, and will be filtered from the identified modes.

Example: Stochastic Subspace Identification

Using computer code developed in Matlab and the System Identification Toolbox R2007b [169], the SSI technique is applied to data obtained from measurements recorded approximately two years after construction completion of Latitude tower. The response time histories are displayed as part of the FDD example in Figure 4.3. The stability limits are $\Delta f = 0.01$, $\Delta \zeta = 0.05$, and $\Delta \mathrm{MAC} = 0.99$. For this example the model order has been increased by two at each iteration to improve the legibility of the stability plot displayed in Figure 4.8. The average normalised power spectral density of all input channels is also displayed as a guide to the stability plot.

The points in the stability plot (denoted by ▲) indicate a stable mode of vibration according to the simultaneous application of the limits described in Section 4.4.4 for natural frequency, damping ratio, and mode shape. If any of the three criteria are not satisfied the identified mode is not considered to be stable and is
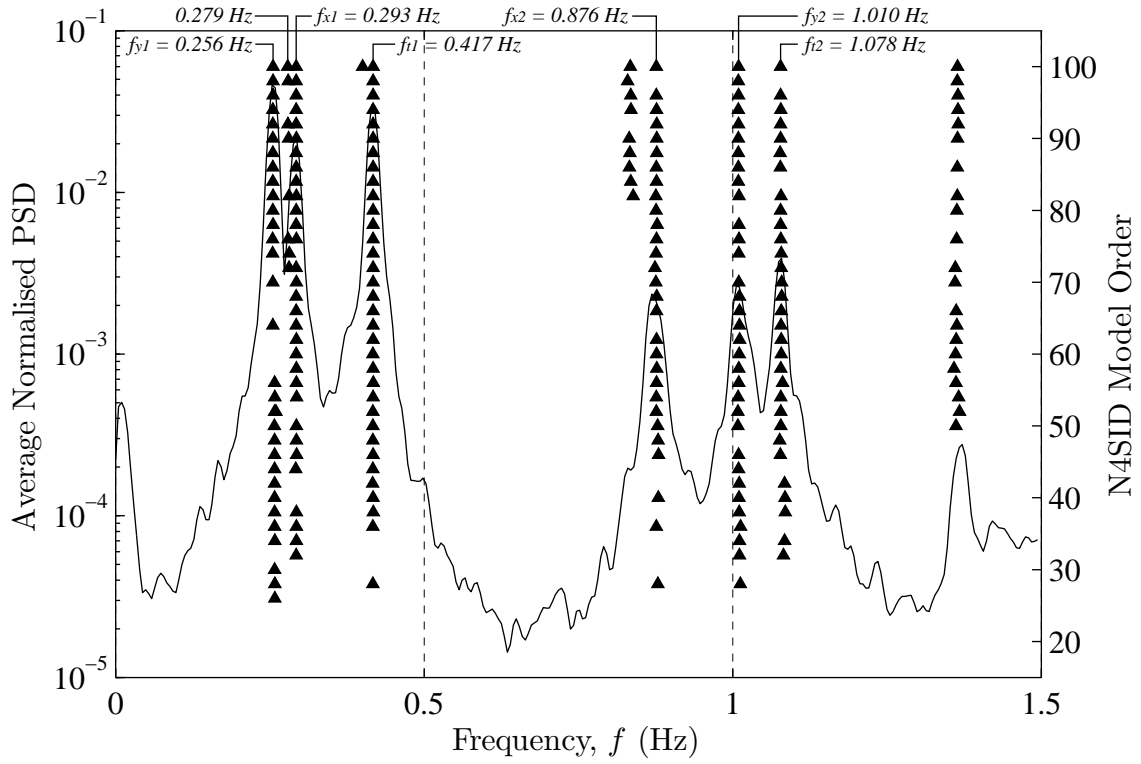
Figure 4.8: Stability plot for SSI time domain system identification. Stability limits: $\Delta f = 0.01$, $\Delta \zeta = 0.05$, and $\Delta\text{MAC} = 0.99$. (▲ Stable SSI Model, — Power Spectral Density)

not plotted. The first three modes of vibration, between the frequencies $0.2\,\text{Hz}$ and $0.5\,\text{Hz}$, are observed in both the SSI output and the spectral plot. They represent the fundamental modes of vibration for y-axis translation, x-axis translation, and torsion. The modes identified between the frequencies $0.7\,\text{Hz}$ and $1.2\,\text{Hz}$ represent the second modes of vibration for x-axis translation, y-axis translation, and torsion. The natural frequency and damping ratio estimates for the first six modes of vibration are presented in Table 4.2. The standard deviation in the damping ratio estimate σ_ζ is reported as a percentage of the damping ratio. A comparison of the mode shapes for the SSI and FFD analysis produced a MAC value greater than 0.98 for all mode shapes, and therefore the mode shapes for the SSI are virtually identical to those displayed in Figure 4.7.

The stability plot in Figure 4.8 identifies three modes of vibration between $0.25\,\text{Hz}$ and $0.30\,\text{Hz}$ when the model order exceeds approximately 70. This additional mode has a natural frequency of $0.279\,\text{Hz}$, which is approximately equal to the FDD estimate of $0.286\,\text{Hz}$. The intermittent nature of the stable orders for this mode indicates weak stability. As concluded for the FDD analysis, this mode is due to modal interference between the fundamental y-axis translation mode at $f_{y1} = 0.256$ Hz and the fundamental x-axis translation mode at $f_{x1} = 0.293$ Hz.

	f (Hz)	ζ (%)	σ_ζ (%)	$\ddot{q}_{max}$ (mg$_n$)
Translation X1	0.293	0.94	10.3	0.07
Translation Y1	0.256	0.91	5.5	0.13
Torsion T1	0.417	1.02	3.3	0.15
Translation X2	0.876	0.83	4.8	–
Translation Y2	1.010	1.18	3.4	–
Torsion T2	1.078	0.92	3.3	–

Table 4.2: Results for SSI time domain system identification.

The SSI derived mode shape of this additional mode is a superposition of the these two fundamental modes. The estimates for the dynamic characteristics of the fundamental modes used the model orders above 70. By using these higher model orders, the results are less likely to be influenced by the presence of modal interference.

4.4.5 Random Decrement Technique

The Random Decrement (RD) technique is a time domain system identification technique that generates the free-response of a linear single degree of freedom system from ambient excitation forces. The basic idea of the RD technique is to average time segments extracted from a response measurement, with the time segments being selected according to a trigger condition. The technique was initially developed to determine the dynamic characteristics and in-service damage detection of aerospace structures from measured responses [31]. The technique has the ability to estimate the amplitude dependence of the natural frequency and damping ratio for a mode of vibration.

The concept of the RD technique is explained by considering the following. For a system excited by random input forces, the response at time $t_0 + t$ is composed of three parts: a step response of the structure from an initial displacement at t_0, an impulse response from an initial velocity at t_0, and a random response due to the applied load in the time interval t. By selecting segments from the response time history that begin with a specified displacement response amplitude, and then combining these segments via superposition, it is observed that as the number of segments increases, the random response part will tend to zero. Furthermore, the sign of the initial velocity is expected to vary randomly with time, resulting in a zero initial velocity. Since the impulse response and random response parts are zero, the remaining part is the step response from the initial displacement. The resulting curve from this process is known as the random decrement signature.

The concept of the RD technique is described in Figure 4.9. Mathematical proofs
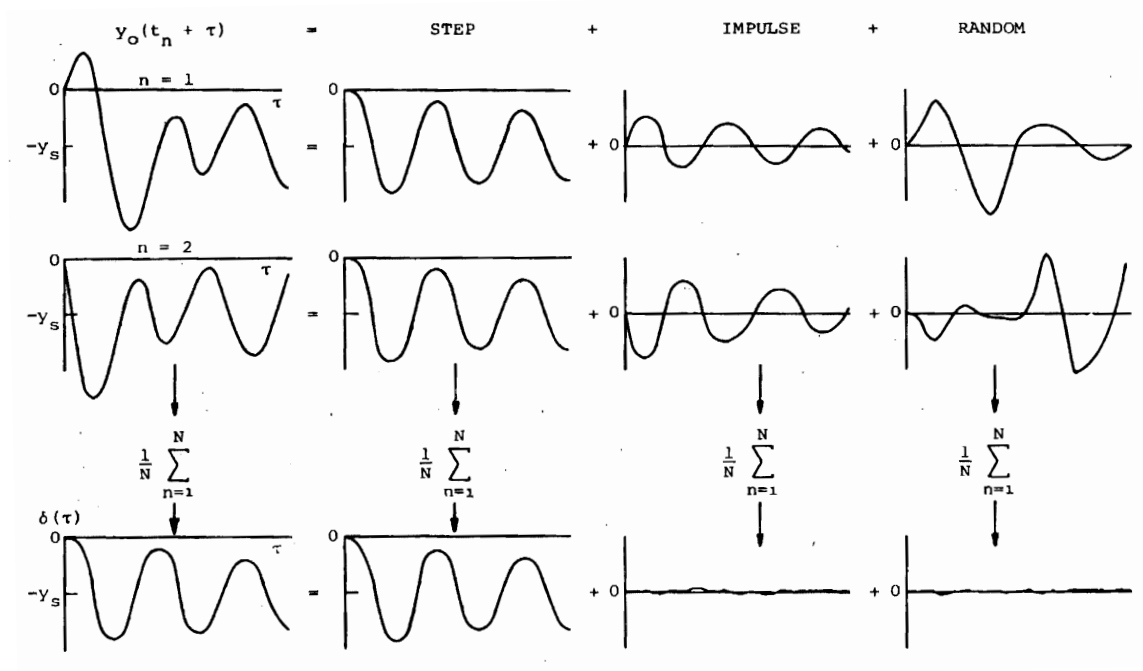
Figure 4.9: Random decrement technique (Source: Cole 1973 [31])

of the RD technique have been conducted [144, 177] to establish generalised models of the random decrement signature. The generalised models found the RD function to be proportional to the auto correlation function of an ergodic Gaussian distribution [177]. This proportionality between the RD function and the auto correlation function means the RD technique is directly comparable with spectral density functions, since the correlation functions are attained from the inverse Fourier transform of spectral density functions.

For a lightly damped structure excited by random input forces, such as wind loading, the step response represents the single degree of freedom free vibration trace that is produced when the structure is initially displaced by the distance used in the segment selection process described above, and allowed to decay back to a zero amplitude. The natural frequency and damping ratio of the system can be extracted from the decay trace using numerous techniques, such as the logarithmic decrement or curve fitting discussed in Section 4.3.3. The step response derived from an initial displacement has been used in the description of the RD technique, but any response type — displacement, velocity, acceleration — can be used with the technique.

An important aspect in the application of the RD technique is the trigger condition used to select the segments for averaging. Consider the RD signature defined by;

$$D_{xx}(\tau) = \mathrm{E}[x(t+\tau)|x(t) = a_r] \tag{4.72}$$

where $D_{xx}(\tau)$ is an estimate of the RD function over the time lag τ, and $\mathrm{E}[x|T_c]$ is the conditional expected value of x for the condition defined by T_c. Equation (4.72) represents the RD function estimate for a level crossing trigger condition, with the level being defined by the reference amplitude a_r. Assuming the response $x(t)$ is ergodic, the expected value is replaced with the time average to produce;

$$D_{xx}(\tau) = \frac{1}{N_s} \sum_{i=1}^{N_s} x(t_i + \tau)|x(t_i) = a_r \qquad (4.73)$$

where N_s is the number of segments used to generate the RD signature.

Another trigger condition is the use of peak amplitudes in the response time history, and is known as the Ranked Random Decrement [163].

$$D_{xx}(\tau) = \frac{1}{N_s} \sum_{i=1}^{N_s} x(t_i + \tau)|\dot{x}(t_i) = 0, x(t_i) = a_r \qquad (4.74)$$

Two conditions are specified in the ranked RD technique: $\dot{x}(t_i) = 0$ requires $x(t)$ to be a peak when the response is at the reference amplitude specified by $x(t_i) = a_r$. Since practical applications of the RD technique use discrete time sampled response data, the probability of $x(t_i) = a_r$ occurring in the time series is low without careful selection of the reference amplitude. Depending on the amount of response data available, this can lead to insufficient segments being selected, which can cause significant errors in the estimation of the dynamic characteristics. Therefore, a reference amplitude tolerance Δa_r is introduced to broaden the extents of the acceptance interval about the reference amplitude, and thereby increase the probability of trigger events occurring. The estimate of the RD function is given by;

$$D_{xx}(\tau) = \frac{1}{N_s} \sum_{i=1}^{N_s} x(t_i + \tau)|\dot{x}(t_i) = 0, x(t_i) \in [a_r \pm \Delta a_r] \qquad (4.75)$$

The ranked RD technique is described in Figure 4.10. The trigger condition defined by the ranked RD technique can be used to estimate the dynamic characteristics for a particular response amplitude. By generating multiple RD functions for incremental values of the reference amplitude, the amplitude dependence of the dynamic characteristics can be observed.

In addition to the selection of a suitable trigger condition, the practical implementation of the RD technique requires consideration for the following aspects:

- The response data used to generate the RD function must be for a single degree of freedom system. All structures have multiple modes of vibration, which means the vibration mode of interest must be isolated prior to applying the RD technique. This can be achieved with bandpass filtering the response data.
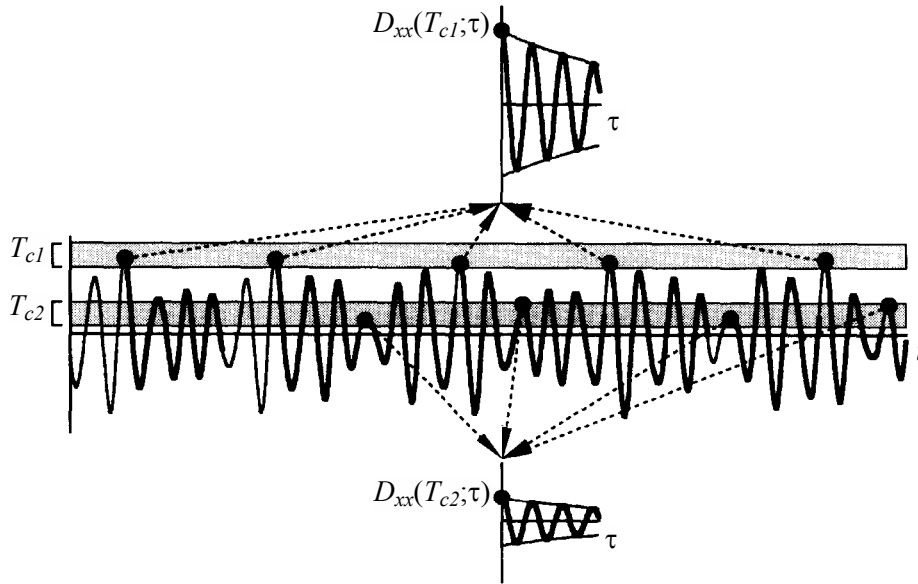
Figure 4.10: Ranked RD concept (Source: Tamura and Suganuma 1996 [163] with notation adjustments)

Careful selection of the upper and lower cut-off frequencies is required to ensure unwanted modes are removed, without altering the response information for the mode of interest.

- A suitable reference amplitude tolerance for the ranked RD technique is required to ensure sufficient segments are used to generate the RD function. As the amount of response data increases, the reference amplitude can decrease, because the reduced probability of detecting a peak in the narrower trigger range is offset by the increased quantity of response data, thereby maintaining the number of segments used. For a reduced quantity of response data, the reference amplitude tolerance must increase the number of segments detected, whilst not influencing the estimates of natural frequency and damping ratio. This is particularly important when using the RD function for investigating the amplitude dependence of the dynamic characteristics.

- Establishing a minimum threshold for the number of segments (N_s) used to generate the RD function is important for maintaining the accuracy of the natural frequencies and damping ratios. The estimation of the damping ratio is expected to be more sensitive to the number of segments used. Previous research has recommended the minimum number of segments to be 2000 [27, 163], although stability in the damping ratio estimates has been observed for as little as 200 segments [22, 90].

- The number of cycles (N_c) used to extract the dynamic characteristics from

the RD function is particularly important when investigating the amplitude dependence of the dynamic characteristics. The variance of the RD function increases with the number of cycles, which implies the first cycle is expected to provide a more accurate damping ratio estimate. However, the damping estimate errors using the first cycle is found to be high, and it has been recommended that improved results are obtained using five cycles [90]. This recommendation is in contrast to other research that has observed increasing overestimation of the damping ratio as the number of cycles increases [163]. Furthermore, there is the potential to dilute the amplitude dependent effects on the damping ratio estimates by increasing the number of cycles. This will introduce the latter parts of the RD function, which are not associated with the response amplitude of interest, to the estimation process.

As for the FDD and SSI techniques, the RD technique requires the measured response to be from a system excited by a Gaussian, white noise input force with zero mean. Furthermore, the system is assumed to have a single degree of freedom with linear, or small non-linear behaviour [73]. compared with FDD and SSI techniques, the RD technique is less complex to implement since only three relatively simple steps are performed: detection of trigger points, extraction of the time history segments, and averaging of the time history segments. However, the RD technique requires large quantities of data in order to achieve satisfactory estimates of the natural frequency and damping ratio. Therefore, the RD technique is applied to the data obtained from the wind-induced monitoring programme described in Section 3.5, in order to determine the amplitude dependence of the natural frequencies and damping ratios of Latitude tower.

Example: Random Decrement Technique

The Random Decrement analysis used in this research was programmed using Matlab R2007b [170]. Figure 4.11 displays the RD function generated from multiple response time histories collected during the monitoring programme at Latitude tower. The ranked RD technique was used with the following trigger condition parameters: $a_r = 0.3\,\mathrm{mg_n}$, $\Delta a_r = 0.05$. A tenth order Butterworth bandpass filter with upper and lower frequencies of $0.21\,\mathrm{Hz}$ and $0.28\,\mathrm{Hz}$ respectively was used to isolate the mode of interest. The natural frequency and damping ratio results using a curve fit are listed below. The damping ratio estimate 95% confidence interval for the curve fit is also reported in parentheses. The curve fit was applied over the first five, three, and then two cycles of the RD function.

- $N_c = 5$, $f_{y1} = 0.254$ Hz, $\zeta = 1.60\%$ (1.57, 1.63)

- $N_c = 3$, $f_{y1} = 0.254$ Hz, $\zeta = 1.38\%$ (1.34, 1.43)
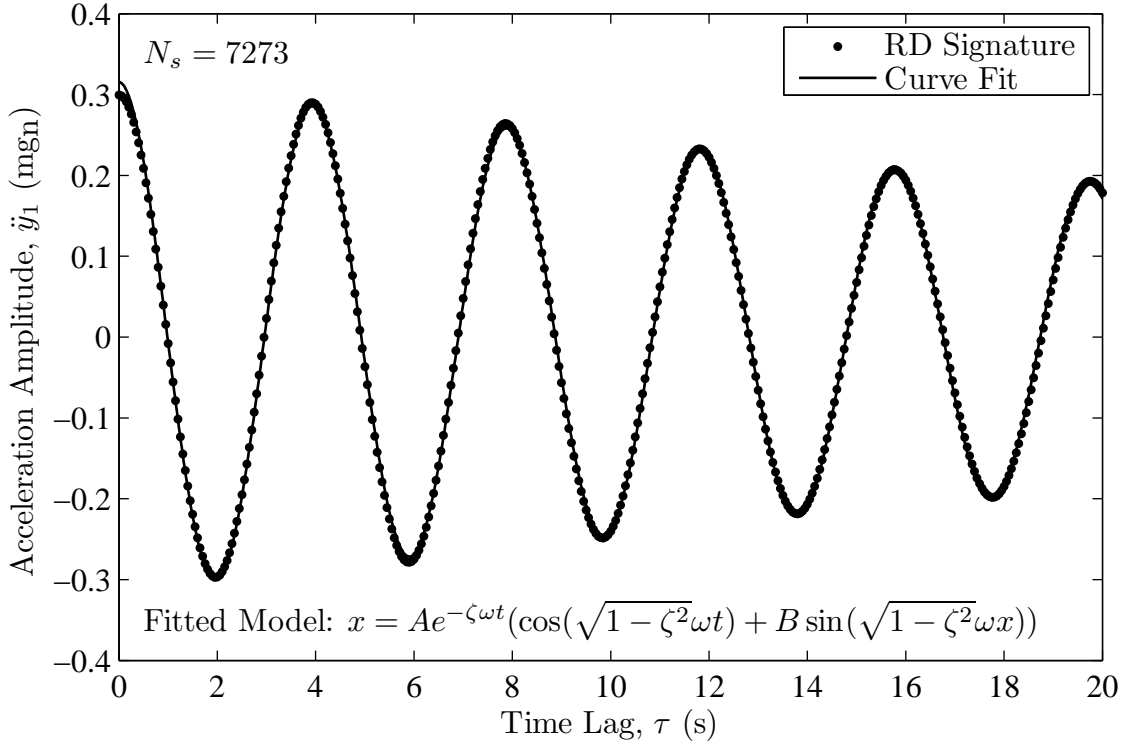
Figure 4.11: Ranked RD function for the fundamental x-axis translation vibration mode, generated from data obtained during the monitoring programme at Latitude tower.

- $N_c = 2$, $f_{y1} = 0.254$ Hz, $\zeta = 1.02\%$ (0.98, 1.06)

4.5 Summary

This chapter described vibration models of structures and the system identification techniques used to determine dynamic characteristics from ambient vibration data. Finite element models were initially discussed to introduce the formation of the equations of motion for discrete systems with multiple degrees of freedom, and to describe the solution methods for damped and undamped systems.

For the damped system case, proportional damping and general viscous damping cases are discussed. The equations of motion for the general viscous damping case was used as the basis for the system identification techniques. Three system identification techniques were described: a frequency domain technique, and two time domain techniques. All three techniques estimate the dynamic characteristics via the response measurements from a structure excited by unmeasured random excitation — a technique also known as operational modal analysis.

The frequency domain technique described is known as frequency domain decomposition. It is an extension of the peak picking method, with the addition of

singular value decomposition of the spectral response matrix. Compared with the peak picking method, this additional step in FDD improves the estimates of dynamic characteristics, particularly damping ratios, and allows for improved identification of closely spaced modes of vibration. The first time domain system identification technique discussed is known as stochastic subspace identification. It is a parametric technique that has similar advantages to FDD — namely the ability to separate closely spaced modes of vibration. The random decrement technique was finally introduced in order to determine the amplitude dependence of the natural frequency and damping ratio.

The FDD and SSI techniques were applied to wind-induced acceleration responses recorded approximately two years after construction completion of Latitude tower. Natural frequencies and damping ratios for the first six modes of vibration were estimated. The first six modes comprised three fundamental modes of vibration, including translation in the x-axis and y-axis and a torsional mode, and corresponding second modes of vibration for these fundamental modes. The natural frequency estimates for the FDD and SSI techniques for all modes differed by less than 1%. The damping ratio estimates displayed more variability between the techniques. The damping ratio estimates for the fundamental modes differed by less than 28%, but the second modes displayed larger differences, with the SSI estimates being more than twice the FDD estimates for the second y-axis translation and second torsional modes.

Multiple system identification techniques were used to gain more confidence in the estimates of dynamic parameters. This is particularly relevant to the estimation of the damping ratios when using unmeasured ambient vibrations as the excitation force. The results from applying the system identification techniques to the vibration tests conducted during construction of Latitude tower are presented in the following chapter, in addition to comparisons with finite element models.

Chapter 5

Estimating Dynamic Characteristics

5.1 Introduction

The main focus of this chapter is the estimation of the natural frequencies and damping ratios of tall buildings. Results are presented for data obtained during both the construction cycle, and during the post construction stages with tenant occupation. A description of the tests and the equipment is included in Section 3.4. The tests comprised forced and ambient vibration tests, and a comparison between the results from the two test types is presented.

The natural frequency results during construction are discussed with attention to the structural changes that occurred between consecutive vibration tests. The goal is to further the understanding of links between changes in the stiffness and mass of a structure, and the influence on the natural frequency. This will enable more accurate models of structures to be generated, which will improve the natural frequency estimates. In addition, a finite element analysis is also included as part of the natural frequency estimation process. Using the natural frequencies measured during the early stages of construction, a finite element model representing the structure at the time of testing is updated in order to achieve improved accuracy between the model and the full-scale natural frequencies. The updated model attributes are then applied to a model representing the completed structure. The knowledge obtained from vibration testing, conducted during the early stages of construction, is expected to improve the natural frequency estimates from the finite element model of the completed structure. This is important for two reasons. Firstly, it provides an evaluation of the assumptions and techniques used in the design, and the outcomes of the evaluation can benefit future designs. Secondly, for buildings that require auxiliary damping, a more accurate natural frequency estimate will benefit the design of the damping devices.

The damping ratio estimates during construction are discussed in parallel with the structural changes. For a complex structure such as a tall building, it is difficult to attribute damping changes to particular changes in the structural and non-structural elements. The goal in this instance is to determine the change in the damping ratio between the initial stages of construction and after construction completion. A relationship between these damping ratio estimates would prove useful in removing much of the uncertainty in the damping ratio estimates for similar tall building structures.

5.2 Forced Vibration Tests

The primary source of input excitation force for the series of vibration tests conducted was from ambient excitations. The forced vibration tests (FVT) were conducted to allow comparisons with the ambient vibration test (AVT) results, and provided a validation of these results to give more confidence in the natural frequency and damping ratio estimates.

Two input sources were used for the forced vibration tests: synchronised human movement, and mechanical shaker. In both cases the natural frequency and damping ratios were estimated from the decay trace of a vibration mode. The structure was initially set in motion at a particular mode of vibration, with repeated forced inputs to increase the oscillation amplitude. Once the amplitude plateaued or attained a sufficient level above the ambient vibrations, the forced input was halted, and the vibration amplitude was allowed to decay back to ambient vibration levels. The natural frequency was estimated using the zero crossings of the decay trace. The logarithmic decrement technique, discussed in Section 4.3.3, was applied to the decay trace to estimate the damping ratio.

The decay traces often displayed amplitude beat characteristics due to closely spaced vibration modes. In theory, the frequency of amplitude beating is approximately equal to the average of the two interfering frequencies. Large structural systems generally have low damping values, and are therefore classified as narrowband systems. Since the dominant modes are contained over a narrow frequency band, the beating may result from more than two closely spaced modes. Therefore, beating occurrences may not be periodic. To account for the beating, a linear least squares fit of the logarithm of the decay trace peaks was used to determine the damping ratio, and the peak of each beat cycle was selected to define the decay trace envelope.

The damping values from forced vibration tests may be underestimated due to the influence of unmeasured ambient excitation forces. These forces will increase the vibration amplitude of the structure during the decay phase of the time series, which

will result in a reduction of the slope of the logarithmic decrement. Effort was made to conduct the tests during calm wind conditions, and when the cranes and lifts were not in use, however it is impossible to completely avoid ambient excitations.

5.2.1   Synchronised Human Movement

Forced vibration tests using synchronised human movement were used for the first three test dates in the schedule. Figure 5.1 is an example decay trace generated using synchronised human movement. The first 20 seconds display increasing oscillation amplitudes from repeated pushes from those involved in generating the input force. The vibration amplitude peaks at approximately $0.24\,\mathrm{mg_n}$, and the input force was halted at this point. The latter portion of the time series displays the decay trace of the mode of vibration, and amplitude beat characteristics are clearly evident from $45\,\mathrm{s}$ onwards.

The results for all forced vibration tests using synchronised human movement are included in Table 5.1. Only the fundamental modes of vibration were tested: first mode translation in the x-axis (east-west), first mode translation in the y-axis (north-south), and first mode torsion about the vertical z-axis. The reported damping ratios are within the range 0.76–0.97 % for all test dates and vibration modes.

The expected error in the damping ratios is represented by the standard deviation of the damping ratio estimates σ_ζ, which is reported as a percentage of the damping ratio estimate. Some of the errors are significant, particularly for the x-axis translation on the test date 2003-05-27. A potential reason for these errors is the variation in the decay trace peaks caused by oscillation amplitude fluctuations that most likely originate from beating, or energy exchange, between the fundamental modes of vibration as observed in other structures [92]. These fluctuations reduce the linearity of the decay trace peaks, which is evident when plotted against a logarithmic axes, and therefore reduce the quality of a linear fit when using the logarithmic decrement technique. Since the slope of the decay trace is the only required output from the linear fit in order to estimate the damping ratio, the presence of the beating-induced vibration oscillations will have less effect on the damping estimates than what is suggested by the error estimations.

The peak accelerations for the vibration tests are displayed in the final column of Table 5.1. It is noted that some of the accelerations are relatively low, and differences of more than a factor of two are displayed between test dates for a particular vibration mode.
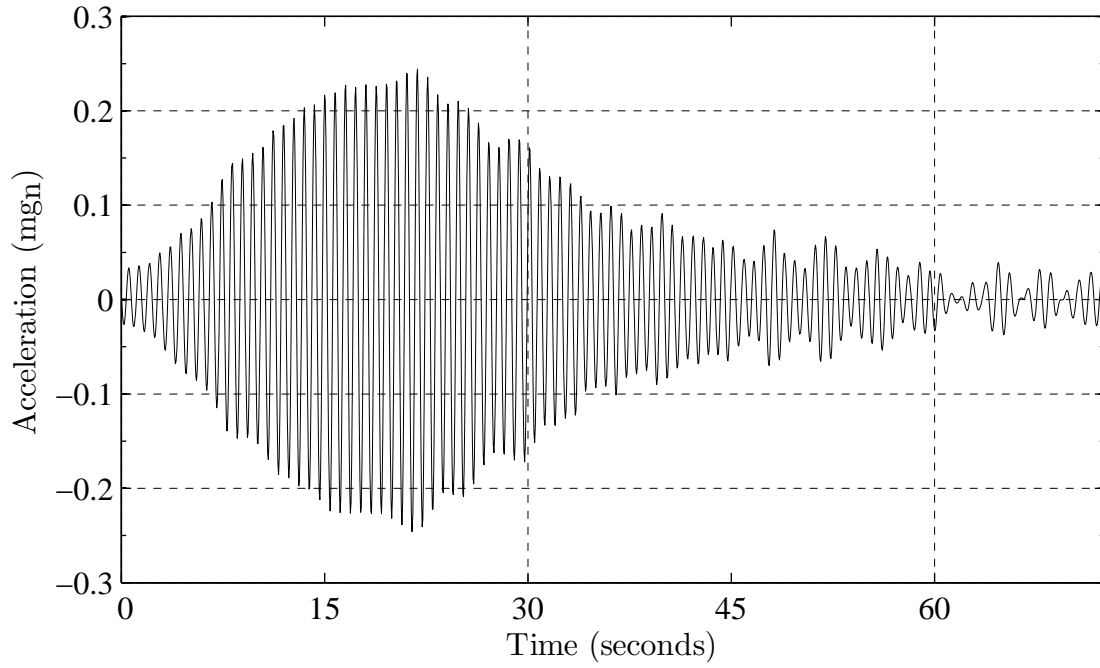
Figure 5.1: Response signal for the fundamental y-axis translational vibration mode from a forced vibration test using synchronised human movement. Test date: 2003-07-08, $f_{y1} = 1.328\,\text{Hz}$, $\zeta = 0.76\%$, $\sigma_\zeta = 14.5\%$.

Vibration Mode	Test Date	f (Hz)	ζ (%)	σ_ζ (%)	$\ddot{q}_{\max}$ (mg$_n$)
Translation	2003-05-27	1.261	0.95	36.8	0.13
X1	2003-06-17	1.162	0.83	7.8	0.20
	2003-07-08	1.050	0.86	21.5	0.09
Translation	2003-05-27	1.690	0.92	13.0	0.20
Y1	2003-06-17	1.509	0.91	12.1	0.20
	2003-07-08	1.328	0.76	14.5	0.21
Torsion	2003-05-27	2.020	0.84	10.8	0.12
T1	2003-06-17	1.758	0.97	8.2	0.07
	2003-07-08	1.548	0.94	21.4	0.12

Table 5.1: Results for forced vibration testing using synchronised human movement.

5.2.2   Mechanical Shaker

At the completion of the main structure, and prior to the completion of the facade and internal fit-out, two forced vibration tests using a mechanical shaker were conducted. Figure 5.2 displays a typical trace from a mechanical shaker test. Similar to the decay trace for the synchronised human movement tests, the time history displays the increasing oscillations, followed by a plateau that indicates the input energy is equivalent to the energy dissipation per cycle. For this test, the vibration amplitude peaks at approximately $0.29\,mg_n$. After halting the movement of the mechanical shaker, the decay trace is observed from $270\,s$ onwards.

Table 5.2 lists the results for the forced vibration tests using the mechanical shaker. The damping ratios for the two translational modes of vibration display significant differences for the damping ratio estimates, particularly the y-axis translation mode. This could be explained by the use of less mass (some of the lead weights were stolen) in the mechanical shaker for the test date 2004-12-22, resulting in lower peak accelerations. The published literature on damping estimation [63, 81] and the results in Section indicate that damping is dependent on the amplitude of vibration. A reduced vibration amplitude results in a lower damping estimation. The results in Table 5.2 also reflect this relationship between vibration amplitude and damping for the first two modes of vibration (x-axis translation and y-axis translation). The final column of the table shows the acceleration magnitudes ($\ddot{q}_{max}$). The reduced mass in the mechanical shaker for the tests conducted on 2004-12-22 resulted in a lower excitation force and therefore a lower vibration amplitude.

Despite the increased vibration amplitudes reported for the test date 2004-06-07, similar error estimates to those from the synchronised human movement tests are evident. The mode shapes for the first three vibration modes of Latitude tower are displayed in Figure 5.3. Note that each mode shape plot shows the x-axis component, y-axis component, and rotational component of the mode shape. Mode 2 has a complex mode shape, being a combination of an x-axis translation component and a rotational component about the vetical z-axis.

5.2.3   Comparison with Ambient Vibration Results

The data captured for the forced vibration tests did not coincide with the ambient vibration test data. This was due to the need to conduct the forced vibration tests during calm wind conditions, and the ambient vibration tests required windy conditions to produce meaningful results. This requirement means it is highly likely that the two tests cannot be conducted on the same day. The time difference between forced and ambient vibration tests was minimised as much as possible, and the timing was established in order to avoid significant structural changes. Therefore,
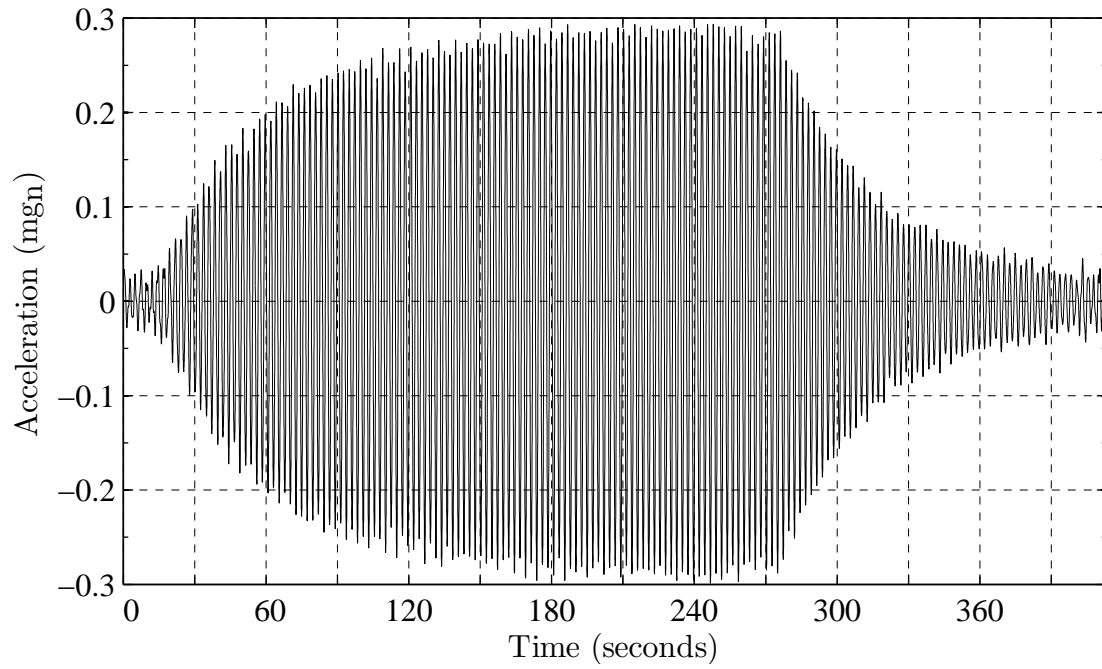
Figure 5.2:   Response signal for the fundamental torsional vibration mode from a forced vibration test using a mechanical shaker. Test date: 2004-12-22, $f_{t1} = 0.421\,\mathrm{Hz}$, $\zeta = 0.86\%$, $\sigma_\zeta = 5.8\%$.

Vibration Mode	Test Date	f (Hz)	ζ (%)	σ_ζ (%)	$\ddot{q}_{\max}$ ($\mathrm{mg_n}$)
Translation	2004-06-07	0.315	1.09	16.5	0.38
X1	2004-12-22	0.299	0.78	14.1	0.07
Translation	2004-06-07	0.276	1.14	10.5	0.44
Y1	2004-12-22	0.260	0.64	23.4	0.17
Torsion	2004-06-07	0.447	0.75	25.2	0.39
T1	2004-12-22	0.421	0.86	5.8	0.29

Table 5.2: Results for forced vibration testing using mechanical shaker.
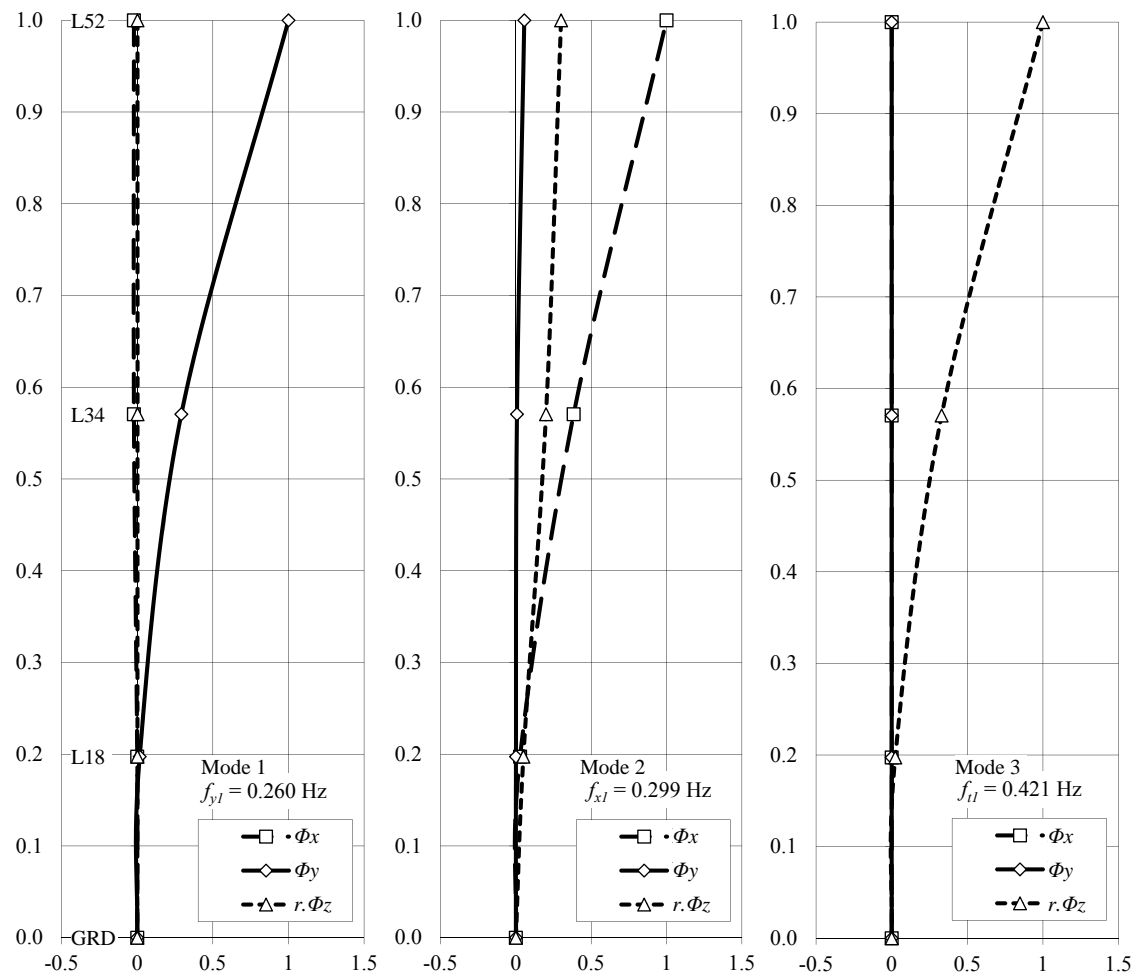
Figure 5.3: Normalised fundamental mode shapes of Latitude tower.

despite the time lag, which was minimal, between forced and ambient vibration tests, the structure state can be considered constant for both instances.

The difference in natural frequency estimates for FVT, FDD, and SSI were all within 5%, with most values being within 1%. Due to this negligible difference, a tabulated comparison of the natural frequency results for each technique is not included. The set of natural frequency results from the FDD technique are used in subsequent figures and tables for analysis and discussion.

The damping ratio estimates for FVT, FDD, and SSI are displayed in Table 5.3. The damping ratio estimates include structural and aerodynamic damping components, however the latter is expected to be negligible considering the low vibration amplitudes observed during testing. Three test dates are used to compare the damping ratio estimates. The first two test dates include FVT using synchronised human movement, while the final test date includes FVT using the mechanical shaker.

The differences between the damping ratio estimates from each technique are typically less than 30%. The only exception is the SSI damping ratio estimate for test date 2003-06-17, which is greater than the FVT and FDD estimates by a factor of 1.73 and 1.79 respectively. The results do not appear to indicate any consistent pattern of the AVT techniques either under or overestimating the damping ratios reported by the FVT technique. Although, if the SSI damping ratio estimate for the x-axis translation mode is excluded on test date 2003-06-17, the AVT results tended to underestimate the FVT results.

The peak acceleration amplitudes for all tests ranged between approximately 0.05–0.40 mg_n. This may result in amplitude dependence effects in the damping ratio estimates, however the results in Table 5.3 do not show any positive correlations between acceleration amplitude and damping ratio. Furthermore, the impact of the amplitude dependence may be obscured by the errors inherent to each of the estimation techniques.

5.3   Natural Frequency Results

5.3.1   Change during Construction

The natural frequencies for the fundamental modes of vibration measured during the construction of Latitude tower are displayed in Table 5.4. The height of the core above the base of the tower h_b is included. Note that multiple measurements are included for core heights of 132.930 m and 203.370 m. Referring to the construction schedule in Figure 3.27, these heights correspond to level 37 and level 55 respectively. The two vibration tests conducted when the core was at level 37 differ by the addition of a floor plate. At level 55 the core was completed, and three vibration tests were conducted to record the changes from the addition of floor plates, facade, and

Translation X1

	FVT			FDD			SSI	
Test	ζ	σ_ζ	$\ddot{x}_{1\mathrm{max}}$	ζ	σ_ζ	$\ddot{x}_{1\mathrm{max}}$	ζ	σ_ζ
Date	(%)	(%)	($\mathrm{mg_n}$)	(%)	(%)	($\mathrm{mg_n}$)	(%)	(%)
2003-06-17	0.83	7.8	0.20	0.81	13.2	0.05	1.44	4.2
2003-07-08	0.86	21.5	0.09	0.82	5.2	0.19	0.82	3.4
2004-06-07	1.09	16.5	0.38	0.87	13.0	0.32	1.05	7.1

Translation Y1

	FVT			FDD			SSI	
Test	ζ	σ_ζ	$\ddot{y}_{1\mathrm{max}}$	ζ	σ_ζ	$\ddot{y}_{1\mathrm{max}}$	ζ	σ_ζ
Date	(%)	(%)	($\mathrm{mg_n}$)	(%)	(%)	($\mathrm{mg_n}$)	(%)	(%)
2003-06-17	0.91	12.1	0.20	0.88	25.1	0.05	0.89	8.5
2003-07-08	0.76	14.5	0.21	0.96	1.5	0.09	0.77	5.6
2004-06-07	1.14	10.5	0.44	0.98	12.2	0.16	0.89	21.5

Torsion T1

	FVT			FDD			SSI	
Test	ζ	σ_ζ	$\ddot{y}_{2\mathrm{max}}$	ζ	σ_ζ	$\ddot{y}_{2\mathrm{max}}$	ζ	σ_ζ
Date	(%)	(%)	($\mathrm{mg_n}$)	(%)	(%)	($\mathrm{mg_n}$)	(%)	(%)
2003-06-17	0.97	8.2	0.07	0.74	17.2	0.05	0.91	4.0
2003-07-08	0.94	21.4	0.12	0.84	1.7	0.07	0.85	18.0
2004-06-07	0.75	25.2	0.39	0.92	29.2	0.05	1.01	21.7

Table 5.3: Comparison between damping ratio estimates from forced vibration tests (FVT) and ambient vibration tests (FDD and SSI).

internal fit-out.

A plot of the fundamental natural frequencies during construction is displayed in Figure 5.4, with the height of the core above the structure base as the abscissa. The measurements begin at a core height of 80 m because, as discussed in Section 3.2.3, the original structure was completed to this height.

The decrease in natural frequency with increasing height displayed in Figure 5.4 confirms the inverse relationship between natural frequency and height of the building (length of beam) that is described in the theoretical models of idealised cantilever beams in Equations (2.1) and (2.2). The spacing between the natural frequencies also decreases with increasing height. For the first test, the difference between the frequencies for f_{y1} and f_{t1} is approximately 0.33 Hz, and for f_{y1} and f_{x1} the difference is approximately 0.43 Hz. For the final test the differences reduce to approximately 0.044 Hz and 0.12 Hz.

For the first test, the order of the modes according to ascending natural frequency is f_{x1}, f_{y1}, and f_{t1}. When approximately 80% of the building was constructed, corresponding to a building height of 166.815 m, the frequencies of the translational modes f_{x1} and f_{y1} converged, and from that point onwards the natural frequency of the fundamental y-axis translation mode was lower then the fundamental x-axis translation mode.

For all three fundamental modes of vibration, the slope of the natural frequency plots in Figure 5.4 display three distinct segments. The three segments observed are bounded by the following core heights above ground: first segment between 78.965–132.930 m, second segment between 132.930–193.975 m, and the third segment between 193.975–203.370 m. The boundaries between these segments mark identifiable changes in the slope of the plots. These abrupt changes in slope are of interest because, from the perspective of the dynamic characteristics, they imply a significant change in the structural properties has occurred.

In the first segment, the slope of the plots for f_{x1}, f_{y1}, and f_{t1} are approximately -0.013, -0.019, and -0.022 Hz/m respectively. This portion of the plots represents the most rapid reduction in the natural frequencies during the construction cycle. This rapid reduction is expected in this stage of construction if the building is behaving as either a shear beam or flexural beam model, or a combination of both.

During the stages of construction bounded by the first segment, the demolition of the floor slabs between levels 11 and 15 was conducted. Removing the floor plates will decrease the mass of the structure, as well as reducing the stiffness. Considering the relationship between natural frequency, mass, and stiffness in Equation (4.15), a decrease in mass will increase the natural frequency, while a decrease in stiffness will decrease the natural frequency. It is unlikely that the removal of these floor slabs will have a significant impact on the lateral stiffness of the structure, because

the core shear walls are the dominant lateral force resisting elements.

The commencement of the facade installation also occurred during the first segment. The largest lag between the facade and the floor plate level, compared with subsequent stages of construction, is observed in the vibration test schedule in Figure 3.27. Furthermore, no facade is installed prior to the completion of the core to level 35 on test date 2003-08-27. Therefore, the latter stages of the first segment see the gradual introduction of the facade elements. At the test date 2003-10-27, which coincides with the change in slope between the first and second segments, the facade was installed between levels 16 and 29 and covered approximately 40% of the above ground portion of the structure.

If the stiffness of the facade elements, and their connections to the main structure, are sufficient to influence the natural frequencies, the point at which the change in slope occurs would imply that the amount of facade, in this case approximately 40% of the building height, or the lag between the facade and the top of the structure, are important to mobilising the facade in the lateral force resisting system.

The design of typical facade elements installed at Latitude tower should ensure any inter-storey shears are not transferred to the facade elements. The intended outcome is to avoid the possibility of the glass acting as a compression strut, which is likely to cause serviceability issues for the glass facade. This is achieved by including relatively large movement joints between the panels, as well as allowing for movement at the connections to the floor slabs. From this discussion, it can be concluded that it is unlikely the facade will have a significant impact on the stiffness of the structure. The influence of the facade will be via the additional mass introduced to the system, which will decrease the natural frequencies.

In the second segment, the slope of the plots for f_{x1}, f_{y1}, and f_{t1} reduce to approximately -0.0030, -0.0048, and $-0.0044\,\mathrm{Hz/m}$ respectively. The most significant structural change during segment two is the introduction of the core outrigger and offset outriggers at the plant rooms between levels 34 and 36.

Observing the impact of the core outriggers directly after installation is questionable. It is unlikely any significant impact will be observed. This is due to the outriggers being effective in transferring bending moments from the core to the columns. Without significant curvature in the core generated by bending action, the core outriggers will not be mobilised. Participation in resisting shear action between the floors plates is a possibility, but the core shear walls are more likely to dominate in this case.

The offset outriggers at the facade use the same principle as the core outriggers to transfer bending moments to the columns. The difference is the moment is first transferred to the offset outriggers via the floor plate. Similar to the core outriggers, the lack of bending action at this stage of construction means the offset outriggers

Test Date	$h_{b,\text{core}}$ (m)	f_{x1} (Hz)	f_{y1} (Hz)	f_{t1} (Hz)
2003-05-27	78.965	1.261	1.690	2.020
2003-06-17	90.260	1.162	1.528	1.748
2003-07-08	94.025	1.050	1.323	1.548
2003-08-01	112.850	0.772	1.006	1.211
2003-08-07	116.635	0.754	0.961	1.148
2003-08-27	125.025	0.654	0.820	0.972
2003-09-12	129.165	0.615	0.752	0.884
2003-09-30	132.930	0.576	0.674	0.825
2003-10-10	132.930	0.566	0.649	0.820
2003-10-27	144.225	0.552	0.601	0.791
2003-11-17	159.285	0.513	0.542	0.732
2003-12-17	166.815	0.474	0.479	0.679
2004-02-12	193.975	0.390	0.360	0.557
2004-03-01	198.040	0.361	0.332	0.508
2004-06-07	203.370	0.313	0.269	0.440
2004-08-06	203.370	0.305	0.259	0.427
2004-12-22	203.370	0.303	0.259	0.427

Table 5.4: Change in natural frequency of the fundamental modes of vibration during construction.

will not be mobilised. In the case of shear actions, the offset outriggers will have an influence.

The core outrigger construction comprises steel encased concrete beams integrated with the floor slabs and spanning between the core and the perimeter columns. Two steel diagonals between the beams in a k-frame arrangement complete the brace. The concrete beams include stressing tendons that were stressed, and therefore became fully effective, approximately 28 days after pouring of the level 36 slab. This occurred between test dates 2003-11-17 and 2003-12-17. At this stage the f_{y1} value continues to decrease, and crosses the f_{x1} value at test date 2003-12-17.

The third and final segment in Figure 5.4 includes the last five vibration tests starting at 2004-02-12. During this segment the natural frequencies decrease faster than the previous segment. At the start of the segment, the concrete core was two levels from completion, the floor plates were 10 levels from completion, and the facade was completed to level 39. Assuming the floor slabs have little contribution to the lateral stiffness, the last segment is characterised by the addition of mass, which decreases the natural frequency of all the modes.

Table 5.5 compares the fundamental natural frequencies for the completed struc-
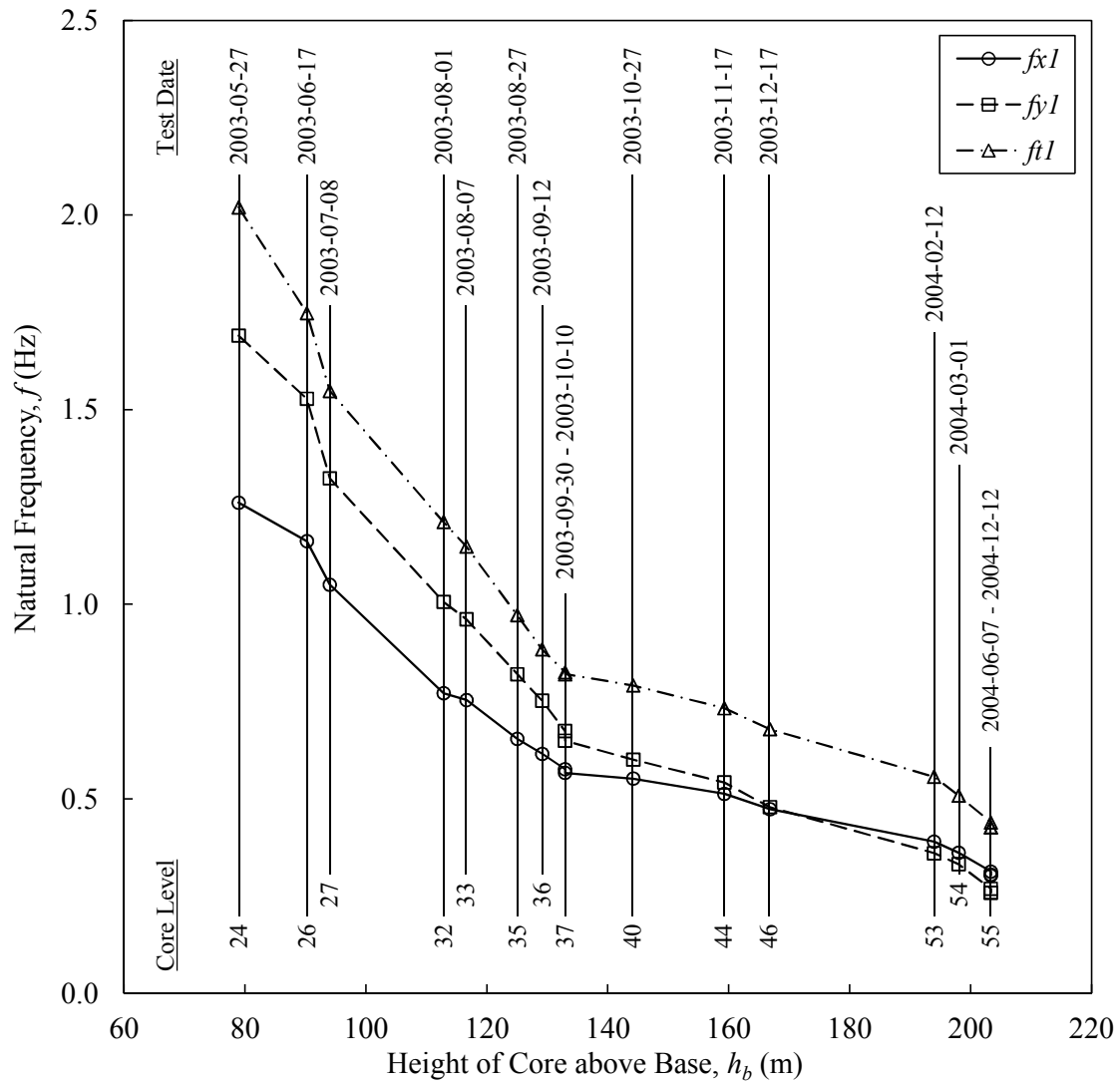
Figure 5.4: Change in natural frequency of the fundamental modes of vibration during construction.

	Measured	Empirical Formula		
	f (Hz)	Formula	f (Hz)	Difference
Translation Y1	0.256	$f_{y1} = 46/h$	0.263	3%
Translation X1	0.292	$f_{x1} = 58/h$	0.331	13%
Torsion T1	0.417	$f_{t1} = 72/h$	0.411	2%

Table 5.5: Comparison between measured fundamental natural frequencies and empirical estimates from Ellis 1980 [47] (Measured values from after construction of Latitude tower).

ture with the empirical estimates proposed by Ellis [47]. The measured natural frequencies are from data recorded approximately two years after the building was completed. At the time the entire building was occupied, with all internal fit-out completed. The empirical formulas are based on the height above ground (h). The measured y-axis mode and torsional mode natural frequencies are within 3% of the estimates from the empirical formula. The empirical estimate for the x-axis natural frequency is 13% more than the measured value.

The natural frequencies of the second modes of vibration are presented in Table 5.6 and Figure 5.5. The change in these modes of vibration during construction is similar to that observed for the fundamental modes of vibration. The two tests conducted when the core was at level 37 displayed a larger decrease in the natural frequencies for the second modes compared with the first modes. The structural changes between the two tests consisted of the addition of one floor level, and the addition of the facade elements between levels 25 and 27. The decrease in the second mode frequencies is between 4–6 %, while for the first modes the decrease is between 1–4 %.

The observability of stiffness changes, due to discrete changes in structural elements such as the addition of outriggers and the joining of the eastern core wall at level 16, between consecutive tests is obscured by the curing time of the concrete and the simultaneous nature of the construction. By the time the concrete has achieved sufficient strength such that the change in question becomes effective, other changes to the structure have occurred, thus preventing observations of the changes in isolation.

5.3.2   Relationships between Modes

The ratios of the natural frequencies for the fundamental mode and second mode of vibration during construction are displayed in Table 5.7 and Figure 5.6. Using these ratios it is possible to gain insight into the structural actions of the building. An idealised flexure beam with uniform mass and stiffness has a frequency ratio

Test Date	$h_{b,\text{core}}$ (m)	f_{x2} (Hz)	f_{y2} (Hz)	f_{t2} (Hz)
2003-05-27	78.965	–	–	–
2003-06-17	90.260	3.809	4.683	4.961
2003-07-08	94.025	3.174	4.214	4.462
2003-08-01	112.850	2.588	3.008	3.545
2003-08-07	116.635	2.357	–	–
2003-08-27	125.025	2.314	2.832	3.018
2003-09-12	129.165	2.046	2.686	2.788
2003-09-30	132.930	1.924	2.485	2.568
2003-10-10	132.930	1.816	2.383	2.471
2003-10-27	144.225	1.743	2.153	2.310
2003-11-17	159.285	1.567	1.924	2.075
2003-12-17	166.815	1.392	1.777	1.934
2004-02-12	193.975	1.147	1.382	1.523
2004-03-01	198.040	1.030	1.240	1.367
2004-06-07	203.370	0.928	1.055	1.152
2004-08-06	203.370	0.919	1.046	1.122
2004-12-22	203.370	0.908	1.025	1.106

Table 5.6: Change in natural frequency of the second modes of vibration during construction.
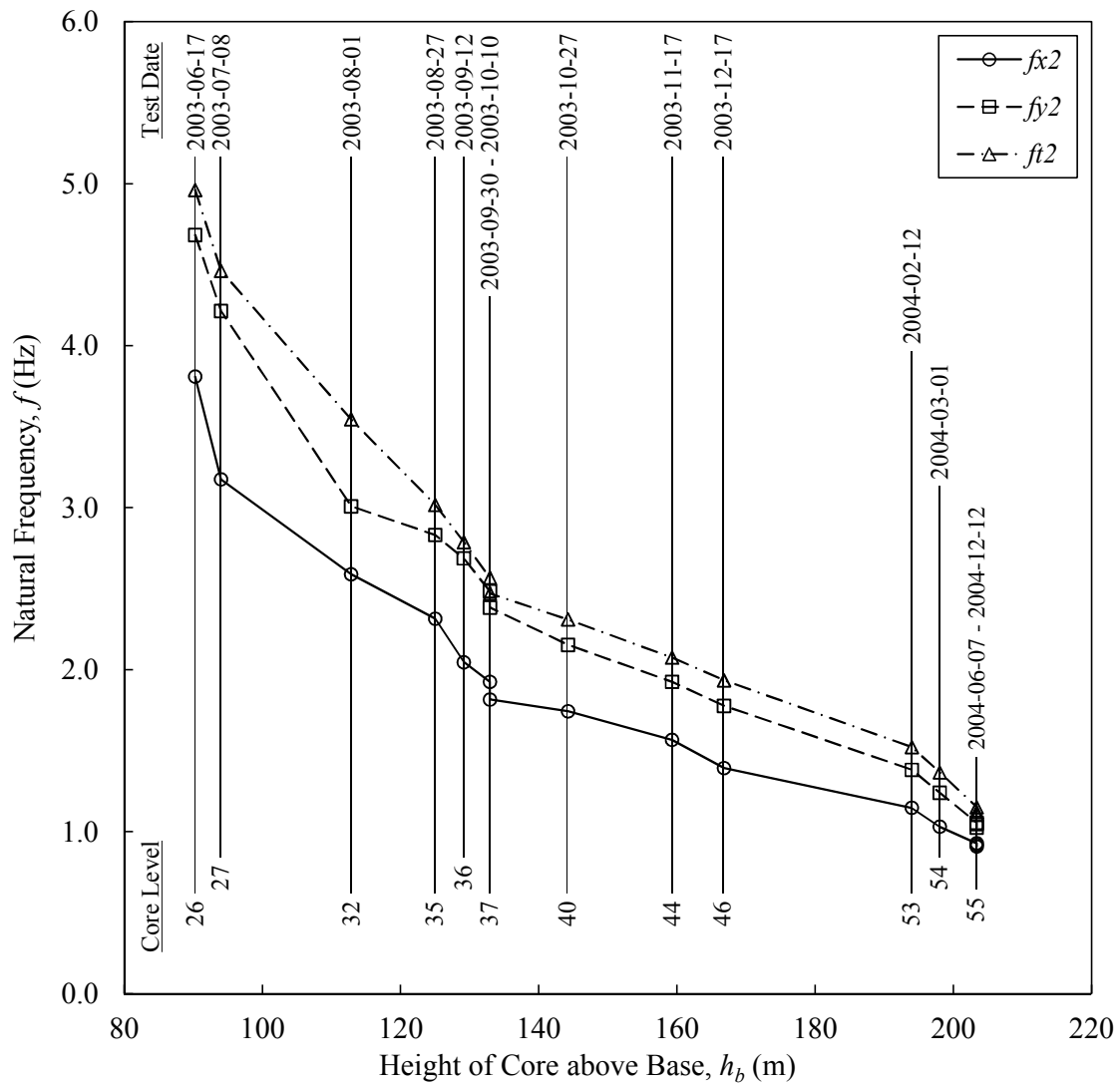
Figure 5.5: Change in natural frequency of the second modes of vibration during construction.

between the first and second modes of 2.5:1, while a shear beam has a ratio of 3:1. The structural system in this case will be a combination of both flexural and shear actions. Latitude tower has relatively uniform mass, but the stiffness decreases with height due to reductions in the size of the core. This reduction in stiffness with height can be approximated by an idealised beam with uniform mass and tapering stiffness. The influence of tapering on the natural frequencies of idealised beams, which is discussed in Section 2.2.1, are not considered in the ratios.

In Figure 5.6, the ratios for the x-axis modes are approximately equivalent to a shear beam model after the core height reaches approximately 135 m. Prior to this, the x-axis ratios gradually increase to a value of 3.5, and this stage of construction corresponds to the demolition of the floor slabs between levels 11 to 15. The reduction in the mass at these levels may be an explanation for the increase in the ratios for all the modes during these stages of construction.

For the torsional modes, the ratios gradually reduce after test date 2003-09-12 to a final value of 2.6. Torsional deflections are purely associated with shearing actions, and therefore a ratio closer to 3 would be expected. However, the concrete core does not have uniform stiffness over the building height, while the mass does remain approximately uniform. Therefore, the idealised uniform beam ratios are likely to be reduced due to the tapering effect of the concrete core stiffness [7].

The ratios for the y-axis modes are consistently above 3.5 after test date 2003-09-12, and then increase after the completion of the concrete core to a value of 4.0. During this increase, the only changes to the structure included internal fit-out and the addition of facade elements between levels 52 to 55. This implies either the added mass at the top of the building was a greater influence on reducing the first mode frequency in the y-axis, or the elements added at the top of the building had an influence on increasing the stiffness of the second mode frequency in the y-axis. An increase in the ratio is also observed for the x-axis modes. Facade elements adding stiffness to the second mode natural frequencies was reported for a 24 storey steel frame tower [118].

The stressing of the core outriggers between test dates 2003-11-17 and 2003-12-17 corresponds to an increase in the y-axis ratios. The stiffening effect of the core outriggers was expected to have most influence on the fundamental mode of vibration. Therefore, it was expected that the y-axis ratio would decrease with the introduction of the core outriggers. The offset outriggers, acting in the x-axis, were installed between test dates 2003-10-27 and 2003-11-17. The date at which the floor slabs bounding the offset outriggers attain a 28 day concrete strength is between test dates 2003-11-17 and 2003-12-17. For these test dates, the x-axis ratio decreases more rapidly compared to the previous values, indicating the x-axis fundamental natural frequency has increased relative to the second mode natural

Test Date	$h_{b,\text{core}}$ (m)	f_{x2}/f_{x1} (Hz)	f_{y2}/f_{y1} (Hz)	f_{t2}/f_{t1} (Hz)
2003-05-27	78.965	–	–	–
2003-06-17	90.260	3.3	3.1	2.8
2003-07-08	94.025	3.0	3.2	2.9
2003-08-01	112.850	3.4	3.0	2.9
2003-08-07	116.635	–	–	–
2003-08-27	125.025	3.5	3.5	3.1
2003-09-12	129.165	3.3	3.6	3.2
2003-09-30	132.930	3.3	3.7	3.1
2003-10-10	132.930	3.2	3.7	3.0
2003-10-27	144.225	3.2	3.6	2.9
2003-11-17	159.285	3.1	3.6	2.8
2003-12-17	166.815	2.9	3.7	2.9
2004-02-12	193.975	2.9	3.8	2.7
2004-03-01	198.040	2.9	3.7	2.7
2004-06-07	203.370	3.0	3.9	2.6
2004-08-06	203.370	3.0	4.0	2.6
2004-12-22	203.370	3.0	4.0	2.6

Table 5.7: Ratios of the natural frequencies for the fundamental mode and second mode of vibration during construction.

frequency.

The ratio between the fundamental torsional mode and the fundamental translational modes is displayed in Table 5.8. This ratio is useful in confirming the estimate of the torsional mode when the fundamental mode is estimated with sufficient accuracy. During construction, the ratio of the torsional mode to the x-axis translational mode gradually decreases from 1.60 to 1.41, while the ratio of the torsional mode to the y-axis translational mode increases from 1.20 to 1.65. At the start of testing, the first mode of vibration was translation in the x-axis, and by the end of construction the first mode had changed to translation in the y-axis. Therefore, buildings similar to Latitude tower could be expected to have a ratio between the first torsional mode and the first translational mode of approximately 1.6.

5.3.3   Amplitude Dependence

The amplitude dependence of the fundamental natural frequencies was determined using the Ranked Random Decrement technique, and the results are displayed in Figures 5.7 to 5.9. The number of segments (N_s) used to attain the natural frequency estimates is indicated by the vertical dashed lines. For the x-axis translation mode,
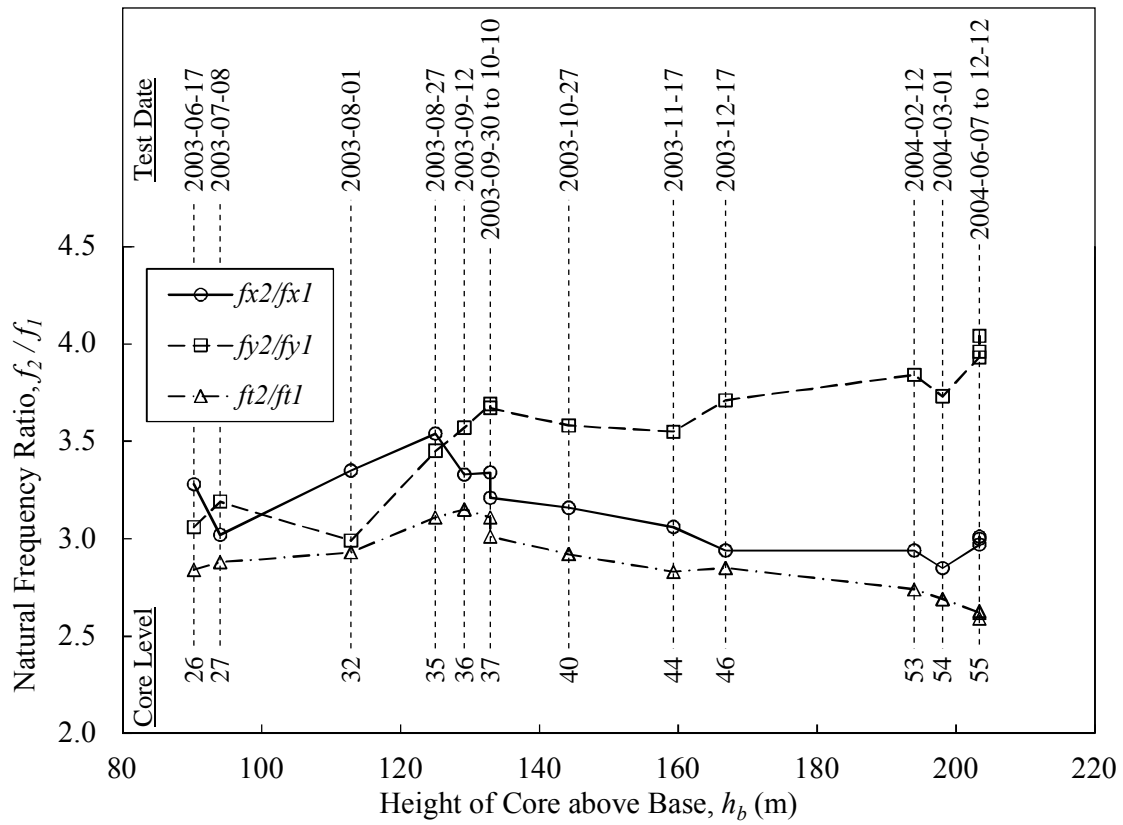
Figure 5.6: Ratios of the natural frequencies for the fundamental mode and second mode of vibration during construction.

Test Date	$h_{b,\text{core}}$ (m)	f_{t1}/f_{x1} (Hz)	f_{t1}/f_{y1} (Hz)
2003-05-27	78.965	1.60	1.20
2003-06-17	90.260	1.50	1.15
2003-07-08	94.025	1.48	1.17
2003-08-01	112.850	1.56	1.22
2003-08-07	116.635	1.52	1.19
2003-08-27	125.025	1.51	1.19
2003-09-12	129.165	1.45	1.20
2003-09-30	132.930	1.44	1.22
2003-10-10	132.930	1.45	1.27
2003-10-27	144.225	1.44	1.32
2003-11-17	159.285	1.43	1.36
2003-12-17	166.815	1.44	1.41
2004-02-12	193.975	1.42	1.50
2004-03-01	198.040	1.42	1.53
2004-06-07	203.370	1.39	1.63
2004-08-06	203.370	1.41	1.67
2004-12-22	203.370	1.41	1.65

Table 5.8: Natural frequency ratios between the fundamental torsional mode and the fundamental translational modes during construction.

the estimates with an acceleration amplitude greater than $0.45\,mg_n$ used less than 2000 segments, and for acceleration amplitudes greater than $0.70\,mg_n$ the number of segments reduces to less than 200. The y-axis translation mode and torsional mode display higher acceleration amplitude thresholds for the 2000 and 200 segment indicators in Figures 5.8 and 5.9. The number of segments used is more critical for the damping estimates, which are discussed in Section 5.4.3, compared with the natural frequency estimates.

The number of cycles (N_c) of the random decrement function used to estimate the natural frequency has little influence on the final result. For the x-axis translation mode and the torsional mode in Figures 5.7 and 5.9, increasing the number of cycles tended to increase the natural frequency estimates at each acceleration amplitude, whereas the opposite is observed for the y-axis translation mode in Figure 5.8.

Despite the influence of the number of segments and number of cycles used, the change in the natural frequencies is very low over the acceleration amplitude range. The approximate reductions are;

- Translation X1: 3.4%

- Translation Y1: 2.3%

- Torsion T1: 2.6%

For all fundamental modes, the change in the natural frequency over the acceleration amplitude range does not follow a linear trend. The rate of reduction is greatest at the lower amplitudes, and decreases as the amplitudes increase. Once the amplitude reaches a certain level, each mode displays a discontinuity in the rate of natural frequency reduction, which is apparent in the sudden decrease observed at the acceleration amplitudes $1.3\,mg_n$, $0.9\,mg_n$, and $1.2\,mg_n$ for the x-axis translation, y-axis translation, and torsion modes respectively. These discontinuities could be due to degradation of the random decrement function from insufficient segments. Alternatively, these discontinuities may be due to structural or non-structural element connections reaching a slipping threshold, and therefore contributing less stiffness to the structure.

5.4 Damping Ratio Results

This section discusses the damping ratio estimates during construction. The estimates for the fundamental modes of vibration are presented. The higher modes of vibration typically displayed large errors in the damping ratio estimates when applying the FDD and SSI techniques. This was due to the ambient excitation force in the frequency range of the higher modes being insufficient to excite these modes. It
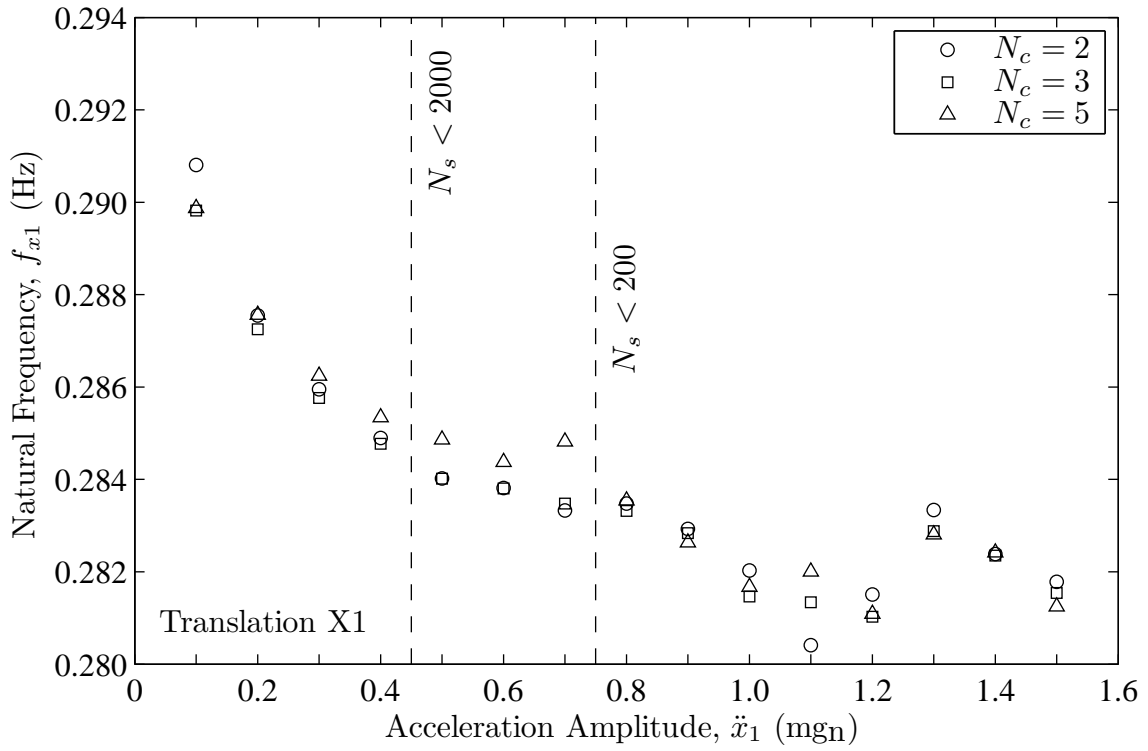
Figure 5.7: Amplitude dependence of natural frequency for the fundamental x-axis translational mode of vibration (Ranked RD output).
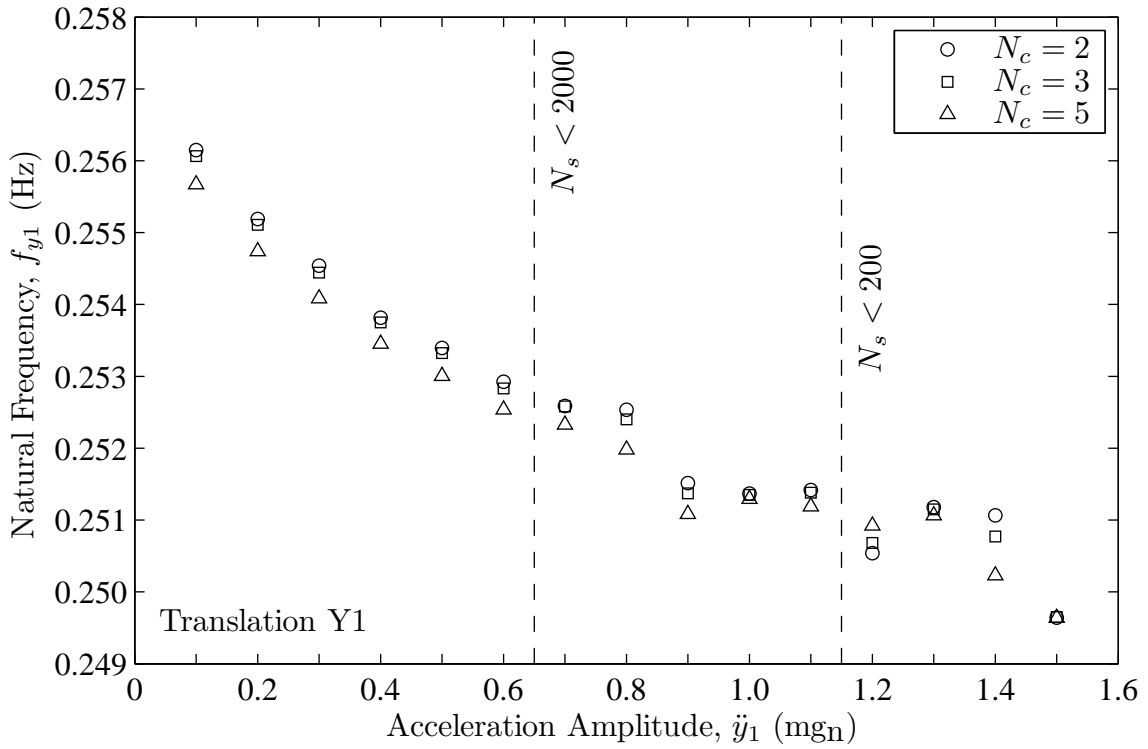
Figure 5.8: Amplitude dependence of natural frequency for the fundamental y-axis translational mode of vibration (Ranked RD output).
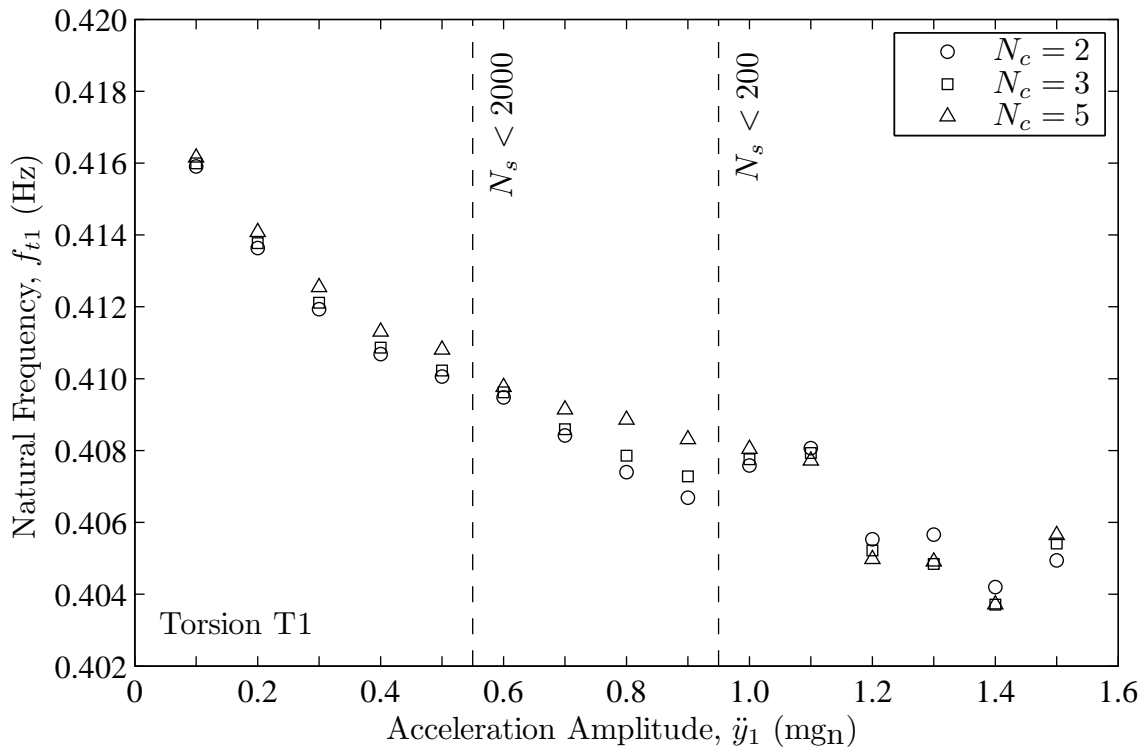
Figure 5.9: Amplitude dependence of natural frequency for the fundamental torsional mode of vibration (Ranked RD output).

was observed that the operation of the construction cranes attached to the structure tended to excite the higher modes of vibration. Time series data recorded during crane activity were excluded from damping ratio estimates since the type of loading does not satisfy the requirements for random excitation, which is an assumption of the FDD and SSI techniques.

5.4.1 Change during Construction

Estimates of the damping ratios for the fundamental x-axis translation mode during construction are displayed in Table 5.9 and Figure 5.10. The upper and lower bound of the estimates are between approximately 0.8–1.1 %, with the exception of the SSI estimate for test date 2003-06-17. The acceleration amplitudes reported are significantly lower than what is expected for serviceability excitation levels. It is noted that the final FVT results on test date 2004-12-22 have a very low acceleration amplitude. This was due to less mass being used in the mechanical shaker compared with test date 2004-06-07.

Some of the scatter in the results can be explained by the difference in excitation amplitudes between tests. Figure 5.11 plots the damping ratio estimates against the acceleration amplitude, and Figure 5.12 plots the damping ratio estimates against the normalised displacement amplitude. A linear least squares fit of the data implies

Test Date	$h_{b,\text{core}}$ (m)	FVT			FDD			SSI	
		ζ (%)	σ_ζ (%)	$\ddot{x}_{1\text{max}}$ (mg$_\text{n}$)	ζ (%)	σ_ζ (%)	$\ddot{x}_{1\text{max}}$ (mg$_\text{n}$)	ζ (%)	σ_ζ (%)
2003-05-27	78.965	0.95	36.8	0.13	–	–	–	–	–
2003-06-17	90.260	0.83	7.8	0.20	0.81	13.2	0.05	1.44	4.2
2003-07-08	94.025	0.86	21.5	0.09	0.82	5.2	0.19	0.82	3.4
2003-08-01	112.850	–	–	–	0.91	28.0	0.27	0.99	4.6
2003-08-07	116.635	–	–	–	–	–	–	–	–
2003-08-27	125.025	–	–	–	1.07	16.6	0.55	1.03	8.7
2003-09-12	129.165	–	–	–	0.98	20.8	0.07	0.90	22.8
2003-09-30	132.930	–	–	–	0.96	8.2	0.22	1.08	7.3
2003-10-10	132.930	–	–	–	0.89	12.1	0.22	0.88	14.1
2003-10-27	144.225	–	–	–	0.94	33.3	0.05	0.94	8.3
2003-11-17	159.285	–	–	–	0.99	27.9	0.28	0.87	6.8
2003-12-17	166.815	–	–	–	0.99	40.5	0.23	1.08	7.1
2004-02-12	193.975	–	–	–	0.87	30.6	0.10	0.99	11.0
2004-03-01	198.040	–	–	–	0.94	15.2	0.24	1.13	10.0
2004-06-07	203.370	1.09	16.5	0.38	0.87	13.0	0.32	1.05	7.1
2004-08-06	203.370	–	–	–	0.92	10.6	0.18	0.96	3.5
2004-12-22	203.370	0.78	14.1	0.07	–	–	–	–	–

Table 5.9: Damping ratios during construction for the fundamental x-axis translation vibration mode.

the damping ratios are increasing with increasing acceleration, but the scatter in the plot results in a statistically weak correlation.

The noise floor of the acceleration measurement equipment was discussed in Section 3.3.6. The standard deviation noise floor estimate was $0.077\,\text{mg}_\text{n}$. It is important to note that measurements for an acceleration less than this noise floor have a 31.8% chance of being noise. Furthermore, the estimates for an acceleration amplitude greater than two standard deviations of the noise floor have a 4.6% chance of being noise. For the damping versus acceleration amplitude plot, the acceleration values below $0.1\,\text{mg}_\text{n}$ are likely to have a low signal to noise ratio when considering the noise floor of the acceleration measurement equipment.

Table 5.10 and Figure 5.13 display the damping ratio results for the fundamental y-axis translation mode during construction. The damping ratios are generally within the range of 0.8–1.2 %, with the exception of the final FVT estimate of 0.64 %. This value is significantly lower than the other estimates, and is likely due to distortions in the decay trace from ambient excitations. Figures 5.14 and 5.15 plot the damping ratios against acceleration amplitude and normalised displacement respec-

Figure 5.10: Damping ratio versus core height above base for the fundamental x-axis translation vibration mode during construction.

Figure 5.11: Damping ratio versus acceleration amplitude for the fundamental x-axis translation vibration mode during construction.

Figure 5.12: Damping ratio versus normalised displacement amplitude for the fundamental x-axis translation vibration mode during construction.

tively. As for the x-axis mode, the y-axis mode displays amplitude dependence in the normalised displacement plot in Figure 5.15, particularly for the FVT damping ratio estimates.

The damping ratio estimates for the fundamental torsional mode were lower than the estimates for the translational modes. Figure 5.16 displays the torsional damping ratio estimates during construction to be mostly between 0.7–1.1 %. In addition, the plots of damping ratio against acceleration amplitude in Figure 5.17, and damping ratio against normalised displacement in Figure 5.18, suggest that the damping ratio is decreasing with increasing vibration amplitude.

The results presented above suggest that the damping ratios for low amplitude vibrations are not influenced by the structural changes during construction. This is a particularly useful outcome, since it implies the damping ratios for the first three vibration modes of Latitude tower were known with a degree of confidence when approximately 38% of the building height was completed. This conclusion can also be more broadly applied to other buildings that share similar structural and non-structural characteristics as Latitude tower. Furthermore, it has important implications for determining auxiliary damping requirements for wind sensitive structures. Confirming the level of damping inherent to the structure at an early stage of construction allows more accurate assessments of the amount of auxiliary damping required. If the inherent damping levels in the structure are confirmed to be sufficient, auxiliary damping devices will be unnecessary. This results in significant financial benefits by avoiding the installation of auxiliary damping devices, as well as gaining the space reserved for the damping device installation, which can be

Test Date	$h_{b,\text{core}}$ (m)	FVT ζ (%)	σ_ζ (%)	$\ddot{y}_{1\max}$ (mg$_\text{n}$)	FDD ζ (%)	σ_ζ (%)	$\ddot{y}_{1\max}$ (mg$_\text{n}$)	SSI ζ (%)	σ_ζ (%)
2003-05-27	78.965	0.92	13.0	0.20	–	–	–	–	–
2003-06-17	90.260	0.91	12.1	0.20	0.88	25.1	0.05	0.89	8.5
2003-07-08	94.025	0.76	14.5	0.21	0.96	1.5	0.09	0.77	5.6
2003-08-01	112.850	–	–	–	0.81	12.2	0.12	1.08	4.6
2003-08-07	116.635	–	–	–	–	–	–	–	–
2003-08-27	125.025	–	–	–	1.01	15.6	0.17	1.09	15.0
2003-09-12	129.165	–	–	–	0.89	26.1	0.07	0.84	10.8
2003-09-30	132.930	–	–	–	0.93	9.1	0.24	0.99	4.4
2003-10-10	132.930	–	–	–	1.14	5.0	0.30	0.83	5.9
2003-10-27	144.225	–	–	–	1.06	17.5	0.06	1.03	7.4
2003-11-17	159.285	–	–	–	0.96	12.3	0.19	0.85	10.8
2003-12-17	166.815	–	–	–	1.17	25.7	0.35	0.89	11.4
2004-02-12	193.975	–	–	–	0.98	34.2	0.23	1.08	3.9
2004-03-01	198.040	–	–	–	0.92	24.6	0.22	0.99	7.8
2004-06-07	203.370	1.14	10.5	0.44	0.98	12.2	0.16	0.89	21.5
2004-08-06	203.370	–	–	–	1.05	12.3	0.28	0.98	5.2
2004-12-22	203.370	0.64	23.4	0.17	–	–	–	–	–

Table 5.10: Damping ratios during construction for the fundamental y-axis translation vibration mode.
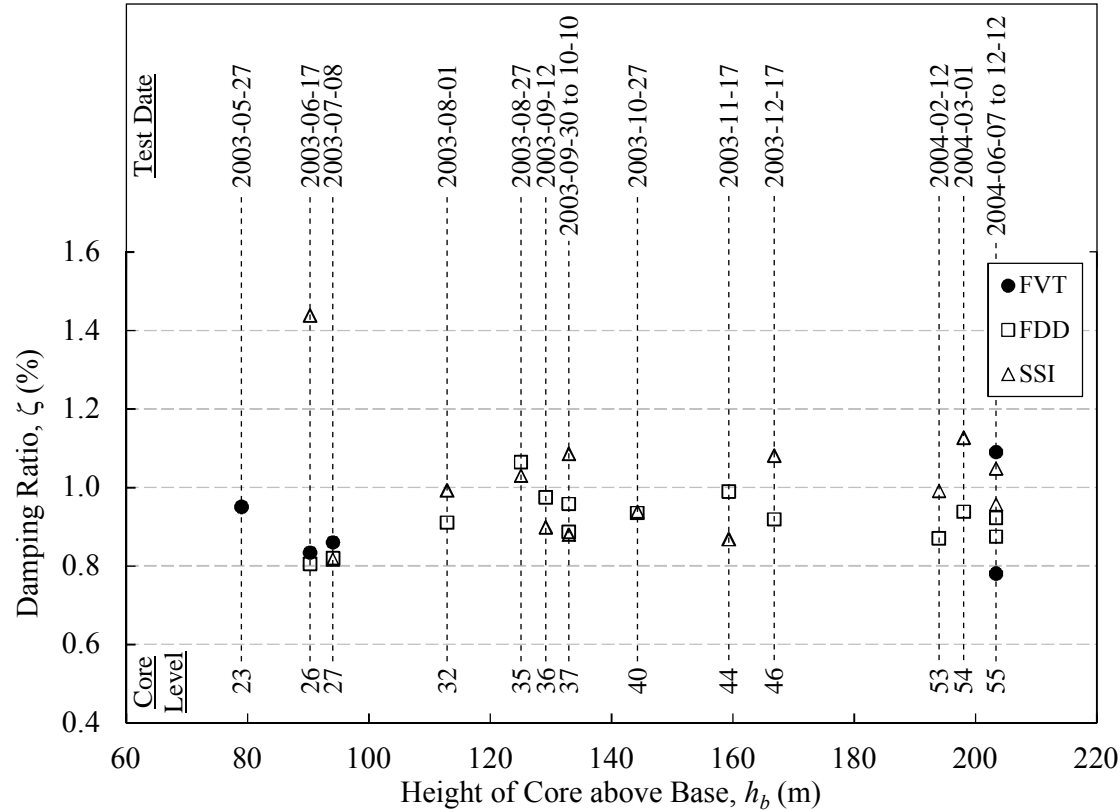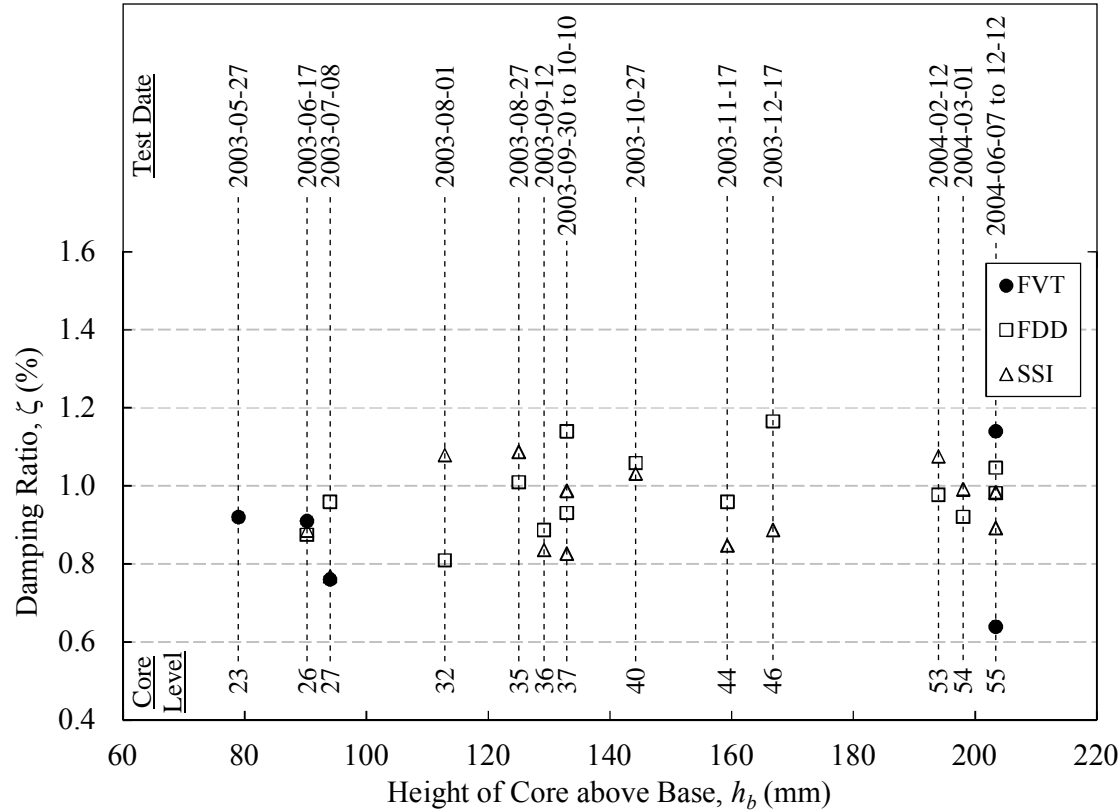
Figure 5.13: Damping ratio versus core height above base for the fundamental y-axis translation vibration mode during construction.
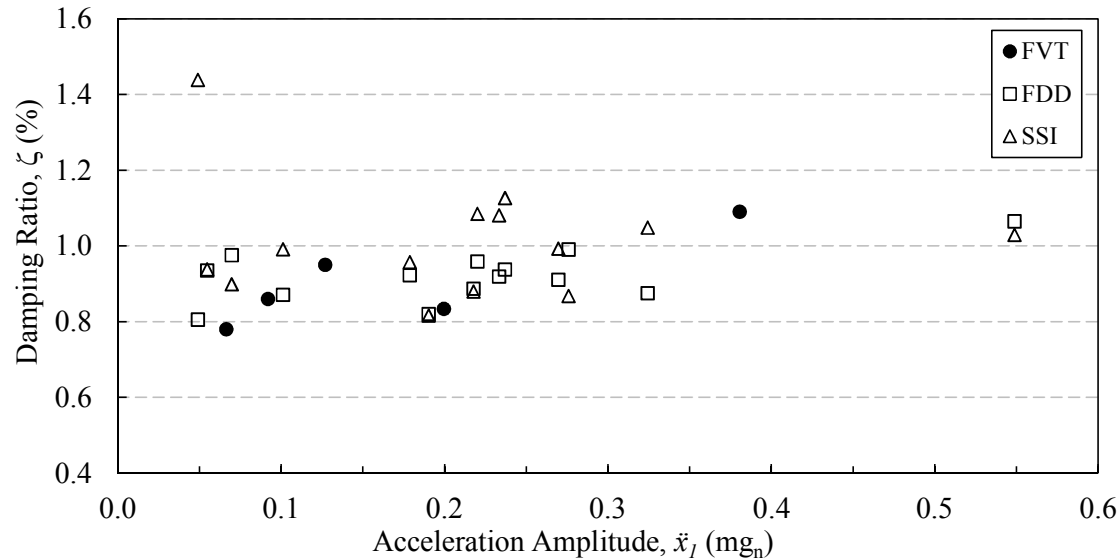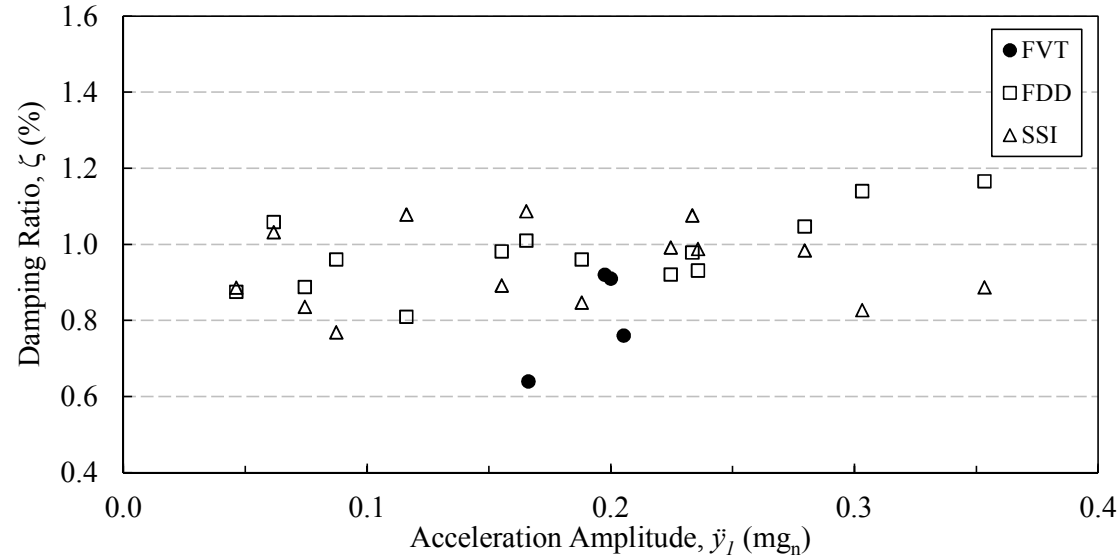

Figure 5.14: Damping ratio versus acceleration amplitude for the fundamental y-axis translation vibration mode during construction.
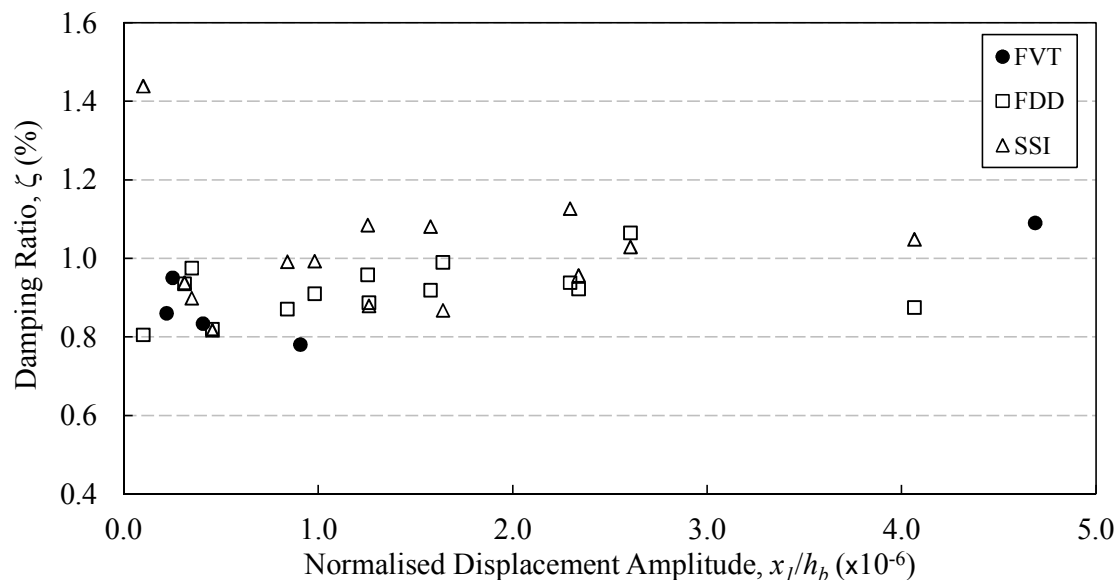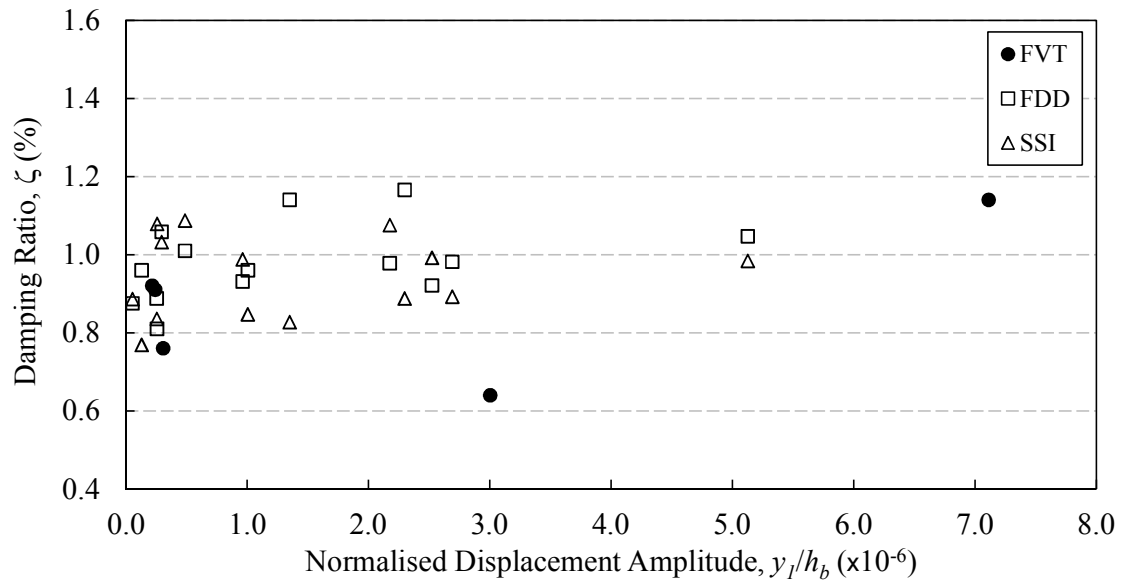
Figure 5.15: Damping ratio versus normalised displacement amplitude for the fundamental y-axis translation vibration mode during construction.

Test Date	$h_{b,\text{core}}$ (m)	FVT			FDD			SSI	
		ζ (%)	σ_ζ (%)	$\ddot{y}_{2\text{max}}$ (mg$_n$)	ζ (%)	σ_ζ (%)	$\ddot{y}_{2\text{max}}$ (mg$_n$)	ζ (%)	σ_ζ (%)
2003-05-27	78.965	0.84	10.8	0.12	–	–	–	–	–
2003-06-17	90.260	0.97	8.2	0.07	0.74	17.2	0.05	0.91	4.0
2003-07-08	94.025	0.94	21.4	0.12	0.84	1.7	0.07	0.85	18.0
2003-08-01	112.850	–	–	–	0.83	7.7	0.09	1.02	43.8
2003-08-07	116.635	–	–	–	–	–	–	–	–
2003-08-27	125.025	–	–	–	0.82	47.4	0.13	1.00	14.9
2003-09-12	129.165	–	–	–	0.90	51.7	0.06	1.10	33.7
2003-09-30	132.930	–	–	–	0.75	19.4	0.18	0.89	19.9
2003-10-10	132.930	–	–	–	0.90	34.0	0.22	0.95	9.2
2003-10-27	144.225	–	–	–	0.88	28.7	0.05	0.76	14.2
2003-11-17	159.285	–	–	–	0.96	24.9	0.14	1.55	6.4
2003-12-17	166.815	–	–	–	0.85	34.1	0.33	1.29	7.6
2004-02-12	193.975	–	–	–	0.86	16.7	0.11	0.82	16.8
2004-03-01	198.040	–	–	–	0.98	26.2	0.14	1.00	12.7
2004-06-07	203.370	0.75	25.2	0.39	0.92	29.2	0.05	1.01	21.7
2004-08-06	203.370	–	–	–	1.07	30.3	0.17	0.90	2.7
2004-12-22	203.370	0.86	5.8	0.29	–	–	–	–	–

Table 5.11: Damping ratios during construction for the fundamental torsion vibration mode.
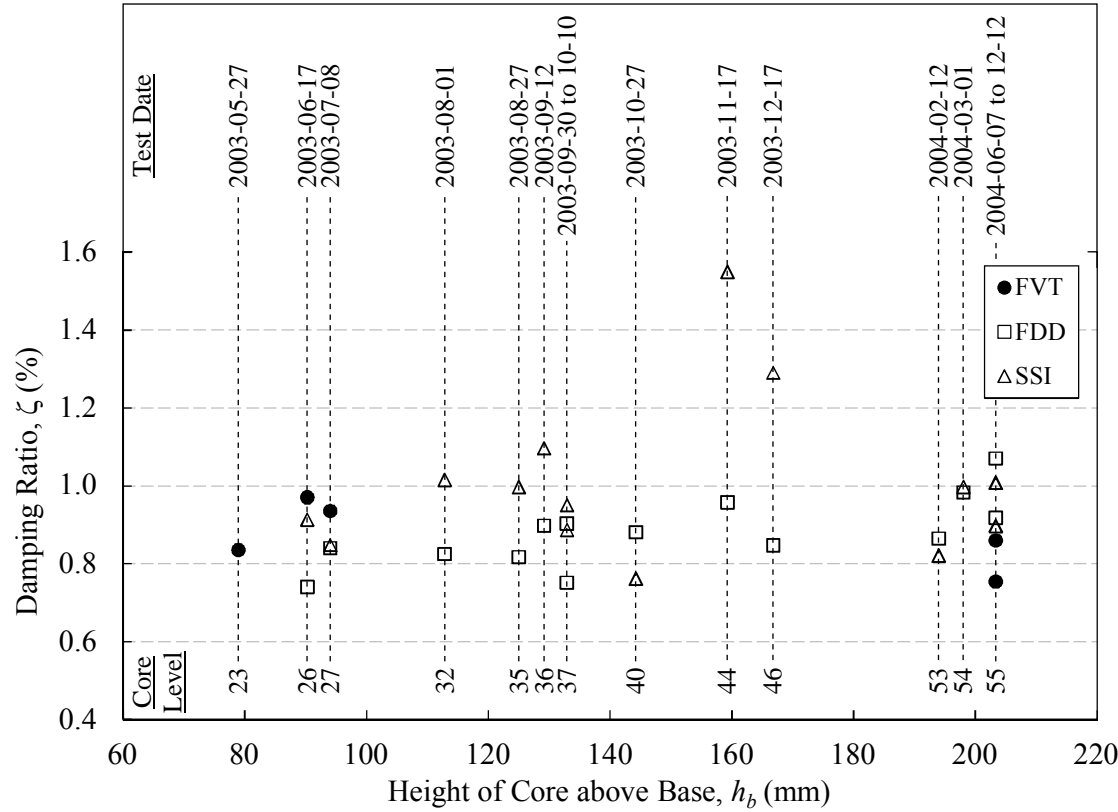
Figure 5.16: Damping ratio versus core height above base for the fundamental torsion vibration mode during construction.
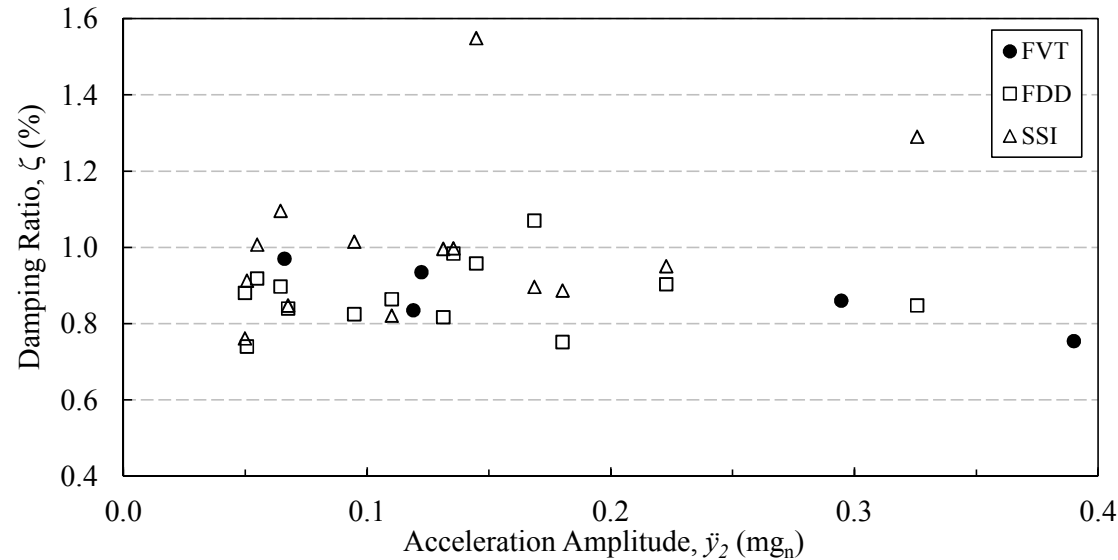
Figure 5.17: Damping ratio versus acceleration amplitude for the fundamental torsion vibration mode during construction.
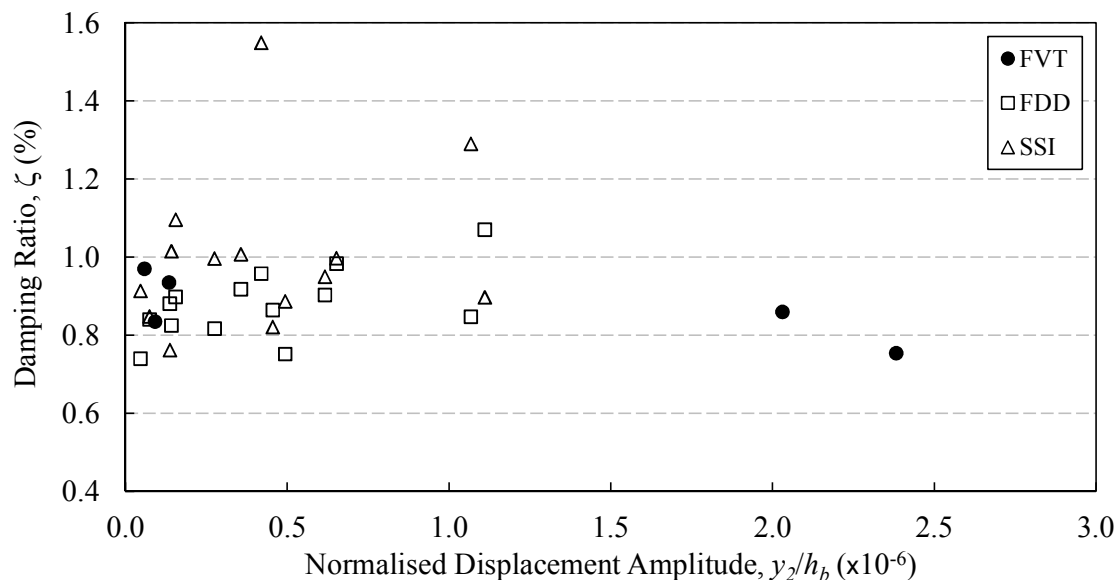
Figure 5.18: Damping ratio versus normalised displacement amplitude for the fundamental torsion vibration mode during construction.

reconfigured into a rentable space.

The damping ratio could be expected to increase during construction as more independent damping mechanisms are added from sources such as the steelwork, facade, and internal fit-out. At first testing the structure was predominantly reinforced concrete, and increasing proportions of steelwork were added. The addition of steelwork means more joints, with the potential to add slipping friction damping mechanisms. Therefore, it could be expected that the damping ratios would increase with the addition of significant amounts of steelwork. Two aspects may contradict this expectation. Firstly, during initial testing the structure included temporary steelwork for construction purposes, which may have introduced slip friction damping mechanisms. Secondly, the levels of vibration may have been insufficient to mobilise damping mechanisms from joint friction in the steelwork.

5.4.2 Comparison with Previous Research

A discussion of previous research on full-scale damping ratio estimates was included in Section 2.3.2. The previous measurements established a range of damping ratios between approximately 0.5–1.5 % for buildings comparable with Latitude tower. In addition, all of the previous research discussed were for measurements recorded during low amplitude events and typically include the structural and aerodynamic components, which is the case for the measured damping ratio estimates at Latitude tower.

During the final stages of construction of Latitude tower, when the core was

complete and only the floor plates, facade, and internal fit-out were being completed, the damping ratios for the fundamental translational modes were between 0.78–1.1 %. For the completed structure, with tenants in the building, the damping ratios were between 0.86–1.0 % — from Tables 4.1 and 4.2. The torsional coupling observed in the fundamental x-axis mode did not correspond with a greater damping ratio for this mode of vibration, which has been observed in other structures [140]. The measured damping ratios for the translational modes at Latitude tower are within the range of measurements on comparable structures.

For the fundamental torsional mode, the damping ratios for the almost completed structure were between 0.75–1.1 %, and when tenants were in the building the range was 0.8–1.0 % for low amplitude vibrations. These values are similar to those discussed in Section 2.3.2.

5.4.3 Amplitude Dependence

The amplitude dependence of the damping ratios for the fundamental vibration modes were determined using the Ranked Random Decrement technique. The results are displayed in Figures 5.19 to 5.21. The number of segments (N_s) used to attain the damping ratio estimates is indicated by the vertical dashed lines. Estimates that are to the right of the $N_s < 2000$ indicator used less than 2000 segments, and another indicator is included for estimates that used less than 200 segments.

The number of cycles (N_c) of the random decrement function used to estimate the damping ratios has a significant influence on the results. For all modes of vibration, the damping ratio estimates typically increase as the number of cycles increases. The increase is greater for between two and three cycles, compared with three and five cycles. For estimates using more than 2000 segments, the y-axis translation mode and the torsional mode display a 30% and 20% gain in the damping ratio estimates between two and three cycles. The gain is reduced to approximately 15% and 10% when the estimates for three and five cycles are compared. This result is similar to that observed by previous research [163], however the magnitude of the change is greater in this case.

For the fundamental x-axis translation mode, damping ratio estimates for acceleration amplitudes below $0.5\,\mathrm{mg_n}$ used more than 2000 segments. For these acceleration amplitudes, all of the damping ratios are greater than 1.5%, and display a decreasing trend with increasing amplitude. This trend is not typical of the amplitude dependent effects on damping ratios [41, 63, 81, 106]. In addition, the estimated values are at least twice the magnitude of the estimates from FVT and AVT tests conducted at the completion of construction, which are displayed in Table 5.9. It is possible that the damping ratio estimates for the x-axis translational mode in Figure 5.19 are distorted by the modal interference between the first and second

modes observed in Figure 4.4.

The amplitude dependence of the fundamental y-axis translation mode is displayed in Figure 5.20. The 2000 and 200 segment threshold are $0.7\,\text{mg}_\text{n}$ and $1.1\,\text{mg}_\text{n}$ respectively, and these values are the largest amongst the fundamental modes. This is expected since the fundamental y-axis translation mode is the first vibration mode, and will therefore be the dominant mode of vibration. The plot displays an increasing damping ratio as the acceleration amplitude increases. The estimates obtained for two cycles have damping values that are approximately 10% larger than the values obtained from FVT and AVT in Table 5.10. Overestimation of damping ratios was also observed in other applications of the Ranked Random Decrement technique [163].

The shape of the plot for $N_c = 2$ in Figure 5.20 displays an initial increase between 0.1–$0.2\,\text{mg}_\text{n}$, followed by a plateau between 0.2–$0.4\,\text{mg}_\text{n}$, and then another increase between 0.4–$0.8\,\text{mg}_\text{n}$. These changes in the rate of increase of the damping ratios could be due to extra damping sources being mobilised as certain amplitude thresholds are reached. Beyond an acceleration amplitude of $0.8\,\text{mg}_\text{n}$, the damping ratio drops by 15% and is followed by another increase. These values beyond $0.8\,\text{mg}_\text{n}$ are expected to be of poor quality due to insufficient segments being used to generate the random decrement function.

Figure 5.21 displays the amplitude dependence of the fundamental torsional mode. The 2000 and 200 segment thresholds are $0.5\,\text{mg}_\text{n}$ and $0.9\,\text{mg}_\text{n}$ respectively. The damping ratio estimates for $N_c = 2$ do not closely match the FVT and AVT values in Table 5.11. The largest difference is approximately 60%. The damping ratio estimates are increasing with increasing acceleration amplitude between acceleration amplitudes 0.1–$0.6\,\text{mg}_\text{n}$, and the slope of the plot is also increasing. This is in contrast to the fundamental y-axis mode, which displayed a mixture of positive slopes and plateaus. For this mode of vibration, the slope of the plot between 0.1–$0.5\,\text{mg}_\text{n}$ suggested that more damping sources are being mobilised with each incremental increase in the acceleration amplitude. As observed with the y-axis translation mode, the damping ratio estimates become more scattered after the number of segments decreases below 2000, and the quality of the estimates becomes insufficient to allow further conclusions to be established.

5.5 Finite Element Analysis

A finite element model was constructed using the Strand7 finite element analysis system [155]. The mass and stiffness parameters used in the model were typical of those likely to be used in a design case for determining the dynamic characteristics. The following sections include a description of the initial assumptions, the updating
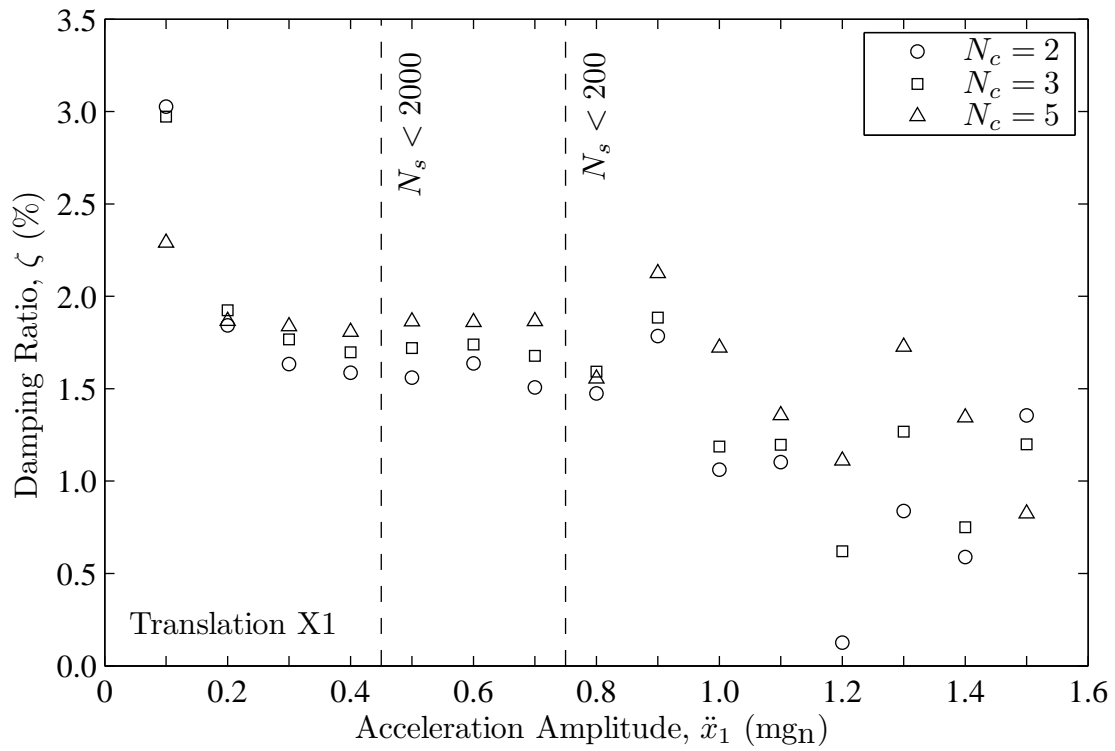
Figure 5.19: Amplitude dependence of the damping ratio for the fundamental x-axis translational mode of vibration (Ranked RD output).
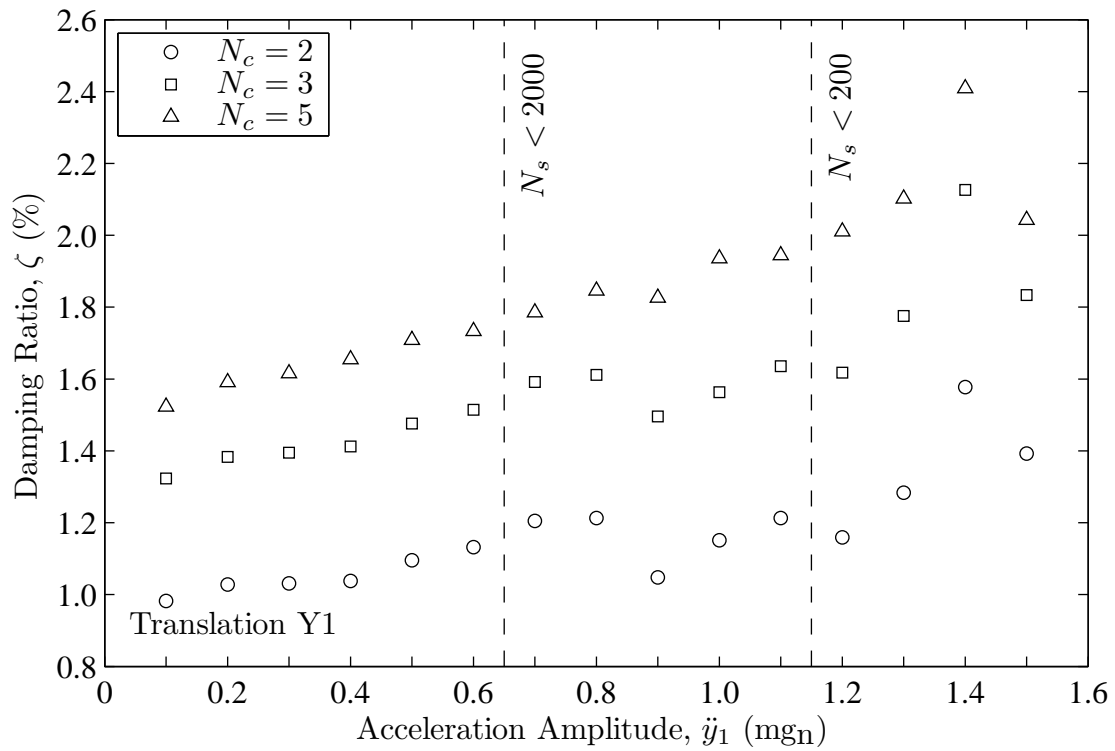
Figure 5.20: Amplitude dependence of the damping ratio for the fundamental y-axis translational mode of vibration (Ranked RD output).
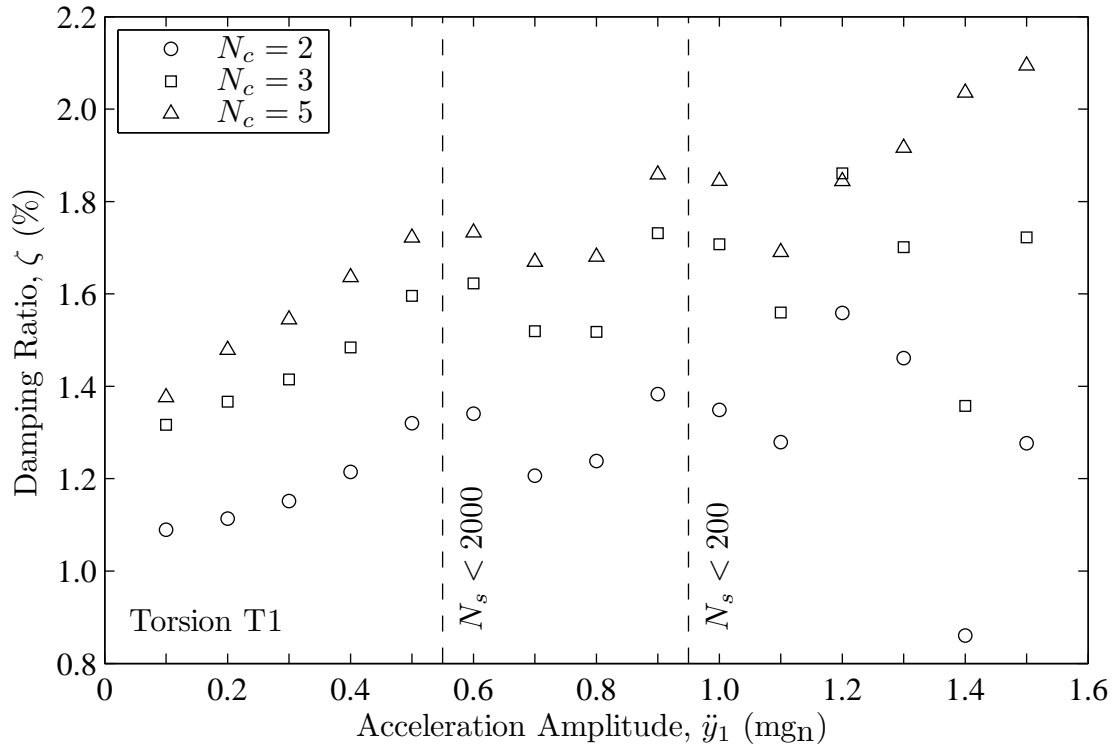
Figure 5.21: Amplitude dependence of the damping ratio for the fundamental torsional mode of vibration (Ranked RD output).

methodology, and the results from comparing both the initial and updated models with full-scale measurements.

5.5.1 Initial Assumptions

Model Detail

Finite element models of tall buildings can range from simple stick models to three dimensional models that closely resemble the prototype. Stick models typically comprise a single vertical beam element that models the vertical distribution of stiffness. Uniform mass properties can be specified for the beam element, or it can be subdivided into multiple segments with lumped masses and rotational masses assigned to the nodes, which model the mass inertia and mass moment of inertia respectively. These lumped masses and rotational masses typically represent the influence of the floor plates, which often contain a significant portion of the total mass.

In order to facilitate the updating process, the level of detail used to create the finite element model for this research was relatively high. Latitude tower comprises a complex structural arrangement compared with more typical tall buildings. The structure below level 16 is relatively simple, with reinforced concrete core walls,

columns, and floor plates. Above level 16, complexities arise due to column transfers between levels 16 to 20, the extended floor plates at level 20 and above, and the outrigger bracing at the plant room between levels 34 and 36. Furthermore, the non-sequential construction method also adds complexities due to the demolition of structural elements at lower levels while construction of upper levels progressed.

Considering the preceding discussion, a three dimensional finite element model of Latitude tower was generated. The model was constructed according to the geometry and dimensions described in Section 3.2. Few simplifying assumptions were used to reduce the geometric complexity of the model. The goal was to create a model that closely resembled the actual geometry of the structure. This would allow fine tuning of mass and stiffness properties during the updating process.

The shear walls and floor slabs were modelled using plate elements that allow both in-plane and out-of plane actions. The in-plane rigidity of the floor slabs was the only source of rigid diaphragm action — no other elements, in addition to the floor slab plates, were used to model the rigid diaphragm action of the floor plates. The columns, braces, and trusses were modelled using beam elements, with appropriate action releases assigned at the beam ends. No structural elements were included to model the facade, as it was deemed to have little influence on the structural stiffness.

Mass Distribution

Due to the level of detail used in the model, most of the structural mass was modelled via the structural elements. The exception was the steel beams supporting the floor slabs, which were excluded from the model. These beams are designed as simply supported members, and the lack of moment actions at the connection to columns means these beams will not contribute to the lateral stiffness of the structure. The mass of these beams was included via the addition of equivalent non-structural mass uniformly distributed over the floor plate area.

The mass of the facade was modelled by a non-structural mass applied around the perimeter of each floor plate. The weight of the facade was estimated to be $0.5\,\text{kPa}$, and for a typical level with a floor height of $3.765\,\text{m}$, this results in a uniformly distributed load of $192\,\text{kg/m}$ applied to the edge of the floor plates. The mass of the fire stairs located on the western facade was also included as a non-structural mass.

Table 5.12 lists the standard dead loads (SDL) and live loads (LL) applied to the model. In the Australian design standard on structural design actions [150], these two loads are known as permanent actions and imposed actions respectively. The SDL represents the mass associated with fittings and finishes, such as floor coverings and false ceilings. The LL represents the mass from the intended use and occupancy of the structure. For models of the structure during construction, the

Floor Type	SDL (kPa)	LL (kPa)
Plant	2.5	7.5
Office	1.1	1.5
Lobby	1.5	4.0
Retail	1.5	2.0
Parking	0.2	2.5

Table 5.12: Standard dead loads and live loads used in the finite element modelling.

		f'_c (MPa)	E_c (MPa)
Core Walls	Typical	50	34800
	L34–L36	80	39600
Columns	L1–L36	80	39600
	L36–L41	60	36500
	L41–L55	40	32800
Floor Slabs	Typical	40	32800

Table 5.13: Concrete properties for the initial finite element model.

SDL values were only applied to levels included in the fit-out, and LL were only applied to occupied levels.

Material Properties

The characteristic compressive strength of concrete at 28 days (f'_c) that was specified on the structural drawings for various structural elements are listed in Table 5.13. The table includes the modulus of elasticity (E_c) for the specified concrete. These values were sourced from the Australian design code for concrete structures [152]. The core walls also included minor sections of masonry infill. These sections were modelled with a modulus of elasticity of 25 000 MPa.

Shear Wall Link Beams

It is typical that some walls within a reinforced concrete core have large openings at each floor level for doors, elevators, and services. The vertical alignment of the openings tends to divide the wall into separate wall segments that are connected via short beams. These beams link the walls, such that the effective depth of the wall section is increased to a value between the individual wall sections and the total wall

section when no openings are present. The modelling of the link beams will have a significant influence on the stiffness of the structure.

For the modelling of Latitude tower, all link beams were modelled with dimensions specified on the structural drawings. No reduction in the effective stiffness of the link beams was modelled since the excitation levels experienced over the life of the structure are significantly less than the lateral loads for the serviceability case, and are therefore unlikely to be cracked.

Boundary Conditions

A description of the foundations is included in Section 3.2.2. Pad footings were used for wall and column foundations, and the underlying ground material is high class Sydney sandstone. In this configuration it is unlikely that significant compression of the underlying ground material under cyclical loading will occur, and the influence on the dynamic characteristics will be negligible [48]. For this reason, the nodal restraints at the base of the structure were assumed to be fixed in the three translational directions. For the below ground levels above the base, a sufficient gap between the structure and the surrounding soil is typically required to prevent forces from rock heave. No other restraints were applied to the model.

Non-structural Elements

The intended use of the tower was for commercial offices, and therefore very few internal partitions were constructed. Any stiffness associated with non-structural elements was not included in the finite element model.

5.5.2   Model Updating Methodology

The are a number of model updating methodologies that have been used in previous research. The most basic method is manually applying updates to the model using knowledge of the structure to select the most appropriate parameters for updating. Previous studies have shown this method can achieve good correlation between experimental results and analytical models for large civil structures [94, 179]. The disadvantage of this method is the time required to iterate the updating process to test alternative structural configurations.

The time disadvantage of the manual method can be overcome by using an automatic updating method. In this method the entire stiffness and mass matrices of the model are subject to changes to produce models that are representative of the system [54]. This automated approach can result in arbitrary changes to system properties in order to force a match between the model and experimental results. A potential outcome is a model with properties that are not physically realisable or

	Measured (Hz)	FEM1 (Hz)	Ratio (–)
f_{x1}	1.261	1.057	1.19
f_{y1}	1.690	1.235	1.37
f_{t1}	2.020	1.522	1.33

Table 5.14: Comparison between measured and FEM1 natural frequencies.

meaningful. A strategy to mitigate this is by placing limitations on the selections of parameters to be modified by the automatic updating process [93, 180]. However, at the end of the process the model changes still need to be reviewed, using sound engineering judgement, to determine if they are realistic.

Compared with automatic updating, the manual updating process has the benefit of avoiding arbitrary changes to system properties to force a match between the finite element model and experimental results. For this reason, a manual methodology was used to update the model using knowledge of the structure and the experimental results recorded during and after construction.

5.5.3 Partial Structure Modelling

A model of the structure on test date 2003-05-27 was created for correlation with the test results. The finite element model for this test date is displayed in Figure 5.22, and is denoted FEM1. The natural frequencies for this model prior to any updating are compared with the measured frequencies in Table 5.14.

Updating Material Properties

Adjusting the stiffness of a structure can have significant impacts on its natural frequencies. Unfortunately, in the case of reinforced concrete structures, accurately determining the modulus of elasticity of concrete is difficult and highly variable. The variability depends on the quality of the supplied concrete, the age of the concrete, and the rate of loading as well as other factors.

The specified concrete strength for the core sections of the test structure was f'_c = 50 MPa. The expected strength of the supplied concrete is likely to be higher than specified, as suppliers are required to ensure no more than 5% of the concrete delivered is below specification. This results in expected compressive strengths that are likely to be approximately 10% greater then specified. Furthermore, these strength values are for concrete at 28 days, which needs to be adjusted by a factor that accounts for strength increases as the concrete ages. Almost all of the concrete in the structure at test date 2003-05-27 was poured more than five years prior. After one year, the Cement and Concrete Association of Australia recommends a factor
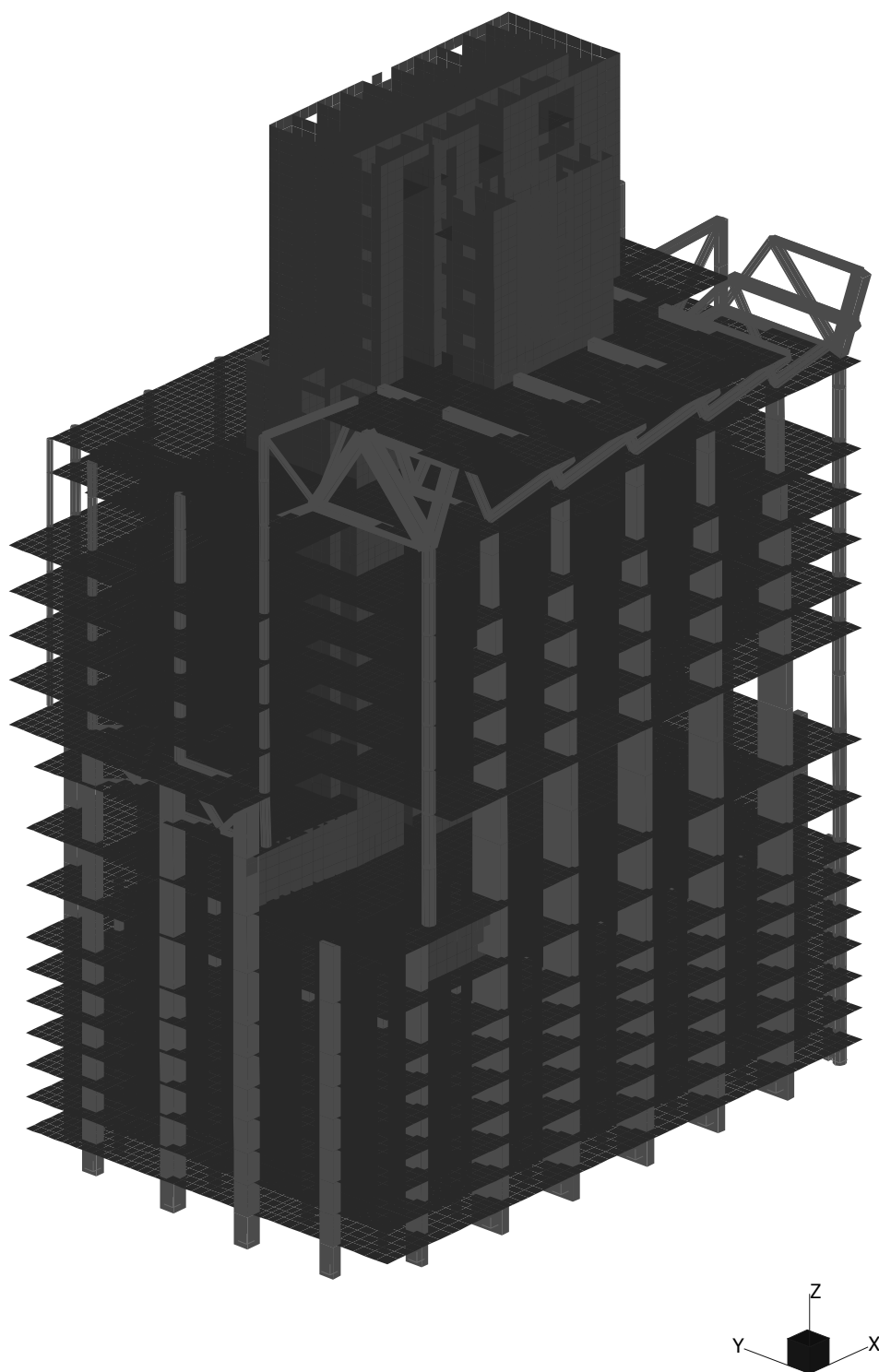
Figure 5.22: Finite element model for test date 2005-05-27.

	Measured (Hz)	FEM2 (Hz)	Ratio (–)
f_{x1}	1.261	1.190	1.06
f_{y1}	1.690	1.411	1.20
f_{t1}	2.020	1.746	1.16

Table 5.15: Comparison between measured and FEM2 natural frequencies.

of 1.3 for normal Portland cement [183]. The strength gains after this time period are significantly less, and the recommended factor has been used in this updating process.

The rate of loading also influences the compressive strength of concrete, resulting in higher reported strengths when concrete is loaded at a faster rate than specified in standard compressive strength tests. Mirza et. al. [119] proposed the following equation to determine the effect of loading rates on the expected elastic modulus of concrete.

$$E_{cR} = (1.16 - 0.08 \log t_{cR}) E_c \tag{5.1}$$

The parameter t_{cR} is the loading duration in seconds, and E_c is the elastic modulus of concrete. This correction is applicable due to the dynamic nature of the loading. The first mode period of vibration for test date 2003-05-27 is approximately $0.8\,\text{s}$, resulting in a $0.2\,\text{s}$ loading duration. Cracking of the core sections was not included in the stiffness estimates due to the continuous compression force applied to core elements, and the lack of prior significant events to cause cracking of the core walls.

Applying the above factors and corrections to the specified concrete for the test structure results in an elastic modulus of approximately $49\,000\,\text{MPa}$, which is approximately 40% higher than the $34\,800\,\text{MPa}$ used in FEM1. This elastic modulus adjustment is included in FEM2, and Table 5.15 indicates the adjusted elastic modulus value has considerably improved the natural frequency estimations. The impact of this change on the natural frequency estimates is greatest for the fundamental mode of vibration. In this case the ratio of the measured to finite element model estimate reduces from 1.19 to 1.06.

Floor Beams

The concrete floor beams were not included in the initial model. These beams are part of the floor plates between levels 2 to 15. The typical dimensions are a depth of 500 mm and a width of 1000 mm. The beams are aligned to the y-axis and span between the core and the perimeter columns. A similarly sized edge beam is located at the perimeter, and is aligned with the centre of the perimeter columns. Table 5.16 displayed the results for FEM3, which includes the concrete beams in the floor

	Measured (Hz)	FEM3 (Hz)	Ratio (−)
f_{x1}	1.261	1.226	1.03
f_{y1}	1.690	1.460	1.16
f_{t1}	2.020	1.780	1.13

Table 5.16: Comparison between measured and FEM3 natural frequencies.

	Measured (Hz)	FEM4 (Hz)	Ratio (−)
f_{x1}	0.303	0.265	1.14
f_{y1}	0.259	0.221	1.17
f_{t1}	0.427	0.401	1.06

Table 5.17: Comparison between measured and FEM4 natural frequencies.

plates for levels 2 to 15.

The addition of the concrete beams to the floor plates increased the natural frequencies from the FEM1 model by approximately 3%. This indicates the floor beams have little influence on the stiffness of the system.

Completed Structure

A finite element model for the structure at test date 2004-12-22 is displayed in Figure 5.23, and is denoted FEM4. At this stage of construction, the main structure was completed and the internal fit-out was being conducted. The SDL assignments reflected the extent of the fit-out. A comparison between the measured natural frequencies and those from FEM4 are displayed in Table 5.17.

The updating conducted in the FEM1 and FEM2 models provided valuable information for improving the natural frequency estimates of the completed structure. This is particularly the case for FEM2, which provided an indication of the likely concrete properties. The knowledge gained from the updates conducted on FEM2 and FEM3 were then applied to the completed model in FEM4 to attain an improved estimate of the natural frequencies for the completed structure. The updates accounted for the reduced concrete age at higher levels of the structure. In addition, the fundamental natural period was 3.9 s, and according to Equation (5.1) the dynamic elastic modulus of the concrete is estimated by a factor of 1.08 times the elastic modulus. Model FEM5 denotes this final updated model, and Table 5.18 compares the measured natural frequencies with the estimates from FEM5.

The updating of the final model using insight gained from updating a partial model of the structure during construction produced improved estimates of the nat-
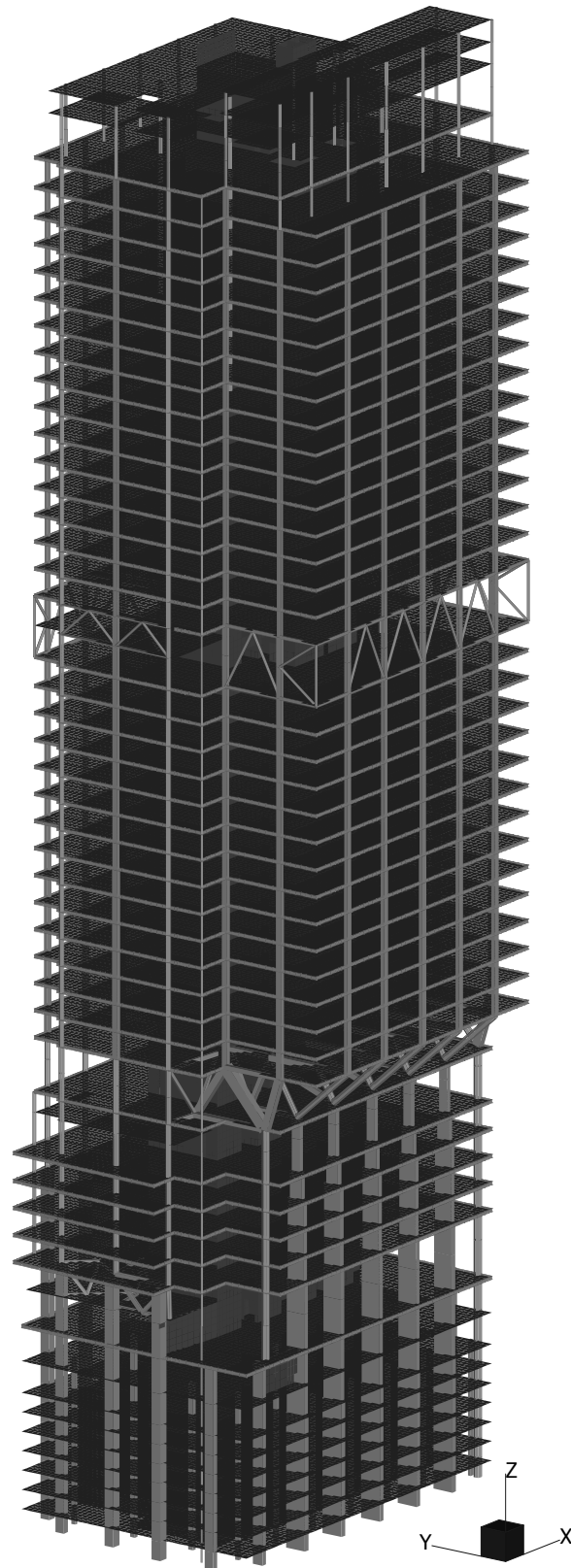
Figure 5.23: Finite element model for test date 2005-05-27.

	Measured (Hz)	FEM5 (Hz)	Ratio (−)
f_{x1}	0.303	0.294	1.03
f_{y1}	0.259	0.243	1.07
f_{t1}	0.427	0.433	0.99

Table 5.18: Comparison between measured and FEM5 natural frequencies.

ural frequencies. The differences between the natural frequency estimates for the updated model and the measured values are less than 7%, and two of the fundamental mode estimates are within 3% of the measured values. This is compared with 17% for the model prior to updating.

The natural frequencies reported for the first two modes from FEM5 are less than the measured values. This implies the full-scale results are indicating the building is stiffer than the estimate from the FE model. The facade and internal partitions were not included in the FEM5 model, and these will have the effect of stiffening the structure. This could explain some of the residual difference between the full-scale measurements and the estimates from FEM5.

Depending on the structure, the extrapolation of structural parameters from the early stages of construction to the completed structure presents a useful approach to validating design assumptions and improving estimates of natural frequencies. It is a technique that can be conducted with a simple vibration test, and could form part of a series of tests that focus on multiple aspects of the structure, such as non-destructive material tests. This approach to improving the design of tall buildings has been applied to more recent building projects that feature some of the worlds tallest structures [130].

5.6   Summary

A comparison between the vibration testing techniques showed the natural frequency results from FVT and AVT were all within 5%. The difference in damping ratio estimates were typically less than 30%, and most results were within 20%. There was no consistent pattern of the AVT techniques either over or underestimating the damping ratios reported by the FVT. The amplitude dependence of the damping ratios did not explain the difference between the techniques. These results show the AVT techniques are suitable for determining estimates of the dynamic characteristics, particularly the natural frequencies. Appropriately conducted forced vibration tests provided the most reliable damping estimates in this instance, however the AVT techniques proved suitable for establishing a damping ratio range from mul-

tiple response records, and is a beneficial technique for determining the dynamic characteristics if FVT is not possible.

Observing the influence of structural components in isolation was difficult due to the simultaneous nature of the construction schedule. Even if tests were conducted immediately before and after a single change was made, the gradual increase in concrete strength meant the impact was unlikely to be observed between the two tests. For concrete structural elements, the impact will be gradual, according to the increase in concrete strength. This is unlike steel structures, where materials have uniform strength over time.

The addition of the facade appeared to have more influence on the mass of the structure and not the stiffness. When the facade was initially added, the natural frequencies for the fundamental modes and second modes were all decreasing at the fastest rate recorded during construction. When the main structure was complete, the influence of the facade could be better observed as the only obscurity was the added mass from internal fit-out. During this stage, all of the natural frequencies decreased, however the decrease in the second modes was less than the decrease in the fundamental modes. This could indicate the facade was increasing the stiffness of the structure, but the additional stiffness was only effective for the second modes of vibration. The stiffening of the second modes and not the fundamental modes is a possibility, since the second modes will have higher components of shear action, and the facade is more likely to provide additional shear strength as opposed to bending strength. Alternatively, the different rates of natural frequency decrease could reflect the mode shape influence on added mass in the structure. Increasing the mass at the top of the building will have more influence on the fundamental modes, due to the mode shapes, as opposed to the second modes of vibration. It is possible that a combination of added mass and stiffness was provided by the facade, however there was no evidence in the results to support the latter.

By conducting a vibration test during the early stages of construction at Latitude tower, the uncertainty in the estimation of the dynamic characteristics was reduced. The updating of the finite element model for the partially completed structure yielded improved estimates for the natural frequencies from the model of the completed structure, from within 17% to 7% error. The lack of internal partitions coupled with the level of detail in the model put focus on the material properties as the major source of error in the natural frequency estimates. This assumes the facade has negligible stiffness contributions and the total mass has been accurately modelled. This made a strong case for underestimation of concrete strength as a likely source of natural frequency underestimation, as opposed to stiffness gains from internal partitions, which were not prevalent throughout the structure.

Comparing the measured and predicted natural frequencies, it is observed that

further understanding of the mechanisms that affect the dynamic behaviour of tall buildings is achievable. By accounting for the over specification of concrete strengths and the loading rate effects on concrete stiffness due to dynamic loading, a higher elastic modulus was estimated and used for sections of the core where typical design elastic modulus values had been initially specified. Furthermore, the inclusion of the floor plate beams was shown to improve the natural frequency estimates by approximately 4% for the translational vibration mode aligned with the beams.

The low amplitude damping ratio estimates were confirmed by a vibration test at the early stages of construction. The damping ratios during construction were typically between 0.8–1.1 %, 0.8–1.2 %, and 0.7–1.1 % for the fundamental x-axis translation, y-axis translation, and torsional modes respectively. Amplitude dependence of the damping ratios during construction was observed for the translational vibration modes, and accounted for some of the range in the measured damping ratios during construction. Considering the tolerances in the estimates, a vibration test conducted at 38% of final building height yielded a similar result to the final measurement. The difference in the damping ratio estimates between the 38% and 100% completion points was less than 15% for all modes of vibration, and taking account of the different amplitudes used for each test. This result reduces the damping ratio estimation uncertainty at an early stage of construction, and for wind sensitive buildings with similar structural systems as Latitude tower, this approach could be used to confirm auxiliary damping requirements, and their design if necessary. It is noted that the damping ratio estimates from AVT include the structural and aerodynamic damping components, however the latter is expected to be negligible considering the low vibration amplitudes observed during testing.

For the structure used in this research, vibration testing during construction was an effective strategy to mitigate uncertainty in the dynamic properties. The benefit arises from early detection of dynamic properties that deviate from those used in design, and the potential to reduce the cost of subsequent remedial works via the early detection.

Chapter 6

Wind-induced Response

6.1   Introduction

The successful design of tall buildings relies on accurate estimations of the expected forces and responses. Each tall building is unique, and often comprises significantly different structural systems and geometries compared with previous designs. The verification of the design is only achievable once the structure is completed and a full-scale test is conducted. This is unlike other industries that have the ability to iteratively improve the prototype design via full-scale testing. This approach is infeasible for large civil engineering structures, both financially and practically. This means tall building design is entirely reliant on response estimation techniques, which include theoretical, empirical, numerical, and scaled model testing.

The full-scale testing of tall buildings allows the verification of the response estimation techniques, as well as gaining further understanding of the wind-induced response of tall buildings. This chapter focuses on these two aspects. The results of the the wind-induced response monitoring programme at Latitude tower are presented and discussed. The monitoring programme included the measurement of the wind velocity, accelerations, and displacements at the top of the building. A description of the wind characteristics recorded at Latitude tower is presented, followed by the acceleration and displacement response measurements. The final section compares the full-scale acceleration response measurements with estimates from a scaled model wind tunnel test.

6.2   Wind Events

Before analysing the recorded wind events a wind tunnel test was conducted to determine the influence of the structure on the wind speeds and turbulence intensities at the anemometer location. A 1:400 scale rigid model of Latitude tower and surrounds was tested in the Boundary Layer Wind Tunnel at the School of Civil

Engineering, The University of Sydney. A detailed description of the wind tunnel configuration is included in Section 6.4.2. A hotwire anemometer was used to measure the wind speeds at the anemometer location, and a Pitot-static tube was used to determine the mean wind speed of the free stream. The Pitot-static tube was positioned upstream of the model and at the same height as the hotwire anemometer. Tests were conducted at 10° intervals. The relationship between the cardinal wind directions and the building orthogonal axes are defined in Figure 3.18.

Figure 6.1 displays the influence of the structure on the wind speeds at the anemometer location. The values plotted on the radial graph are the ratios of the hotwire wind speeds at the anemometer location to the free stream mean wind speed. The location of the anemometer in the south-west corner of the roof was expected to be detrimental to the recording of wind events originating from azimuths between 0–90°, which is confirmed by the variability of the results for this range. Winds approaching from southerly directions have ratios that are approximately one, which indicates there was little impact from the structure on the wind speeds measured by the anemometer. For the ranges 100–130° and 240–330°, the ratio is approximately 1.1, which indicates an increase in the wind speeds at the anemometer location due to the structure. All subsequent mean wind speed results have been corrected using the ratios in Figure 6.1.

The wind tunnel test was repeated using a TFI Cobra Probe to determine the influence of the building and surrounds on the turbulence intensities at the anemometer location. Figure 6.2 is a plot of the turbulence intensities measured by the Cobra Probe. Similar to the velocity corrections, the turbulence intensities have significant variability between 330–110°. A terain category 3 profile was used in the tunnel, as shown in Figure 6.32, which according to AS1170.2-2011 has a turbulence intensity of 0.14. Figure 6.3 reproduces the section of turbulence intensities between 90–330° on a finer scale. Between 120–300° the turbulance intensities are typically within the range of 0.120–0.145°, which is comparable to the AS1170.2-2011 value.

As for the velocity correction results, the erroneous turbulence intensity values between the NW and SE directions are due to the influence of the Latitude tower roof structure and also the close proximity of World Tower directly to the north. Therefore, results for wind directions in this zone are not discussed in the following sections.

6.2.1 Distribution of Mean Wind Speeds

The monitoring of the wind-induced response of Latitude tower commenced on 15 August 2005 and ended on 23 April 2007. A total of 13562 records of 17 minute lengths were recorded during this period. A distribution of the anemometer and accelerometer measurements according to time and wind direction is displayed in
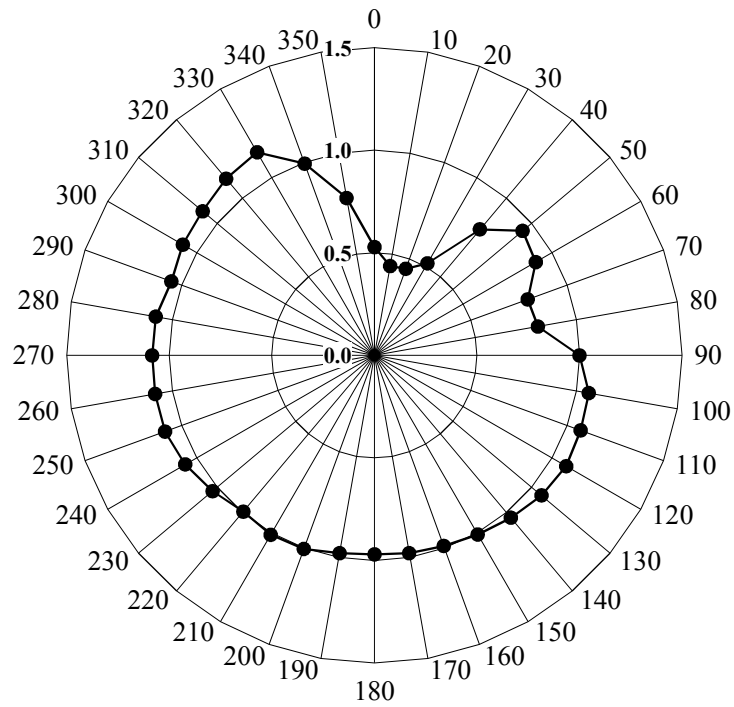
Figure 6.1: Latitude tower anemometer velocity corrections from wind tunnel test.
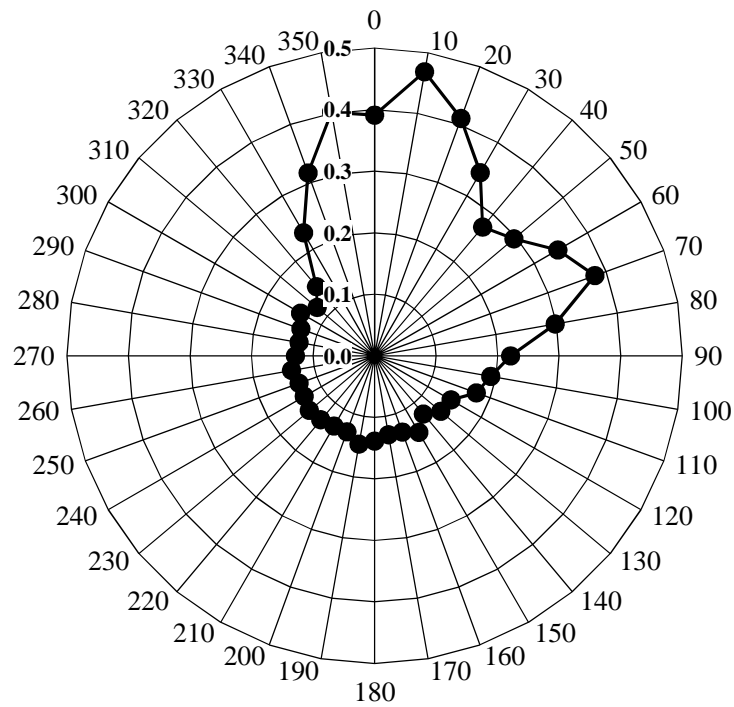
Figure 6.2: Latitude tower wind tunnel measurements of turbulence intensity at anemometer location.
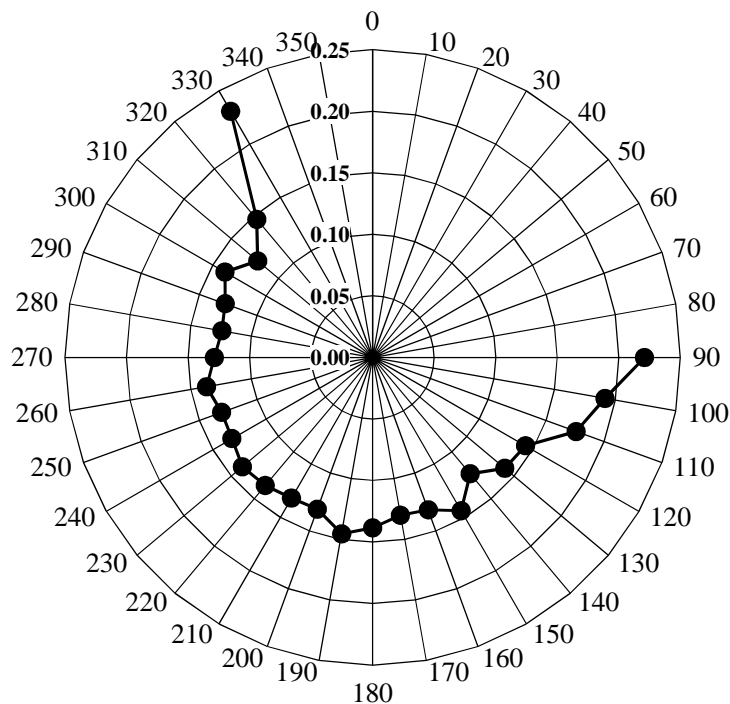
Figure 6.3: Latitude tower wind tunnel measurements of turbulence intensity at anemometer location.

Figure 6.4. Each point on the graphs represents a single record. The colour of the point indicates the mean wind direction for the record. In the mean wind speed plot, the diameter of the plotted points indicates the turbulence intensity. It is observed that as the mean wind speed increases the point diameters are decreasing, and therefore the turbulence intensity is decreasing with increasing mean wind speed.

The standard deviation acceleration plots in Figure 6.4 indicate the largest acceleration responses were recorded during southerly wind events. Similar mean wind speeds were also recorded for westerly wind events, however the acceleration responses in the east-west direction are significantly less than the north-south acceleration responses for southerly wind events. This is likely due to the fundamental vibration mode being a translation in the north-south direction.

Two gaps in the data set are observed during November 2005 and June/August 2006. These gaps were due to data acquisition hardware failures. Finally it is noted that the data acquisition trigger condition was disabled in November 2006. The trigger condition was originally set for a wind speed threshold of 5 m/s. The disabling of the trigger condition is the reason for the increase in low wind speed measurements from late November 2006 till the end of the monitoring programme.

The distribution of the mean wind speeds recorded at Latitude tower are displayed as a wind rose in Figure 6.5. A majority of the strong wind events recorded during the monitoring programme originate from southerly and westerly directions.
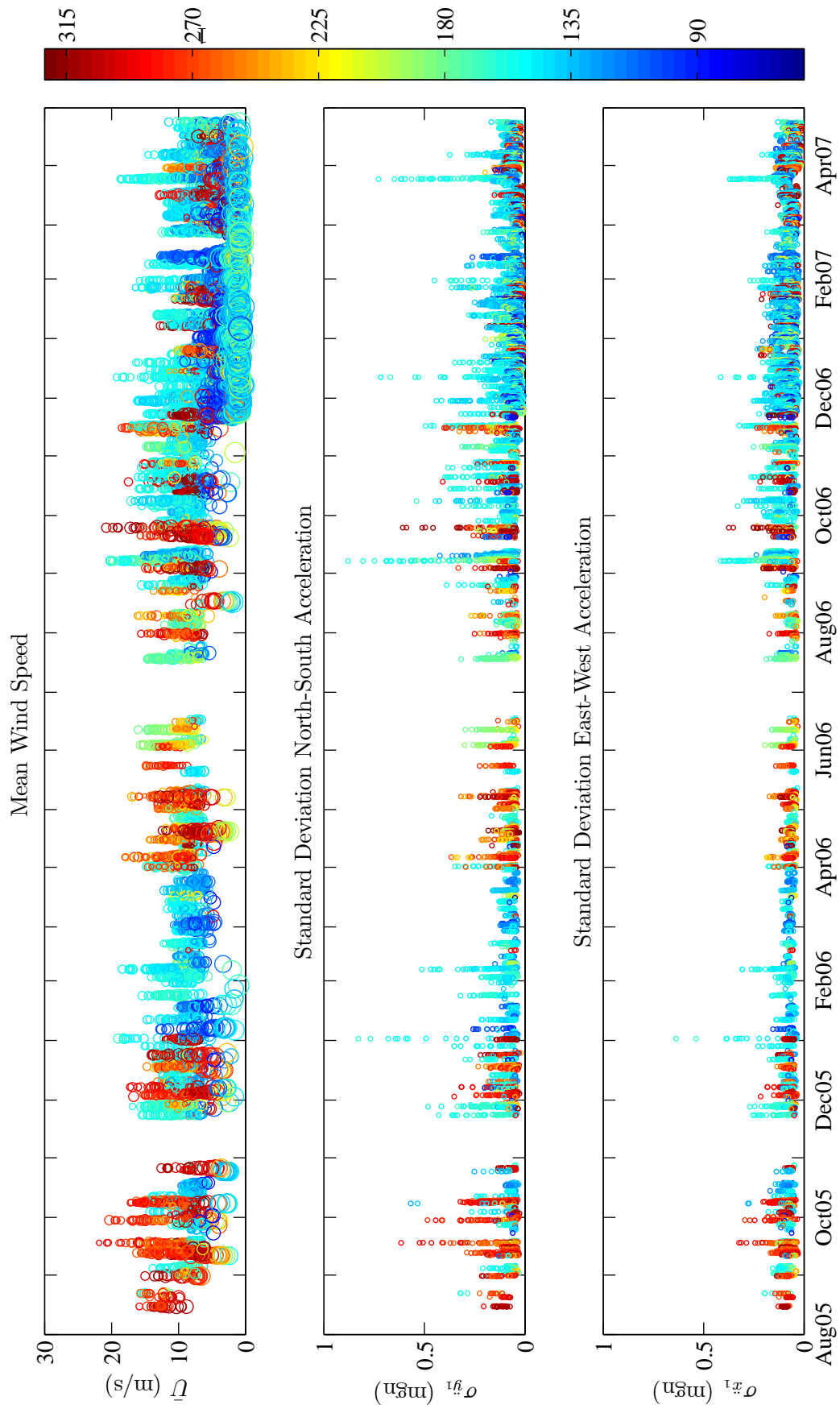
Figure 6.4: Temporal and directional distribution of measurements from the Latitude tower anemometer and accelerometers.

The wind rose also illustrates the lack of measurements for directions between 315–90° due to the anemometer being located within the influence zone of the structure. Regardless of moving the anemometer out of the influence zone of Latitude tower for all wind directions, the location and proximity of World Tower to the north of Latitude tower would also prevent the measuring of the free stream wind velocity from azimuths between approximately North and North-East.

For comparison, a wind rose for the Sydney Airport anemometer is presented in Figure 6.6. This anemometer is positioned at approximately 10 m height, and its location relative to Latitude tower is displayed in Figure 3.16. The same time period as the monitoring programme at Latitude tower was used to generate the Sydney Airport wind rose. As for the Latitude tower wind rose, the southerly and westerly directions yielded a greater proportion of strong wind events. Significant mean wind speeds originating between directions 0–90° are also observed in the Sydney Airport wind rose.

Comparing the wind roses for Latitude tower and Sydney Airport, it is observed that a greater number of low wind speed records are included for the latter. There are two reasons for this difference. Firstly, the anemometers are located at different heights, and since wind speed increases with height for boundary layer synoptic winds, the Latitude tower anemometer is expected to record higher wind speeds. For a terrain category of 3, the ratio of the mean wind speed at 10 m to the mean wind speed at 187 m is approximately 0.54, and increases to 0.65 for terrain category 2 [149]. In addition to the height difference, the minimum wind speed threshold trigger condition used in the data acquisition at Latitude tower will also cause greater proportions of higher wind speeds to be recorded at Latitude tower compared with Sydney Airport, which continuously records the local wind velocity.

Another difference between the wind roses is the Latitude tower results indicate the dominant winds originate from the SSE direction, while the Sydney Airport results indicate a S direction. This discrepancy may be due to differences between the local surrounds at each of the anemometers. For example, the Latitude tower anemometer may incur directionality influences from the flow pattern around Latitude tower. Furthermore, the discrepancy may be exaggerated by the relatively coarse direction resolution used in the wind rose plots.

The scale of the wind events recorded during the monitoring period are relatively small compared with typical return periods used in design. The one year return period event as defined in AS1170.2-2009 did not occur during the monitoring period. A more detailed comparison between the Latitude tower and Sydney Airport anemometers could be undertaken, such as transfering the airport data to the Latitude tower anemometer location. However, in light of the low return period wind events experienced a more detailed comparison was deemed unecessary for the
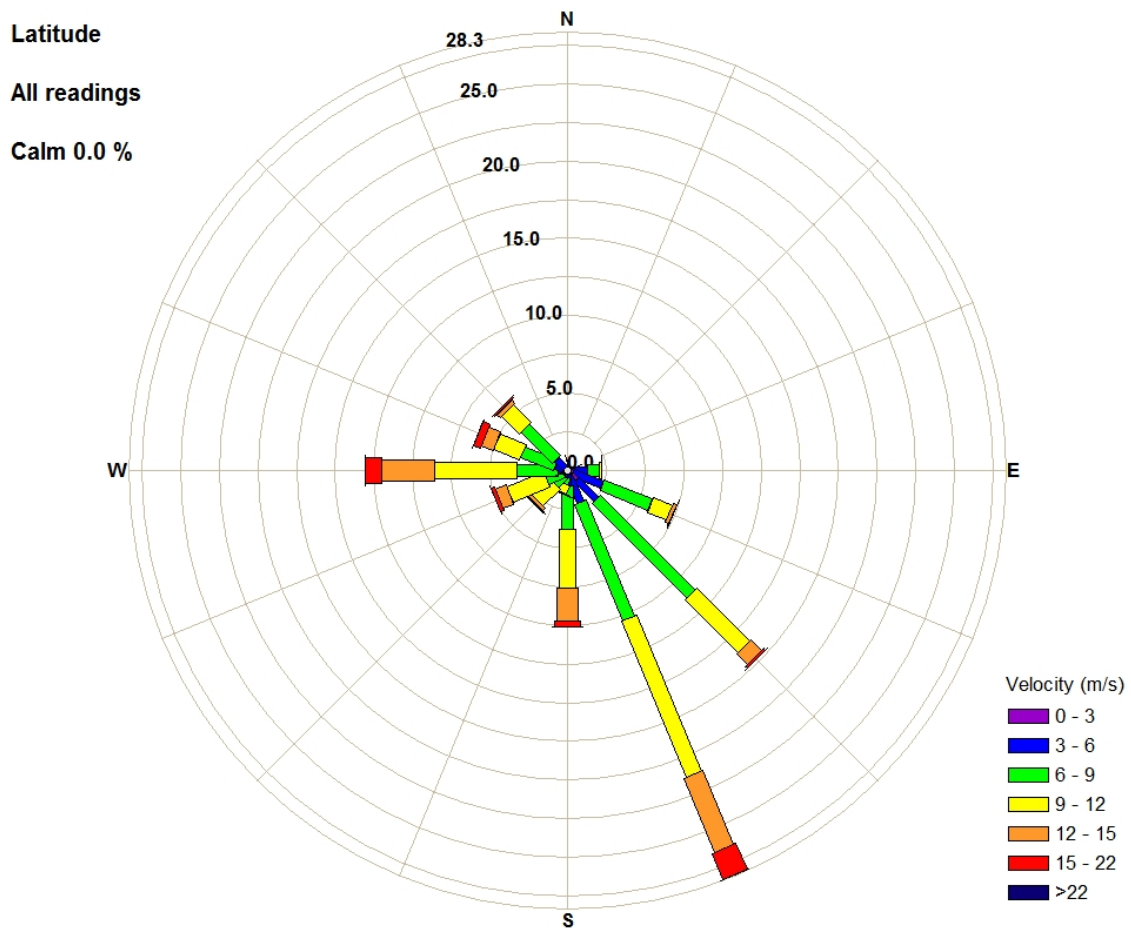
Figure 6.5: Wind rose for the Latitude tower anemometer for August 2005 to May 2007.

purposes of the research.

6.2.2   Turbulence Intensity

The fluctuations in wind velocities, and the resulting fluctuations in forces on structures, represent a form of dynamic loading that may cause resonance in wind sensitive structures. It is therefore important to quantify the fluctuating component of wind velocities when investigating the dynamic response of structures to wind loading. Fluctuations in wind velocities are also known as turbulence, and the level of turbulence in wind speed measurements can be determined by calculating the standard deviation of the wind speed components. The components correspond to the horizontal longitudinal component $u(t)$, the horizontal lateral component $v(t)$, and the vertical component $w(t)$. The ratio of the standard deviation of the component to the mean value is known as the turbulence intensity.

Table 6.1 displays the mean values of the turbulence intensity for the horizontal longitudinal component. The results are for record lengths of 10 minutes. All of the records from the monitoring programme were grouped according to wind speed and
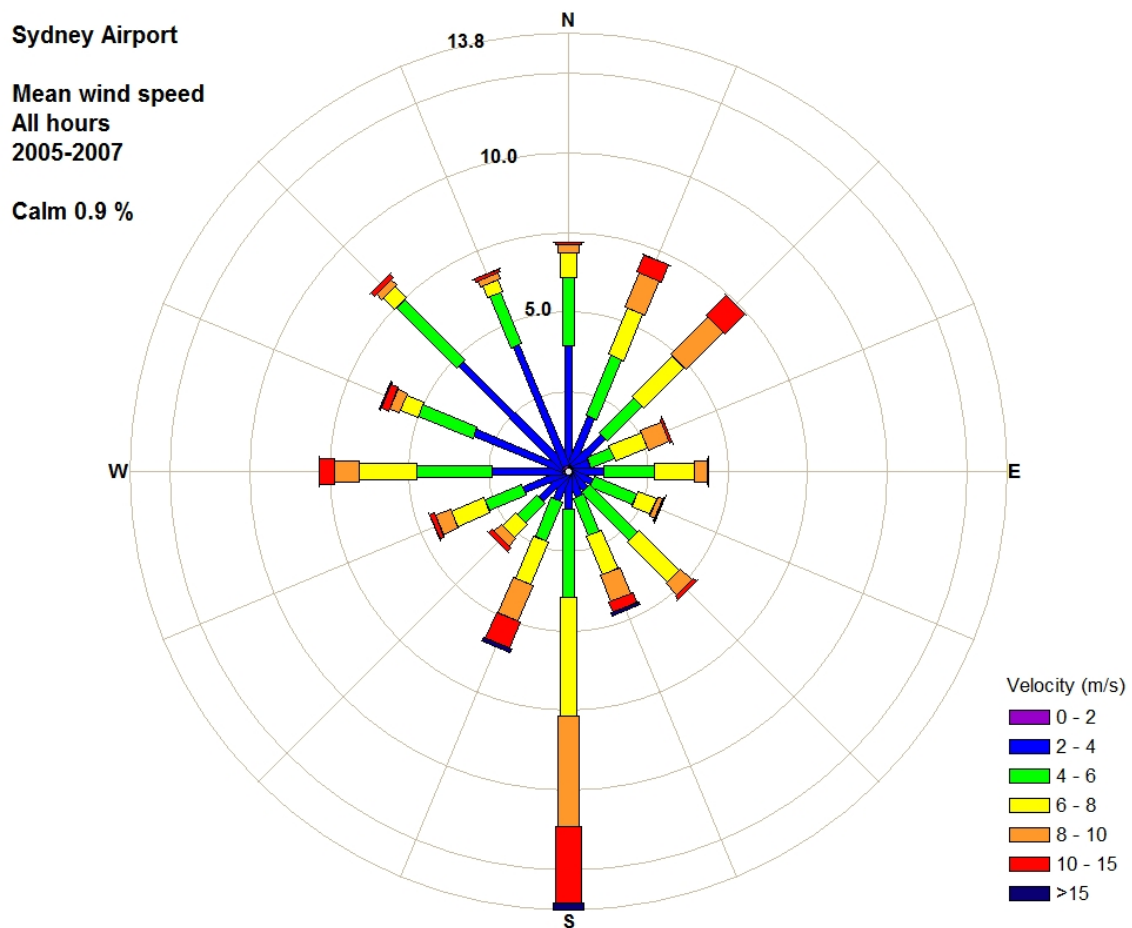
Figure 6.6: Wind rose for the Sydney Airport anemometer for August 2005 to May 2007.
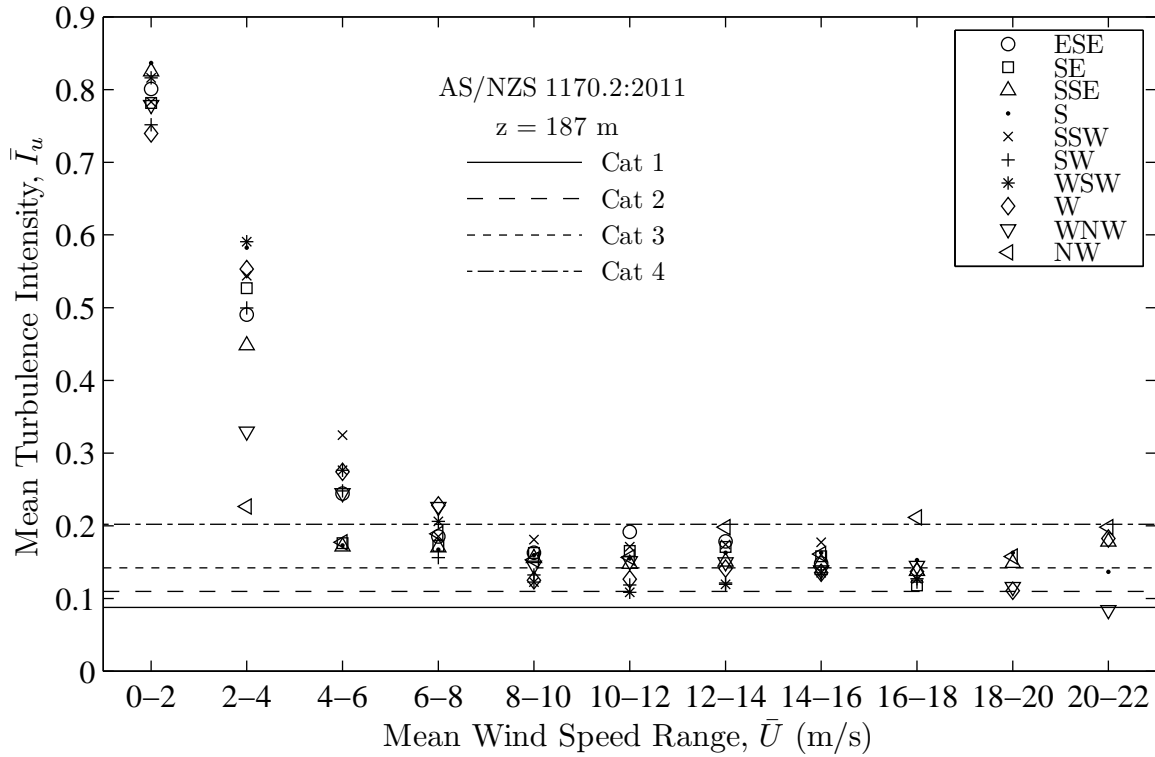
Figure 6.7: Mean turbulence intensity versus mean wind speed for the Latitude tower anemometer measurements.

direction, and the mean turbulence intensity values are reported for each of these groups. The results are plotted in Figure 6.7, in addition to the turbulence intensity estimates from the current Australian wind code [153] for terrain categories 1 to 4.

For mean wind speeds less than 6 m/s, the mean turbulence intensities for all directions are typically greater than the Australian wind code values. For mean wind speeds greater then 8 m/s, the mean turbulence intensity values are mostly between the Australian wind code estimates for terrain categories 2 and 4. Focusing on the SSE and W directions, the mean turbulence intensity is approximately equal to a terrain category 3 estimate when the mean wind speed is between 8–18 m/s. For mean wind speeds in the range 20–22 m/s, the values increase to 0.18, which is 10% less than a terrain category 4 estimate. For the WNW direction, the turbulence intensity drops to approximately 0.1 for wind speeds between 20–22 m/s, which is equivalent to a terrain category 1. This result is unexpected since the terrain to the west of Latitude tower comprises urban areas equivalent to terrain category 3. However, turbulence characteristics in different meteorological and micro-meteorological events can be highly variable, even during the same event as observed in Figures 6.21 and 6.22.

The horizontal longitudinal wind speed was the only component recorded by the Latitude tower anemometer. Despite not recording the horizontal lateral component,

$\bar{U}$	ESE		SE		SSE		S		SSW	
(m/s)	$\bar{I}_u$	σ_{I_u}	$\bar{I}_u$	σ_{I_u}	$\bar{I}_u$	σ_{I_u}	$\bar{I}_u$	σ_{I_u}	$\bar{I}_u$	σ_{I_u}
$0-2$	0.80	0.11	0.78	0.12	0.82	0.13	0.84	0.11	0.78	0.10
$2-4$	0.49	0.20	0.53	0.24	0.45	0.28	0.58	0.23	0.54	0.20
$4-6$	0.24	0.12	0.18	0.07	0.17	0.06	0.17	0.07	0.32	0.21
$6-8$	0.19	0.06	0.17	0.05	0.17	0.05	0.17	0.05	0.19	0.04
$8-10$	0.16	0.05	0.16	0.04	0.16	0.04	0.16	0.04	0.18	0.04
$10-12$	0.19	0.06	0.17	0.04	0.15	0.04	0.15	0.03	0.17	0.03
$12-14$	0.18	0.03	0.17	0.05	0.15	0.04	0.16	0.03	0.17	0.03
$14-16$	0.15	0.03	0.16	0.04	0.15	0.04	0.16	0.03	0.18	0.02
$16-18$	–	–	0.12	0.03	0.14	0.03	0.15	0.03	–	–
$18-20$	–	–	–	–	0.15	0.03	0.16	0.03	–	–
$20-22$	–	–	–	–	0.18	0.01	0.14	0.01	–	–

$\bar{U}$	SW		WSW		W		WNW		NW	
(m/s)	$\bar{I}_u$	σ_{I_u}	$\bar{I}_u$	σ_{I_u}	$\bar{I}_u$	σ_{I_u}	$\bar{I}_u$	σ_{I_u}	$\bar{I}_u$	σ_{I_u}
$0-2$	0.75	0.13	0.82	0.13	0.74	0.08	0.78	0.17	–	–
$2-4$	0.50	0.21	0.59	0.17	0.55	0.13	0.33	0.18	0.23	0.11
$4-6$	0.25	0.22	0.28	0.24	0.27	0.23	0.24	0.19	0.18	0.11
$6-8$	0.16	0.05	0.21	0.17	0.23	0.18	0.23	0.14	0.19	0.10
$8-10$	0.13	0.04	0.12	0.05	0.12	0.07	0.15	0.09	0.15	0.10
$10-12$	0.12	0.05	0.11	0.04	0.13	0.06	0.15	0.06	0.16	0.09
$12-14$	0.12	0.04	0.12	0.03	0.14	0.05	0.15	0.06	0.20	0.05
$14-16$	0.13	0.02	0.14	0.05	0.14	0.04	0.14	0.03	0.16	0.02
$16-18$	0.12	0.03	0.13	0.03	0.14	0.03	0.14	0.04	0.21	0.07
$18-20$	–	–	–	–	0.11	0.01	0.12	0.02	0.16	0.01
$20-22$	–	–	–	–	0.18	0.01	0.08	0.02	0.20	0.01

Table 6.1: Mean and standard deviation turbulence intensity for the Latitude tower anemometer measurements.
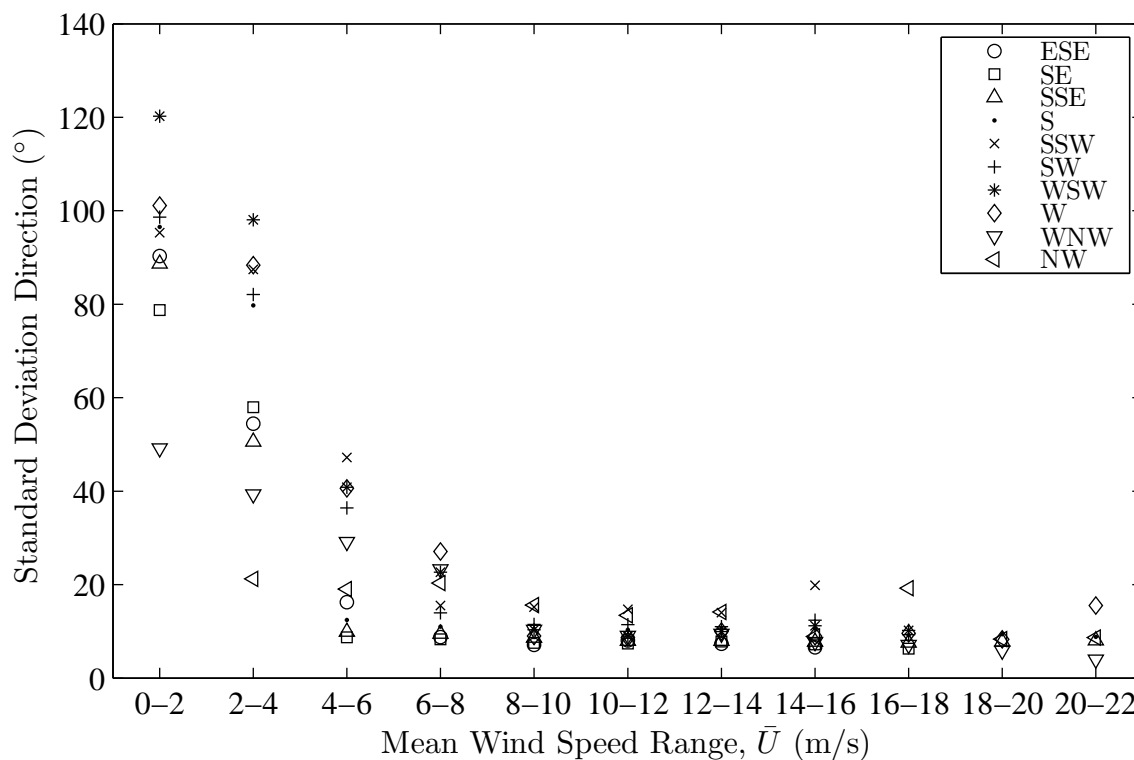
Figure 6.8: Standard deviation wind direction versus mean wind speed for the Latitude tower anemometer measurements.

an indication of the turbulence intensity for this component can be attained via the recorded wind direction. Figure 6.8 and Table 6.2 display the standard deviations of the wind directions, with grouping according to mean wind speed and direction. As observed for the longitudinal component, for mean wind speeds above 8 m/s the standard deviation direction values tended to stabilise at approximately 10°.

6.2.3 Wind Spectrum

Converting the wind speed time series measurements to the frequency domain provides a description of the distribution of turbulence according to frequency. The frequency content of wind fluctuations is of interest when considering the dynamic response of wind sensitive structures. Resonance will occur if the natural frequencies of such structures coincide with frequency bands in the wind spectrum that contain significant energy from wind fluctuations. With regard to the along-wind response, it is the buffeting of the structure from the approaching wind fluctuations that will cause a dynamic response in the along-wind direction [40, 181]. A majority of the wind fluctuation energy is typically at frequencies that are much lower than the fundamental natural frequency of most tall buildings, and the energy decreases with increasing frequency.

Figures 6.9, 6.10, and 6.11 display the spectrum of wind speeds for directions

$\bar{U}$	Standard Deviation Wind Direction (°)									
(m/s)	ESE	SE	SSE	S	SSW	SW	WSW	W	WNW	NW
$0-2$	90	79	89	97	95	99	120	101	49	–
$2-4$	54	58	51	80	87	82	98	88	39	21
$4-6$	16	9	10	12	47	36	41	41	29	19
$6-8$	9	8	10	11	16	14	23	27	23	20
$8-10$	7	8	9	11	15	11	10	9	10	16
$10-12$	8	7	8	10	15	11	9	9	9	13
$12-14$	7	8	8	11	14	11	10	10	9	14
$14-16$	7	7	8	11	20	12	11	9	8	9
$16-18$	–	6	8	9	–	9	10	10	7	19
$18-20$	–	–	8	9	–	–	–	8	6	8
$20-22$	–	–	8	9	–	–	–	16	4	9

Table 6.2: Standard deviation wind direction for the Latitude tower anemometer measurements.

160°, 275°, and 287° respectively. The spectra are calculated from an hour time series that correspond to peak events recorded during the monitoring programme. The measurements collected during the monitoring programme were recorded at 17 minute intervals, and hour length records were generated by combining adjacent 15 minute records. The data was first corrected using Figure 6.1. The spectrum for 160° closely matches the estimated distribution from the Australian wind code [153]. For reduced frequencies below 0.05, the spectra for 160° and 275° are greater than the code estimates, while the 287° spectra is less than the code estimate. This is due to variations in the mean wind speeds for the hour long time series used.

The spectrum for 275° reports lower energy levels at reduced frequencies greater than two. This implies the measured wind fluctuations contain less energy at the higher frequencies compared with the code estimate. Similarly, the spectrum for 287° is indicating lower energy levels across the entire redeuced frequency range. The fundamental natural frequencies of Latitude tower correspond to reduced frequencies of between 2–3 on wind spectrum plots. Therefore, using the code estimate of the wind spectrum for the 275° and 287° wind directions will overestimate the final along-wind response compared with the measured spectrum.

6.3   Wind-induced Response

The wind-induced response of Latitude tower was monitored via the recording of accelerations and displacements at the top of the building. The equipment specification and configuration is included in Sections 3.3 and 3.5. The following sections discuss
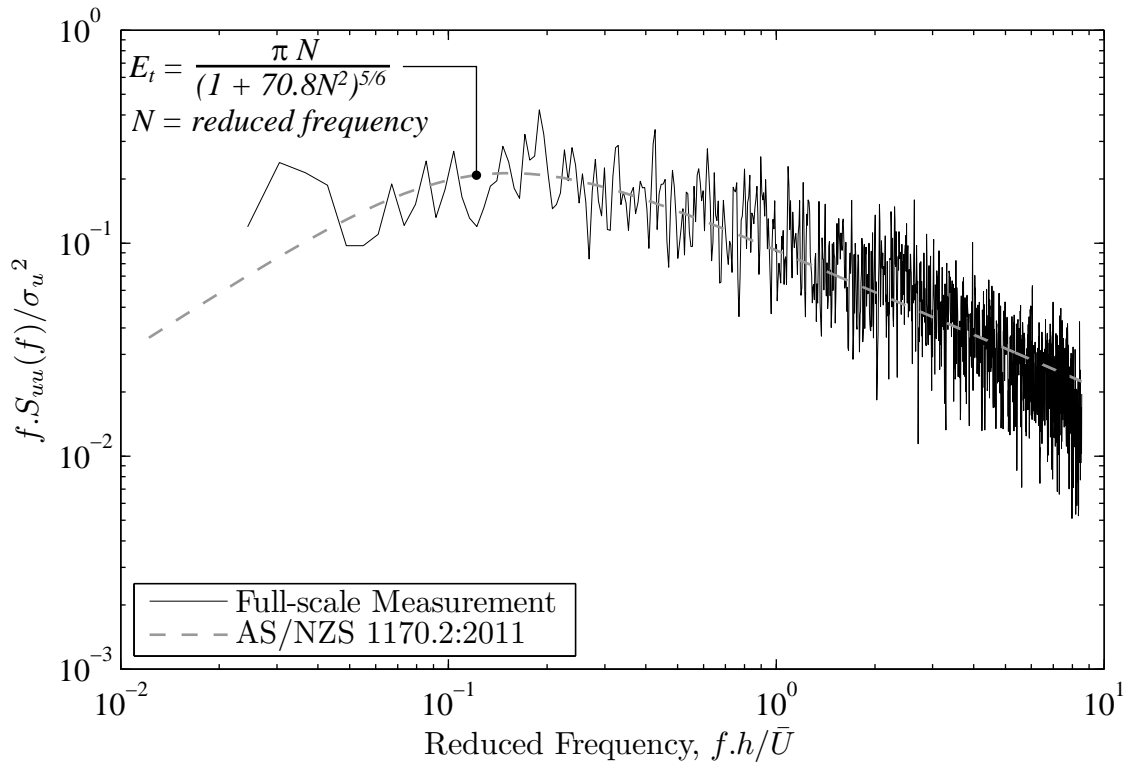
Figure 6.9: Spectrum of longitudinal wind velocity for 2006-09-07 08:30. Mean wind direction = 160° (h=187 m)
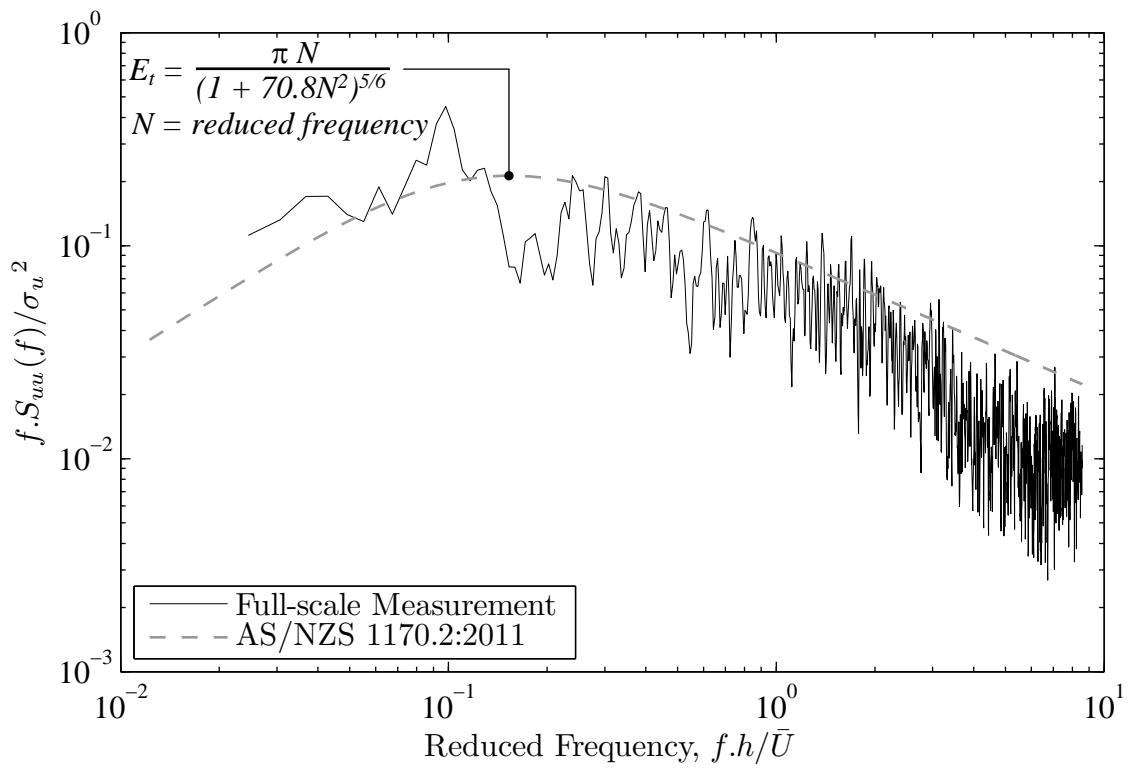
Figure 6.10: Spectrum of longitudinal wind velocity for 2005-09-29 11:05. Mean wind direction = 275° (h=187 m)

$$E_t = \frac{\pi N}{(1 + 70.8N^2)^{5/6}}$$

$N = $ *reduced frequency*
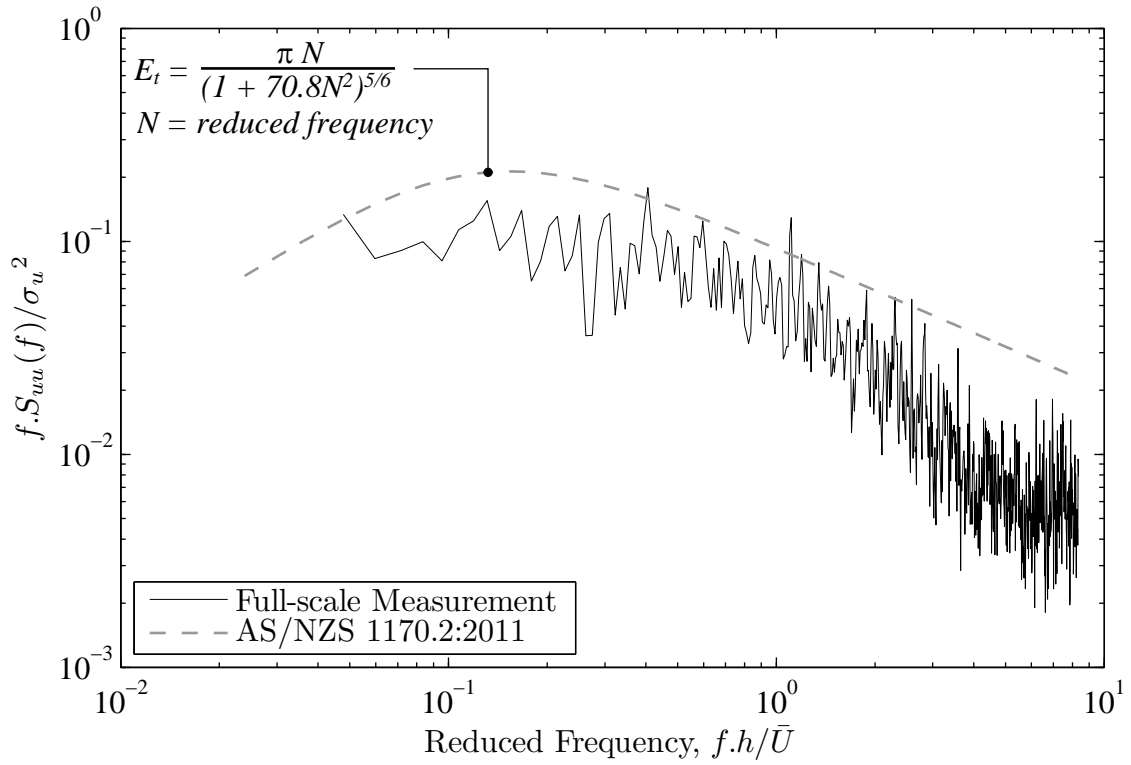
Figure 6.11: Spectrum of longitudinal wind velocity for 2005-09-17 18:20. Mean wind direction $= 287°$ (h=187 m)

a selection of the measured responses. The results presented focus on three wind events that recorded some of the highest wind speeds and responses during the monitoring period. The first is a southerly wind event recorded on 7 September 2006, and the second and third are westerly wind events recorded on 29 September 2005 and 17 September 2005. The acceleration results presented are those measured by the orthogonal accelerometer pair located at point 1 in Figure 3.29.

Referring to Figure 6.4, there are seven wind events during the monitoring period with standard deviation acceleration responses above $0.5\,\mathrm{mg_n}$. The three wind events discussed in this section are a small portion of all the collected data, but they represent some of the highest wind speeds and responses recorded during the monitoring period, and therefore were deemed more suitable for further analysis. The wind speeds recorded during the events are less than the 1 year return period values in the Australian Wind Code.

6.3.1   Acceleration Response

The acceleration response of Latitude tower from a southerly wind event is displayed in Figure 6.12. The wind direction is relatively constant at a mean azimuth of 160° and the turbulence intensity is approximately equivalent to a terrain category 3. The expected peak and standard deviation y-axis accelerations are greater than the

x-axis accelerations by a factor of approximately 2.1. The measured peak y-axis acceleration occurs at time 200 s, and is 1.3 times greater than the expected peak from an upcrossing analysis. This peak coincides with a short, abrupt increase in the wind speed, and the large increase in the acceleration response may have occurred from the dynamic motion of the building being in phase with a large scale gust.

A plot of the y-axis versus x-axis accelerations are displayed in Figure 6.13. The envelope of the response is elliptic with a dominant y-axis (along-wind) component and a minor x-axis (cross-wind) component that skews the envelope. A number of acceleration excursions beyond the envelope are observed. The most notable is the measured peak event at the top of the ellipse. The acceleration response displays significant x and y axes components as the envelope is exceeded, before becoming mostly y-axis acceleration. This may suggest energy transfer between vibration modes.

A frequency domain representation of the acceleration time histories is displayed in Figure 6.14. The fundamental mode of vibration corresponds to translation in the y-axis, and this mode dominates the response. The fundamental torsion mode at 0.42 Hz also contributes significantly to the total response, and this is important to consider when assessing occupant comfort requirements. The second modes of vibration are at frequencies between 0.8–1.2 Hz, and they contribute orders of magnitude less energy to the total response compared with the fundamental y-axis translation and fundamental torsional modes.

The acceleration response for the westerly wind event recorded on 2005-09-29 11:05 is displayed in Figure 6.15. The mean wind speed is similar to the southerly event in Figure 6.12, but the turbulence intensity is less in this case and equivalent to a terrain category 2. Despite the incident wind being aligned with the x-axis (along-wind), the y-axis (cross-wind) acceleration response is greater than the x-axis accelerations by a factor of approximately 1.5. This is due to a combination of reduced longitudinal turbulence buffeting in the along-wind direction, increased lateral turbulence and cross-wind wake excitation in the y-axis, and the tendency of the structure to vibrate at the fundamental mode of vibration. Based on the very low reduced velocity of 1.77 for the westerly event the wake excitation will be minimal, and therefore the response is more likely due to increased turbulence buffeting in the cross-wind direction.

The maximum acceleration recorded in the y-axis occurs at time 570 s. This maximum acceleration coincides with a reduction in the mean wind velocity. In this case, the maximum value could be biased by noise in the measurements. A plot of the y-axis versus x-axis accelerations for the westerly wind event are displayed in Figure 6.16. The response envelope is elliptic, and displays a greater contribution from x-axis translations to the total response compared with the southerly event.
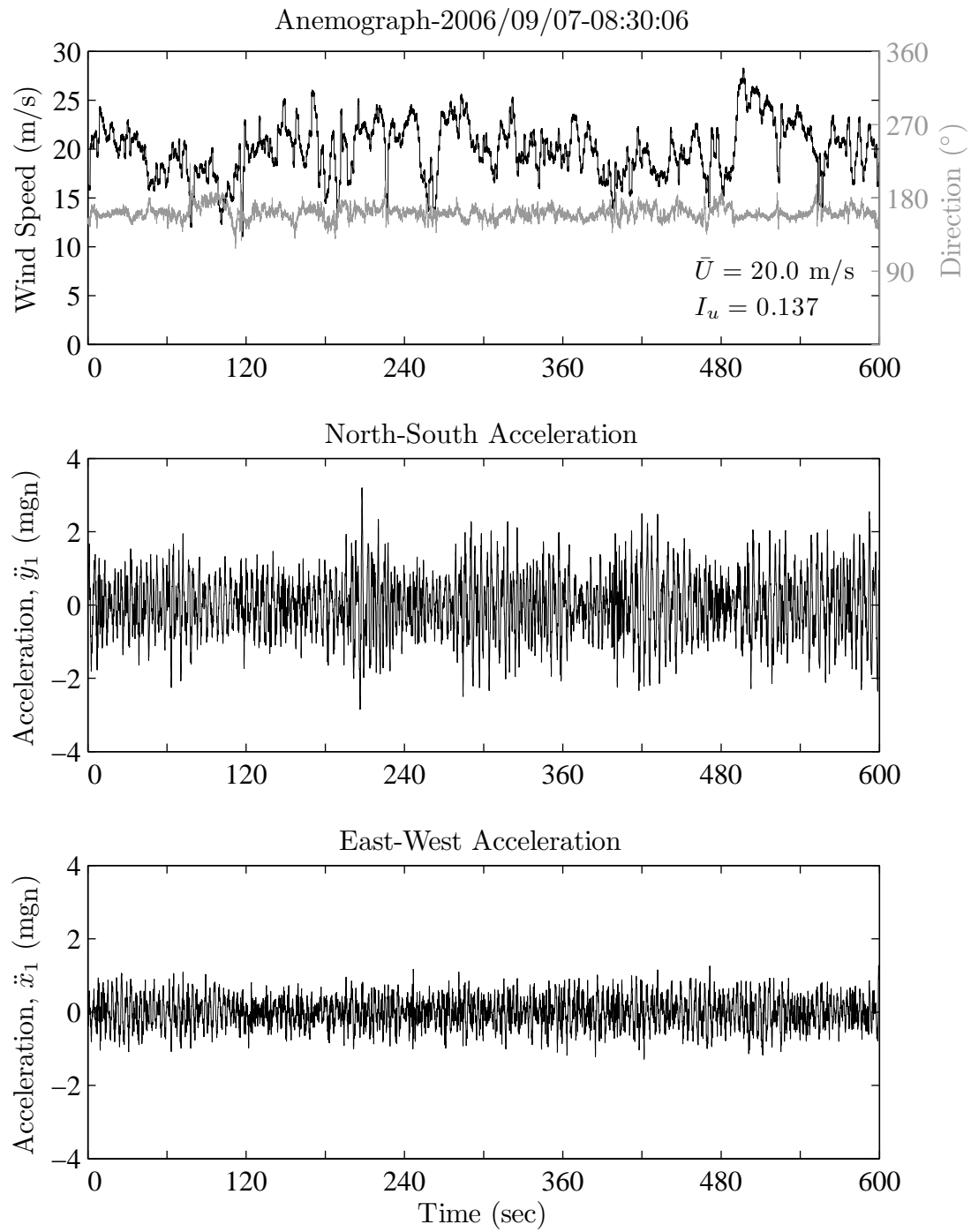
Figure 6.12: Wind speed, direction, and acceleration response for 2006-09-07 08:30.
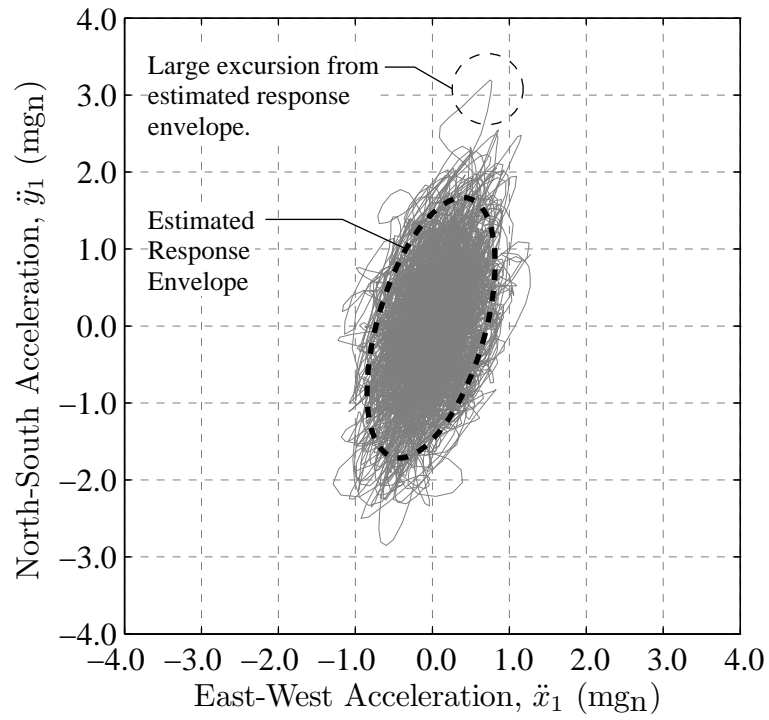
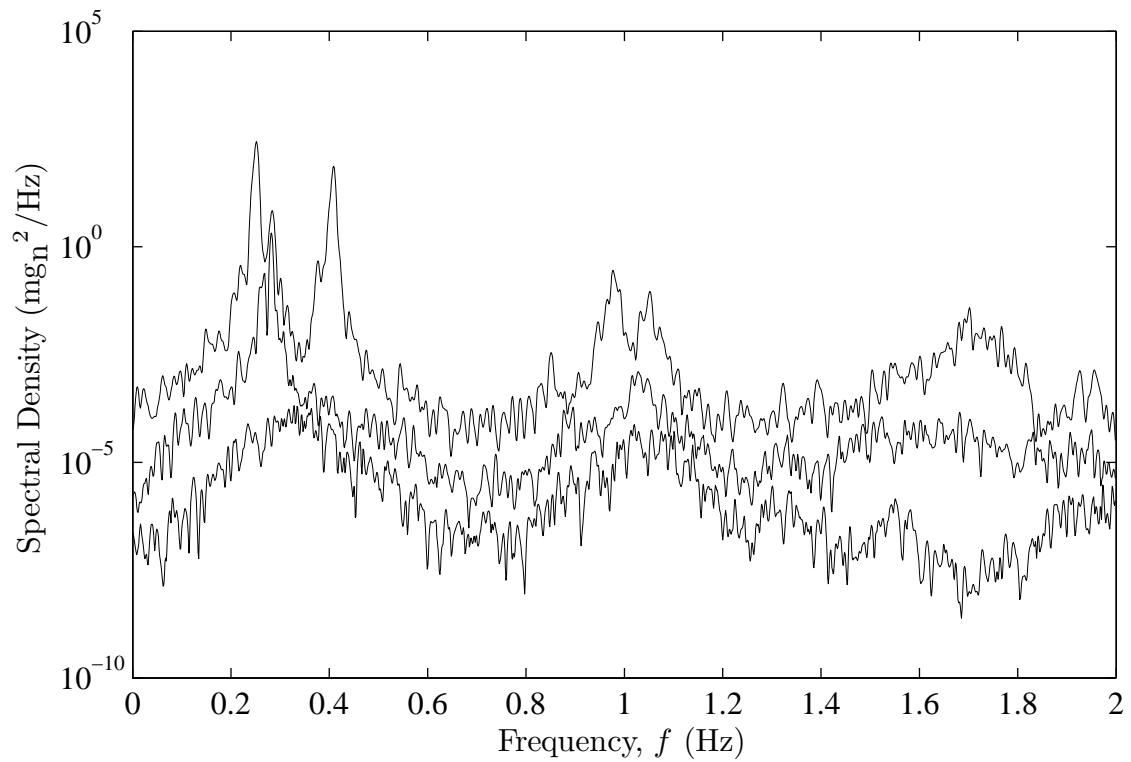Figure 6.13: Acceleration response envelope for 2006-09-07 08:30.

Figure 6.14: Singular value plot for 2006-09-07 08:30.

	β	$\bar{U}$	I_u	σ_{Dir}	$\hat{\ddot{y}}_1$	$\sigma_{\ddot{y}_1}$	$\hat{\ddot{x}}_1$	$\sigma_{\ddot{x}_1}$
	(°)	(m/s)	(–)	(°)	(mg$_n$)	(mg$_n$)	(mg$_n$)	(mg$_n$)
2006-09-07	160	20.0	0.137	8	2.53	0.81	1.17	0.39
2005-09-29	275	19.9	0.110	9	1.32	0.41	0.84	0.27
2005-09-17	287	23.4	0.065	3	1.92	0.62	1.00	0.32

Table 6.3: Comparison of x and y axes acceleration responses for the southerly and westerly wind events.

This can be attributed to buffeting from the longitudinal turbulence since the x-axis represents the along-wind response. The spectrum of the acceleration responses in Figure 6.17 displays a larger peak for the fundamental x-axis translation mode at 0.28 Hz compared with the spectrum for the southerly event. The second modes of vibration between 0.8–1.2 Hz are also contributing more to the total response compared with the southerly event.

The acceleration responses for the second westerly event on 2005-09-17 is displayed in Figure 6.18. As displayed in Table 6.3 this event has an increased mean wind speed of 23.4 m/s and a significantly lower turbulence intensity of 0.065. The response envelope in Figure 6.19 has a more dominant y-axis component (cross-wind) compared with the westerly event recorded on 2005-09-29. Comparing the spectra in Figures 6.17 and 6.20, the westerly event reocrded on 2005-09-17 has more energy associated with the fundamental y-axis vibration mode, which corresponds to the cross-wind direction.

Table 6.3 presents a comparison between the peak and standard deviation accelerations in the x and y axes for the southerly and westerly wind events. The y-axis accelerations for the southerly event are greater by a factor of two compared with the westerly event, and the x-axis accelerations are greater by a factor of 1.4.

Acceleration responses for a westerly wind event that lasted approximately two days are displayed in Figures 6.21 and 6.22. The time stamps differ by nine hours, and these records are included in the discussion due to the unusual nature of the longitudinal turbulence. The mean wind speeds and direction differ by approximately 6% and 3% respectively, but the turbulence intensities differ by a factor of 3.5. The turbulence intensity for the first record is equivalent to terrain category 2, while the turbulence intensity of the second record is three times less than a terrain category 1. To the west of Latitude tower, the terrain is mostly urban and would be equivalent to terrain category 3 according to the Australian wind code [153].

Table 6.4 presents a summary of the wind statistics and acceleration responses for these records. The y-axis accelerations correspond to the cross-wind direction, and the reduction in the turbulence intensity results in a 27% and 20% reduction in the peak and standard deviation accelerations respectively. This suggested the

Figure 6.15: Wind speed, direction, and acceleration response for 2005-09-29 11:05.
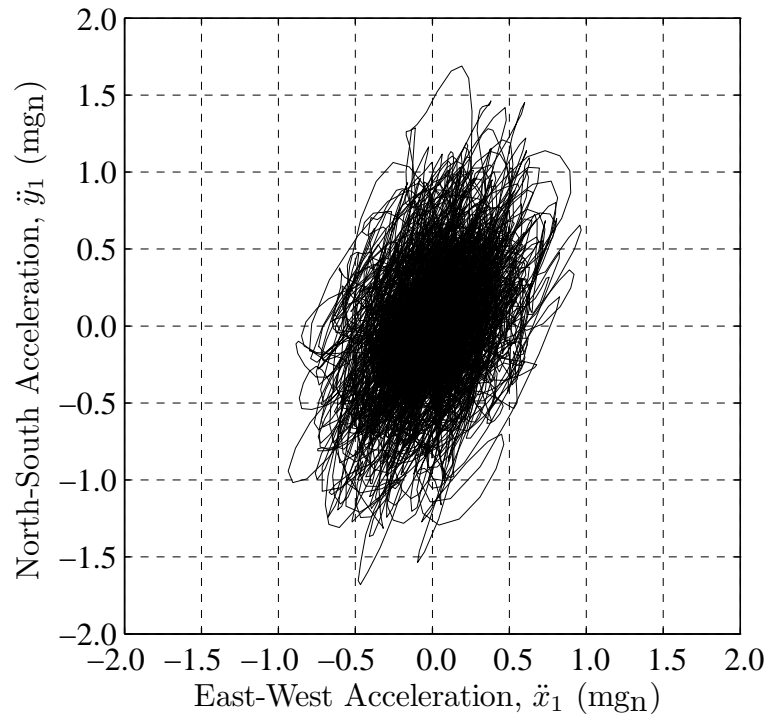
Figure 6.16: Acceleration response envelope for 2005-09-29 11:05.

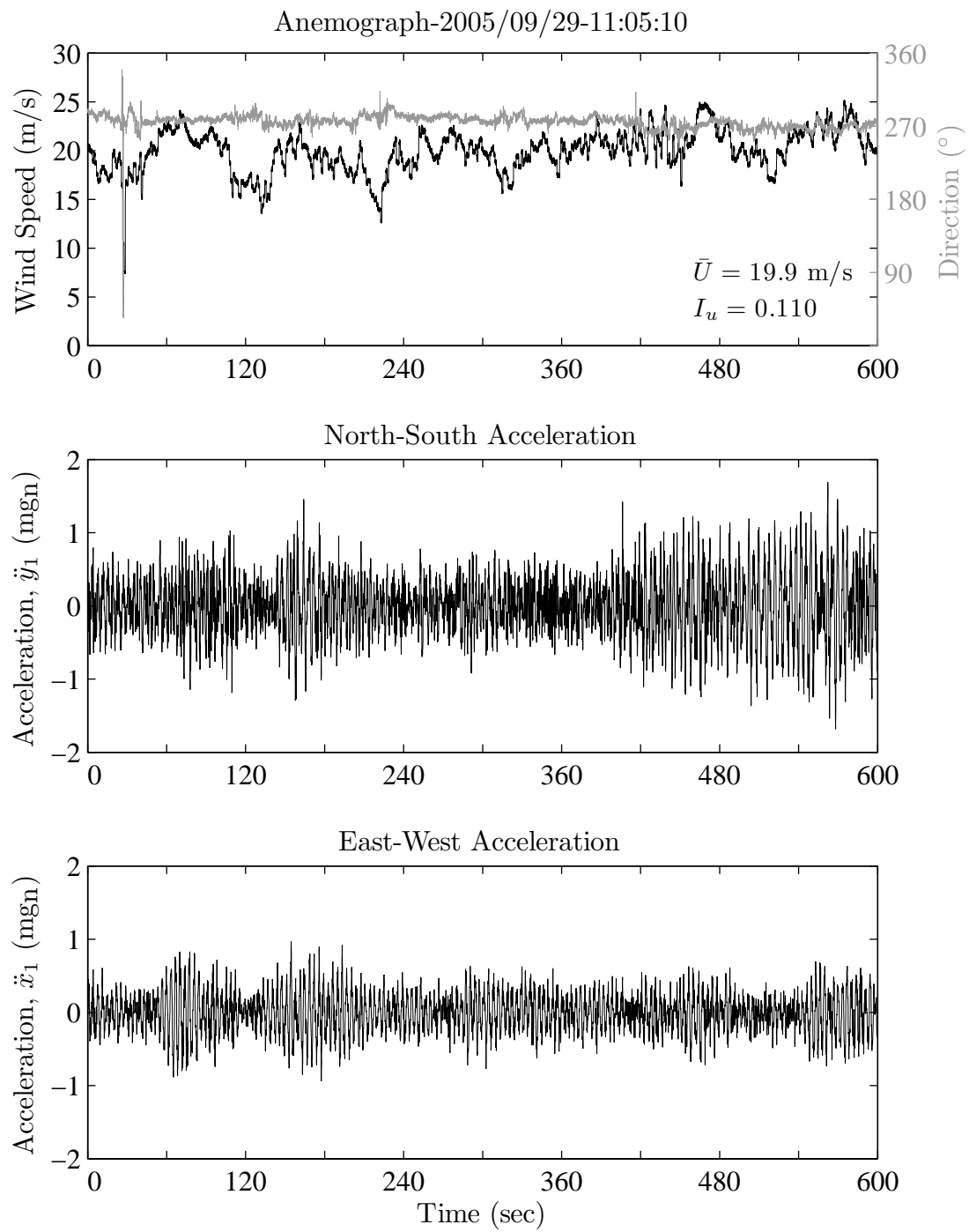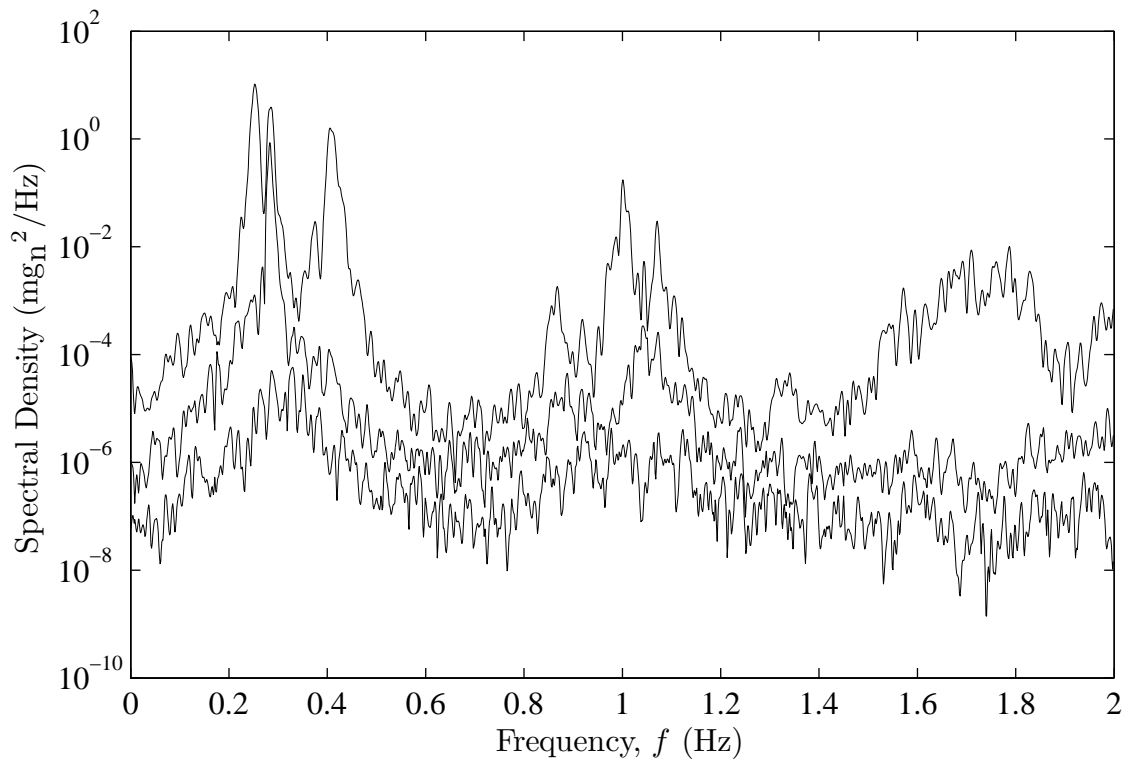Figure 6.17: Singular value plot for 2005-09-29 11:05.
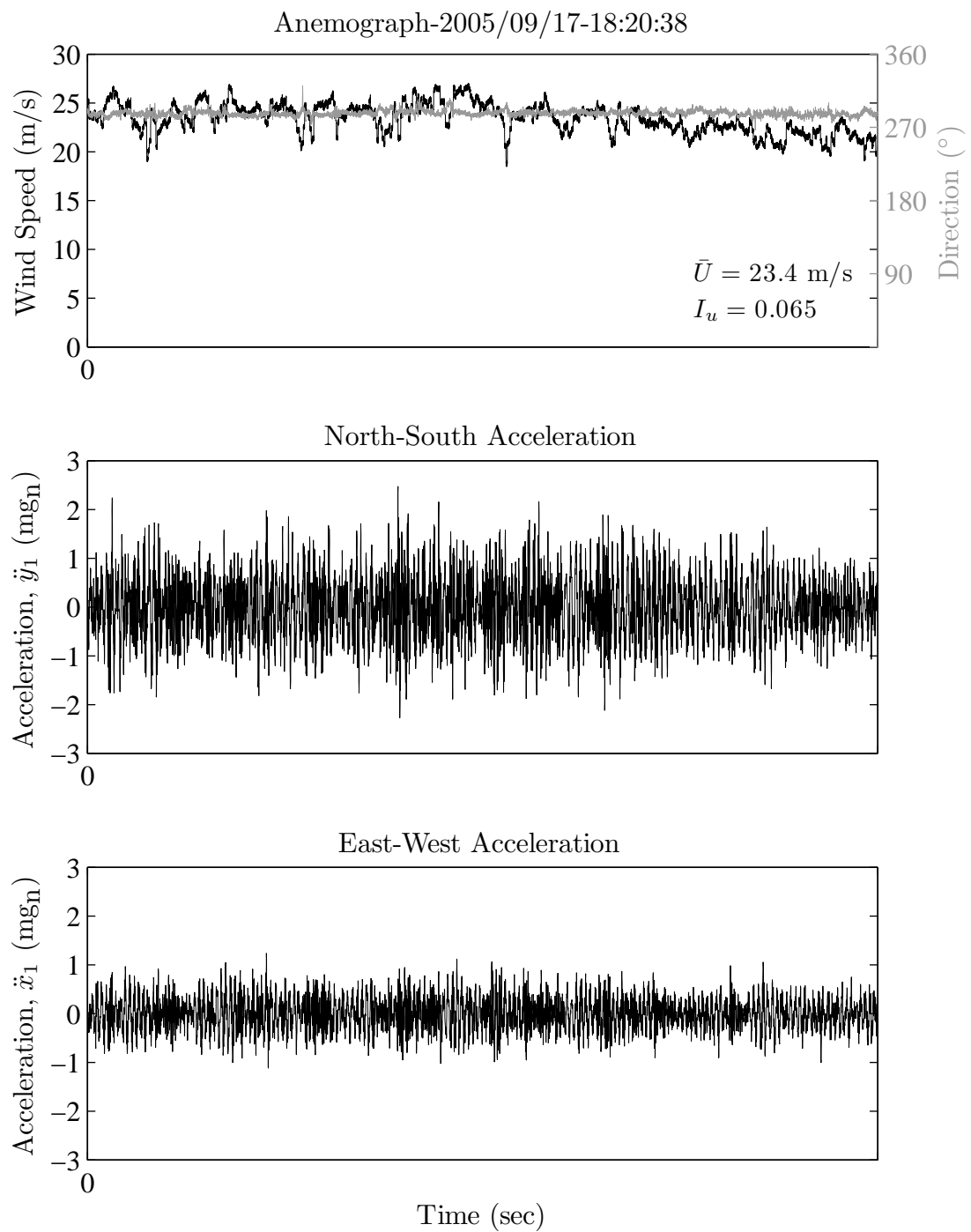
Figure 6.18: Wind speed, direction, and acceleration response for 2005-09-17 18:20.
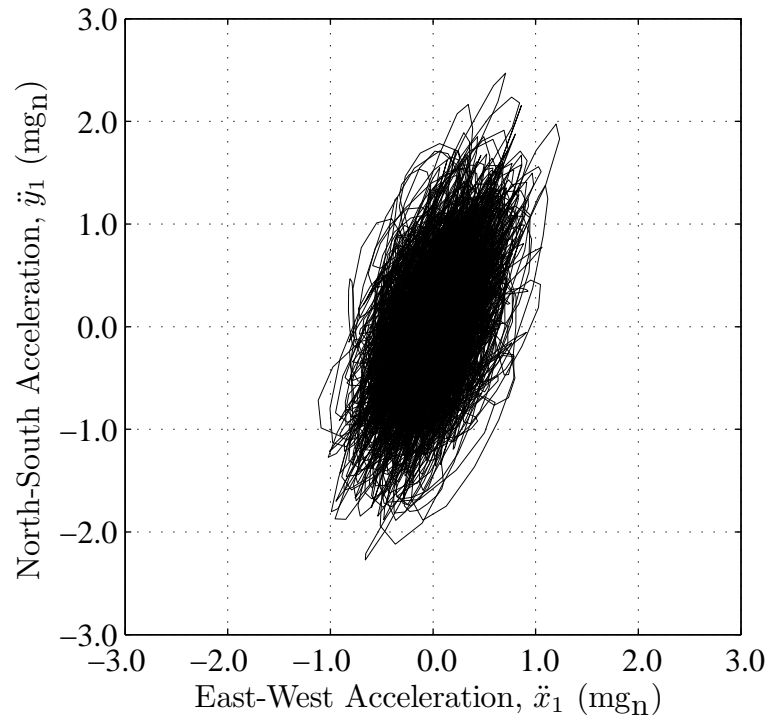
Figure 6.19: Acceleration response envelope for 2005-09-17 18:20.
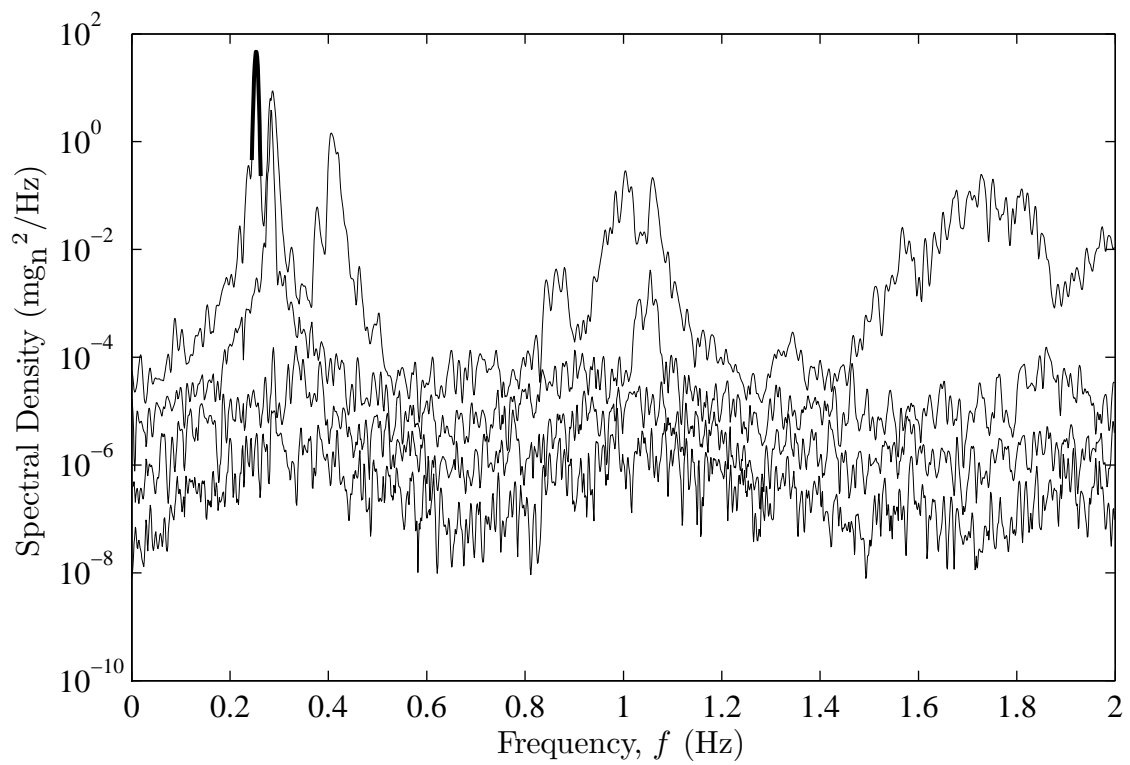
Figure 6.20: Singular value plot for 2005-09-17 18:20.

	β	$\bar{U}$	I_u	σ_{Dir}	$\hat{\ddot{y}}_1$	$\sigma_{\ddot{y}_1}$	$\hat{\ddot{x}}_1$	$\sigma_{\ddot{x}_1}$
	(°)	(m/s)	(–)	(°)	(mg$_n$)	(mg$_n$)	(mg$_n$)	(mg$_n$)
2006-05-07	274	15.7	0.108	7	0.92	0.27	0.47	0.15
2006-05-08	266	14.8	0.031	2	0.67	0.22	0.49	0.15

Table 6.4: Comparison of x and y axes acceleration responses for westerly wind events with different turbulence intensities recorded between 2006-05-07 to 2006-05-08.

lateral turbulence is contributing to the cross-wind response for the higher turbulence event, particularly since the standard deviation wind direction (σ_{Dir}) is 70% less for the low turbulence event. The reduced velocity is 1.39 for the westerly event 2006-05-07, which is low and implies the wake excitation will be minimal, and therefore the response is more likely due to increased turbulence buffeting in the cross-wind direction. The accelerations for the along-wind direction are unchanged between the two records. This result is unexpected, since a reduction in the turbulence intensity would reduce the along-wind dynamic response from turbulence buffeting. This could be due to the interaction between the first two modes of vibration and the tendancy of the structure to: 1) predominantly oscillate in the first mode of vibration, and 2) to decay into the first mode of vibration if higher modes are initially excited.

Figure 6.21: Wind speed, direction, and acceleration response for 2006-05-07 19:46.

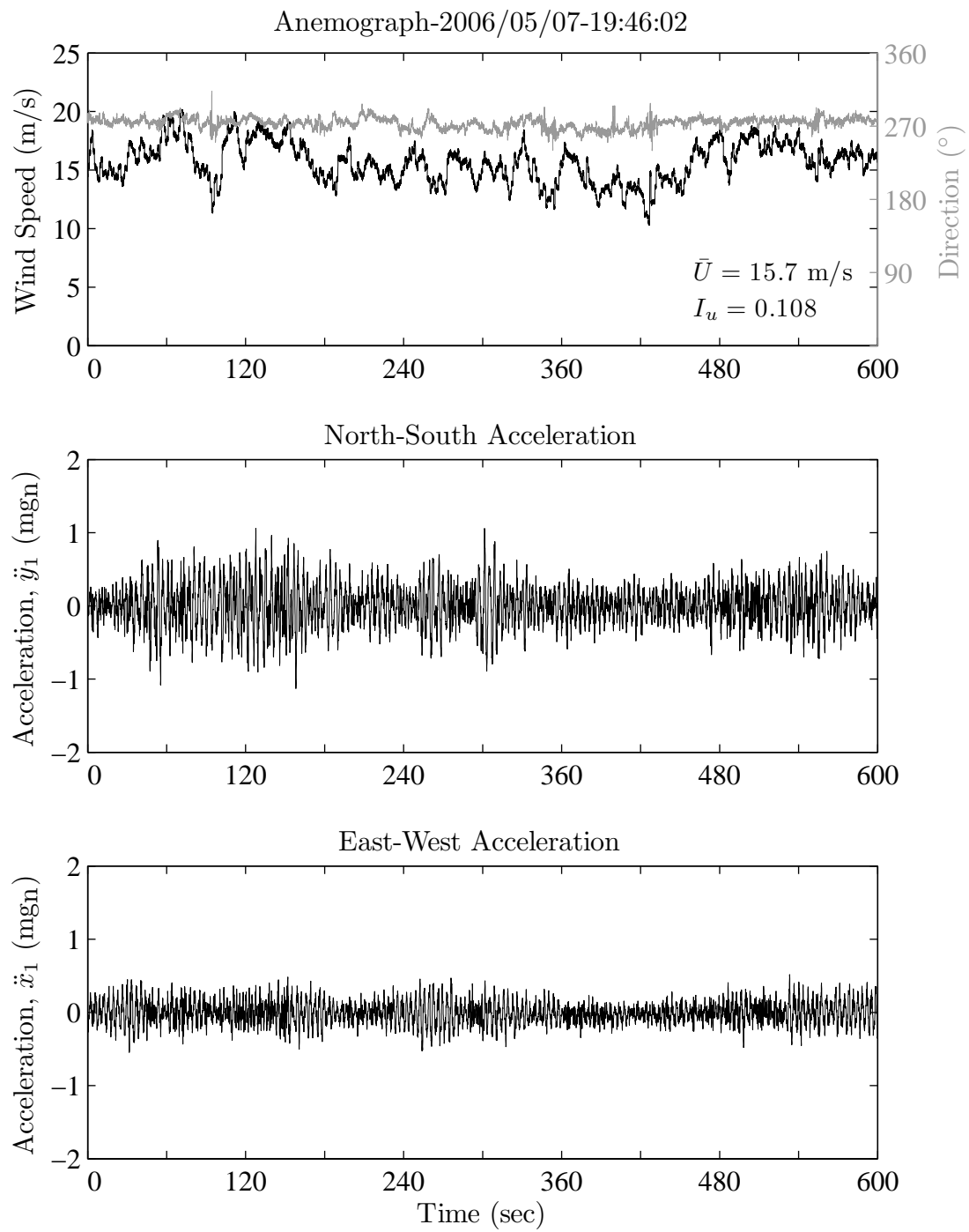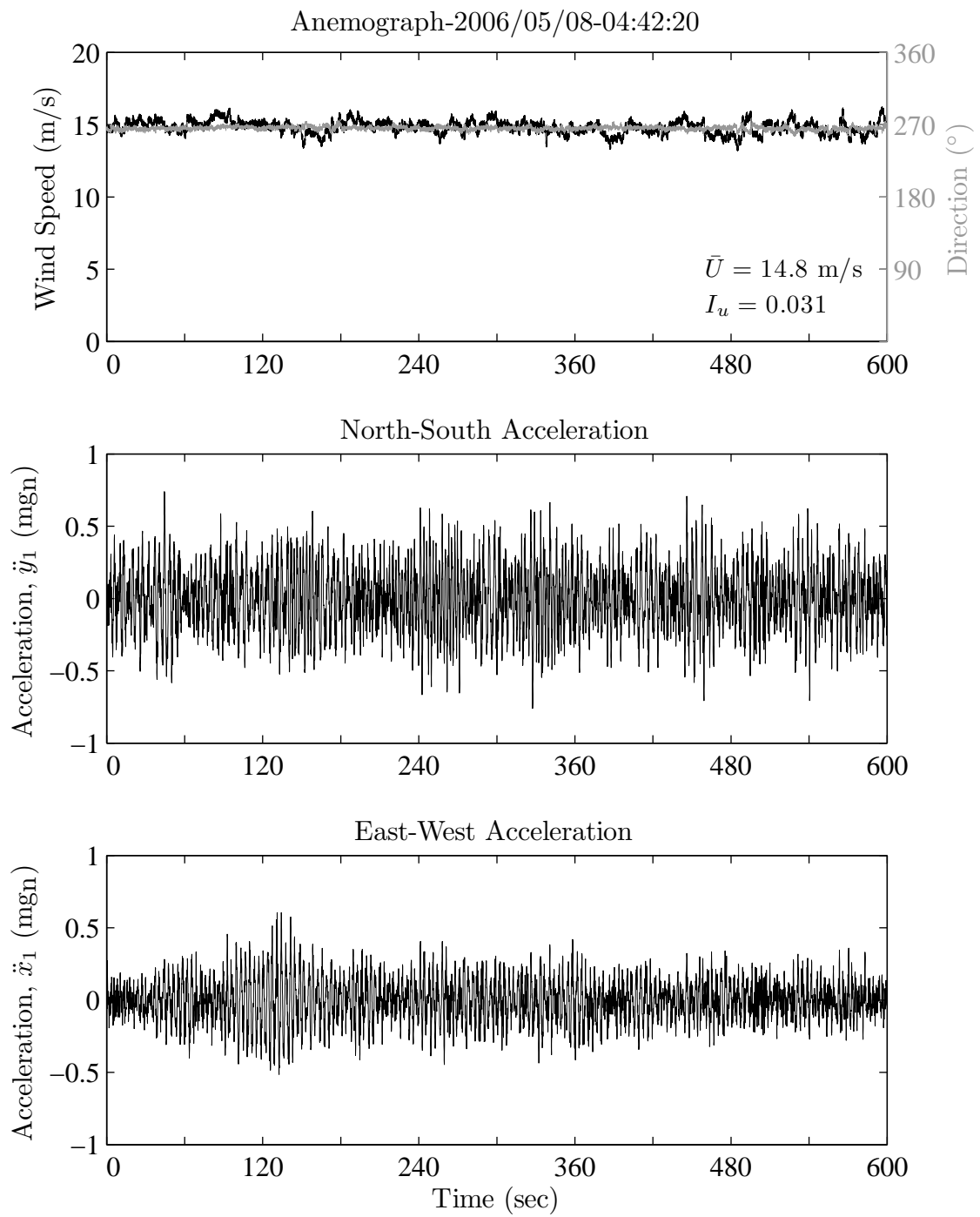Figure 6.22: Wind speed, direction, and acceleration response for 2006-05-08 04:42.

6.3.2   Background Response

The displacement results corresponding to the southerly wind event recorded on 2006-09-07 are presented in this section. For this wind event the reference receiver at UNSW was not operating correctly, and therefore the QUEENS reference receiver operated by the SydNET GPS reference network infrastructure in NSW was used to correct the atmospheric errors. The QUEENS reference receiver has a baseline of 1.5 km from Latitude tower, but only recorded data at 1 Hz sampling frequency. Therefore, the displacement measurements are reported for this sampling frequency, despite the roving receiver at Latitude tower sampling at 10 Hz. A sampling frequency of 1 Hz is sufficient for monitoring the background response, and since the first three modes of vibration for Latitude tower are below the Nyquist frequency of 0.5 Hz, the dynamic component from these modes will also be recorded. The raw receiver data was processed using Leica software and precise ephemeris data for the GPS satellites.

Establishing a base point for analysing the displacement measurements is difficult to due to instrumentation drift and temperature effects on the structure. The temperature effects manifest as differential heating of the structure, which causes movement due to disproportionate expansion of parts of the structure relative to others. Since the instrumentation drift and temperature effects were not accounted for in the analysis, it was not possible to compare the absolute deflection under a certain wind speed with its resting position during still conditions. Instead the change in deflection between the position prior to and during the wind event are reported.

Figure 6.23 displays the change in the mean wind speed and direction, and the displacements measured in the North-South direction for the southerly wind event recorded on 2006-09-07. The time series totals six hours, and the start corresponds to 4 am. The mean wind speeds and directions are for ten minute intervals. The North-South displacement plot displays fluctuations that do not correlate with the mean wind speeds. Dilution of precision errors from suboptimal positioning of satellites are likely to be present in the data, in addition to multipath errors due to the location of the GPS receiver near buildings.

For the first two hours of the event, the mean wind speed and direction is between 6.2–10.1 m/s and 271–281 ° respectively. The mean of the GPS position measurements during the first two hours was used as the reference position, which is indicated by the dashed red line at zero displacement. At a time of approximately two hours, the mean wind speed and direction abruptly change to values in the ranges 17.2–18.4 m/s and 151–156 ° respectively. This mean wind speed and direction is sustained over a period of two hours, and the mean displacement in the North-South direction increases to approximately 11 mm. A further increase in the

	Frequency (Hz)	
	Acceleration	Displacement
Translation Y1	0.252	0.252
Translation X1	0.284	0.283
Torsion T1	0.410	0.405

Table 6.5: Comparison of natural frequency estimates from acceleration and displacement responses for southerly wind event 2006-09-07.

mean wind speed to a range of 19.4–20.2 m/s is observed at an elapsed time of four hours, and this speed is sustained for approximately one hour. During this period, the mean displacement increases to approximately 13 mm. The quasi-static component has not been highlighted in Figure 6.23 because dilution of precision errors and multipath errors have not been corrected in the data.

An upcrossing analysis of the y-axis accelerations was conducted to determine the peak accelerations for the time period included in the displacement measurements for the southerly event. From these peak accelerations, the resonant displacements were calculated using the relationship $\ddot{y}_1 = -\omega^2 y$. During the first two hours, the resonance displacements along the y-axis were between 0.4–1 mm. Between the two and four hour time period the resonance displacements increase to 7–9 mm, and for the four hour to five hour period there was a further increase to 10–11 mm. These resonance displacement account for some of the fluctuations about the mean values displayed in Figure 6.23.

A plot of the North-South displacements versus the East-West displacements are displayed in Figure 6.24. The grey line indicates the two hour period prior to the southerly wind event. The mean of the points included in this time period are centred on zero displacement in the North-South and East-West directions. The black line is the four hour period during the southerly wind event. The 11–13 mm change in the mean North-South displacement is visible, and there is practically no change in the mean East-West displacement. The envelope of the displacement plot is elliptical and is similar to the acceleration response displayed in Figure 6.13.

Figure 6.25 displays the spectra for the North-South and East-West displacements. The fundamental translation modes in the x-axis (X1) and y-axis (Y1) are visible in the spectra. The fundamental torsional mode (T1) is less defined in the spectra compared with the translational modes. Table 6.5 presents a comparison between natural frequency estimates from the displacement spectra with estimates from the singular value plot of the accelerometer time series in Figure 6.14. All of the natural frequency estimates are practically identical, which shows the capability of the GPS measurements to capture the resonant component of the response.
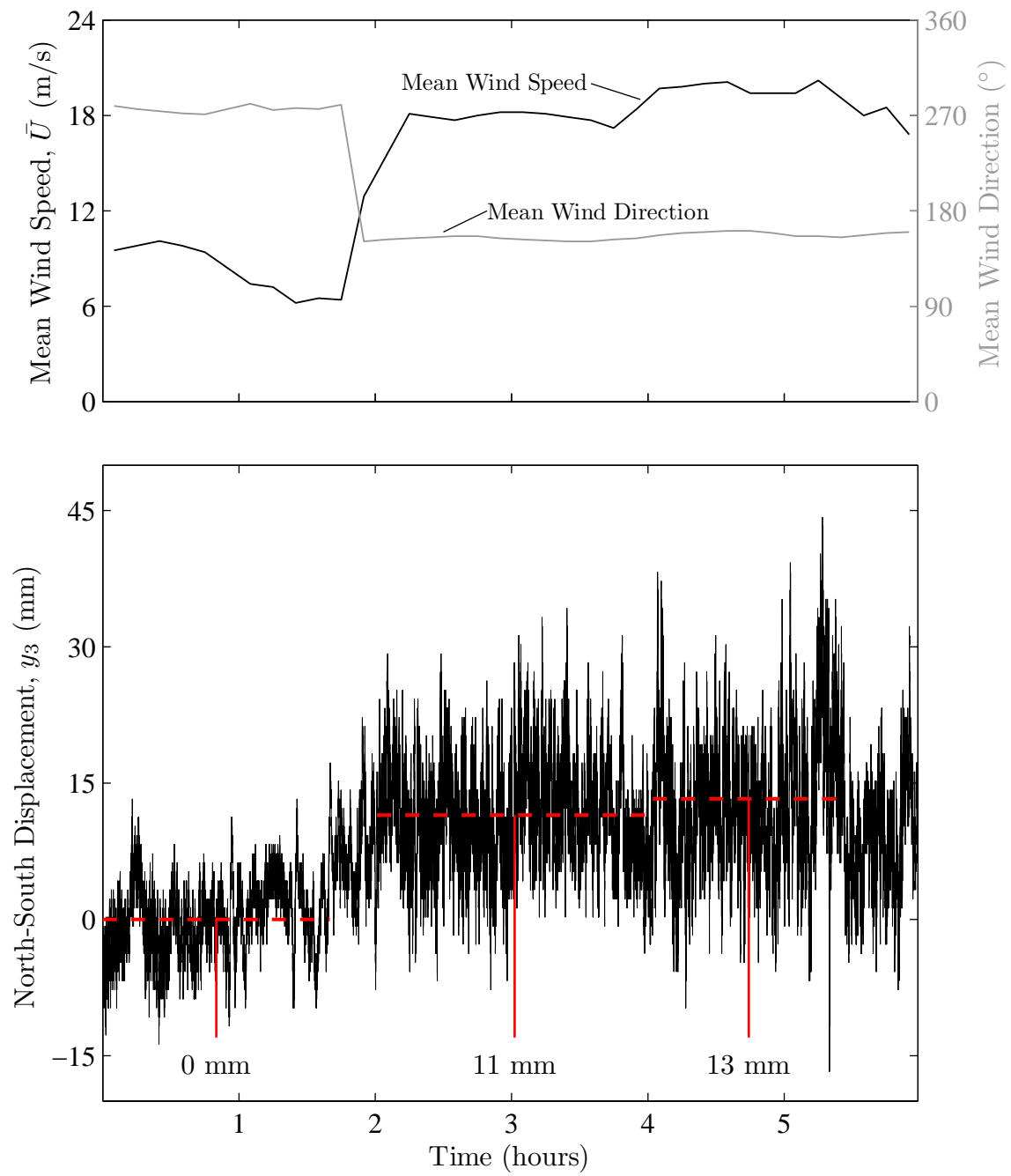
Figure 6.23: Mean wind speed and direction, and North-South displacement versus time for southerly wind event on 2006-09-07.
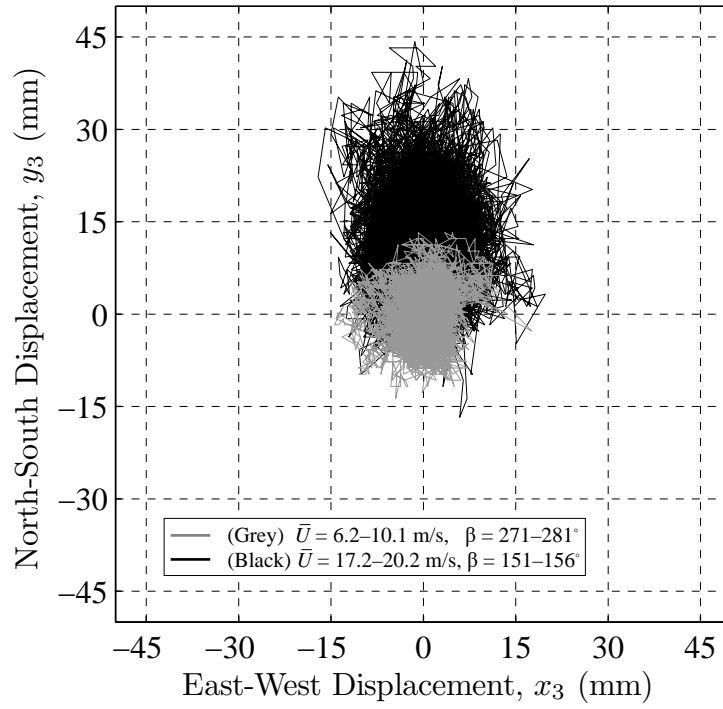
Figure 6.24: Displacement response for southerly wind event on 2006-09-07.

6.3.3 Peak Factors

The peak and standard deviation accelerations versus reduced velocity are displayed in Figures 6.26 and 6.27 for wind directions $160°$ and $275°$ respectively. The acceleration values are for hour length records. As discussed previously, the hour length records were generated by combining adjacent 15 minute records. The peak values were determined from an upcrossing analysis according to the theory in Section 2.5.3, and a probability of $P > 0.001$ was used.

The selection of records was based on the following criteria: The wind direction was restricted to records within $5°$ of the specified wind direction; records with mean wind speeds below $5\,\mathrm{m/s}$ were excluded; and the standard deviation wind direction was restricted to $20°$. A linear least squares fit of the selected records is also displayed for the peak and standard deviation values.

The southerly wind events ($\beta = 160°$) recorded the largest along-wind responses, which suggests turbulence buffeting, being the main excitation source in the along-wind direction, is greater for the southerly wind events. This is supported by the longitudinal turbulence results presented in Table 6.1, which indicate the SE, SSE, S, and SSW directions have greater turbulence intensities compared with the W and WNW directions. The slope of the fitted curves for the along-wind responses are greater than the cross-wind responses, which indicates the along-wind responses are increasing more rapidly with increasing mean wind speed.

The acceleration responses for the westerly winds ($\beta = 275°$) in Figure 6.27
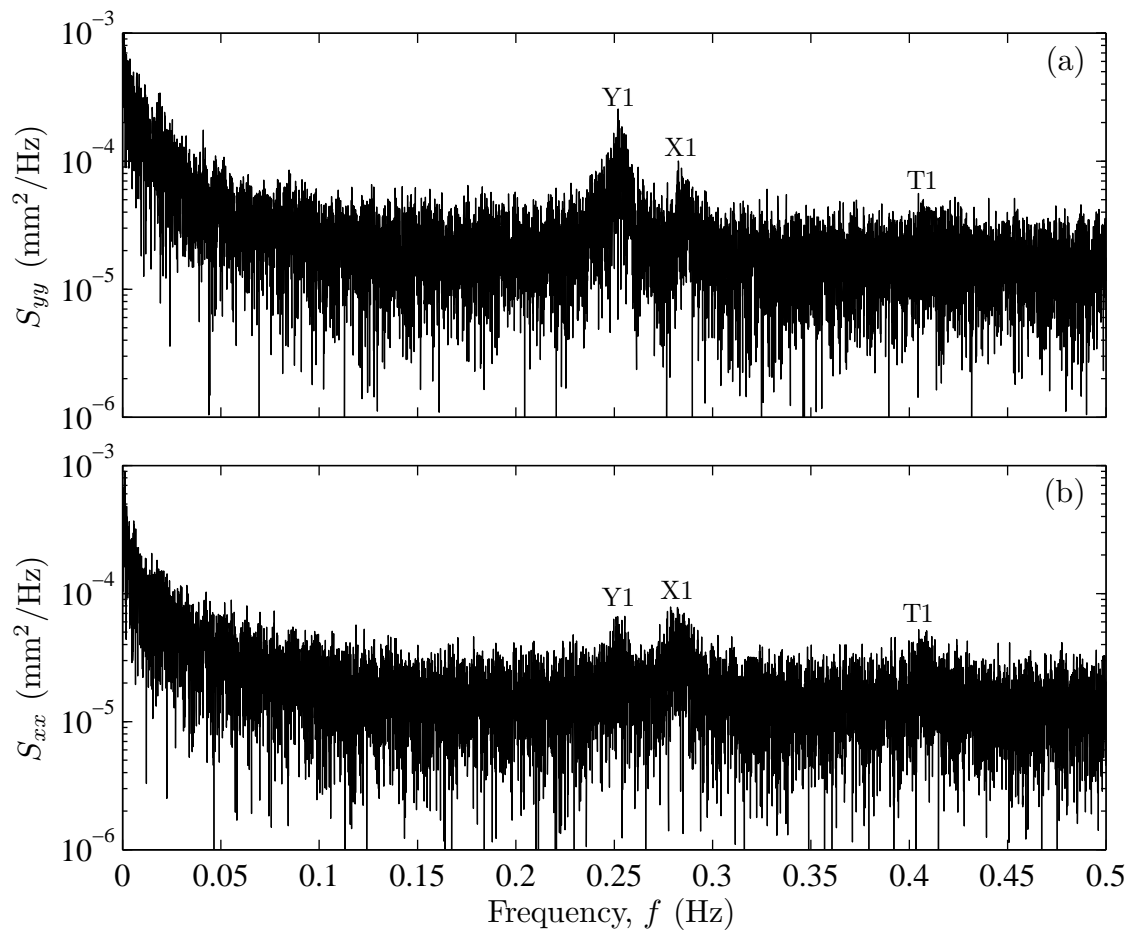
Figure 6.25: Spectra for southerly wind event on 2006-09-07; (a) North-South displacement spectrum, (b) East-West displacement spectrum.

are less than the responses for the southerly events. The cross-wind response is greater than the along-wind response, as was observed in Section 6.3.1, and the cross-wind response increases more rapidly compared with the along-wind response. The dominant cross-wind response is possibly due to increased lateral turbulence in the westerly winds compared with the southerly winds as displayed in Table 6.2. Another possibility is the transfer of energy between the closely spaced fundamental vibration modes, observed in the modal interference between the fundamental translational modes, as the structure will tend to vibrate at its lowest natural frequency.

The velocity range of the measurements is considerably less than the one year return period estimate from the Australian wind loading code. The monitoring period was conducted over a two year period, and the wind speed measurements were expected to be closer to the code estimate. It is noted that the one year return period regional wind speed for regions A1 to A7 was increased from 26 m/s in the 2002 edition to 30 m/s in the 2011 edition of the Australian loading code.

Figures 6.28 to 6.31 display the probability distributions from upcrossing analyses of selected hour length records. The first two figures are for a southerly wind event with a mean wind speed of 18.8 m/s and turbulence intensity of 0.18. The slope of the linear least squares fit is greater for the along-wind response compared with the cross-wind response. The next two figures are for a westerly wind event with a mean wind speed of 19.1 m/s and turbulence intensity of 0.16. As observed for the southerly event, the slope of the along-wind linear least squares fit is greater than the cross-wind slope.

Comparing the along-wind responses, the slope of the westerly event is greater than the southerly event. This result is unusual considering the turbulence intensity is greater for the southerly event. An explanation for this result is the horizontal shift towards larger abscissa values at lower probabilities of exceedance for the westerly wind event. This is due to a constant crossing frequency at consecutive probabilities of exceedance. The result is an increase in the slope of the linear fit. Another explanation for deviations from a Gaussian distribution is due to the change in mean wind speed during the hour time series.

The peak factors for the southerly wind events are approximately 4.1 and 4.0 for the along-wind and cross-wind responses respectively. For the westerly wind event, the along-wind and cross-wind peak factors are 4.5 and 4.2 respectively. The corresponding peak factor estimate from Equation (2.23) is 3.9 for along-wind responses in both the y-axis and x-axis. It is noted that the measured wind speeds are significantly less than extreme events, and the additional turbulence at the lower wind speeds compared with higher wind speeds is likely to cause larger peak factor estimates from the results presented. Therefore the along-wind probability distributions are likely to be more Gaussian at higher wind speeds. In summary, the
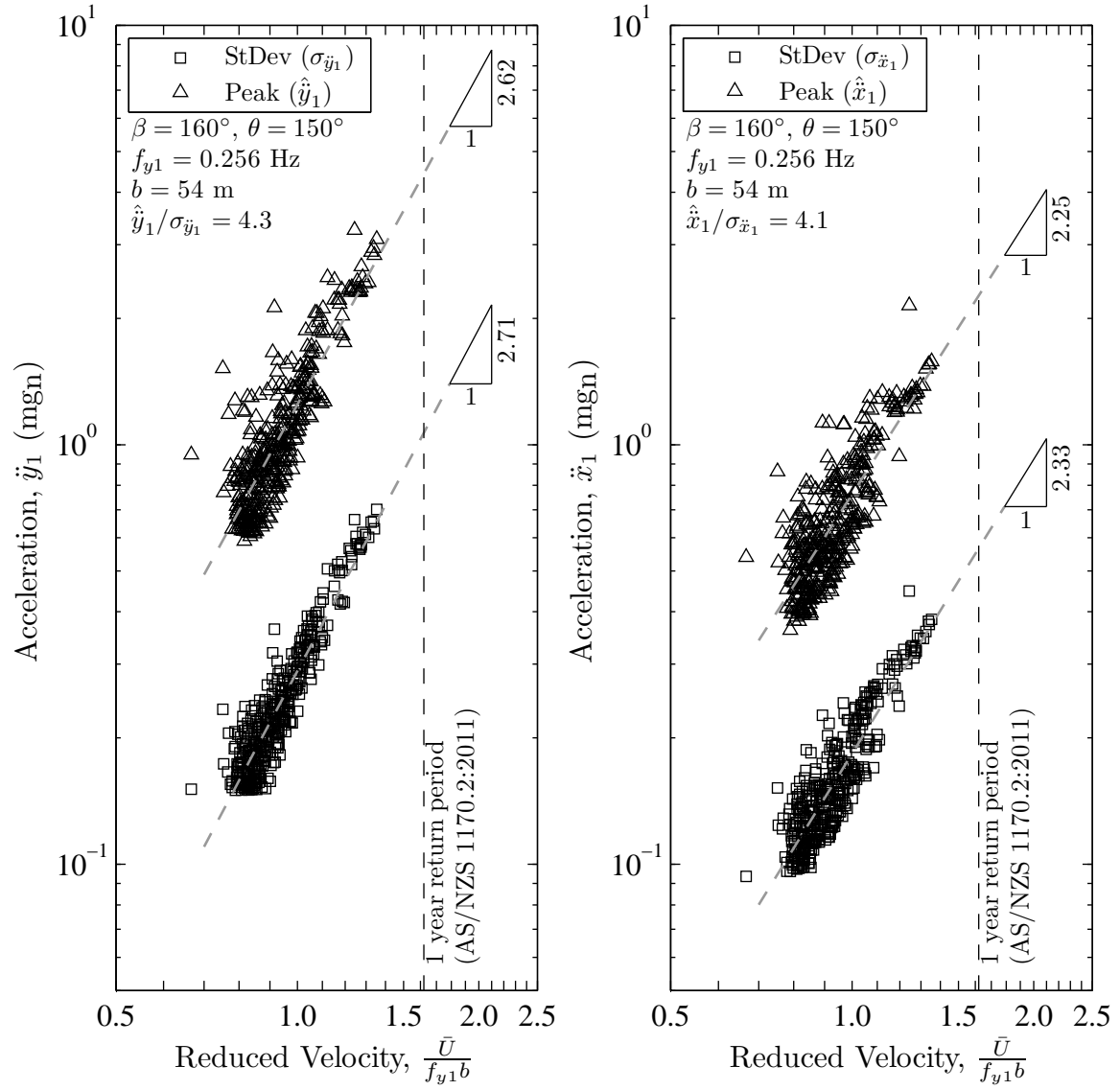
Figure 6.26: Peak and standard deviation acceleration versus reduced velocity for mean wind direction $\beta = 160°$ ($\ddot{y}_1$ = along-wind, $\ddot{x}_1$ = cross-wind).
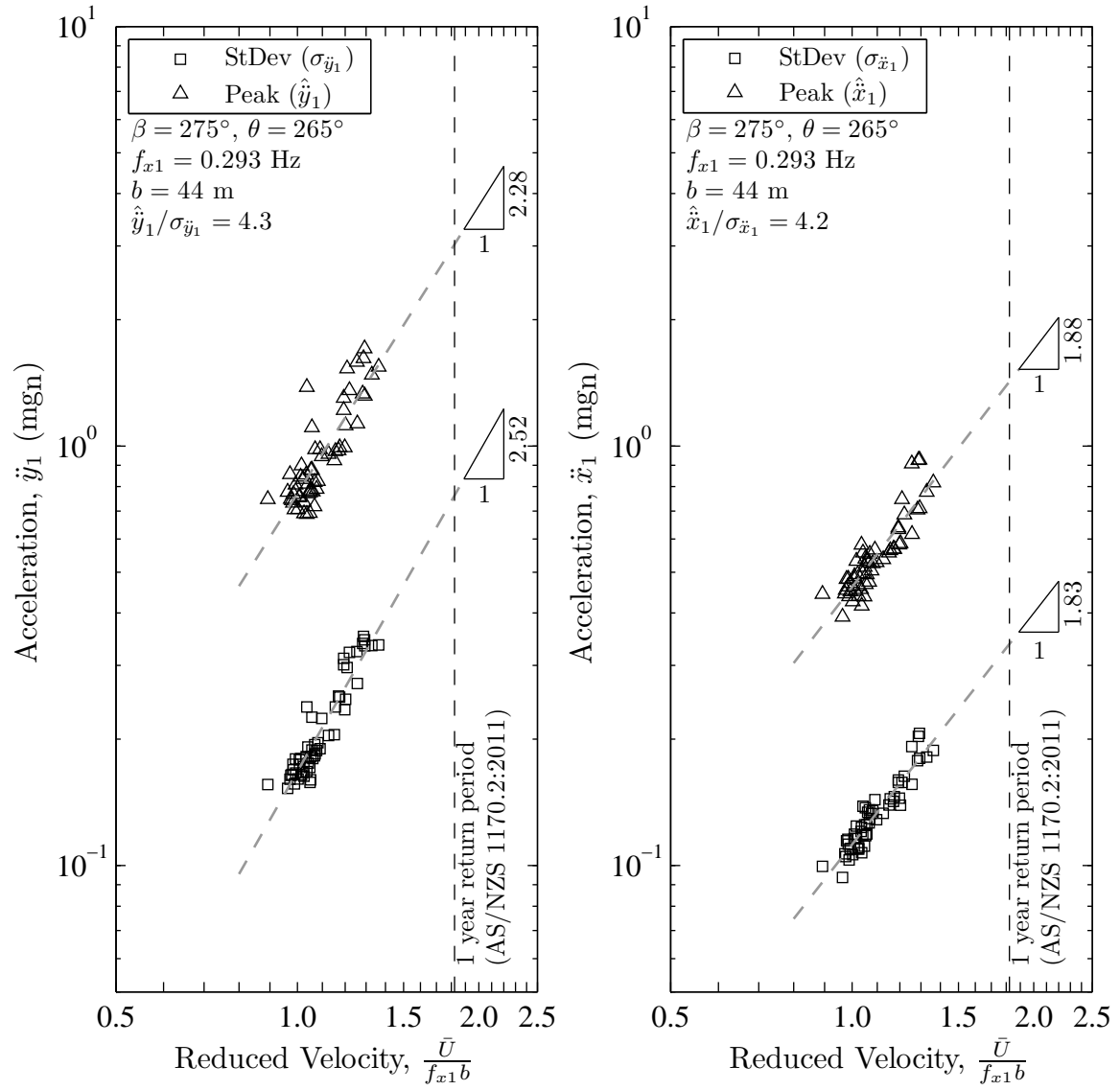
Figure 6.27: Peak and standard deviation acceleration versus reduced velocity for mean wind direction $\beta = 275°$ ($\ddot{x}_1$ = along-wind, $\ddot{y}_1$ = cross-wind).
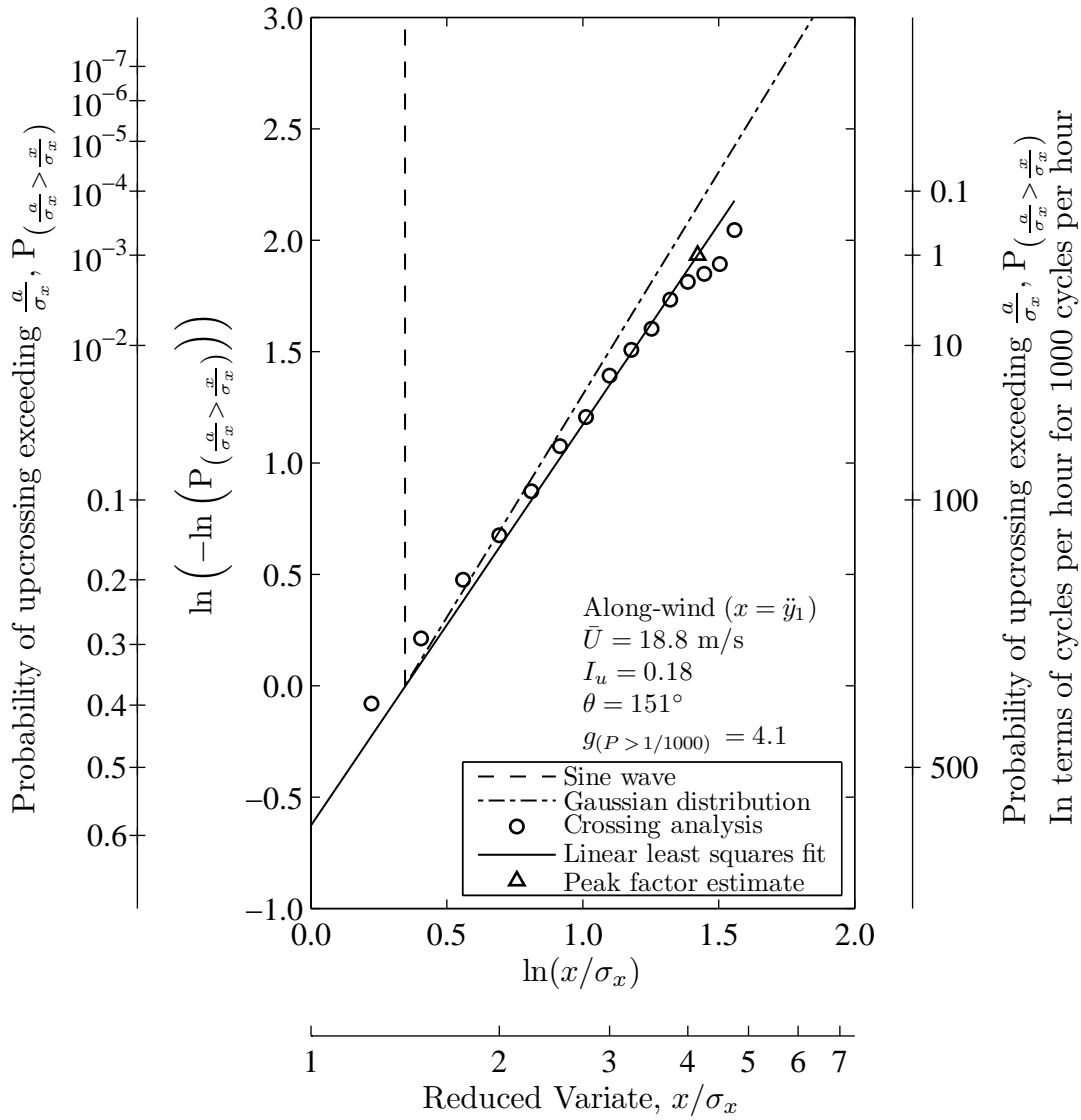
Figure 6.28: Probability distribution of upcrossings for the acceleration response in the along-wind direction for mean wind direction $\beta = 161°$.

probability distributions are not significantly different to a Gaussian distribution.

6.4 Wind Tunnel Response Estimation

This section describes the scaled model wind tunnel testing of Latitude tower and compares the acceleration response results with the measured values from the full-scale monitoring programme. The high frequency base balance (HFBB) technique is used to model Latitude tower in a boundary layer wind tunnel.
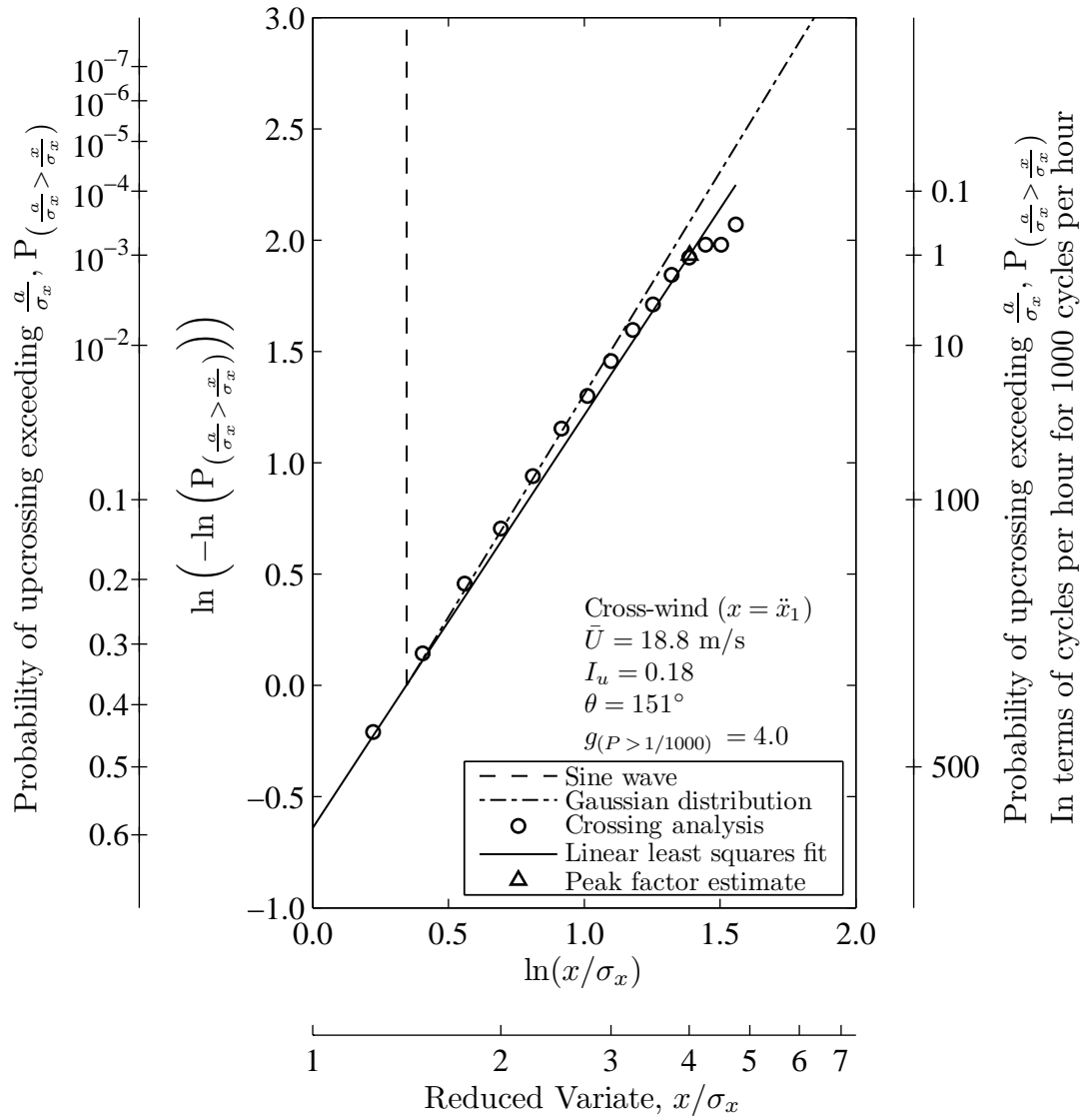
Figure 6.29: Probability distribution of upcrossings for the acceleration response in the cross-wind direction for mean wind direction $\beta = 161°$.
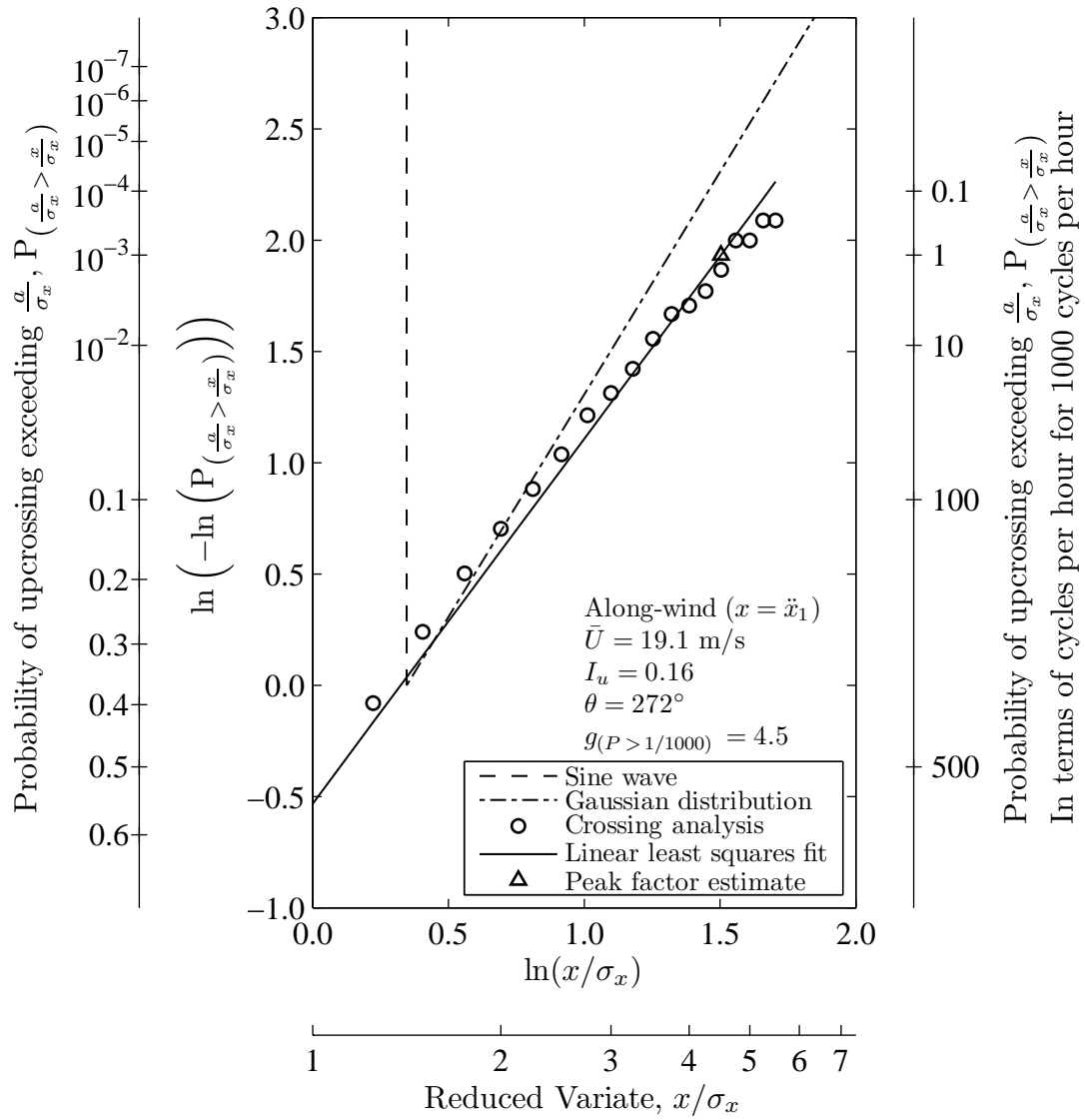
Figure 6.30: Probability distribution of upcrossings for the acceleration response in the along-wind direction for mean wind direction $\beta = 282°$.
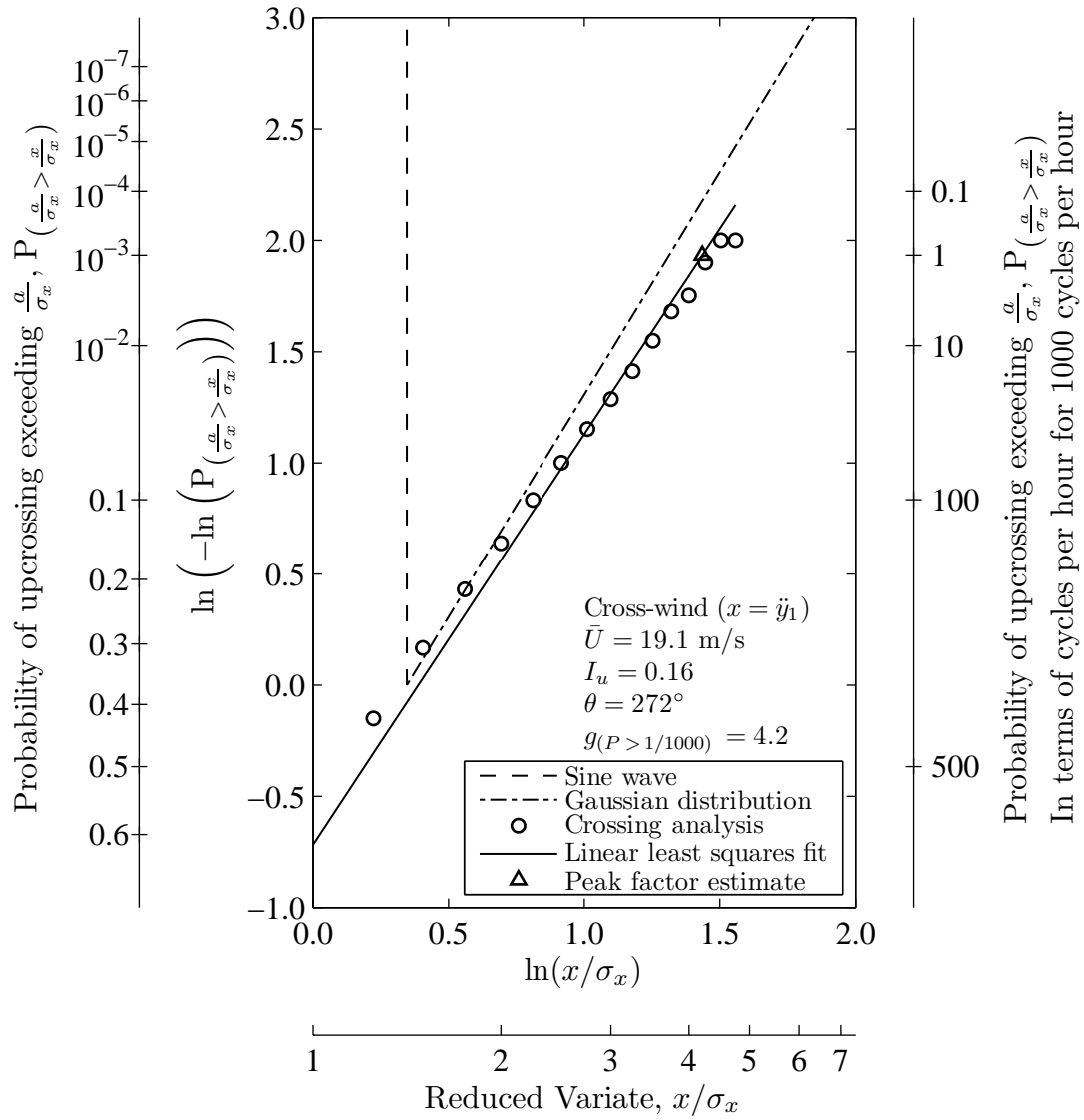
Figure 6.31: Probability distribution of upcrossings for the acceleration response in the cross-wind direction for mean wind direction $\beta = 282°$.

6.4.1 High Frequency Base Balance Technique

The HFBB technique [174] uses a rigid model of the prototype structure, and only the external geometry of the structure is modelled. This is unlike aeroelastic techniques [76], which also physically model the stiffness, mass, and damping of the structure. For the HFBB technique, the stiffness, mass, and damping characteristics of the structure are included via analytical techniques during the post processing stage of the wind tunnel measurements.

The output from an aeroelastic wind tunnel test is the final response spectrum. For the HFBB technique, the spectrum of modal force is measured during the wind tunnel testing. The final response of the structure to the modal force is determined analytically, which allows parametric studies of the response to changes in the dynamic characteristics without needing to retest the model in the wind tunnel.

The fundamental premise of the HFBB technique is that the modal forces exerted on a building by the wind can be estimated from the measured base overturning and torsional moments experienced by a rigid model. A modal force is defined as the applied force weight by the mode shape at the point of application, and integrated over the building height.

6.4.2 Wind Tunnel Modelling

A 1:400 scale rigid model of Latitude tower was mounted on a JR3 [83] force balance, and the overall mass and stiffness of the combined system produced translational and torsional natural frequencies greater than the frequency range of interest for the tests. The base balance was calibrated by applying a range of known static loads to the model and measuring the output from the base balance. The axis notation and centre of stiffness is displayed in Figure 6.32. Referring to Figure 3.2, the base moments were measured at Level 1, at RL $-13.05\,\text{m}$. The model was tested in the No. 1 Boundary Layer Wind Tunnel at the School of Civil Engineering, The University of Sydney.

The approaching wind was modelled in the wind tunnel by air flow passing over a fetch of floor-mounted roughness elements preceded by a vorticity-generating fence spanning the width of the tunnel. The approach wind velocity profile and wind turbulence characteristics, displayed in Figure 6.33, were consistent with a 1:400 scale model of a terrain category 3 boundary layer profile as defined in AS/NZS 1170.2:2002. Measurements were recorded for 10° intervals from North.

6.4.3 Comparison with Full-scale Measurements

The first three vibration modes of Latitude tower were considered in the analysis. The natural frequencies of these modes are presented in Table 4.1. The damping
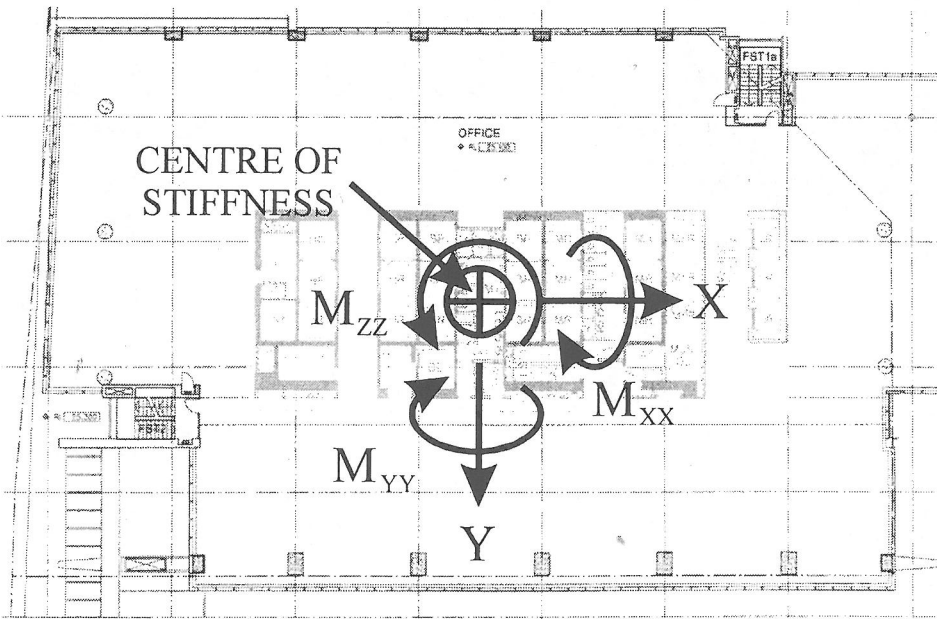
Figure 6.32: HFBB axis notation and centre of stiffness.
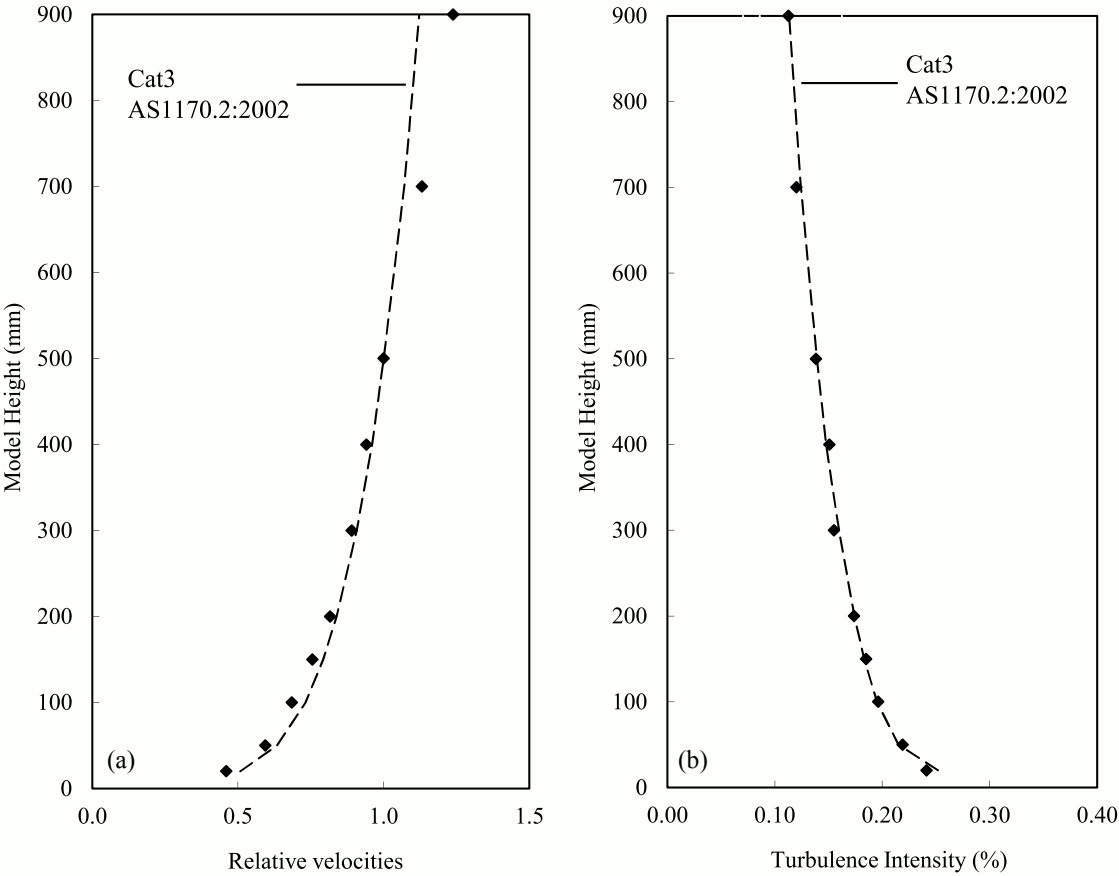
Figure 6.33: (a) Mean wind velocity profile and (b) Longitudinal turbulence intensity profile.
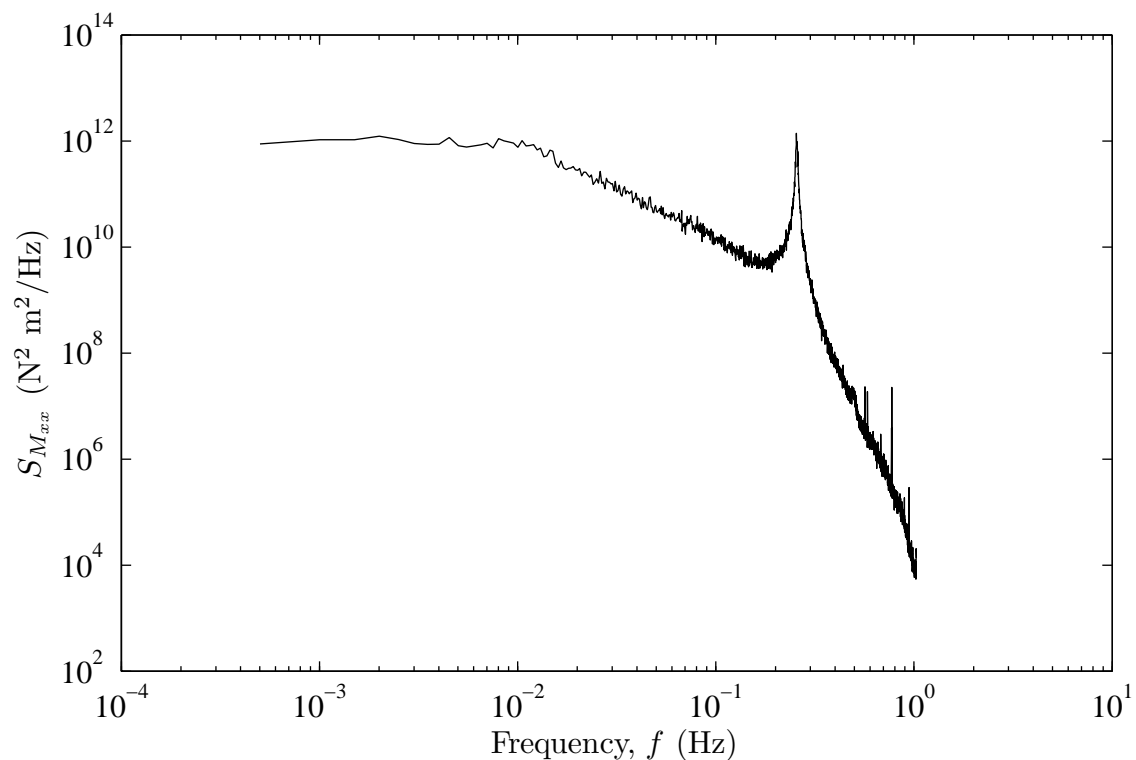
Figure 6.34: Power spectral density plot for the prototype base moment about the x-axis.

ratios used in the analysis were sourced from the FVT estimates presented in Table 5.2. The values used were 1.09%, 1.14%, and 0.86% for the x-axis, y-axis, and torsional modes respectively. The mode shapes used are displayed in Figure 5.3. Mode shape correction factors of 0.85 and 0.7 were used for the translational and torsional modes respectively.

The mass estimation was representative of the completed building with SDL and LL from tenant occupation as presented in Table 5.12. The average mass per level was 2.0×10^6 kg, resulting in an overall structure density of $230 \, \text{kg/m}^3$. The average mass moment of inertia at each level was 670×10^6 kgm^2. An example power spectral density plot for the prototype base moment about the x-axis is displayed in Figure 6.34. This plot is a combination of the modal force spectrum and the mechanical admittance function for the first mode of vibration, hence the peak at a frequency of 0.256 Hz.

The acceleration responses were estimated at point 1 in Figure 3.29 to allow direct comparison with the full-scale measurements. The complete quadratic combination (CQC) method [44] was used to combine the acceleration responses in the analysis.

Two wind events recorded during the monitoring period were used for comparison with the wind tunnel results. The first is a southerly event that occurred on 1 January 2006. The time series for the southerly event is displayed in Figure 6.35.

	β	$\bar{U}$	I_u	σ_{Dir}	$\hat{\ddot{y}}_1$	$\sigma_{\ddot{y}_1}$	$\hat{\ddot{x}}_1$	$\sigma_{\ddot{x}_1}$
	(°)	(m/s)	(−)	(°)	(mg$_\text{n}$)	(mg$_\text{n}$)	(mg$_\text{n}$)	(mg$_\text{n}$)
Southerly	160	17.8	0.145	8	2.5	0.62	1.3	0.35
Westerly	290	20.8	0.126	7	2.0	0.48	1.1	0.27

Table 6.6: Summary of full-scale results for comparison with HFBB results.

	$\sigma_{\ddot{a}_r}$		
	Full-Scale	HFBB	Difference
	(mg$_\text{n}$)	(mg$_\text{n}$)	(%)
Southerly	0.71	0.55	29
Westerly	0.55	0.75	27

Table 6.7: Comparison of combined standard deviation resonant acceleration response from the wind tunnel with full-scale measurements.

The second is a westerly wind event that occurred on 17 September 2005, which is displayed in Figure 6.36. The details of these wind events are presented in Table 6.6. These wind events were selected for comparison with the HFBB results because: they are representative of the peak events from the monitoring period; they have the most constant wind speed and direction over the hour period compared with the other records; and they have turbulence intensities similar to that modelled by the wind tunnel.

A comparison between the combined standard deviation resonant acceleration responses from the wind tunnel results and the full-scale measurements are presented in Table 6.7. For the southerly wind event, the HFBB underestimated the full-scale measurement by 29%. For the westerly wind event, the HFBB overestimated the full-scale measurement by 27%. It is noted that the measured turbulence intensity for the westerly event is 10% less than the wind tunnel turbulence intensity, which was modelled according to an AS/NZS 1170.2:2002 terrain category 3 profile. This may explain some of the difference between the measured and estimated responses for the westerly event.

A parametric study was conducted to determine the influence of changes in the natural frequencies and damping ratios on the acceleration response estimates from the HFBB test. The study included two scenarios: a 50% reduction in the natural frequencies; and a 50% reduction in the damping ratios. Table 6.8 presents a comparison between the original results with the two scenarios. For both wind events, halving the natural frequencies had the most impact on the acceleration responses. The southerly wind event has similar increases for the two scenarios, with increases of 49% and 42% for halving the natural frequencies and damping ratios respectively.
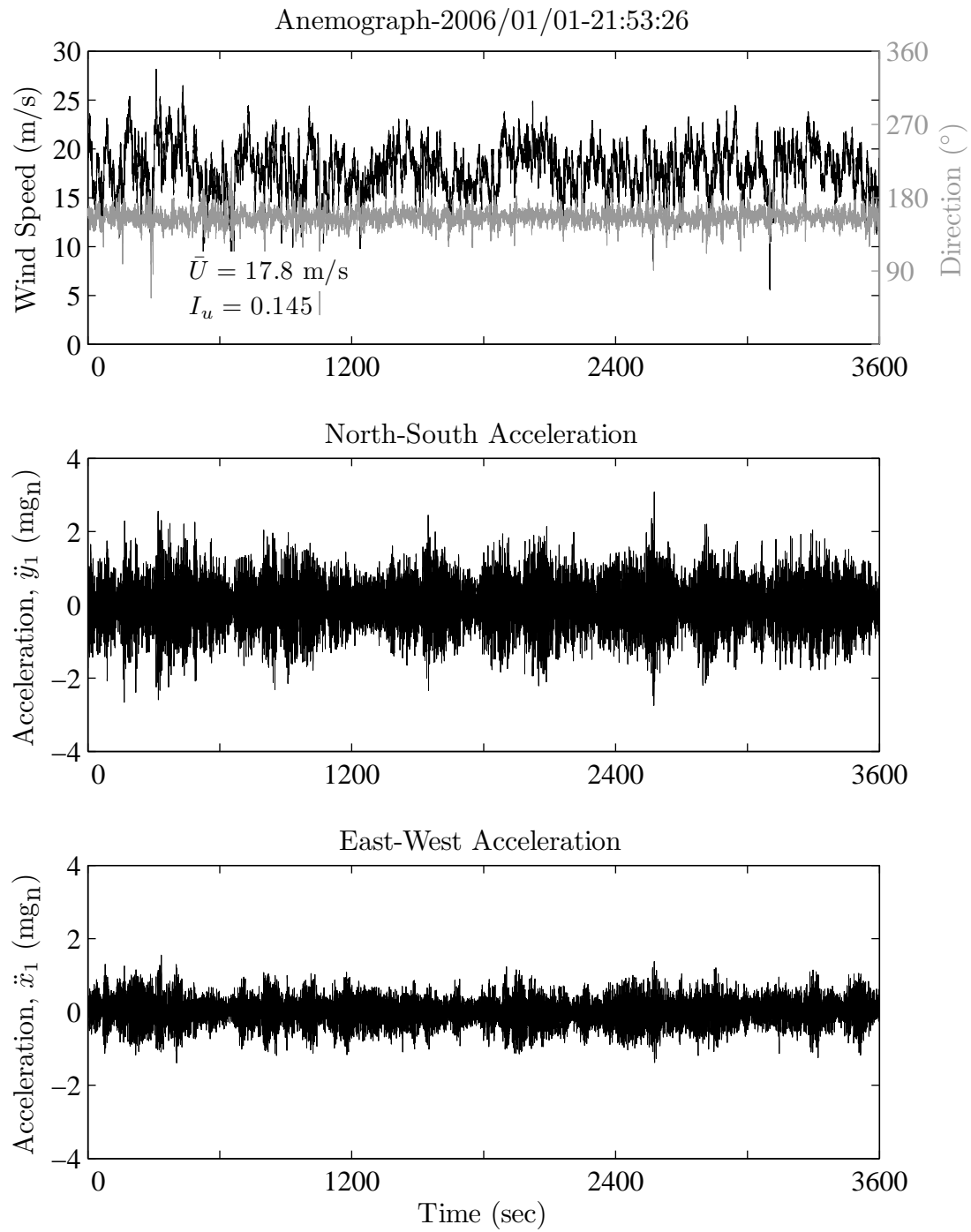
Figure 6.35: Wind speed, direction, and acceleration response for southerly wind event on 2001-01-01 21:53.
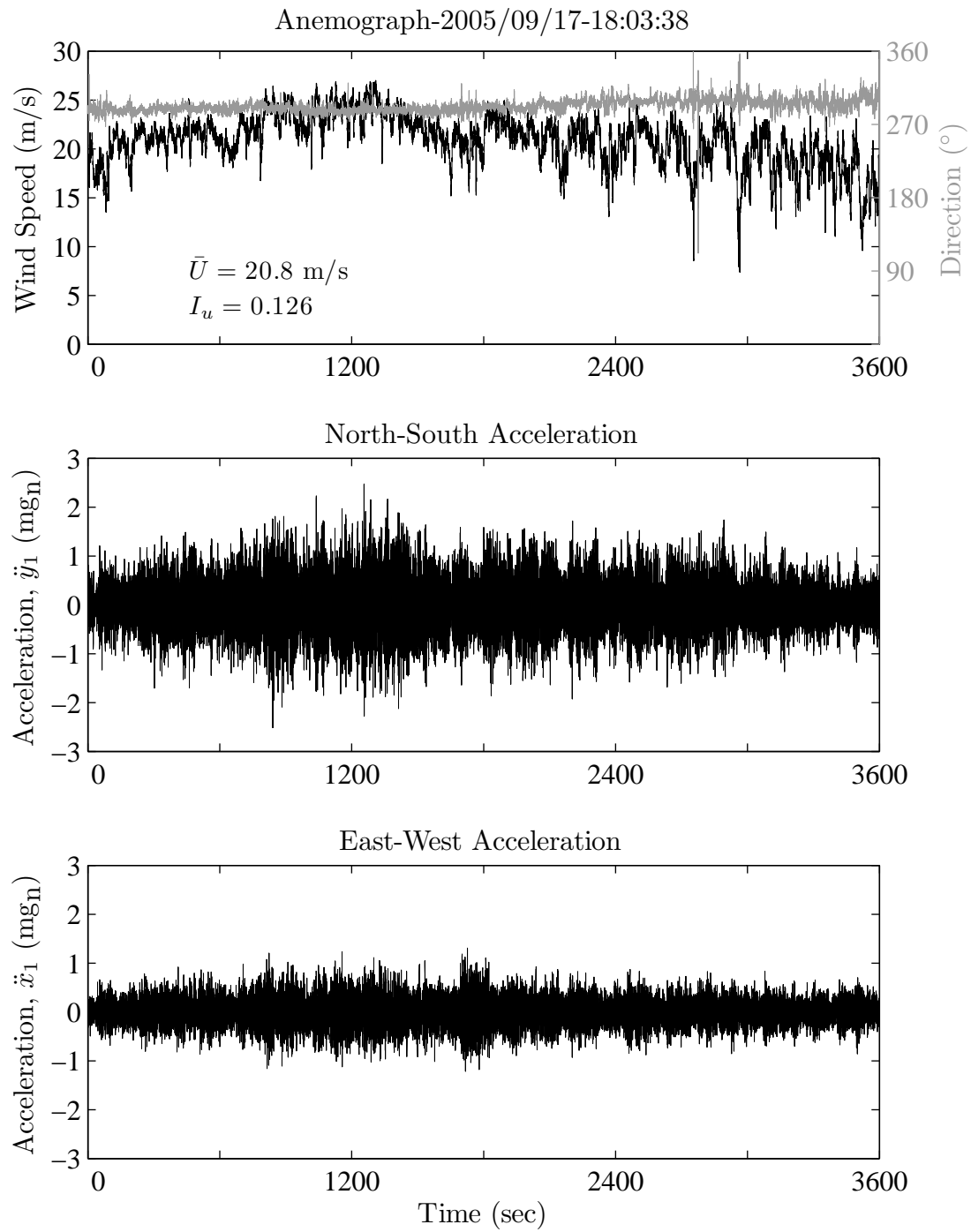
Figure 6.36: Wind speed, direction, and acceleration response for southerly wind event on 2005-09-17 18:03.

	Original	$0.5f_i$		$0.5\zeta_i$	
	$\sigma_{\ddot{a}_r}$	$\sigma_{\ddot{a}_r}$	Diff.	$\sigma_{\ddot{a}_r}$	Diff
	$(\mathrm{mg_n})$	$(\mathrm{mg_n})$	(%)	$(\mathrm{mg_n})$	(%)
Southerly	0.55	0.82	49	0.78	42
Westerly	0.75	1.3	73	1.0	33

Table 6.8: HFBB parametric study results.

The westerly event is more sensitive to changes in the natural frequencies compared with the damping ratios. The response increased by 73% when the natural frequencies were halved, while halving the damping ratios increased the response by 33%. For a wind sensitive structure, the level of overestimation from combining these scenarios could lead to the unnecessary inclusion of auxiliary damping devices. This highlights the need for accurate estimation of the natural frequency and damping ratios for inclusion in response estimates due to wind loading.

6.5   Summary

The wind-induced response of Latitude tower, recorded between August 2005 and April 2007, was presented in this chapter. The peak wind events typically originated from southerly and westerly directions. The prevailing strong winds in Sydney originate from north-easterly, southerly, and westerly directions. The north-easterly winds were not accurately recorded by the Latitude tower anemometer due to wind-structure interactions.

The mean longitudinal turbulence tended to decrease with increasing mean wind speed, and was generally between terrain category 2–4 for mean wind speeds greater than $8\,\mathrm{m/s}$. The westerly winds had less longitudinal turbulence than the southerly winds. The variability in the turbulence intensities is likely due to different meteorological phenomena and their influence on the wind conditions. The longitudinal wind speed spectrum for a southerly and westerly wind direction were approximately equal to the estimate from the Australian wind loading code [153], with the westerly wind event reporting less energy at reduced frequencies greater than two. An indication of the lateral turbulence was attained from the wind direction measurements. The standard deviation wind direction tended to stabilise at approximately 8–11° for most directions at wind speeds above $8\,\mathrm{m/s}$.

The acceleration responses for peak wind events from southerly and westerly directions were discussed. In both cases, the responses were dominated by the fundamental translational mode of vibration in the y-axis. For the southerly winds this corresponded to the along-wind direction, but for westerly winds this corresponds to

a dominant cross-wind response. This is possibly due to increased lateral turbulence in the westerly winds, as well as energy transfer via modal interference between the closely spaced fundamental translation modes.

The displacement of Latitude tower for a southerly wind event was presented. The southerly wind event was preceded by light westerly winds, before an abrupt change to a mean wind speed between 17.2–18.4 m/s. The GPS measurements recorded an 11–13 mm change in the mean North-South displacement of Latitude tower for this wind event, and little change in the East-West direction. The envelope of the displacements was similar in shape to the acceleration response envelope, and the fundamental vibration modes were visible in the spectra of the North-South and East-West displacements. This highlighted the ability of the GPS receiver to capture the resonant component of the response.

A HFBB wind tunnel test of a 1:400 scaled model was conducted to estimate the wind-induced response. The results were compared with full-scale measurements from two wind events that had similar wind characteristics as those modelled in the wind tunnel. The standard deviation resonant acceleration responses were used to compare the results, and it was found that the wind tunnel estimates were within 29% of the full-scale measurements.

A parametric study of the influence of the natural frequencies and damping ratios on the wind tunnel response estimate was conducted. Halving the natural frequencies increased the response estimates by up to 73%, while halving the damping ratios increased the responses by up to 42%. In this instance, the responses were more sensitive to the natural frequency. This result is important to consider, because large underestimations of natural frequencies have been previously documented [94], and the damping ratio is difficult to accurately estimate. For wind sensitive structures, a combined underestimation of the natural frequencies and damping ratios may lead to overestimation of the responses, resulting in an over-designed structure.

Chapter 7

Conclusions

The design of tall buildings requires an accurate understanding of the expected loading conditions and the resulting responses. For most tall buildings, wind loads form the critical load cases for ultimate and serviceability limit states. The methods for estimating tall building response to wind loading are comprised of theoretical, empirical, and scaled model test techniques. Uncertainty in the response estimates are encountered, and this is particularly true for tall building designs that are significantly different and complex relative to previous designs.

Constructing a tall building represents a singular production run, with little opportunity to iteratively improve the completed structure via full-scale testing. This is unlike other industries that have the ability to test multiple full-scale prototypes and improve the design with test results before releasing the final product. Furthermore, altering the structural arrangement of a tall building to rectify unsatisfactory performance can be extremely difficult and prohibitively expensive. This implies that estimates of loads and responses must be accurate prior to finalising the structural arrangement.

The tested building, Latitude tower, is an office tower in the Sydney central business district with a height of 187 m above ground. The building has a composite design including a reinforced concrete core, and reinforced concrete floor slabs supported by steel beams spanning between the core and perimeter columns. Outriggers linking the core and perimeter columns, as well as offset outriggers at the facade, are located at mid-height.

Two aspects of tall building wind-induced response estimation were investigated. Firstly, the estimation of tall building dynamic characteristics. And secondly, the magnitude of wind-induced responses and the mechanisms causing the response, as well as the validation of wind tunnel test techniques.

Tall building dynamic characteristics include the natural frequencies, damping ratios, and mode shapes. They are important parameters in the wind-induced response estimation process, and errors in these parameters can cause large errors in

the wind-induced response estimates.

Natural Frequency Estimation

Two methodologies for improving the accuracy of natural frequency estimates were used. The first was based on observing changes in the natural frequencies during construction and linking them with the changes in the structure. This has the potential to further the understanding of how changes in the stiffness and mass of a tall building influence the natural frequencies, which can be used to generate more accurate numerical models of future designs for predicting natural frequencies. The second methodology involved using the measured natural frequencies, during the early stages of construction, to update a finite element model representing the structure at the time of testing. The updated model attributes from the partial structure were then applied to the model representing the completed structure. This is important for two reasons. Firstly, it provides an evaluation of the assumptions and techniques used in the design, and the outcomes of the evaluation can benefit future designs. Secondly, for buildings that require auxiliary damping, a more accurate natural frequency estimate will benefit the design of the damping devices.

Observing the influence of structural components in isolation was obscured by the simultaneous nature of the construction schedule. Multiple changes in the structure where included between each test, and determining the contribution from each individual change was not possible. For the addition of concrete elements that have a stiffening influence on the structure, the change will be gradual as the concrete strength increases.

The influence of the facade was observed during the final stages of construction, since the only other changes were from fit-out, which is expected to contribute significantly less mass than the facade. During this stage the decrease in the second modes of vibration was less than the decrease in the fundamental modes. This could indicate the facade was having a stiffening influence on the second modes of vibration. This is a possibility, since the second modes will have higher components of shear action, and the facade is more likely to provide additional shear strength as opposed to bending strength. Alternatively, the different rates of natural frequency decrease could reflect the mode shape influence on added mass in the structure. A mass increase at the top of the building will have more influence on the fundamental modes, due to the mode shapes, as opposed to the second modes of vibration. It is possible that a combination of added mass and stiffness was provided by the facade, however there was no firm evidence in the results to support the latter.

The influence of the outriggers were investigated using the ratios of the natural frequencies for the fundamental mode and second mode of vibration. The addition of the core outriggers was expected to stiffen the first mode natural frequency and result

in a decrease in the ratio. However, the natural frequency ratio increased, which implies the second mode natural frequency increased relative to the fundamental mode. The result was opposite for the offset outriggers aligned to the x-axis, which caused an increase in the fundamental natural frequency relative to the second mode natural frequency. Other changes in the structure overlapped the addition of the outriggers, including the addition of floor plates and core sections, and it is possible these changes obscured the influence of the outriggers. Furthermore, the full impact of the stiffening effect of the outriggers occurs when the structure is complete, and the full extent of bending actions in the core are apparent.

A comparison of the fundamental natural frequencies for the completed structure with empirical estimates [47] showed the y-axis translation and torsional modes were within 3% of the empirical estimates, while the x-axis translation mode was within 13%. The amplitude dependence of the natural frequencies showed a decreasing trend with increasing vibration amplitude, although the change was less than 3.4% for all fundamental modes over the amplitude range 0.1–1.5 mg_n.

A detailed three dimensional finite element model of Latitude tower was constructed for updating using full-scale measurements. The lack of internal partitions coupled with the level of detail in the model put focus on the material properties as the major source of error in the natural frequency estimates. This made a strong case for underestimation of concrete strength as a likely source of natural frequency underestimation, as opposed to stiffness gains from non-structural elements. Accounting for the over specification of concrete strengths and the loading rate effects on concrete stiffness due to dynamic loading, a higher elastic modulus was estimated and used for sections of the core where typical design elastic modulus values had been initially specified. The updating of the finite element model for the partially completed structure yielded improved estimates for the natural frequencies from the model of the completed structure, from within 17% to 7% error. Furthermore, the inclusion of the floor plate beams was shown to improve the natural frequency estimates by approximately 4% for the translational vibration mode aligned with the beams.

Damping Ratio Estimation

The damping ratios measured during construction were typically between 0.8-1.1%, 0.8-1.2%, and 0.7-1.1% for the fundamental x-axis translation, y-axis translation, and torsional modes respectively. Amplitude dependence of the damping ratios during construction was observed for the translational vibration modes, and accounted for some of the range in the measured damping ratios during construction. The damping ratio estimates were within the 0.5–1.5 % range established from previous studies on buildings similar to Latitude tower. It is important to note that

the damping ratio estimates were for vibration levels significantly less than those expected during serviceability loading conditions.

Considering the tolerances in the damping ratio estimates from Latitude tower, the vibration test conducted at 38% of final building height yielded a similar result to the final measurement. Accounting for the different vibration amplitudes recorded in each test, the difference in the damping ratio estimates between the 38% and 100% completion points was less than 15% for all modes of vibration. The results presented above suggest that the damping ratios for low amplitude vibrations are not significantly influenced by the structural changes during construction. This is a particularly useful outcome, since it implies the damping ratios for the first three vibration modes of Latitude tower were known with a degree of confidence when approximately 38% of the building height was completed.

This result could be more broadly applied to other buildings that share similar structural and non-structural characteristics as Latitude tower. Furthermore, it has important implications for determining auxiliary damping requirements for wind sensitive structures. Confirming the level of damping inherent to the structure at an early stage of construction allows more accurate assessments of the amount of auxiliary damping required. If the inherent damping levels in the structure are confirmed to be sufficient, auxiliary damping devices will be unnecessary. This results in significant financial benefits by avoiding the installation of auxiliary damping devices, as well as gaining the space reserved for the damping device installation, which could be reconfigured into a rentable space.

The amplitude dependence of the damping ratios for the fundamental vibration modes were investigated using the ranked random decrement technique. The x-axis translation mode displayed decreasing damping ratios as the vibration amplitude increased, and the estimates were at least 60% larger than the AVT and FVT estimates. It is likely that the uncharacteristic nature of the amplitude dependence for this mode is due to the modal interference between the fundamental translational modes. This will cause some of the vibration energy to transfer from the x-axis accelerations to the y-axis accelerations, which will result in overestimation of the damping ratios for the x-axis vibration mode. The y-axis translation mode damping ratio values were 10% larger than the FVT and AVT values, while the torsional mode was up to 60% larger. Both of these modes displayed an increase in the damping ratios with increasing vibration amplitude. The magnitude of the increase over the range 0.1–$0.6\,\mathrm{mg_n}$ was approximately 20% for both modes.

System Identification

A comparison between the vibration testing techniques and analysis methods showed the natural frequency results from FVT and AVT were all within 5%. The damping

ratio estimates typically differed by less than 30%, and most estimates differed by less than 20%. There was no consistent pattern of the FDD or SSI techniques either over or underestimating the damping ratios reported by the FVT, and the amplitude dependence of the damping ratios did not explain the differences between the techniques. These results show the FDD and SSI techniques are suitable for determining estimates of the dynamic characteristics, particularly the natural frequencies.

The FDD and SSI techniques were specifically chosen for their ability to separate closely spaced modes, as well as their theoretical strengths in damping ratio estimation. Closely spaced modes were encountered in the vibration testing during construction, and in the modal interference between the fundamental translational modes of the completed structure. The FDD and SSI techniques were able to define these modes and achieve damping ratio estimates. The SSI technique required higher model orders than would be normally used in order to separate the modes. Appropriately conducted forced vibration tests provided the most reliable damping estimates in this research, however the AVT techniques proved suitable for establishing a damping ratio range from multiple response records, and was shown to be a beneficial technique for determining the dynamic characteristics if FVT was not possible.

Wind-induced Response

The wind-induced response of Latitude tower was recorded between August 2005 and April 2007. The monitoring programme included the measurement of wind velocities, accelerations in the orthogonal building axes, and displacements at a single point using GPS. The peak wind events recorded by the Latitude tower anemometer originated from southerly and westerly directions. The prevailing strong winds in Sydney originate from north-easterly, southerly, and westerly directions. The north-easterly winds were not accurately recorded by the Latitude tower anemometer due to wind-structure interactions. The discussion of results focused on the southerly and westerly winds.

The mean longitudinal turbulence intensities tended to decrease with increasing mean wind speed, and were between terrain category 2–4 for mean wind speeds greater than 8 m/s. The westerly winds reported less longitudinal turbulence than the southerly winds. Large differences in the turbulence intensities were observed in the westerly winds, with values ranging from 0.031 to 0.108 for one particular event. The variability in the turbulence intensities is likely due to different meteorological phenomena and their influence on the wind conditions.

The longitudinal wind speed spectrum for southerly and westerly wind directions were approximately equal to the estimate from the Australian wind loading code [153]. An indication of the lateral turbulence was attained from the wind di-

rection measurements. The standard deviation wind direction tended to stabilise at approximately 8–11 ° for most directions at wind speeds above 8 m/s.

For peak wind events from southerly and westerly directions, the acceleration responses were dominated by the fundamental translational mode of vibration in the y-axis. For the southerly winds this corresponded to the along-wind direction, but for westerly winds this corresponds to a dominant cross-wind response. This is possibly due to increased lateral turbulence in the westerly winds, as well as energy transfer via modal interference between the closely spaced fundamental translation modes.

The probability distributions of upcrossings for along-wind and cross-wind responses where not significantly different to a Gaussian distribution for both southerly and westerly winds. The slope of the linear least squares fit was greater than two, which suggests intermittent characteristics were present in the acceleration responses. The cross-wind responses had slopes closer to a Gaussian process compared with the along-wind response. For a probability of exceedance of 1/1000, the along-wind peak factors were 4.1 and 4.5 for a southerly and westerly wind respectively, and the cross-wind peak factors were 4.0 and 4.2. The peak factor estimate for a normally distributed process [39] is 3.9 for along-wind responses in both the x and y axes. The measured peak factors are for wind speeds that are significantly less than extreme events, and the additional turbulence at the lower wind speeds compared with higher wind speeds may cause larger peak factor estimates.

Displacements measured by the GPS equipment were presented for a southerly wind event with mean wind speeds between 17.2–18.4 m/s. The GPS measurements recorded an 11–13 mm change in the mean North-South displacement of Latitude tower for this wind event, and little change in the East-West direction. Dilution of precision errors from suboptimal positioning of satellites, in addition to multipath errors due to the location of the rover GPS receiver near buildings, were the likely causes of large fluctuations in the displacement measurements that were unlikely to be from wind loading. The presence of these errors hindered the observation of the quasi-static component of the response. The fundamental vibration modes were visible in the spectra of the North-South and East-West displacements, which highlighted the ability of the GPS receiver to capture the resonant component of the response. Estimates of the resonant displacements from the acceleration measurements along the y-axis (North-South) were between 7–11 mm.

An HFBB wind tunnel test of a 1:400 scaled model was conducted using boundary layer wind conditions equivalent to a terrain category 3 as defined by AS/NZS 1170.2:2002. Full-scale acceleration measurements of one hour duration were selected for comparison with the wind tunnel results. The records were selected based on having similar wind characteristics to those modelled by the wind tunnel, as well

as being representative of the peak event recorded during the monitoring period. The standard deviation resonant acceleration responses were used to compare the results.

For a southerly wind, the HFBB underestimated the full-scale acceleration response by 29%. The results for a westerly wind showed the HFBB overestimated the response by 27%. For the westerly wind, the measured turbulence intensity was 10% less than the wind tunnel value, which may explain some of the difference between the wind tunnel and full-scale acceleration responses.

A parametric study of the HFBB results show that halving the natural frequencies increased the response estimates by up to 73%, while halving the damping ratios increased the responses by up to 42%. This result is important to consider, because large underestimations of natural frequencies have been previously reported, and the damping ratio is also prone to significant variability between measured and predicted values. For wind sensitive structures, a combined underestimation of the natural frequencies and damping ratios may lead to significant overestimation of the responses, resulting in an over-designed structure. This represents extra cost, as well as potential loss of returns from decreased tenant space from the increased size of structural elements, or the space required to install auxiliary damping devices to mitigate excessive wind-induce responses.

Recommendations for Future Research

• *Further observations of structures during construction*: This approach has been shown to be effective in reducing uncertainty in natural frequency and damping ratio estimates. One building was used in this research, and the previous research is limited. More buildings of various geometries, heights, structural systems, and material properties will need to be observed before more firm conclusions can be stated regarding the ability to improve estimates of the dynamic characteristics for a wider range of structures. Many completed buildings have been tested to determine their dynamic characteristics, and the database of results have been invaluable for the determination of empirical formulas as well as providing guidance to future designs. A similar database of results for structures during construction may be equally as useful.

• *Earlier observations of structures during construction*: For this research, vibration tests started at a later stage of construction due to the unusual nature of the construction schedule — building atop an existing structure. The conclusions from this research suggest that the uncertainty in estimating the dynamic characteristics of a building can be mitigated via vibration testing of the partially completed structure. The most benefit is achieved if the uncertainty is mitigated as soon as possible after construction starts, which gives more time for amending the structure should

an undesirable forecast of the dynamic characteristics eventuate. The question is, how early in the construction cycle can tests be conducted, and do earlier tests have the same ability to provide improved forecasts? Or, does the forecasting ability diminish with decreasing percentage of completed construction?

- *System identification techniques*: Improved system identification techniques, particularly for the estimation of damping ratios from ambient vibration testing, would be beneficial to future research on tall building dynamics and wind-induced response. Natural frequency and mode shape estimates are relatively robust for ambient vibration testing, yet damping ratio estimates are subject to variability.

- *Local versus global monitoring*: Dynamic properties are examples of global updating parameters. There are benefits in using a local approach to gain more information regarding structural behaviour, which can be used to create more accurate models. A local monitoring approach implies finer grained monitoring, for example member forces/stresses and displacements/strains. This can be achieved via embedded sensors and this is starting to be implemented in tall buildings [130], but there is little published research regarding this approach for tall buildings.

- *Further full-scale validation of buildings*: The monitoring programme in this research only captured low level acceleration responses. The question remains as to how this building, and many others, would respond to wind events with larger return periods. The amount of full-scale data that is collected for tall building dynamics and wind response is small compared with the number that are constructed. In the absence of a comprehensive amount of full-scale data the current methods for estimating tall building response to wind may produce conservative results, which can cause unecessary use of more resources and additional construction costs. Further full-scale validation of buildings is necessary and is becoming easier due to the rise of structural health monitoring and the unprecedented heights achieved in current buildings — both are making owners realize the importance of monitoring structures.

- *Improved displacement measurement*: GPS theoretically has sufficient accuracy for wind-induced response monitoring, however the detrimental effects on signal quality from multipath errors are at present difficult to avoid in typical installations. Either improved multipath mitigation algorithms or hardware are required to ensure GPS provides reliable wind-induced displacement data. Alternatively, different displacement measurement techniques could be developed, or enhanced in the case of existing techniques, to achieve the accuracy and reliability required.

Bibliography

[1] R.J. Allemang and D.L. Brown. A correlation coefficient for modal vector analysis. In *Proceedings of the 1st International Modal Analysis Conference (IMAC)*, pages 110–116, Orlando, Florida, 1982. Union College, Schenectady, NY, USA.

[2] R.J. Allemang and D.L. Brown. A complete review of the complex mode indicator function (cmif) with applications. In *ISMA2006 - International Conference on Noise and Vibration Engineering*, Katholieke Universiteit Leuven, Belgium, September 2006.

[3] A. W. Anderson, J. A. Blume, H. J. Degenkolb, H. B. Hammil, E. M. Knapik, H. L. Marchand, H. C. Powers, J. E. Rinne, G. A. Sedgwick, and H. O. Sjoberg. Lateral forces of earthquake and wind. *Proceedings of the American Society of Civil Engineers*, 77(66):1–38, April 1951.

[4] Rex Barry and Phil Witty. *Accelerometer Conditioning Unit ASC650V2 Operation and Parts Manual*. Wind Engineering Services, The University of Sydney, 1st edition, February 1997.

[5] Julius S. Bendat and Allan G. Piersol. *Random data : analysis and measurement procedures*. Wiley, New York, 2nd edition, 1986. ISBN 0471040002.

[6] Julius S. Bendat and Allan G. Piersol. *Engineering applications of correlation and spectral analysis*. Wiley, New York, 2nd edition, 1993. ISBN 0471570559.

[7] Robert D. Blevins. *Formulas for Natural Frequency and mode Shape*. Van Nostrand Reinhold Company, New York, 1st edition, 1979.

[8] J.A. Blume and R.W. Binder. Periods of a modern multi-storey office building during construction. In *Proceedings of the Second World Conference on Earthquake Engineering*, volume 2, pages 1195–1205, Tokyo and Kyoto, Japan, July 1960. Science Council of Japan.

[9] John A. Blume. A machine for setting structures and ground into forced vibration. *Bulletin of the Seismological Society of America*, 25(4):361–379, October 1935.

[10] J.B. Bodeux and J.C. Golinval. Application of armav models to the identification and damage detection of mechanical and civil engineering structures. *Smart Materials and Structures*, 10(3):479–489, June 2001. doi: 10.1088/0964-1726/10/3/309.

[11] R. Brincker, Lingmi Zhang, and P. Andersen. Modal identification from ambient responses using frequency domain decomposition. In *Proceedings of the 18th International Modal Analysis Conference (IMAC-XVIII : A Conference on Structural Dynamics)*, pages 625–630, San Antonio TX, February 2000. Society for Experimental Mechanics.

[12] R. Brincker, P. Andersen, and N.J. Jacobsen. Automated frequency domain decomposition for operational modal analysis. In *Proceedings of the 25th International Modal Analysis Conference (IMAC-XXV)*. Society for Experimental Mechanics, 2007.

[13] Rune Brincker, Carlos E. Ventura, and Palle Andersen. Damping estimation by frequency domain decomposition. In Alfred L. Wicks, editor, *Proceedings of the 19th International Modal Analysis Conference (IMAC-XIX : A Conference on Structural Dynamics)*, pages 698–703, Kissimmee, Florida, USA, February 2001. Society for Experimental Mechanics, SPIE.

[14] Rune Brincker, Lingmi Zhang, and Palle Andersen. Modal identification of output-only systems using frequency domain decomposition. *Smart Materials and Structures*, 10(3):441–445, June 2001. doi: 10.1088/0964-1726/10/3/303.

[15] J. Brownjohn, T.C. Pan, A. Mita, and K.F. Chow. Dynamic and static response of republic plaza. *Journal of the Institution of Engineers Singapore*, 38 (2):35–41, 1998.

[16] James M. Brownjohn and Tso-Chien Pan. Identifying loading and response mechanisms from ten years of performance monitoring of a tall building. *Journal of Performance of Constructed Facilities*, 22(1):24–34, Feb 2008. ISSN 1943-5509. doi: 10.1061/(asce)0887-3828(2008)22:1(24).

[17] J.M.W. Brownjohn. Ambient vibration studies for system identification of tall buildings. *Earthquake Engineering & Structural Dynamics*, 32(1):71–95, January 2003. doi: 10.1002/eqe.215.

[18] J.M.W. Brownjohn, T.C. Pan, and H.K. Cheong. Dynamic response of republic plaza, singapore. *The Structural Engineer*, 76(11):221–226, June 1998.

[19] J.M.W. Brownjohn, T.C. Pan, and X.Y. Deng. Correlating dynamic characteristics from field measurements and numerical analysis of a high-rise building. *Earthquake Engineering & Structural Dynamics*, 29(4):523–543, April 2000. doi: 10.1002/(SICI)1096-9845(200004)29:4⟨523::AID-EQE920⟩3.0.CO;2-L.

[20] S. Campbell, K.C.S. Kwok, and P.A. Hitchcock. Dynamic characteristics and wind-induced response of two high-rise residential buildings during typhoons. *Journal of Wind Engineering and Industrial Aerodynamics*, 93(6):461–482, June 2005. doi: 10.1016/j.jweia.2005.03.005.

[21] S. Campbell, K.C.S. Kwok, P.A. Hitchcock, K.T. Tse, and H.Y. Leung. Field measurements of natural periods of vibration and structural damping of wind-excited tall residential buildings. *Wind and Structures*, 10(5):401–420, September 2007.

[22] Shawn Campbell. Full-scale measurements of wind-induced building motion. Masters thesis, Hong Kong University of Science and Technology, October 2005.

[23] Dean S. Carder. Observed vibrations of buildings. *Bulletin of the Seismological Society of America*, 26(3):245–277, July 1936.

[24] D.S. Carder and L. S. Jacobsen. Vibration observations. In *Earthquake Investigations in California 1934–1935*, volume Special Publication No. 201, pages 49–106. U.S. Department of Commerce, Coast and Geodetic Survey, Washington, D. C., 1936.

[25] T.K. Caughey. Classical normal modes in damped linear dynamic systems. *Journal of Applied Mechanics Series E*, 27(2):269–271, June 1960.

[26] P.D. Cha, J.J. Rosenberg, and C.L. Dyn. *Fundamentals of Modeling and Analyzing Engineering Systems*, chapter State Space Formulations of Systems Problems, pages 288–325. Number 8. Cambridge University Press, 1 edition, 2000.

[27] C. S. Chang. Study of dynamic characteristics of aeroelastic systems utilizing randomdec signatures. NASA Contractor Report NASA-CR-132563, National Aeronautics and Space Administration, Washington, D.C., January 1975.

[28] Anil K. Chopra. *Dynamics of Structures: Theory and Applications to Earthquake Engineering*. Prentice Hall, 3rd edition, 2006.

[29] Anil K. Chopra and Rakesh K. Goel. Building period formulas for estimating seismic displacements. *Earthquake Spectra*, 16(2):533–536, May 2000. doi: 10.1193/1.1586125.

[30] Anthony S. Chu. Vibration transducers. In Harris C.M. and A.G. Piersol, editors, *Harris' Shock and Vibration Handbook*, pages 12.1–12.40. McGraw-Hill, 5th edition, 2002.

[31] Henry A. Cole, Jr. On-line failure detection and damping measurement of aerospace structures by random decrement signatures. NASA Contractor Report NASA-CR-2205, National Aeronautics and Space Administration, Washington, D.C., March 1973.

[32] James W. Cooley and John W. Tukey. An algorithm for the machine computation of complex fourier series. *Mathematics of Computation*, 19(90):297–301, April 1965. doi: 10.1090/S0025-5718-1965-0178586-1.

[33] R. Crawford and H. S. Ward. Determination of the natural periods of buildings. *Bulletin of the Seismological Society of America*, 54(6A):1743–1756, December 1964.

[34] H. Crowley and R. Pinho. Period-height relationship for existing european reinforced concrete buildings. *Journal of Earthquake Engineering*, 8(S1):93–119, January 2004. doi: 10.1142/S1363246904001663.

[35] W.A. Dalgliesh. Comparison of model/full-scale wind pressures on a high-rise building. *Journal of Wind Engineering and Industrial Aerodynamics*, 1(1): 55–66, June 1975. doi: 10.1016/0167-6105(75)90006-9.

[36] A. Danay, J. Gluck, and M. Gellert. A generalized continuum method for dynamic analysis of asymmetric tall buildings. *Earthquake Engineering & Structural Dynamics*, 4(2):179–203, October/December 1975. doi: 10.1002/eqe.4290040207.

[37] A. G. Davenport. Perspectives on the full-scale measurement of wind effects. *Journal of Wind Engineering and Industrial Aerodynamics*, 1:23–54, 1975. doi: 10.1016/0167-6105(75)90005-7.

[38] Alan Garnett Davenport. The application of statistical concepts to the wind loading of structures. *Proceedings of the Institution of Civil Engineers*, 19(4): 449–472, August 1961. doi: 10.1680/iicep.1961.11304.

[39] Alan Garnett Davenport. Note on the distribution of largest values of a random function with application to gust loading. *Proceedings of the Institution of Civil Engineers*, 28(2):187–196, June 1964. doi: 10.1680/iicep.1964.10112.

[40] Alan Garnett Davenport. Gust loading factors. *Journal of the Structural Division*, 93(ST3):11–34, May/June 1967.

[41] Alan Garnett Davenport and P. Hill-Carroll. Damping in tall buildings: Its variability and treatment in design. In N. Isyumov and T. Tschanz, editors, *Building Motion in Wind*, pages 42–57. American Society of Civil Engineers, ASCE, April 1986.

[42] R.O. Denoon, G.S. Wood, P.A. Hitchcock, and K.C.S. Kwok. Full-scale measurement of dynamic characteristics of an apartment block during construction. In *Proceedings of the Australasian Structural Engineering Conference*, pages 501–505, Auckland, October 1998. Structural Engineering Society of New Zealand.

[43] Dale Depriest. *A GPS User Manual: Working With Garmin Receivers*. Authorhouse, June 2003.

[44] Armen Der Kiureghian. Structural response to stationary excitation. *Journal of the Engineering Mechanics*, 106(6):1195–1213, November/December 1980.

[45] Stanley Dunkerley. On the whirling and vibration of shafts. *Philosophical Transactions of the Royal Society of London. A*, 185:279–360, 1894. ISSN 02643820.

[46] Gustave Eiffel. *Travaux scientifiques exécutés à la tour de trois cents mètres de 1889 à 1900*. L. Maretheux, Paris, 1900.

[47] B.R. Ellis. An assessment of the accuracy of predicting the fundamental natural frequencies of buildings and the implications concerning the dynamic analysis of structures. *Proceedings of the Institution of Civil Engineers*, 69(3): 763–776, September 1980. doi: 10.1680/iicep.1980.2376.

[48] B.R. Ellis. The significance of dynamic soil-structure interaction in tall buildings. *Proceedings of the Institution of Civil Engineers*, 81(2):221–242, June 1986. doi: 10.1680/iicep.1986.601.

[49] B.R. Ellis and T. Ji. Dynamic testing and numerical modelling of the cardington steel framed building from construction to completion. *The Structural Engineer*, 74(11):186–192, June 1996.

[50] B.R. Ellis and J.D. Littler. Dynamic response of nine similar tower blocks. *Journal of Wind Engineering and Industrial Aerodynamics*, 28(1-3):339–349, August 1988. doi: 10.1016/0167-6105(88)90130-4.

[51] *Eurocode 1: Actions on structures — Part 1-4: General actions — Wind actions.* European Committee for Standardization, Brussels, en 1991-1-4:2005 edition, April 2005.

[52] D.J. Ewins. *Modal Testing: Theory, Practice and Application.* Taylor & Francis Group, 2nd edition, August 2001.

[53] Andreas Johann Felber. *Development of a hybrid bridge evaluation system.* PhD thesis, The University of British Columbia, Canada, December 1993.

[54] M.I. Friswell and J.E. Mottershead. *Finite element model updating in structural dynamics*, volume 38 of *Solid mechanics and its applications.* Kluwer Academic Publishers, Dordrecht ; Boston ; London, 1995. ISBN 0792334310.

[55] N. Fukuwa, R. Nishizaka, S. Yagi, K. Tanaka, and Y. Tamura. Field measurement of damping and natural frequency of an actual steel-framed building over a wide range of amplitudes. *Journal of Wind Engineering and Industrial Aerodynamics*, 59(2-3):325–347, March 1996. ISSN 0167-6105. doi: 10.1016/0167-6105(96)00015-3.

[56] S. Gade, N.B. Møller, H. Herlufsen, and H. Konstantin-Hansen. Frequency domain techniques for operational modal analysis. In *Proceedings of the 24th International Modal Analysis Conference (IMAC-XXIV: A Conference and Exposition on Structural Dynamics)*, St Louis, Missouri, USA, January 2006. Society for Experimental Mechanics, Curran Associates Inc.

[57] G.K. Georgoussis. A simple model for assessing periods of vibration and modal response quantities in symmetrical buildings. *The Structural Design of Tall and Special Buildings*, 15(2):139–151, June 2006. doi: 10.1002/tal.286.

[58] M. J. Glanville and K. C. S. Kwok. Wind-induced deflections of freestanding lattice towers. *Engineering Structures*, 19(1):79–91, January 1997. ISSN 0141-0296. doi: 10.1016/S0141-0296(96)00025-9.

[59] M.J. Glanville, K.C.S. Kwok, and R.O. Denoon. Full-scale damping measurements of structures in australia. *Journal of Wind Engineering and Industrial Aerodynamics*, 59(2-3):349–364, March 1996. doi: 10.1016/0167-6105(96)00016-5.

[60] Rakesh K. Goel and Anil K. Chopra. Period formulas for concrete shear wall buildings. *Journal of Structural Engineering*, 124(4):426–433, April 1998. doi: 10.1061/(ASCE)0733-9445(1998)124:4(426).

[61] Jingiun Guo and Shengjie Ge. Research of displacement and frequency of tall building under wind load using gps. In *Proceedings of the 1997 10th International Technical Meeting of the Satellite Division of the Institute of Navigation, ION GPS-97*, pages 1385–1388, Alexandria, VA, USA, September 1997. Institute of Navigation, Institute of Navigation.

[62] C.M. Harris and A.G. Piersol, editors. *Harris' Shock and Vibration Handbook*. McGraw-Hill, 5th edition, 2002.

[63] Gary C. Hart and Ramaswami Vasudevan. Earthquake design of buildings:damping. *Journal of the Structural Division*, 101(ST1):11–30, January 1975.

[64] Arthur C. Heidebrecht and Bryan Stafford Smith. Approximate analysis of tall wall-frame structures. *Journal of the Structural Division*, 99(2):199–221, February 1973.

[65] T. Hisada and K. Nakagawa. Vibrations of buildings in japan part ii: Vibration tests of various types of building structures up to failure. In *Proceedings of the World Conference on Earthquake Engineering*, pages 7II–1–7II–10, Berkeley, California, June 1956. Earthquake Engineering Research Institute and Department of Engineering, University of California.

[66] J. D. Holmes. Listing of installations. *Engineering Structures*, 17(9):676–678, November 1995. ISSN 0141-0296. doi: 10.1016/0141-0296(95)90027-6.

[67] Honeywell. *Q-Flex QA-650 Accelerometer Data Sheet*. Honeywell International Inc., Washington, USA, January 2001.

[68] G.W. Housner and A.G. Brady. Natural periods of vibration of buildings. *Journal of the Engineering Mechanics Division*, 89(EM4):31–65, August 1963.

[69] Donald E. Hudson. A new vibration exciter for dynamic tests of full scale structures. Technical Report CaltechEERL:1961.EERL.1961.001, California Institute of Technology, Pasadena, California, September 1961.

[70] Donald E. Hudson. Synchronized vibration generators for dynamic tests of full-scale structures. Technical Report CaltechEERL:1962.EERL.1962.001, Earthquake Engineering Research Laboratory, California Institute of Technology, Pasadena, California, November 1962.

[71] Donald E. Hudson. Resonance testing of full-scale structures. *Journal of the Engineering Mechanics Division*, 90(EM3):1–19, June 1964.

[72] Donald E. Hudson, W. O. Keightley, and N. N. Nielsen. A new method for the measurement of the natural periods of buildings. *Bulletin of the Seismological Society of America*, 54(1):233–241, February 1964.

[73] S.R. Ibrahim. Random decrement technique for modal identification of structures. *Journal of Spacecraft and Rockets*, 14(11):696–700, 1977.

[74] Daniel J. Inman. *Engineering Vibration*. Prentice-Hall, 1994.

[75] *ISO 2394:1998 — General principles on reliability for structures.* International Organization for Standardization, June 1998.

[76] N. Isyumov. The aeroelastic modeling of tall buildings. In Timothy A. Reinhold, editor, *Wind tunnel modeling for civil engineering applications: Proceedings of the International Workshop on Wind Tunnel Modeling Criteria and Techniques in Civil Engineering Applications*, pages 373–407, Gaithersburg, Maryland, USA, April 1982. National Bureau of Standards, U.S. Department of Commerce, USA, Cambridge University Press. ISBN 0-521-25278-4.

[77] L.S. Jacobsen. Damping in composite structures. In *Proceedings of the Second World Conference on Earthquake Engineering*, pages 1029–1044, Tokyo, Japan, 1960.

[78] Lydik S. Jacobsen. Natural periods of uniform cantilever beams. *Proceedings of the American Society of Civil Engineers*, 64(3):431–460, March 1938.

[79] A. P. Jeary. *Designer's Guide To Dynamic Response Of Structures*. Routledge, USA, 1998.

[80] A.P. Jeary. Establishing non-linear damping characteristics of structures from non-stationary response time-histories. *The Structural Engineer*, 70(4):61–66, February 1992.

[81] A.P. Jeary. Damping in structures. *Journal of Wind Engineering and Industrial Aerodynamics*, 72:345–355, November-December 1997. doi: 10.1016/S0167-6105(97)00263-8.

[82] A.P. Jeary and B.R. Ellis. A study of the measured and predicted behaviour of a 46-storey building. In C.A. Brebbia, P.L. Gould, and J. Munro, editors, *Proceedings of the First International Conference on Environmental Forces on Engineering Structures*, pages 121–135, Imperial College, London, UK, July 1979. Pentech Press.

[83] *Data Sheet - 100M40*. JR3, Inc., California, USA, 2006.

[84] S. H. Ju and M. C. Lin. Comparison of building analyses assuming rigid or flexible floors. *Journal of Structural Engineering*, 125(1):25–31, January 1999. doi: 10.1061/(ASCE)0733-9445(1999)125:1(25).

[85] Kiyoshi Kanai and Shizuyo Yoshizawa. On the damping of vibration of actual buildings. i. *Bulletin of the Earthquake Research Institute*, 30(2):121–126, June 1952.

[86] Kiyoshi Kanai and Shizuyo Yoshizawa. On the period and the damping of vibration in actual buildings. *Bulletin of the Earthquake Research Institute*, 39(3):477–489, December 1961.

[87] Kiyoshi Kanai, Teiji Tanaka, and Tomisaburo Suzuki. Vibration experiments with the actual buildings. *Bulletin of the Earthquake Research Institute*, 27(1/4):91–95, June 1950.

[88] Igor A. Karnovsky and Olga I. Lebed. *Formulas for Structural Dynamics - Tables, Graphs, and Solutions*, chapter Transverse Vibration Equations, pages 1–13. McGraw-Hill, 2001.

[89] Hirosi Kawasumi and Kiyoshi Kanai. Vibrations of buildings in japan part i: Small amplitude vibrations of actual buildings. In *Proceedings of the World Conference on Earthquake Engineering*, pages 7I–1–7I–14, Berkeley, California, June 1956. Earthquake Engineering Research Institute and Department of Engineering, University of California.

[90] Tracey Kijewski and Ahsan Kareem. Reliability of random decrement technique for estimates of structural damping. In *8th ASCE Specialty Conference on Probabilistic Mechanics and Structural Reliability*. ASCE, ASCE, New York, NY, USA, 2000.

[91] Tracey Kijewski-Correa, John Kilpatrick, Rachel Bashor, Dae-Kun Kwon, Bradley S. Young, Robert C. Sinn, Jon Galsworthy, Dave Morrish, Nicholas Isyumov, and Ahsan Kareem. Full-scale validation of the wind-induced response of tall buildings: Updated findings from the chicago monitoring project. In *Metropolis & Beyond: Proceedings of the 2005 Structures Congress and the 2005 Forensic Engineering Symposium*, volume 171, pages 63–63, New York, April 2005. ASCE. doi: 10.1061/40753(171)63.

[92] Tracy Kijewski-Correa and Audrey Bentz. Wind-induced vibrations of buildings: role of transient events. *Proceedings of the ICE - Structures and Buildings*, 164(4):273–284, Aug 2011. ISSN 1751-7702. doi: 10.1680/stbu.2011.164.4.273.

[93] Gyeong-Ho Kim and Youn-Sik Park. An improved updating parameter selection method and finite element model update using multiobjective optimisation technique. *Mechanical Systems and Signal Processing*, 18(1):59–78, January 2004. doi: 10.1016/S0888-3270(03)00042-6.

[94] Ji Young Kim, Eunjong Yu, Dae Young Kim, and Sang-Dae Kim. Calibration of analytical models to assess wind-induced acceleration responses of tall buildings in serviceability level. *Engineering Structures*, 31(9):2086–2096, September 2009. ISSN 0141-0296. doi: 10.1016/j.engstruct.2009.03.010.

[95] P. H. Kirkegaard and P. Andersen. State space identification of civil engineering structures from output measurements. In *Proceedings of the 15th International Modal Analysis Conference (IMAC)*, pages 889–895, Orlando, Florida, February 1997. Society for Experimental Mechanics, Society for Experimental Mechanics.

[96] Shoji Kobayashi. Sway observation of tall building in strong wind : Keio plaza hotel building 170m high. *Transactions of the Architectural Institute of Japan*, 192:33–39, 88, February 1972. ISSN 03871185.

[97] K. C. S. Kwok and B. Samali. Performance of tuned mass dampers under wind loads. *Engineering Structures*, 17(9):655–667, November 1995. ISSN 0141-0296. doi: 10.1016/0141-0296(95)00035-6.

[98] K.C.S. Kwok. Natural frequencies of vibration and damping ratios of tall buildings and structures. In Cheng Wenrang and Lu Qin, editors, *Proceedings of the 2nd International Conference on High-rise Buildings*, pages 396–401, Nanjing, China, March 1992.

[99] K.C.S. Kwok, L.W. Apperley, I.J. Matesic, and C.B. Mangion. Measurement of natural frequencies of vibration and damping ratios of tall buildings and structures. In *Second National Structural Engineering Conference*, National conference publication no. 90/10, pages 23–27, Adelaide, October 1990. Institution of Engineers Australia, Institution of Engineers Australia.

[100] S. Lagomarsino. Forecast models for damping and vibration periods of buildings. *Journal of Wind Engineering and Industrial Aerodynamics*, 48(2-3):221–239, October 1993. doi: 10.1016/0167-6105(93)90138-E.

[101] Benjamin Joseph Lazan. *Damping of Materials and Members in Structural Mechanics*. Pergamon Press, 1968.

[102] Leica. Introduction to gps (global positioning system) v 1.0. Leica Geosystems AG, Heerbrugg, Switzerland, 1999.

[103] Steven J. Leon. *Linear Algebra with Applications*. Prentice-Hall, 4th edition, 1994.

[104] B. Li, G. L. Hutchinson, and C. F. Duffield. The influence of non-structural components on tall building stiffness. *The Structural Design of Tall and Special Buildings*, -:–, 2009. ISSN 1541-7808. doi: 10.1002/tal.565.

[105] Q. S. Li. A new exact approach for determining natural frequencies and mode shapes of non-uniform shear beams with arbitrary distribution of mass or stiffness. *International Journal of Solids and Structures*, 37(37):5123–5141, September 2000. ISSN 0020-7683. doi: 10.1016/S0020-7683(99)00201-2.

[106] Q. S. Li, Ke. Yang, C. K. Wong, and A. P. Jeary. The effect of amplitude-dependent damping on wind-induced vibrations of a super tall building. *Journal of Wind Engineering and Industrial Aerodynamics*, 91(9):1175–1198, September 2003. ISSN 0167-6105. doi: 10.1016/S0167-6105(03)00080-1.

[107] Q. S. Li, Lun-Hai Zhi, Alex Y. Tuan, Chin-Sheng Kao, Sheng-Chung Su, and Chien-Fu Wu. Dynamic behavior of taipei 101 tower: Field measurement and numerical analysis. *Journal of Structural Engineering*, 137(1):143–155, January 2011. doi: 10.1061/(ASCE)ST.1943-541X.0000264.

[108] Q.S. Li and J.R. Wu. Correlation of dynamic characteristics of a super-tall building from full-scale measurements and numerical analysis with various finite element models. *Earthquake Engineering & Structural Dynamics*, 33 (14):1311–1336, November 2004. doi: 10.1002/eqe.405.

[109] Q.S. Li, J.R. Wu, S.G. Liang, Y.Q. Xiao, and C.K. Wong. Full-scale measurements and numerical evaluation of wind-induced vibration of a 63-story reinforced concrete tall building. *Engineering Structures*, 26(12):1779–1794, October 2004. doi: 10.1016/j.engstruct.2004.06.014.

[110] Q.S. Li, Y.Q. Xiao, J.Y. Fu, and Z.N. Li. Full-scale measurements of wind effects on the jin mao building. *Journal of Wind Engineering and Industrial Aerodynamics*, 95(6):445–466, June 2007. doi: 10.1016/j.jweia.2006.09.002.

[111] J. D. Littler. An assessment of some of the different methods for estimating damping from full-scale testing. *Journal of Wind Engineering and Industrial Aerodynamics*, 57(2-3):179–189, July 1995. doi: 10.1016/0167-6105(94)00109-Q.

[112] John David Littler. *The Response of a Tall Building to Wind Loading.* PhD thesis, University College London, London, U.K., March 1991.

[113] Lennart Ljung. *System Identification: Theory for the User.* PTR Prentice Hall, Upper Saddle River, NJ, 2nd edition, 1999.

[114] J.W. Lovse, W.F. Teskey, G. Lachapelle, and M.E. Cannon. Dynamic deformation monitoring of tall structure using gps technology. *Journal of Surveying Engineering*, 121(1):35–40, February 1995. doi: 10.1061/(ASCE)0733-9453(1995)121:1(35).

[115] H. H. Mabie and C. B. Rogers. Transverse vibrations of double-tapered cantilever beams. *Journal of the Acoustical Society of America*, 51(5B):1771–1774, May 1972. doi: 10.1121/1.1913028.

[116] W. H. Melbourne. Probability distributions associated with the wind loading of structures. *Institution of Engineers, Australia – Civil Engineering Transactions*, CE 19(1):58–67, 1977.

[117] A. M. Memari, A. A. Aghakouchak, M. Ghafory Ashtiany, and M. Tiv. Full-scale dynamic testing of a steel frame building during construction. *Engineering Structures*, 21(12):1115–1127, December 1999. doi: 10.1016/S0141-0296(98)00068-6.

[118] M. Meyyappa, H. Palsson, and J. I. Craig. Modal parameter estimation for highrise building using ambient response data taken during construction. In G.C. Hart, editor, *Dynamic Response of Structures: Experimentation, Observation, Prediction, and Control*, pages 141–151. American Society of Civil Engineers, ASCE, New York, NY, USA, January 1980.

[119] Sher Ali Mirza, Michael Hatzinikolas, and James G. MacGregor. Statistical descriptions of strength of concrete. *Journal of the Structural Division*, 105 (ST6):1021–1037, June 1979.

[120] Koichi Miyashita, Masaru Itoh, Kunio Fujii, Junichi Yamashita, and Toshio Takahashi. Full-scale measurements of wind-induced responses on the hamamatsu act tower. *Journal of Wind Engineering and Industrial Aerodynamics*, 74-76:943–953, April 1998. ISSN 0167-6105. doi: 10.1016/S0167-6105(98)00086-5.

[121] B.J. Morgan, S.C. Larson, and R.G. Oesterle. Field measured dynamic characteristics of buildings. In D.R. Sherman, editor, *Building Structures: Proceedings of the Sessions of Structures Congress 87*, pages 250–257, New York, August 1987. American Society of Civil Engineers.

[122] R. Shankar Nair. Belt trusses and basements as "virtual" outriggers for tall buildings. *Engineering Journal*, 35(4):140–146, Fourth Quarter 1998.

[123] Tachu Naito, Morio Takeuchi, Yasuo Tanaka, Nobuji Nasu, Goro Kubota, and Michiya Hara. Vibrational characteristics of actual buildings determined by vibration test. *Bulletin of Science and Engineering Research Laboratory, Waseda University*, No. 16:3–9, 1961.

[124] Kyoji Nakagawa. Vibrational characteristics of buildings part ii: Vibrational characteristics of reinforced concrete buildings existing in japan. In *Proceedings of the Second World Conference on Earthquake Engineering*, volume 2, pages 973–982, Tokyo and Kyoto, Japan, July 1960. Science Council of Japan.

[125] Robert K. Otnes and Loren Enochson. *Digital time series analysis*. John Wiley & Sons Inc, New York, November 1972.

[126] Tso-Chien Pan, Xuting You, and James M. W. Brownjohn. Effects of infill walls and floor diaphragms on the dynamic characteristics of a narrow-rectangle building. *Earthquake Engineering & Structural Dynamics*, 35(5): 637–651, February 2006. doi: 10.1002/eqe.550.

[127] Bart Peeters and Guido De Roeck. Reference-based stochastic subspace identification for output-only modal analysis. *Mechanical Systems and Signal Processing*, 13(6):855–878, November 1999. doi: 10.1006/mssp.1999.1249.

[128] A.W. Phillips and R.J. Allemang. Data presentation schemes for selection and identification of modal parameters. In *Proceedings of the 23rd International Modal Analysis Conference (IMAC-XXIII: A Conference and Exposition on Structural Dynamics)*, page 10pp, Orlando, Florida, January-February 2005. Society for Experimental Mechanics, Curran Associates Inc.

[129] Charles L. Phillips, John M. Parr, and Eve A. Riskin. *Signals, Systems, and Transforms*. Pearson Prentice Hall, Upper Saddle River, N.J., 3rd edition, August 2003.

[130] Nadine M.. Post. Dubai supertower is 'supersensored'. *Engineering News-Record*, 264(2):10–11, January 2010.

[131] M. Prevosto. *Algorithmes D'Identification des Caractéristiques Vibratoires de Structures Mecaniques Complexes*. PhD thesis, Université de Rennes 1, France, 1982.

[132] J.C. Rathbun. Wind forces on a tall building. *Transactions of the American Society of Civil Engineers*, 105(Paper 2056):1–41, 1940.

[133] John William Strutt Rayleigh. *The Theory of Sound*, volume 1. Macmillan, London, 1877.

[134] Moshe F. Rubinstein. Effect of axial deformation on the periods of a tall building. *Bulletin of the Seismological Society of America*, 54(1):243–261, February 1964.

[135] Avigdor Rutenberg. Approximate natural frequencies for coupled shear walls. *Earthquake Engineering & Structural Dynamics*, 4(1):95–100, July 1975. doi: 10.1002/eqe.4290040107.

[136] M. Ruzzene, A. Fasana, L. Garibaldi, and B. Piombo. Natural frequencies and dampings identification using wavelet transform: application to real data. *Mechanical Systems and Signal Processing*, 11(2):207–218, March 1997. doi: 10.1006/mssp.1996.0078.

[137] Peter Rybaczyk. *Expert Network Time Protocol: An Experience in Time with NTP*. Apress, 2005.

[138] M.G. Salvadori and E. Heer. Periods of framed buildings for earthquake analysis. *Journal of the Structural Division*, 86(ST12):59–71, December 1960.

[139] N. Satake, K. Suda, T. Arakawa, A. Sasaki, and Y. Tamura. Damping evaluation using full-scale data of buildings in japan. *Journal of Structural Engineering*, 129(4):470–477, April 2003. doi: 10.1061/(ASCE)0733-9445(2003)129:4(470).

[140] Naoki Satake and Haruhiko Yokota. Evaluation of vibration properties of high-rise steel buildings using data of vibration tests and earthquake observations. *Journal of Wind Engineering and Industrial Aerodynamics*, 59(2-3):265–282, March 1996. ISSN 0167-6105. doi: 10.1016/0167-6105(96)00011-6.

[141] Norman David Schuster. Dynamic characteristics of a 30 storey building during construction detected from ambient vibration measurements. Master of applied science thesis, Department of Civil Engineering, The University of British Columbia, Vancouver, Canada, October 1994.

[142] A.F. Seybert. Estimation of damping from response spectra. *Journal of Sound and Vibration*, 75(2):199–206, March 1981. ISSN 0022-460X. doi: 10.1016/0022-460X(81)90339-4.

[143] C. Y. Shih, Y. G. Tsuei, R. J. Allemang, and D. L. Brown. Complex mode indication function and its applications to spatial domain parameter estimation. *Mechanical Systems and Signal Processing*, 2(4):367–377, October 1988. ISSN 0888-3270. doi: 10.1016/0888-3270(88)90060-X.

[144] P. D. Spanos and B. A. Zeldin. Generalized random decrement method for analysis of vibration data. *Journal of Vibration and Acoustics*, 120(3):806–813, July 1998. doi: 10.1115/1.2893901.

[145] Neil R. Sparks. Building vibrations. *Bulletin of the Seismological Society of America*, 25(4):381–386, October 1935.

[146] Bryan Stafford Smith and Alex Coull. *Tall Building Structures: Analysis and Design*. Wiley-Interscience, 1 edition, July 1991. ISBN 0471512370.

[147] Bryan Stafford Smith and Elizabeth Crowe. Estimating periods of vibration of tall buildings. *Journal of Structural Engineering*, 112(5):1005–1019, May 1986. doi: 10.1061/(ASCE)0733-9445(1986)112:5(1005).

[148] J. R. Stagner and G. Hart. Damping estimation and digital filtering applied to structural motion studies. Technical Report UCLA-ENG-7181, School of Engineering and Applied Science, University of California, Los Angeles, December 1971.

[149] *AS/NZS 1170.2:1989 Minimum design loads on structures — Part 2: Wind loads.* Standards Australia, Sydney, Australia, amendment no. 3 edition, December 1993.

[150] *AS/NZS 1170.0:2002 Structural design actions — General principles.* Standards Australia, Sydney, Australia, amendment no. 4 edition, April 2005.

[151] *AS/NZS 1170.2:2002 Structural design actions — Part 2: Wind actions.* Standards Australia, Sydney, Australia, amendment no. 1 edition, April 2005.

[152] *AS 3600:2009 Concrete Structures.* Standards Australia, Sydney, Australia, amendment no. 1 edition, November 2010.

[153] *AS/NZS 1170.2:2011 Structural design actions — Part 2: Wind actions.* Standards Australia, Sydney, Australia, March 2011.

[154] Roy M. Stephen, Jeffrey P. Hollings, and Jack G. Bouwkamp. Dynamic behavior of a multistory pyramid-shaped building. Technical Report EERC 73-17, Earthquake Engineering Research Centrer, University of California, Berkeley, September 1973.

[155] *Strand7 Software: Theoretical Manual.* Strand7 Pty Ltd, Sydney, Australia, 1st edition, January 2005.

[156] R.K.L. Su, A.M. Chandler, M.N. Sheikh, and N.T.K. Lam. Influence of non-structural components on lateral stiffness of tall buildings. *The Structural Design of Tall and Special Buildings*, 14(2):143–164, June 2005. doi: 10.1002/tal.266.

[157] Kenichi Suda, Naoki Satake, Junichiro Ono, and Atsushi Sasaki. Damping properties of buildings in japan. *Journal of Wind Engineering and Industrial Aerodynamics*, 59(2-3):383–392, March 1996. ISSN 0167-6105. doi: 10.1016/0167-6105(96)00018-9.

[158] Somsak Swaddiwudhipong, Seng-Lip Lee, and Qin Zhou. Effect of axial deformation on vibration of tall buildings. *Struct. Design Tall Build.*, 10(2):79–91, 2001. ISSN 1099-1794. doi: 10.1002/tal.175.

[159] Morio Takeuchi. Vibrational characteristics of buildings part i: Vibrational characteristics of actual buildings determined by vibration tests. In *Proceedings of the Second World Conference on Earthquake Engineering*, volume 2, pages 961–971, Tokyo and Kyoto, Japan, July 1960. Science Council of Japan.

[160] Y. Tamura, K. Suda, and A. Sasaki. Damping in buildings for wind resistant design. In Chang-Koon Choi, Givanni Solari, Jun Kanda, and Ahsan Kareem, editors, *Proceedings of the First International Syposium on Wind and Structures for the 21st Century*, pages 115–129, Cheju, Korea, January 2000. Techno Press.

[161] Y. Tamura, M. Matsui, L. Pagnini, R. Ishibashi, and A. Yoshida. Measurement of wind-induced responses of buildings using rtk-gps. *Journal of Wind Engineering and Industrial Aerodynamics*, 90(12-15):1783–1793, December 2002. doi: 10.1016/S0167-6105(02)00287-8.

[162] Yukio Tamura. Application of damping devices to suppress wind-induced responses of buildings. *Journal of Wind Engineering and Industrial Aerodynamics*, 74-76:49–72, April 1998. ISSN 0167-6105. doi: 10.1016/S0167-6105(98)00006-3.

[163] Yukio Tamura and Shin-ya Suganuma. Evaluation of amplitude-dependent damping and natural frequency of buildings during strong winds. *Journal of Wind Engineering and Industrial Aerodynamics*, 59(2-3):115–130, March 1996. doi: 10.1016/0167-6105(96)00003-7.

[164] Yukio Tamura, Lingmi Zhang, Akihito Yoshida, Shinji Nakata, and Takayoshi Itoh. Ambient vibration tests and modal identification of structures by fdd and 2dof-rd technique. In Katsumi Yano, editor, *SEWC2002: Structural Engineers World Congress*, Yokohama, Japan, October 2002.

[165] Teiji Tanaka, Shizuyo Yoshizawa, Yutaka Osawa, and Toshizo Morishita. Period and damping of vibration in actual buildings during earthquakes. *Bulletin of the Earthquake Research Institute*, 47(6):1073–1092, December 1969.

[166] George T. Taoka, Augustine S. Furumoto, and Arthur N. L. Chiu. Dynamic properties of tall shear-wall buildings. *Journal of the Structural Division*, 100 (ST2):305–317, February 1974.

[167] B.S. Taranath. Optimum belt truss locations for high-rise structures. *Engineering Journal*, 11(1):18–21, First Quarter 1974.

[168] Bungale S. Taranath. *Steel, Concrete, and Composite Design of Tall Buildings*. McGraw-Hill, 1 edition, December 1997. ISBN 0070629145.

[169] The MathWorks Inc. *Matlab and System Identification Toolbox Release 2007b*. Natick, Massachusetts, United States, v7.5.0.342 edition, August 2007.

[170] The MathWorks Inc. *Matlab and Signal Processing Toolbox Release 2007b*. Natick, Massachusetts, United States, v7.5.0.342 edition, August 2007.

[171] William T. Thomson. *Theory of Vibration with Applications*. Unwin Hyman, 3rd edition, 1988.

[172] S.P. Timoshenko. *Vibration Problems in Engineering*. D. Van Nostrand Company, 2nd edition, 1937.

[173] M.D. Trifunac. Ambient vibration test of a 39-strory steel frame building. Technical Report EERL 70-02, California Institute of Technology, Earthquake Engineering Research Laboratory, July 1970.

[174] T. Tschanz and Alan Garnett Davenport. The base balance technique for the determination of dynamic wind loads. *Journal of Wind Engineering and Industrial Aerodynamics*, 13(1-3):429–439, December 1983. doi: 10.1016/0167-6105(83)90162-9.

[175] F.E. Udwadia and M.D. Trifunac. Ambient vibration tests of full-scale structures. In *Proceedings of the Fifth World Conference on Earthquake Engineering*, volume 2, pages 1430–1439, Rome, 1974.

[176] Peter Van Overschee and Bart De Moor. N4sid: Subspace algorithms for the identification of combined deterministic-stochastic systems. *Automatica*, 30 (1):75–93, January 1994. doi: 10.1016/0005-1098(94)90230-5.

[177] J. K. Vandiver, A. B. Dunwoody, R. B. Campbell, and M. F. Cook. A mathematical basis for the random decrement vibration signature analysis technique. *Journal of Mechanical Design*, 104(2):307–313, April 1982. doi: 10.1115/1.3256341.

[178] Carlos E. Ventura and Norman D. Schuster. Structural dynamic properties of a reinforced concrete high-rise building during construction. *Canadian Journal of Civil Engineering*, 23(4):950–972, August 1996. doi: 10.1139/l96-901.

[179] C.E. Ventura and T. Horyna. Measured and calculated modal characteristics of heritage court tower invancouver, b.c. In *2000 IMAC XVIII - 18th International Modal Analysis Conference*, 2000.

[180] C.E. Ventura, J.F. Lord, M. Turek, R. Brincker, P. Andersen, and E. Dascotte. Fem updating of tall buildings using ambient vibration data. In *The proceedings of 6th International Conference on Structural Dynamics (EURODYN)*, pages 237–242, Rotterdam, The Netherlands, September 2005. Millpress.

[181] B.J. Vickery. On the assessment of wind effects on elastic structures. *Institution of Engineers, Australia – Civil Engineering Transactions*, CE 8(2): 183–192, October 1966.

[182] Han-chung Wang and Will J. Worley. Tables of natural frequencies and nodes for transverse vibration of tapered beams. NASA Contractor Report NASA-CR-443, National Aeronautics and Space Administration, University of Illinois, April 1966.

[183] R.F Warner, B.V. Rangan, A.S. Hall, and K.A. Faulkes. *Concrete Structures*. Longman, 1998.

[184] P. Welch. The use of fast fourier transform for the estimation of power spectra: A method based on time averaging over short, modified periodograms. *IEEE Transactions on Audio and Electroacoustics*, 15(2):70–73, June 1967. doi: 10.1109/TAU.1967.1161901.

[185] E. L. Wilson and J. Penzien. Evaluation of orthogonal damping matrices. *International Journal for Numerical Methods in Engineering*, 4(1):5–10, January/February 1972. ISSN 1097-0207. doi: 10.1002/nme.1620040103.

[186] J. R. Wu and Q. S. Li. Finite element model updating for a high-rise structure based on ambient vibration measurements. *Engineering Structures*, 26(7):979–990, June 2004. doi: 10.1016/j.engstruct.2004.03.002.

[187] T. A. Wyatt. Mechanisms of damping. In *Symposium on Dynamic Behavior of Bridges*, number TRRL Supplementary Report 275, pages 10–21, Crowthorne, Berkshire, England, May 1977. Transport and Road Research Laboratory.

[188] Y.L. Xu, K.C.S. Kwok, and B. Samali. Torsion response and vibration suppression of wind-excited buildings. *Journal of Wind Engineering and Industrial Aerodynamics*, 43(1-3):1997–2008, October 1992. doi: 10.1016/0167-6105(92) 90623-I.

[189] H.P. Yin. A new theoretical basis for the bandwidth method and optimal power ratios for the damping estimation. *Mechanical Systems and Signal Processing*, 22(8):1869–1881, November 2008. ISSN 0888-3270. doi: 10.1016/j.ymssp.2008. 01.011.